PECULIAR PEROVSKITES: UNRAVELING THE UNIQUE OPTICAL RESPONSE OF HYBRID ORGANIC-INORGANIC PEROVSKITES FROM FIRST PRINCIPLES

BY

JOSHUA A. LEVEILLEE

DISSERTATION

Submitted in partial fulfillment of the requirements
for the degree of Doctor of Philosophy in Materials Science and Engineering
in the Graduate College of the
University of Illinois at Urbana-Champaign, 2019

Urbana, Illinois

Doctoral Committee:

Assistant Professor André Schleife, Chair
Professor Dallas Trinkle
Professor Moonsub Shim
Assistant Professor Josh Vura-Weis

Abstract

Hybrid organic-inorganic perovskite (HOP) materials and their layered analogs (LHOP) have been extensively applied to optoelectronic applications including solar cells, light-emitting diodes, optical detectors, and spintronics due to their unique atomic, electronic, and optical properties. HOPs and LHOPs are hosts to fascinating microscopic interactions that influence their macroscopic optical and electronic properties. Researchers still debate how interactions between optically excited charge carriers, free-carriers, lattice vibrations, and atomic geometry influence the measured optical response of HOPs. First principles simulations provide a window to examine how these atomic-scale interactions contribute piece-by-piece to the measurable optical properties of materials. In this PhD thesis, I apply and develop first principles optical calculations based on density functional theory and many-body perturbation theory to determine how the optical response and excitonic properties of HOPs and LHOPs are influenced by the presence of free-carriers, polar lattice vibrations, and layer stoichiometry. In order to describe polar lattice screening, I extend the lattice screened Coulomb interaction in the Fan-Migdal self energy to the electron-hole interaction by the Shindo approximation and subsequently construct model screening functions from the generalized and simple Fröhlich models for the electron-phonon vertex. Additionally, I apply optical response calculations to predict how the choice of organic spacer layers in LHOPs can be used to design novel triplet light-emitting materials with emission wavelengths spanning the visible range.

To my parents, Dr. Mary Leveillee and Ronald Leveillee, and my sister, Alexandra.

Acknowledgments

I would like to thank and acknowledge my Ph.D advisor, Prof. André Schleife for his guidance, mentoring, and advising. Under his instruction I have learned and grown immensely as a researcher in the past five and a half years. I would like to thank my collaborators: Dr. Amanda J. Neukirch, Prof. Josh Vura-Weis, Dr. Sergei Tretiak, Prof. Claudine Katan, and Prof. Jacky Even. I would also like to thank my lab mates and coworkers, Xiao Zhang, Cheng-Wei (Oscar) Lee, Alina Kononov, Tatiane Pereira dos Santos, Ethan Shapera, Kisung Kang, Erick Hernandez, Max Verkamp, Brendan Smith, and Sina Lewis for their support and fruitful research discussions. The support of my friends in graduate school has been immeasurable; thank you Kara Kearney, Charles Smith, Siddharth Krishnan, Nicole Johnson-Glauch, Katie Lakomy, William Wheeler, Michael Darrow, Emiliana Cofell, and Emily Skiba for forming a wonderful community of people in Urbana-Champaign. Lastly, but certainly not least, I would like to thank my parents Dr. Mary Leveillee and Ronald Leveillee, my sister Alexandra Leveillee, and the rest of my amazing extended family for the unwavering support and love they have shown me throughout my life and studies.

I am thankful for the funding support from the National Science Foundation (Grant No. CBET 1437230), Los Alamos Laboratory Directed Research and Design, and the Racheff Teaching Fellowship through the Materials Science and Engineering Department at the University of Illinois, Urbana-Champaign. This work would not be possible without the computational resources and support from the National Center for Supercomputing Applications (NCSA) Blue Waters supercomputer, the University of Illinois Campus Cluster, and the Los Alamos National Laboratory High Performance Computing facilities.

TABLE OF CONTENTS

CHAPTER 1

INTRODUCTION

A primary societal imperative as we move through the 21st century is to supply clean, reliable energy to a growing global population. While fossil fuels currently supply a high energy density method for powering our everyday needs, their supply is limited and their deleterious influence on the environment through air pollution and greenhouse gas emission are difficult to understate. Photovoltaic energy has emerged as a reliable and sustainable alternative for daily energy needs. Most commercially available efficient solar cells are hetero junction Silicon designs. Within the last decade, a new class of photovoltaic material has emerged: hybrid organic-inorganic perovskites (HOPs) and their lower dimensional variant layered hybrid organic-inorganic perovskites (LHOPs). The most popular HOP, $CH_3NH_3PbI_3$ (abbreviated $MAPbI_3$) - recently boasts a greater than 22% photo-conversion efficiency [1, 2, 3, 4]. $MAPbI_3$ thin film devices are also cheap and quick to manufacture. Applications for HOPs have extended beyond solar cells to light-emitting diodes (LEDs) [5], catalysis for water splitting [6], and high energy radiation detection [7]. Successes of LHOP materials designs has also led highly efficient and stable solar cells [8], tuned light-emitting diodes (LEDs) [9, 10, 11, 12], and possible spintronics [13]. Before delving into the current investigation, it will be informative to examine the history of hybrid perovskites and develop an understanding of their properties and functions.

The history of perovskites extends back to the middle of the nineteenth century. The mineral $CaTiO_3$, later known as the first discovered perovskite compound, was discovered in Russia by Gustav Rose in 1839. The mineralogist Lev Perovski, for which the perovskite crystal structure was named, studied the structure. The crystal structure was first explored by Victor Goldschmidt in 1926. By this time, multiple metal-titinates had been discovered. The first crystallographic publication describing a perovskite compound, $BaTiO_3$, was written by Helen Dick Megaw in 1945 and is considered the founding study of perovskite crystal structures. Perovskite materials have since permeated the technological world with applications in piezo-electronics, magnetic devices, informatics, opto-electronics, and much more [14]. Despite most attention on HOP and LHOP solar cells in the past decade, the first studies on the optical properties of HOPs and LHOPs were undertaken in the early 1990s [1]. It was found that one can replace the typical inorganic A^{1+} cation in

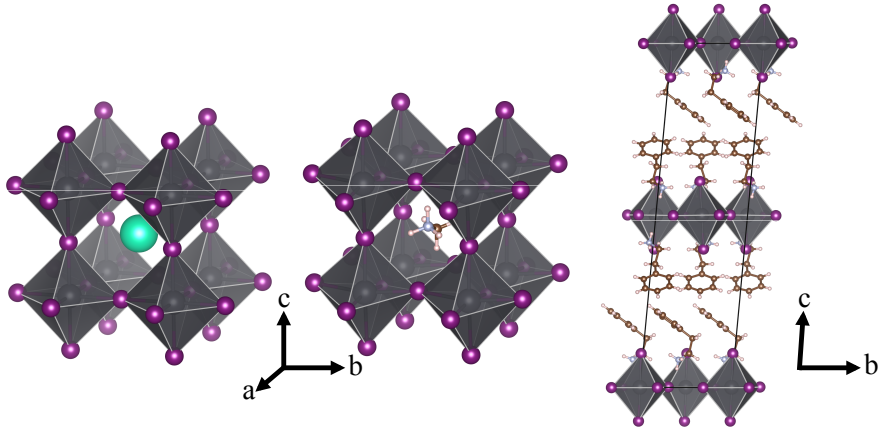

Figure 1.1: Schematic of perovskite crystals structures, from left to right: (1) inorganic perovskite of ABX_3 form $CsPbI_3$, (2) hybrid organic-inorganic perovskite (HOP) of ABX_3 form $MAPbI_3$, and (3) layered hybrid organic-inorganic perovskite (LHOP) of A_2BX_3 form PEA_2PbI_3 (PEA=phenethylammonium).

the ABX_3 structure with a small organic cation. Teruya Ishihara synthesizes and characterized the optical properties of $MAPbI_3$ and associated layered A_2PbI_4 varieties in 1994. Ishihara was the first to observe a low exciton binding energy (the energy required to separate an optically excited electron and hole) of 45 meV in $MAPbI_3$ and an increasing binding energies of 170–320 meV in the layered structures. The 1994 study did not focus on the energy harvesting capability of hybrid perovskites but rather on the dielectric confinement effects on exciton binding energy, originally described by Rytova [15] and later by Kyldesh [16]. However, the observation of a strong optical absorption onset with relatively weak binding energy, i.e one close to the room temperature thermal energy of 26 meV, in $MAPbI_3$ was made and would later spark intense interest for solar cell applications.

The first design iteration of HOP solar cells focused on dye sensitizing a charge transporting scaffold with $MAPbI_3$. In 2009, Kojima *et al.* used $MAPbI_3$ to dye mesoporous TiO_2 to building a modest solar cell of 3.8% photo-conversion efficiency [17]. This record was far superseded in 2012 when Kim *et al.* developed a meso structured $MAPbI_3$ dye-sensitized solar cell with 9% photo-conversion efficiency (PCE) [18]. A few months later in 2012, Lee *et al.* used a similar design to advance the PCE to 10.9% [19], making $MAPbI_3$ a material of keen interest in the photovoltaic community. By refining the processing techniques, the same laboratory group produced a dye sensitized solar cell with $> 12.0\%$ efficiency [20, 21]. This extraordinary advance from 3.8% to 12.3% PCE launched $MAPbI_3$ into the spotlight as a possible next generation solar cell material. $MAPbI_3$ based solar cells moved away from the dye-sensitized porous oxide model to thin-film heterojunction models in late 2013. This architecture was first explored by Liu *et al.* to achieve a PCE of 15% [22]. Subsequent developments took the efficiency over 20% [23]. Applications for HOPs have now moved beyond solar cells to HOP and LHOP LEDs that can produce wavelength specific or broad white

light emission [12, 24, 25, 26].

Alongside their vast uses as optoelectronic materials, HOPs and LHOPs are hosts of fascinating microscopic physical phenomena that fundamentally determine their functionality at the macroscopic scale. First and foremost, for photovoltaic applications, is the band gap of 1.5-1.7 eV [27] in $MAPbI_3$, allowing for the absorption of red light while maintaining a high internal voltage under illumination. The conduction band edge dispersion is attributed to the Pb_{6p} states and is heavily influenced by strong spin-orbit coupling, as has been confirmed by many first principles studies [28, 29]. Most modern measurements of the exciton binding energy find it to be lower than the room temperature thermal energy of 26 meV, leading to efficient room-temperature formation of free charge carriers [27] and thus enhanced photo-current under illumination. Despite high power conversion efficiency, the mobility of carriers is predicted to be low due to strong coupling with longitudinal optical (LO) lattice vibrations, also known as LO phonon modes [30]. This interaction forms a polaron out of the carriers and surrounding lattice displacement [31], slowing the transport of charges. It has also been proposed that LO phonon modes can dynamically screen the electron-hole interaction, leading to the low exciton binding energy [32]. Lastly, the synthesis of HOPs is error prone, and many final products contain high concentrations of shallow defects that can donate free charges to the material. Such free charges can turn the material slightly n- or p-type, informing their possible applications [33, 34, 35]. These intricate atomic and electronic scale interactions are often difficult to decouple and understand from experimental data. An alternative, predictive method is thus sought to determine how the optoelectronic properties of HOPs and LHOPs depend on these microscopic processes.

First principles calculations are powerful tools to understand the underlying behavior of atomic and electronic properties of materials. Such calculations provide the ability to simulate and disentangle quantum mechanical phenomena that are difficult to determine by experimental methods. Furthermore, the development and improvement of first principles calculations allows scientists to make novel predictions on material behavior prior to experimental verification. Two popular combined techniques in simulating the ground and excited state properties of materials are density functional theory (DFT) and many-body perturbation theory (MBPT) [36, 37, 38, 39, 40, 41]. Along with experimental development of advanced optoelectronic technologies, extensive first principles investigations have been undertaken to better understand the structure and band gap trends in hybrid perovskite solar cell materials [42, 43, 44, 45, 46, 47, 48].

Though modern computational techniques based on DFT and MBPT have been applied to understand the underlying optical physics of HOPs and LHOPs, many mysteries remain. Most DFT+MBPT techniques available currently do not account for the interactions present in HOPs, such as exciton-phonon interaction and free-carriers screening - that fundamentally determine the materials' optoelectronic properties [30, 49].

For example, modern predictions of the exciton binding energy in $MAPbI_3$ span from 30 to 50 meV [32, 50, 51, 52], despite most experimental studies measuring binding energies between 2 and 30 meV [27]. In LHOPs, the influence of stoichiometry in charge-carrier localization upon optical excitation is not well studied. Further, little consideration has been given to the excitonic properties of highly conjugated organic spacer layers, despite previous experiments displaying the ability for spacers to act as efficient triplet light-emitters. Therefore, it is imperative to apply current and novel first principles methodologies to disentangle the mystery of exciton binding energies and to predict how excitons can be utilized in HOP and LHOP materials for solar cell and light-emitting applications.

In this doctoral thesis, I apply and develop state-of-the-art first principles calculations to predict the optical response and excitonic properties of HOPs and LHOPs. The four studies contained in this thesis contribute to a single work that examines how we can better predict the optical response HOP and LHOP systems and how we can use those predictions to make design recommendations to experimental researchers. Prior to discussing my work, I will present the theory of first principles optical response calculations in Chapter 2. I will additionally detail in this chapter the derivation of a model function of the dynamically screened lattice Coulomb interaction and details its connection to previous electron-phonon interaction theory. In Chapter 3 I will present the first study on predicting how the presence of free-carrier introduced by shallow defects in $MAPbI_3$ influence both the optical absorption spectrum and exciton binding energy in the cubic phase of $MAPbI_3$. This chapter will additionally explore the electronic and optical response at the GW_0 level of theory for the orthorhombic and tetragonal phases of $MAPbI_3$. Chapter 4 will explore the application of a dynamically lattice screened Coulomb interaction on the excitonic and optical properties of four semiconducting and insulating compounds: NaCl, MgO, AlN, and GaN. Then, dynamically lattice screening will be applied to $MAPbI_3$ to determine how binding energy is influenced by the low-frequency dielectric screening of the electron-hole Coulomb interaction. I will then, in Chapter 5, move on to predict and study the layer-resolved optical response as a function of halide composition in two LHOP materials: API-PbX_3 and PEA_2-PbX_4, where X=I,Br,Cl. In this effort, I seek to determine how charge carriers can be separated across or confined to the perovskite and organic spacer layers under optical excitation. Additionally, the optical spectrum, accounting for exciton formation, will be calculated for API-PbX_4. In Chapter 6 I will calculated the lowest singlet and triplet excitation energies in conjugated organic spacer candidates for LHOP design. This effort aims to predict which organic spacers can be used to design triplet light-emitting LHOPs for wavelength-tuned applications. In conclusion, Chapter 7 will summarize the major findings of the studies and discuss future prospects in predicting and designing optical response in hybrid perovskite materials from first principles.

CHAPTER 2

THEORY OF OPTICAL RESPONSE FROM FIRST PRINCIPLES

First principles methods for predicting the optical response of solids and molecules extends as far back as quantum mechanics itself. The effort to develop and improve predictive theories continues with significant momentum today. The most common theoretical methodology today to predict optical response of solids from first principles is the three step DFT+GW+BSE [53]. First, DFT is employed to predict the ground state charge density and initial Kohn-Sham wave functions and single-particle energies. Next, the GW approximation (or hybrid functionals) are used to correct the single-particle excitation spectra, rendering a reliable band structure. Finally, the Bethe-Salpeter Equation is used to determine the two-particle excitation energies on top of the DFT+GW electronic structure [41]. In this chapter, I will review the theory and methodologies behind this three step process. Afterwards, I will discuss additional considerations to the screening of electron-hole excitations within the BSE, including Thomas-Fermi screening by free-carrier and lattice screening by polar phonon modes. Finally, I will discuss the use of two different techniques - ΔSCF and Linear-Response Time-Dependent Density Functional Theory - to calculate the optical excitation energies of isolated molecules. This chapter will provide the theoretical foundation to understand the research presented in this thesis.

2.1 The Hartree and Hartree-Fock Models

The first aim in this chapter is to demonstrate the historical re-writing of the many-body Schrödinger equation as a mean field equation. The primary objective of any quantum mechanical calculation is to determine the energy of a collection of interacting particles. In a non-relativistic framework, this can be theoretically performed by solving for the total wave function $\Psi(r_1, r_2, ..., r_N, R_1, R_2, ..., R_{N'})$ of N electrons and N' nuclei and associated total energy E_{tot} using the time-independent Schrödinger Equation in the form of an eigenvalue equation:

$$\hat{H}\Psi(\mathbf{r}_1, \mathbf{r}_2, ..., \mathbf{r}_N, \mathbf{R}_1, \mathbf{R}_2, ..., \mathbf{R}_{N'}) = E_{tot}\Psi(\mathbf{r}_1, \mathbf{r}_2, ..., \mathbf{r}_N, \mathbf{R}_1, \mathbf{R}_2, ..., \mathbf{R}_{N'}) \tag{2.1}$$

The total energy operator is given by the Hamiltonian, $\hat{H}$, and acts on the total wave function Ψ to calculate the total system energy. The Hamiltonian can be expanded into the constituent kinetic energy operators and potential energy operators:

$$\hat{H} = -\frac{1}{2}\sum_i \nabla_i^2 - \frac{1}{2}\sum_I \nabla_I^2 + \frac{1}{2}\sum_{i\neq i'} \frac{4\pi}{|\mathbf{r}_i - \mathbf{r}_{i'}|} + \frac{1}{2}\sum_{I\neq I'} \frac{4\pi Z_I Z_{I'}}{|\mathbf{R}_I - \mathbf{R}_{I'}|} - \frac{1}{2}\sum_{i,I} \frac{4\pi Z_I}{|\mathbf{r}_i - \mathbf{R}_I|} \tag{2.2}$$

Here i and I index over electrons and nuclei, respectively. The electron and nuclei position vectors are given by $\mathbf{r}$ and $\mathbf{R}$, respectively. Z_I are the nuclear charges. The first two terms on the right hand side are the kinetic energy operators of the electrons and nuclei, respectively. The next two terms are the electron-electron potential and the nucleus-nucleus potential. The final term is the electron-nucleus potential. The positions of the electrons and nuclei are treated here as fully dynamic. In seeking to solve for the ground state energy of a system, it behooves one to treat the nuclei as a static, external potential acting on dynamic electrons. This is known as the Born-Oppenheimer approximation which states that the electronic states may equilibrate instantly to the nuclear states as electrons move much faster than nuclei [54]. By the Born-Oppenheimer approximation, the time-independent Schrödinger equation can be written for the total energy and wave function of the electronic system, E_{el} and Ψ_{el}, alone.

$$\hat{H}_{el}\Psi_{el}(\mathbf{r}_1, ..., \mathbf{r}_N) = -\left(\frac{1}{2}\sum_i \nabla_i^2 + \frac{1}{2}\sum_{i\neq i'} \frac{4\pi}{|\mathbf{r}_i - \mathbf{r}_{i'}|} - \frac{1}{2}\sum_{i,I} \frac{4\pi Z_I}{|\mathbf{r}_i - \mathbf{R}_I|}\right)\Psi_{el}(\mathbf{r}_1, ..., \mathbf{r}_N) = E_{el}\Psi_{el}(\mathbf{r}_1, ..., \mathbf{r}_N) \tag{2.3}$$

While the problem has been simplified, the fully interacting Schrödinger equation remains impossible to solve as the electron-electron interaction renders the differential equation non-separable by electronic coordinate. Thus, it becomes important to move away from attempting calculations of the total electronic wave function to garner approximate solutions to the electronic total energy.

An early attempt to find such an approximat solutions was developed by Hartree [55]. The Hartree approximation represents one of the single-particle models to approximate the fully interacting electron-nuclei system. The Hartree model begins by assuming that each electronic wave function is independent of the next, so that the total wave function is approximated by a product of single-particle wave functions ψ:

$$\Psi_{el}(\mathbf{r}_1, ..., \mathbf{r}_N) = \prod_i^N \psi_i(\mathbf{r}_i) \tag{2.4}$$

The goal in the Hartree model becomes solving for the energies and wave functions of single, non-interacting electronic states. The Hartree Hamiltonian does just this. The electron-electron interaction is replaced by

the Hartree functional of single-particle wave functions.

$$\hat{H}_H\psi_i(\mathbf{r}) = \left(\frac{1}{2}\nabla_i + \frac{1}{2}\sum_{i'\neq i}\int d(\mathbf{r}')\frac{4\pi|\psi_{i'}(\mathbf{r}')|^2}{|\mathbf{r}_i - \mathbf{r}'_{i'}|} - \frac{1}{2}\frac{4\pi Z_I}{|\mathbf{r}_i - \mathbf{R}_I|}\right)\psi_i(\mathbf{r}) = \epsilon_i\psi_i(\mathbf{r}) \tag{2.5}$$

Here, ϵ_i are the single electron energies. Of note is that the Hartree potential, the second term in the brackets, depends on the electron density $\rho_{i'}(r') = |\psi_{i'}(\mathbf{r})|^2$ and is an early example of a density functional. The total energy of the system is simply represented as a sum over single-particle energies. The Hartree model was soon refined to the Hartree-Fock model by Fock in 1930 by enforcing the anti-symmetry nature of the electron fermionic wave function and representing Ψ as a Slater determinant of the single-particle wave functions [56, 57]:

$$\Psi_{el}^{HF}(\mathbf{r}_1, ..., \mathbf{r}_N) = \frac{1}{\sqrt{N!}}\begin{vmatrix} \psi_1(\mathbf{r}_1) & \cdots & \psi_N(\mathbf{r}_1) \\ \vdots & \ddots & \vdots \\ \psi_1(\mathbf{r}_N) & \cdots & \psi_N(\mathbf{r}_N) \end{vmatrix}$$

The Hartree-Fock Hamiltonian for the single-particle states is:

$$\hat{H}^{HF}\psi_i(\mathbf{r}_i) = \left(\frac{1}{2}\nabla_i^2 - \frac{1}{2}\frac{4\pi Z_I}{|\mathbf{r}_i - \mathbf{R}_I|}\right)\psi_i(\mathbf{r}_i) + \sum_{i'}\int d(\mathbf{r}')\left[\frac{|\psi_{i'}(\mathbf{r}')|^2}{|\mathbf{r} - \mathbf{r}'|}\psi_i(\mathbf{r}) + \frac{\psi_{i'}(\mathbf{r}')\psi_i(\mathbf{r}')}{|\mathbf{r} - \mathbf{r}'|}\psi_{i'}(\mathbf{r})\right] = \epsilon_i\psi_i(\mathbf{r}_i) \tag{2.6}$$

The total energy in the Hartree-Fock approximation is given by:

$$E_{HF} = -\frac{1}{2}\sum_{i'}\int d\mathbf{r}\psi_{i'}^*(\mathbf{r})\nabla^2\psi_{i'}(\mathbf{r}) + \sum_i\int d(\mathbf{r})\psi_i^*(\mathbf{r})\psi_i(\mathbf{r})V_{ext}(\mathbf{r}) + \left[\frac{1}{2}\sum_{i,i'}\int d\mathbf{r}d\mathbf{r}'\frac{\psi_{i'}^*(\mathbf{r})\psi_i^*(\mathbf{r}')\psi_i(\mathbf{r})\psi_{i'}(\mathbf{r}')}{|\mathbf{r}' - \mathbf{r}|} + \frac{1}{2}\sum_{i,i'}\int d\mathbf{r}d\mathbf{r}'\frac{\psi_{i'}^*(\mathbf{r})\psi_i^*(\mathbf{r}')\psi_i(\mathbf{r}')\psi_{i'}(\mathbf{r})}{|\mathbf{r}' - \mathbf{r}|}\right] \tag{2.7}$$

V_{ext} is the external potential exerted on the electrons by the nuclei. The first term in the square brackets is known as the exchange integral and the second term is known as the Coulomb integral. Both terms represent an effective Coulomb interaction between single-particle states, but the exchange integral emerges as a consequences of the anti-symmetric nature of the Slater wave functions. The Hartree-Fock approximation improves vastly on the Hartree approximation by including the exact *exchange energy* of the system [57]. However, it does not capture higher order contributions from the many-body Coulomb interaction. The energy difference between the true ground state energy and the Hartree-Fock ground state energy, attributed to such higher-order many-body Coulomb interactions, as is called the *correlation energy*. Hartree-Fock,

though an approximate solution to the many-particle interacting system, has lead to major success in modeling the electronic structure of molecular systems. In particular, the highest occupied energy state determined by Hartree-Fock satisfied Koopmans theorem which states that the negative of the energy of the highest-occupied molecular orbital is equal to the ionization energy [58]. Many efforts have been made to include correlation energy on top of the Hartree-Fock approximation, including the widely used Møller-Plesset perturbation theory [59]. Solving for the exchange, Coulomb, and higher order correlation integrals as functionals of single-electron wave functions can become prohibitively expensive. There is thus motivation to move away from integrals over single-electron wave functions and towards functionals of the electron density to approximate all energy terms contributing to the total ground state energy.

2.2 Ground State Properties - Density Functional Theory

Density functional theory (DFT) is, without a doubt, one of the most popular methods to approximate the ground state properties of the interacting electron-nuclei system. The philosophy underlying DFT is that one can replace the many-body interacting system with an auxiliary system of independent electrons interacting with a mean field represented by the electron density. The auxiliary system and the real fully interacting system share the same ground state energy. This section will overview the basic historical realizations of DFT and discuss how calculations of the electronic ground state energy and single-particle energies and wave functions are practically undertaken.

2.2.1 The Hohenberg-Kohn Theorems

The groundwork for DFT was established in 1964 when Hohenberg and Kohn published the twin Hohenberg-Kohn theorems [37]. The program of DFT is to solve for the total ground state electronic energy of a system of interacting electrons as a functional of the electron density. But first, it must be proven that the external potential is, in fact, a unique functional of the electron density. This existence proof is the first Kohn-Sham theorem. The proof shows by *reductio ad absurdum* that the ground state energy and the external potential are unique functionals of the electron density $\rho(\mathbf{r})$. The second Hohenberg-Kohn theorem states that the ground state energy can be obtained variationally by minimizing the ground state energy with respect to the electron density, and that this corresponding density is the *exact* ground state density. These two theorems offer proof that the ground state energies of interacting electronic systems can be determined by optimizing E^0 with respect to ρ by the variational principle.

2.2.2 The Kohn-Sham Equations and the Self-Consistent Formulation

A realistic self-consistent method for solving E^0 variationally with respect to ρ was posed by Kohn and Sham in 1965 [36]. The Kohn-Sham equation for the single electron wave functions and energies of electronic states i reads:

$$\left(\frac{1}{2}\nabla^2 + \hat{v}_{eff}(\mathbf{r})\right)\psi_i(\mathbf{r}) = \epsilon_i\psi_i(\mathbf{r}) \tag{2.8}$$

The effective potential operator contains the external potential of the nuclei $\hat{v}_{ext}$, the electron-electron Hartree potential $\hat{v}_H$, and the exchange-correlation potential $\hat{v}_{xc}$:

$$\hat{v}_{eff}(\mathbf{r}) = \hat{v}_{ext}(\mathbf{r}) + \hat{v}_H(\mathbf{r}) + \hat{v}_{xc}(\mathbf{r}) = \hat{v}_{ext}(\mathbf{r}) + \int d(\mathbf{r}')\frac{\rho(\mathbf{r}')}{|\mathbf{r}-\mathbf{r}'|} + \frac{\delta E_{xc}[\rho(\mathbf{r})]}{\delta\rho(\mathbf{r})} \tag{2.9}$$

The Hartree potential operator represents a mean-field Coulomb interaction. The exchange-correlation potential is expressed as a functional derivative of the exchange-correlation energy with respect to the electron density. The exchange-correlation energy will be discussed at length hereafter. The total energy functional of the density is expressed as:

$$\begin{aligned} &E[\rho(\mathbf{r})] = T[\rho(\mathbf{r})] + \int d(\mathbf{r})v_{ext}(\mathbf{r})\rho(\mathbf{r}) + E_H[\rho(\mathbf{r})] + E_{xc}[\rho(\mathbf{r})] = \\ &\frac{1}{2}\sum_i \int d(\mathbf{r})\psi_i(\mathbf{r})\nabla^2\psi_i(\mathbf{r}) + \int d(\mathbf{r})v_{ext}(\mathbf{r})\rho(\mathbf{r}) + \frac{1}{2}\sum_{i,i'}\int d(\mathbf{r})d(\mathbf{r}')\frac{\rho(\mathbf{r})\rho(\mathbf{r}')}{|\mathbf{r}-\mathbf{r}'|} + \int d(\mathbf{r})\epsilon_{xc}[\rho(\mathbf{r})]\rho(\mathbf{r}) \end{aligned} \tag{2.10}$$

The electron density is expressed as the summed squares of the Kohn-Sham wave functions:

$$\rho(\mathbf{r}) = \sum_i |\psi_i(\mathbf{r})|^2 \tag{2.11}$$

At this point, it is clear that the Kohn-Sham equation relies on functionals of the electron density, yet the electron density relies on a sum over wave functions determined by the Kohn-Sham equation. Therefore, one must solve for the ground state density self-consistently, providing the variational technique proven to apply by the second Hohenberg-Kohn equation. The basic steps for optimizing only the electron density to minimize the ground state electronic energy, are:

1. Guess the initial electron density $\rho(\mathbf{r})$
2. Calculate the effective potential v_{eff}
3. Solve the Kohn-Sham equation for the set of Kohn-Sham wave functions $\psi_i(\mathbf{r})$ and energies ϵ_i
4. Calculate the new electron density $\rho(\mathbf{r})$

5. Calculate the total energy as a functional of the density $E[\rho(\mathbf{r})]$

6. Ask: is the energy converged? If so, stop! If not, return to step 2, change the density by an optimization algorithm of choice, and repeat

2.2.3 Band Structures and Linear Optical Response in DFT

DFT is in principle exact, but as the exact form the exchange-correlation functional is unknown it cannot be used to predict excited state properties such as band structures and optical spectra. Nonetheless, one can define a band structure comprised of Kohn-Sham eigen-energies ϵ_i as a function of wave vector $\mathbf{k}$ and band index n in the Bloch basis, $\epsilon_{n\mathbf{k}}$. This concept will be revisited later in the context of optical response calculations. A linear optical response of the Kohn-Sham auxiliary system can also be formulated by applying the Ehrenreich-Cohen equation to the Kohn-Sham states to calculate the imaginary dielectric function [60].

$$\text{Im } \varepsilon^{\alpha\beta}(\omega) = \varepsilon_2^{\alpha\beta}(\omega) = \frac{8\pi^2}{\Omega} \sum_{cv\mathbf{k}} \frac{\langle \psi_{c\mathbf{k}}^{KS} | \hat{p}_\alpha | \psi_{v\mathbf{k}}^{KS} \rangle \langle \psi_{c\mathbf{k}}^{KS} | \hat{p}_\beta | \psi_{v\mathbf{k}}^{KS} \rangle}{(\epsilon_{c\mathbf{k}} - \epsilon_{v\mathbf{k}})^2} \delta(\epsilon_{c\mathbf{k}} - \epsilon_{v\mathbf{k}} - \omega) \tag{2.12}$$

Here, $\psi_{n\mathbf{k}}^{KS}$ are the Kohn-Sham wave functions of the unoccupied conduction states ($n = c$), occupied valence states ($n = v$), and electron wave number ($\mathbf{k}$) expressed in the Bloch basis, along with their associated energies $\epsilon_{n\mathbf{k}}$. The momentum operator $\hat{p}$ as applied along Cartesian directions and determines the optical polarization vector. Ω is the volume of the simulation cell. Linear optical response calculations of the imaginary dielectric function, also colloquially known as the absorption spectrum, will be revisited at two higher levels of theory. The real part of the electronic frequency-dependent dielectric function $\varepsilon_1(\omega)$ can be recovered by Kramers-Kronig transformation of the imaginary frequency-dependent dielectric function [61]. In this way, one can determine the value of the high-frequency electronic dielectric constant ε_∞ at $\varepsilon_1(\omega = 0)$.

2.2.4 Practical DFT Calculations

Till now, no information has been provided on how to realistically numerical set up a density functional theory calculation of the ground state energy and Kohn-Sham eigen-states. Some important topics include: the treatment of exchange-correlation potential, pseudo-potentials, an the choice of basis. Many excellent texts are available that discuss, in depth, how DFT calculations are performed, and I would direct the interested reader towards these resources [62, 63]. What follows is an abbreviated discussion of the key practical elements pertaining to DFT that are applied in this thesis.

The Exchange-Correlation Energy and Potential

We recall from the Hartree-Fock approximation that the exchange interaction is given as a functional of single-particle wave functions, not the electron density. Additionally, there is *no* known exact functional for the correlation energy. To use DFT, one is faced with the challenge of finding an approximate exchange-correlation energy as a functional of the electron density. The first attempt at doing such produced a method that is remains extremely popular today. The exchange energy of the free electron gas of a given spatially variant density $\rho(\mathbf{r})$ was determined by Paul Dirac in 1930 [64] and is given by the analytic equation:

$$E_x^{LDA}[\rho(\mathbf{r})] = -\frac{3}{4}\left(\frac{3}{\pi}\right)^{1/3}\int d(\mathbf{r})\rho(\mathbf{r})^{4/3} \tag{2.13}$$

This is known as the local density approximation (LDA) for the exchange energy and provides an approximate exchange energy functional of the electron density. This does not address the correlation energy. The correlation energy of the free electron gas is known in the low and high density limits [65]. Values of the correlation energy at intermediate densities are determined by quantum Monte Carlo simulations and these value are used as the basis for the exchange-correlation functional in the LDA [66]. The LDA assumes a locally uniform charge density and thus gradients in the charge density and their influence on exchange and correlation energy are not accounted for [62]. To address this, the generalized gradient approximation (GGA) takes into gradients of the charge density in the exchange-correlation energy functional [67]. The Perdew-Burke-Ernzerhof exchange-correlation functional (PBE) falls into the GGA and is used extensively in this thesis [68].

Pseudo-potentials

Describing all electrons in a molecule or unit cell of a crystal quickly becomes a daunting task. Furthermore, integration of the charge density becomes numerically challenging due to rapid oscillations of the wave functions near the nucleus. It is convenient to instead only include the valence electrons in the calculation and re-formulate the nuclear potentials to include the screening by core and semi-core electrons. This is the concept behind the pseudo-potential method, first introduced by Hans Hellmann in 1935 [69]. A popular way to construct pseudo-potentials is within the projector augmented wave (PAW) method, developed by Blöchl in 1994 [70]. Though I will not detail the pseudo-potential method here, they are used in all following studies to focus on the simulation of valence and near-valence electronic states.

The Bloch Basis for Periodic Crystalline Systems

The work herein is particularly focused on determining the electronic structure and optical response of crystalline solids. The periodic boundary conditions of a crystal are defined by the set of lattice vectors $\vec{\mathbf{R}} = n_1\vec{\mathbf{a}}_1 + n_2\vec{\mathbf{a}}_2 + n_3\vec{\mathbf{a}}_3$ where $\vec{\mathbf{a}}_i$ are the set of primitive unit cell vectors. In reciprocal space, there is a corresponding set of reciprocal lattice vectors $\vec{\mathbf{G}} = n_1\vec{\mathbf{b}}_1 + n_2\vec{\mathbf{b}}_2 + n_3\vec{\mathbf{b}}_3$. In both cases, n_i are integers ranging from $-\infty$ to ∞. The $\mathbf{b}$ vectors relate to the $\mathbf{a}$ vectors by the Fourier transform:

$$\mathbf{b}_1 = \frac{2\pi}{\Omega}\frac{\mathbf{a}_2 \times \mathbf{a}_3}{\mathbf{a}_1 \cdot (\mathbf{a}_2 \times \mathbf{a}_3)} \tag{2.14}$$

As a reminder, coordinate vectors in real space are designated by $\mathbf{r}$ and in reciprocal space by $\mathbf{k}$. A natural consequence of an electron existing in a periodic lattice is that it interacts with a periodic potential V that satisfied the discrete translation $V(\mathbf{r}) = V(\mathbf{r} + \mathbf{R})$. Given this condition, the periodic potential can be expanded in its Fourier components.

$$V(r) = \sum_{\mathbf{G}} V_{\mathbf{G}} e^{i\mathbf{G}\cdot\mathbf{r}} \tag{2.15}$$

The proof of Bloch's theorem, which can be found through many sources[1], concludes that, if the potential obeys discrete translation symmetry under the translation operator $\hat{\mathbf{T}}_{\mathbf{R}}$ and the electrons can be described by independent wave functions with single-particle energies, then the wave functions of the system can be expressed as Bloch wave functions [71]:

$$\psi_{n\mathbf{k}}(\mathbf{r}) = e^{i\mathbf{k}\cdot\mathbf{r}} u_{n\mathbf{k}}(\mathbf{r}) = e^{i\mathbf{k}\cdot\mathbf{r}} \left(\sum_{\mathbf{G}} C_{n,\mathbf{G},\mathbf{k}} e^{-i\mathbf{G}\cdot\mathbf{r}} \right) \tag{2.16}$$

The Bloch wave function is composed of the envelope plane wave $e^{i\mathbf{k}\cdot\mathbf{r}}$, which is not commensurately periodic with the lattice, and the Bloch function $u_{n\mathbf{k}}(\mathbf{r})$, which is periodic with the lattice. The good quantum numbers of the system are the wave number $\mathbf{k}$ and electronic band n. The wave function itself does not share the same periodicity as the lattice, but expectation values are periodic with the lattice. As observables are periodic in the lattice, the integrals to compute these observables can be performed on only the unit cell.

$$\langle \hat{O}_{n\mathbf{k}} \rangle = \langle \psi_{n\mathbf{k}}(\mathbf{r}) | \hat{O} | \psi_{n\mathbf{k}}(\mathbf{r}) \rangle_{\text{u.c}} = \frac{1}{\sqrt{\Omega}} \int_{\text{u.c}} d(\mathbf{r}) \sum_{\mathbf{G}} C^*_{n,\mathbf{G},\mathbf{k}} e^{i\mathbf{G}\cdot\mathbf{r}} \hat{O} \sum_{\mathbf{G}} C_{n,\mathbf{G},\mathbf{k}} e^{-i\mathbf{G}\cdot\mathbf{r}} \tag{2.17}$$

As $\mathbf{k}$ and n are state variables of the wave function, all information that distinguishes one single-particle state from another are contained in the Fourier components $C_{n\mathbf{G},\mathbf{k}}$. When iterating the guess of the single-

[1] Ashcroft and Mermin, "Solid State Physics" (1976)

particle wave functions in density functional theory, one only needs to optimize the array of coefficients. One cannot solve the Kohn-Sham equation on continuous grids of **k**-points and with infinite **G** vectors. Therefore, discrete integration grids and a finite number of contributing **G** vectors are chosen to perform calculations over. The density of the **k**-point grid and the number of **G** vectors are chosen by a convergence criteria energy to keep the total error in total energy as low as possible while retaining computational tractability.

Gaussian Basis for Isolated Molecular Systems

The plane wave basis set has served us well for crystalline, periodic systems. In systems of isolated atomic clusters and molecules in vacuum, we require a basis set that produces square integrable wave functions over all space. A convenient choice is the Gaussian basis set [72]. A single Gaussian basis function takes the form:

$$G_{nlm}(\mathbf{r}) = A_n |\mathbf{r}|^{n-1} e^{-a\mathbf{r}^2} Y_l^m(\theta, \phi) \tag{2.18}$$

Here, Y are the spherical harmonics and l and m are the angular momentum and magnetic quantum numbers, respectively. The integer n is the primary quantum number and ranges from 1 to infinity. Gaussian basis functions are analytically integrable over all space, and thus no intricate numerical integration needs to be performed. The result is a rapid calculation of the ground state energy and observables within the density functional theory formalism. However, a major problem with single Gaussian functions is their inability to mimic true Slater-type orbitals (STOs) near the nuclear position. Thus, it was proposed that using a linear combinations of Gaussian basis functions to approximate STOs could be used for accurate quantum chemical calculations [73]. The concept behind minimal Gaussian basis functions to simulate STOs was vastly expanded to include more terms such as polarization functions to account of orbital orientation [74]. In Chapter 6 this thesis, the 6-31G* Gaussian basis set is used extensively.

2.3 Single-Particle Excitation - The GW Approximation

With the goal of predicting optical properties of materials, the most glaring failure of density functional theory is the inability to predict accurate band energies and, in turn, band gaps of materials. The reason for this is the approximation to the many-body interaction contained in the exchange-correlation functional. When a band structures is measured, say by Angle-Resolved Photo Emission Spectroscopy (ARPES) [75], the removal of an electron triggers a dynamical response from its fellow electronic states, mediated by the Coulomb interactions. This rearrangement due to a many-body interaction fundamentally determines the excited electronic states of materials. The goal of many-body perturbation theory (MBPT) is to expand

the Coulomb interaction between electrons in orders of contributing n-body interactions. The resulting sum produces a "self energy" for each electronic state that contains accurate exchange and correlation contributions. The exchange-correlation self energy at the MBPT level of theory can then replace the exchange-correlation density functional calculated at the DFT level of theory. In this section, a brief overview of many-body perturbation theory will be given which will lead into the well-known GW-approximation for the electronic state self energies. The interested reader should consult another series of excellent texts that cover this topic in great detail [76, 77].

2.3.1 Hedin's Equations and the Random Phase Approximation

The ultimate goal of the GW approximation is to determine the self-energy $\Sigma_{n\mathbf{k}}$ of a single-particle state $\psi_{n\mathbf{k}}$ added to a system [40]. The self energy of valence states and conduction states represent, respectively, the energy change in the addition of a hole and electron to the system. It is simple to start with a non-interacting system of particles, as determined by DFT, and to replace the exchange-correlation functional with this self energy. One can determine a total energy from the single quasi-particle equation. The single quasi-particles, in this case, are the added holes or electrons dressed by the polarization of the system. They have energies $E^{\mathrm{QP}}_{n\mathbf{k}}$ and wave function $\psi^{\mathrm{QP}}_{n\mathbf{k}}(\mathbf{r})$ that are determined by the single quasi-particle equation [40]:

$$(\hat{T}+\hat{V}_{ext}+\hat{V}_H)\psi^{\mathrm{QP}}_{n\mathbf{k}}(\mathbf{r})+\int d(\mathbf{r}')\Sigma_{n\mathbf{k}}(\mathbf{r},\mathbf{r}';\omega=E^{\mathrm{QP}}_{n\mathbf{k}})\psi^{\mathrm{QP}}_{n\mathbf{k}}(\mathbf{r}')=E^{\mathrm{QP}}_{n\mathbf{k}}\psi^{\mathrm{QP}}_{n\mathbf{k}}(\mathbf{r}) \tag{2.19}$$

The mean-field approximation of the exchange-correlation functional that one sees in the Kohn-Sham equation is now given by a self energy containing the many-body interactions. Depending on how many orders of perturbation theory are carried out, Σ will contain exact exchange energy plus increasing contributions of the correlation energy. Σ is defined by Hedin's five self consistent equations, and relies on the Dyson expansion of the single-particle Green's function G, the vertex correction Γ, the polarizability χ, and screened Coulomb interaction W, and the self energy Σ [39]:

$$G(1,2)=G_0(1,2)+\int d(3,4)G_0(1,3)\Sigma(3,4)G(4,2) \tag{2.20}$$

$$\Gamma(1,2,3)=\delta(1,2)\delta(1,3)+\int d(4,5,6,7)\frac{\delta\Sigma(1,2)}{\delta G(4,5)}G(4,6)G(7,5)\Gamma(6,7,3) \tag{2.21}$$

$$\chi(1,2)=\int d(3,4)G(1,3)G(4,2)\Gamma(3,4,2) \tag{2.22}$$

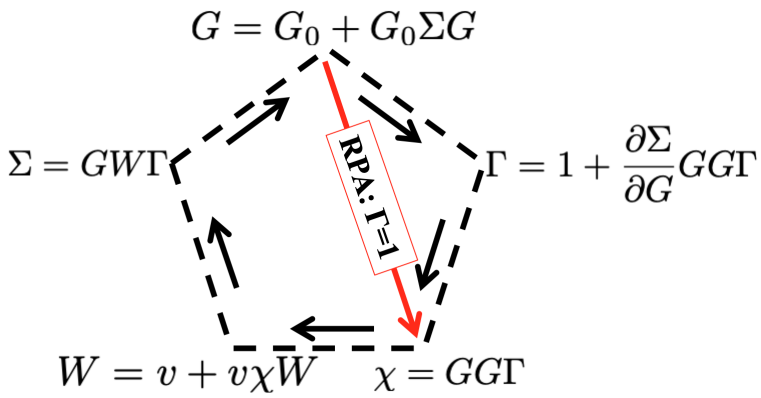

Figure 2.1: Diagram of Hedin's self consistent equations for the quasi-particle self energy Σ The GW approximation is performed in the Random Phase Approximation (RPA) by setting the vertex correct Γ to $\delta_{12}\delta_{13}$.

$$W(1,2) = v_c(1,2) + \int d(3,4)v_c(1,3)\chi(3,4)W(4,2) = \int d(3)\varepsilon^{-1}(3,2)v_c(1,2) \tag{2.23}$$

$$\Sigma(1,2) = \int d(3,4)G(1,3)W(4,1)\Gamma(3,2,4) \tag{2.24}$$

Abbreviated space and time notations is used where $(\mathbf{r}_1, t_1) = 1$. The term v_c is the bare Coulomb interaction. In starting from density functional theory, $G(12)$ is initially approximated by the single-particle Kohn-Sham Green's function in frequency (ω) space:

$$G_0(\mathbf{r}_1, \mathbf{r}_2; \omega) = \sum_{n\mathbf{k}} \frac{\psi^{KS*}_{n\mathbf{k}}(\mathbf{r}_1)\psi^{KS}_{n\mathbf{k}}(\mathbf{r}_2)}{\omega - \epsilon_{n\mathbf{k}} \pm i\eta} \tag{2.25}$$

Here, η is a small infinitesimal added to avoid divergences in the sum over band energies. Next, the vertex correction is set to $\Gamma(1,2,3) = \delta(1,2)\delta(1,3)$. In doing so, contributions arising from greater than single-particle Green's functions are omitted. By restricting Γ in this way, the polarizability χ now only describes the change in electron density induced by interactions between single-particles. One can solve for the polarizability χ as the polarization of the charge density by the total potential. This can be approximated by assuming that the electronic charge density $\rho(\mathbf{r})$ changes only under the influence of the effective external potential $v_{eff}(\mathbf{r})$, leading to the irreducible polarizability χ_0. This approximation is referred to historically as the Random Phase Approximation (RPA). The irreducible polarizability χ_0 relies only in non-interacting single-particle Green's functions and was solved for in reciprocal space by Alder and Wiser in the RPA as

[78, 79]:

$$\chi_{0,\mathbf{GG'}}(\mathbf{q},\omega) = \frac{1}{\Omega}\sum_{nn'\mathbf{k}} \frac{\langle\psi^{KS}_{n',\mathbf{k+q}}(\mathbf{r})|e^{i(\mathbf{q}+\mathbf{G})\cdot\mathbf{r}}|\psi^{KS}_{n,\mathbf{k}}(\mathbf{r})\rangle\langle\psi^{KS}_{n,\mathbf{k}}(\mathbf{r})|e^{-i(\mathbf{q}+\mathbf{G'})\cdot\mathbf{r}}|\psi^{KS}_{n',\mathbf{k+q}}(\mathbf{r})\rangle}{\epsilon_{n',\mathbf{k-q}} + \epsilon_{n,\mathbf{k}} - \omega - i\eta} \tag{2.26}$$

The exponential terms arise from taking Bloch integrals over the unit cell. The dielectric tensor ε in the RPA (only containing contributions from the electronic polarizability) can be computed as:

$$\varepsilon_{\infty,\mathbf{GG'}}(\mathbf{q},\omega) = \delta_{\mathbf{GG'}} - \frac{4\pi}{|\mathbf{q}+\mathbf{G}||\mathbf{q}+\mathbf{G'}|}\chi_{0,\mathbf{GG'}} \tag{2.27}$$

The quantity $\varepsilon_{\infty,\mathbf{GG'}}(\mathbf{q},\omega)$ will be known as the electronic, or high-frequency, dielectric tensor. The head of the electronic dielectric tensor in the static limit ($\mathbf{G} = \mathbf{G'} = \mathbf{q} = 0, \omega = 0$) is the electronic, or high-frequency, dielectric constant ε_∞. Of note is that the electronic dielectric tensor is usually only a part of the total dielectric tensor of the system. If a material contains polar ions or rotational dipole moments, these contributions to the polarizability will be factored in. The contribution from the polar lattice will be discussed later at length. The electronically screened Coulomb interaction can then be determined as:

$$W_{\mathrm{el},\mathbf{GG'}}(\mathbf{q},\omega) = \varepsilon^{-1}_{\infty,\mathbf{GG'}}(\mathbf{q},\omega)V_{\mathbf{GG'}}(\mathbf{q}) = \frac{4\pi\varepsilon^{-1}_{\infty,\mathbf{GG'}}(\mathbf{q},\omega)}{|\mathbf{q}+\mathbf{G}||\mathbf{q}+\mathbf{G'}|} \tag{2.28}$$

Now, since the vertex Γ has been set to $\delta_{12}\delta_{13}$, we recover the namesake of the GW approximation in the equation for the self energy:

$$\begin{aligned}\Sigma_{n\mathbf{k}}(\omega) = \langle\psi_{n\mathbf{k}}|\Sigma(\mathbf{r}_1,\mathbf{r}_2;\omega)|\psi_{n\mathbf{k}}\rangle = \langle\psi_{n\mathbf{k}}|i\int d(\mathbf{r}_3,\mathbf{r}_2)G_0(\mathbf{r}_1,\mathbf{r}_3;\omega)W(\mathbf{r}_4,\mathbf{r}_1;\omega)|\psi_{n\mathbf{k}}\rangle = \\ \frac{i}{\pi\Omega}\sum_{\mathbf{q},\mathbf{G},\mathbf{G'}}\sum_{n'}\int_{-\infty}^{\infty} d\omega' W_{\mathrm{el},\mathbf{GG'}}(\mathbf{q},\omega')\langle\psi^{KS}_{n',\mathbf{k+q}}(\mathbf{r})|e^{i(\mathbf{q}+\mathbf{G})\cdot\mathbf{r}}|\psi^{KS}_{n,\mathbf{k}}(\mathbf{r})\rangle\langle\psi^{KS}_{n,\mathbf{k}}(\mathbf{r})|e^{-i(\mathbf{q}+\mathbf{G})\cdot\mathbf{r}}|\psi^{KS}_{n',\mathbf{k+q}}(\mathbf{r})\rangle \\ \times\left(\frac{1}{\omega+\omega'-\epsilon_{n',\mathbf{k+q}}\pm i\eta} + \frac{1}{\omega+\omega'-\epsilon_{n',\mathbf{k+q}}\mp i\eta}\right)\end{aligned} \tag{2.29}$$

In referring back to the quasi-particle equation, the QP band energies $E^{\mathrm{QP}}_{n\mathbf{k}}$ can be determined by the expectation value:

$$E^{\mathrm{QP}}_{n\mathbf{k}} = \mathrm{Re}\left[\langle\psi^{QP}_{n\mathbf{k}}|\hat{T} + \hat{V}_{ext} + \hat{V}_H + \Sigma(\omega = E^{\mathrm{QP}}_{n\mathbf{k}})|\psi^{QP}_{n\mathbf{k}}\rangle\right] \tag{2.30}$$

As stated before, Hedin's equations for the GW approximation are a self consistent set. Often one or more iterations are required to converge the single quasi-particle energies. Designating an iteration index by $\mathbf{M}$,

the QP energies at the $\mathbf{M}$+1 iteration are given by:

$$E_{n\mathbf{k}}^{\mathrm{QP},\mathbf{M}+1} = E_{n\mathbf{k}}^{\mathrm{QP},\mathbf{M}} + Z_{n\mathbf{k}}^{\mathbf{M}}\mathrm{Re}\left[\langle\psi_{n\mathbf{k}}^{QP,\mathbf{M}}|\hat{T} + \hat{V}_{ext} + \hat{V}_H + \Sigma(\omega = E_{n\mathbf{k}}^{\mathrm{QP},\mathbf{M}})|\psi_{n\mathbf{k}}^{QP,\mathbf{M}}\rangle - E_{n\mathbf{k}}^{\mathrm{QP},\mathbf{M}}\right] \tag{2.31}$$

Here, Z is a normalization factor that reduces the amplitude of of the QP peaks due to satellite formation.

$$Z_{n\mathbf{k}}^{\mathbf{M}} = \left(1 - \mathrm{Re}\left[\langle\psi_{n\mathbf{k}}^{QP,\mathbf{M}}|\frac{\partial\Sigma(\omega)}{\partial\omega}|_{\omega=E_{n\mathbf{k}}^{\mathrm{QP},\mathbf{M}}}|\psi_{n\mathbf{k}}^{QP,\mathbf{M}}\rangle\right]\right)^{-1} \tag{2.32}$$

2.3.2 Practical GW Calculations

In practice, there are many options for how to go about solving the self-consistent equations of the GW approximation. The most common is the G_0W_0 method, also known as single-shot GW, which begins by solving for the Green's function G and the irreducible polarization χ_0 with the Kohn-Sham wave functions and energies as input. The self energies and normalization factors are then evaluated at the Kohn-Sham energies, generating an initial guess for the single quasi-particle energies. Perhaps surprisingly, the G_0W_0 method can produce fairly accurate predictions of band energies with no further iteration of Hedin's equations required, depending on the material and on the quality of the initial band structure estimate from a non-interacting theory like DFT. The GW_0 method continues around the Hedin's equations loop, and updates the Green's functions by using the now-determined single quasi-particle energies. The irreducible polarizability χ_0 is kept the same as determined in the first loop. Finally, quasi-particle self-consistent GW, abbreviated at $QSGW$, updates the wave functions as well as the energies at each iteration [80].

2.4 Two-Particle Excitations and Optical Response - The Bethe-Salpeter Equation

A formalism for predicting reliable ground state and single-particle excited state properties (i.e. band structures) have been reviewed. This does not yet achieve predictive power for optical excitations. We require a method by which to determine the excited state energies of excited electron-hole pairs. A technique for doing this was developed by Salpeter and Bethe in 1951 [81], and has been aptly named the Bethe-Salpeter equation. It describes the energy spectra of two-particle bound states in a relativistic reference frame. It is a broadly applicable equation for any two-particle bound state, but has found significant utility in predicting the excitation and binding energies of electron-hole pairs upon optical excitation [41]. In this section, I will review the theory of the BSE for electron-hole excitations, as well as discuss how realistic computational

approaches are undertaken.

2.4.1 The Bethe-Salpeter Equation

The fundamental observable of the interacting two-particle system is the two-particle correlation function (also referred to as the two-particle Green's function) L. $L(1,2;1',2')$ which measures the probability that one particle moves from coordinate $1' \to 1$ and another moves from $2' \to 2$ while under each other's influence. The Dyson equation for the two-particle correlation function, also known as the BSE, can be derived by many-body perturbation theory [82]:

$$L(1,2;1',2') = L_0(1,2;1',2') + \int d(3,4,5,6) L_0(1,4;1',3)\Xi(3,5;4,6)L(6,2;5,2') \tag{2.33}$$

L_0 is the non-interacting two-particle correlation function, which is simply the product of two single-particle Green's functions $L_0(1,2;1',2') = G(1,1')G(2,2')$. The Dyson series for L includes the integral over the interaction kernel Ξ. The interaction kernel describes the space and time dependent interactions between the two propagating particles. It is determined at the GW level of theory as:

$$\begin{aligned}\Xi(3,5;4,6) = \frac{\delta\left(V(3)\delta(3,4) + \Sigma(3,4)\right)}{\delta G(6,5)} &= \frac{\delta\left(v_c(3)\delta(3,4) + \int d(7,8)G(3,7)W(8,4)\Gamma(3,2,4)\right)}{\delta G(6,5)} \\ &= i\delta(3,4)\delta(5,6)\bar{v}(3,6) - i\delta(3,6)\delta(4,5)W(3,4)\end{aligned} \tag{2.34}$$

The two-particle correlation function can be expressed as a sum over excitation index Λ of the electron-hole wave functions ϕ_Λ.

$$L(12,1',2';\omega) = i\sum_\Lambda \left[\frac{\phi^*_\Lambda(\mathbf{r}_2,\mathbf{r}_{2'})\phi_\Lambda(\mathbf{r}_1,\mathbf{r}_{1'})}{\omega - E_\Lambda} - \frac{\phi_\Lambda(\mathbf{r}_2,\mathbf{r}_{2'})\phi^*_\Lambda(\mathbf{r}_1,\mathbf{r}_{1'})}{\omega + E_\Lambda}\right] \tag{2.35}$$

The electron-hole wave functions are themselves expressed as a linear combination of the product of single-particle wave functions weighted by coefficients A and B:

$$\phi_\Lambda(\mathbf{r},\mathbf{r}') = \sum_{cv\mathbf{k}} A^\Lambda_{cv\mathbf{k}}\psi_{c\mathbf{k}}(\mathbf{r})\psi^*_{v\mathbf{k}}(\mathbf{r}') + B^\Lambda_{cv\mathbf{k}}\psi^*_{c\mathbf{k}}(\mathbf{r})\psi_{v\mathbf{k}}(\mathbf{r}') \tag{2.36}$$

Utilizing the expansion of the electron-hole wave function in the Bloch basis and, subsequently, the expansion of the two-particle correlation function L, one writes the Bethe-Salpeter equation as a coupled excitonic

eigenvalue problem.

$$\left[(E_{c\mathbf{k}} - E_{v\mathbf{k}})A_{cv\mathbf{k}} + \sum_{c'v'\mathbf{k}'} \Xi_{cvk}^{c'v'\mathbf{k}'}(E_\Lambda)A_{c'v'\mathbf{k}'}\right]_{\text{res}} + \left[\sum_{c'v'\mathbf{k}'} \Xi_{cvk}^{c'v'\mathbf{k}'}(E_\Lambda)B_{c'v'\mathbf{k}'}\right]_{\text{coupl}} = E_\Lambda A_{cv\mathbf{k}} \tag{2.37}$$

$$\left[(E_{c\mathbf{k}} - E_{v\mathbf{k}})B_{cv\mathbf{k}} + \sum_{c'v'\mathbf{k}'} \Xi_{cvk}^{c'v'\mathbf{k}'}(E_\Lambda)A_{c'v'\mathbf{k}'}\right]_{\text{anti-res}} + \left[\sum_{c'v'\mathbf{k}'} \Xi_{cvk}^{c'v'\mathbf{k}'}(E_\Lambda)B_{c'v'\mathbf{k}'}\right]_{\text{coupl}} = -E_\Lambda B_{cv\mathbf{k}} \tag{2.38}$$

The first eigenvalue equation determines the excitation energies of the interacting electron-hole (exciton) system. The second solves for the de-excitation energies. To predict absorption spectrum, only the prior is needed. Furthermore, the coupling term is found to have minimal influence on the prediction of the optical excitation energies at $\mathbf{q} \to 0$ and is generally omitted from actual calculations, resulting in the Tamm-Dancoff approximation [83, 84]. Therefore, the final uncoupled excitonic eigenvalue equation in the Tamm-Dancoff approximation is:

$$\left[(E_{c\mathbf{k}} - E_{v\mathbf{k}})A_{cv\mathbf{k}} + \sum_{c'v'\mathbf{k}'} \Xi_{cvk}^{c'v'\mathbf{k}'}(E_\Lambda)A_{c'v'\mathbf{k}'}\right]_{\text{res}} = E_\Lambda A_{cv\mathbf{k}} \tag{2.39}$$

Using equations 2.34 and 2.36, the interaction Kernel matrix elements $\Xi_{cvk}^{c'v'\mathbf{k}'}$ can be expanded in the electron-hole exchange interactions and the electron-hole Screened Coulomb interaction:

$$\begin{aligned}
&\Xi_{cvk}^{c'v'\mathbf{k}'} = 2\bar{v}_{cvk}^{c'v'\mathbf{k}'} - W_{cvk}^{c'v'\mathbf{k}'} = \\
&\int d(\mathbf{r}_1,\mathbf{r}_2)\psi_{c\mathbf{k}}^*(\mathbf{r}_1)\psi_{v\mathbf{k}}(\mathbf{r}_1)\bar{v}(\mathbf{r}_1,\mathbf{r}_2)\psi_{c'\mathbf{k}'}(\mathbf{r}_2)\psi_{v'\mathbf{k}'}^*(\mathbf{r}_2) - \int d(\mathbf{r}_1,\mathbf{r}_2)\psi_{c\mathbf{k}}^*(\mathbf{r}_1)\psi_{c'\mathbf{k}'}(\mathbf{r}_1)W(\mathbf{r}_1,\mathbf{r}_2)\psi_{v\mathbf{k}'}^*(\mathbf{r}_2)\psi_{v'\mathbf{k}'}(\mathbf{r}_2) \\
&= \frac{1}{\Omega}\sum_{\mathbf{G}\neq 0}\frac{4\pi}{|\mathbf{G}^2|}B_{v\mathbf{k}}^{c\mathbf{k}}(\mathbf{G})B_{v'\mathbf{k}'}^{c'\mathbf{k}'}(\mathbf{G}) - \frac{1}{\Omega}\sum_{\mathbf{G},\mathbf{G}'}\frac{4\pi\varepsilon_{\infty,\mathbf{G}\mathbf{G}'}^{-1}(\mathbf{q})}{|\mathbf{k}-\mathbf{k}'-\mathbf{G}||\mathbf{k}-\mathbf{k}'-\mathbf{G}'|}B_{c\mathbf{k}}^{c'\mathbf{k}'}(\mathbf{G})B_{v\mathbf{k}}^{v'\mathbf{k}'}(\mathbf{G})
\end{aligned} \tag{2.40}$$

The terms B are Bloch integrals of the form[85]:

$$B_{n\mathbf{k}}^{n'\mathbf{k}'}(\mathbf{G}) = \frac{1}{\Omega_{BZ}}\int_{\text{u.c}} d\mathbf{r}\psi_{n\mathbf{k}}^*(\mathbf{r})e^{i\mathbf{G}\cdot\mathbf{r}}\psi_{n'\mathbf{k}'}(\mathbf{r}) \tag{2.41}$$

The excitonic Hamiltonian formulation of the BSE of the interacting electron-hole system is a powerful tool for calculating macroscopic observables. At the core of this connection is the relation between the two-particle correlation function L and the irreducible polarizability $\bar{\chi}$ in the RPA: $\bar{\chi}(1,2) = iL(1,1',2,2')$. The primary focus of this thesis is on the imaginary dielectric function which measures the energy loss under an

AC electric field, i.e. photon absorption.

$$\lim_{\mathbf{q}\to 0} \mathrm{Im}\ \varepsilon(\mathbf{q}\to 0,\omega) = \lim_{\mathbf{q}\to 0} \mathrm{Im}\left[\varepsilon_{00}(\mathbf{q},\omega)\right]^{-1} = \lim_{\mathbf{q}\to 0} \mathbf{Im}\left[1 + V(\mathbf{q}+G)\bar{\chi}_{\mathbf{GG'}}(\mathbf{q},\omega)\right] \tag{2.42}$$

As optical excitation wave vectors $\mathbf{q}$ are much smaller than electron wave vectors $\mathbf{k}$, optical excitation spectra are calculate in the $\mathbf{q}\to 0$ limit. The diagonal components of the dielectric tensor in the limit of $\mathbf{q}\to 0$ as a function of excitation frequency ω can be expressed in terms of the excitonic Hamiltonian eigenvectors and values [41, 85, 82].

$$\varepsilon^{\alpha\alpha}(\omega) = 1 + \frac{4\pi}{\Omega}\sum_{\Lambda}\left(2\left[\sum_{cv\mathbf{k}}\frac{\langle\psi_{c\mathbf{k}}|\hat{p}_\alpha|\psi_{v\mathbf{k}}\rangle}{(E_c - E_v)}A^{\Lambda}_{cv\mathbf{k}}\right]^2\delta(E_\Lambda - \omega)\right) \tag{2.43}$$

Here, the re-weighting of the absorption peaks is given by adjusting the transition matrix amplitude by the excitonic Hamiltonian eigenvector elements. In comparison to the single-particle imaginary dielectric function, what is observed is a red-shift of the spectrum to lower energies and an increase in amplitude of the band-edge excitations attributed to exciton formation.

2.4.2 Practical Calculations

Determining accurate absorption spectra and exciton binding energies requires very dense $\mathbf{k}$-point grids to properly capture small $\mathbf{q}$ in the screened Coulomb interaction characteristic of Wannier-Mott excitons. Often, grids of the required density that are evenly spaced over the Brillouin zone are not computationally affordable even on large super computers. Two methods are employed to navigate this issue [86]. The first is the use of hybrid $\mathbf{k}$-point grids to sample closely the Brillouin Zone center to predict reliable exciton binding energies of the lowest optical excitation. The second is the use of randomly shifted and evenly spaced $\mathbf{k}$-point grids that sample the entire Brillouin Zone to determine smooth optical spectra. Both methods are used extensively in this thesis.

A major challenge in calculations of electron-hole excitations by the BSE is the computation and matrix inversion of the high-frequency electronic dielectric tensor $\varepsilon_{\infty,\mathbf{GG'}}(\mathbf{q})$. A full calculation and inversion of the dielectric tensor is needed when exciton binding is very strong and off-diagonal elements in $\varepsilon_{\infty,\mathbf{GG'}}(\mathbf{q})$ are necessary to describe local field effects in the screened Coulomb interaction. In materials with Wannier-Mott excitons where the electron-hole orbit radius is large, the influence of the off-diagonal elements in the dielectric tensor are small and thus local field effects are negligible [79]. This allows for the use of just the diagonal elements $\mathbf{G} = \mathbf{G'}$ to evaluate the screened Coulomb interaction. Another approximation is the

use of a model dielectric function to model the diagonal components of the dielectric tensor. The model screening function proposed by Cappellini *et al.* reliably reproduces the diagonal of the dielectric matrix and is widely used in the literature and in this thesis [87]:

$$\varepsilon(\mathbf{q}+\mathbf{G}=\mathbf{Q}) = 1 + \left[\frac{1}{\varepsilon_\infty - 1} + \alpha\frac{\mathbf{Q}^2}{\mathbf{q}_{\mathrm{TF}}^2} + \frac{\mathbf{Q}^4}{4\omega_p^2}\right]^{-1} \tag{2.44}$$

Here, $\mathbf{q}_{\mathrm{TF}}$ is the Thomas-Fermi wave vector of the valence electrons in the system and ω_p is the plasma frequency. The coefficient α is typically set to unity. ε_∞ is the high-frequency electronic dielectric constant and is calculated by density functional perturbation theory or by determining $\mathrm{Re}\varepsilon(\omega = 0)$ at the DFT or GW level of theory. Use of the model functions allows for the rapid analytic inversion of $\varepsilon(\mathbf{Q})$ and subsequent quick calculation of the screened Coulomb interaction matrix elements.

Even with modern super computers, the exact diagonalization of the excitonic Hamiltonian is often intractable. A time evolution scheme, formulated by Glutsch *et al.* and implemented for the electron-hole problem by Hahn *et al.* [88], can instead be used to iteratively evolve the values of vector elements by multiplication with the excitonic Hamiltonian. This method is used for optical spectrum calculations with excitonic contributions in this thesis.

2.5 Free-Carrier Effects on Optical Response

No crystal is perfect. Intrinsic and extrinsic defects, the latter often referred to as dopants if introduced intentionally, permeate all processed optical materials. Defects often differ in electronic coordination and will donate (n-type defect) or accept (p-type defect) electrons from the system, generating free electrons and free holes, respectively. If an n-type defect energy level is near the conduction band edge, or conversely a p-type defect energy level is near the valence band edge, this donation or acceptance of an electron can occur at low thermal energy and the defects are referred to as shallow. At high concentrations, free-carriers may fill their associated band edges in the material creating a free-carrier gas. This occupation of the band extrema influences optical properties in three distinct ways.

1. The filled band edge can no longer participate in optical response, a phenomenon called **Pauli Blocking**. The result is a shift of the optical response onset to higher energies which is known in experimental observations as the Burstein-Moss shift, abbreviated BMS.

2. **Band gap reduction**, abbreviated BGR, occurs under increased correlation effects of the electron-electron interaction from the free-carrier gas introduced by defects.

3. **Free-carrier screening** of the electron-hole Coulomb interaction by the free-carrier gas which reduces the binding strength of the exciton.

Free-carrier screening not only influences the electron-hole Coulomb interaction, but also electron-electron interaction. This results in the aforementioned band gap reduction.

2.5.1 Practical Calculations

Pauli blocking can be simply simulated by omitting the filled states from the calculation of the imaginary dielectric function. The band gap re-normalization is more difficult to determine. In semiconductors with parabolic band edges, the model of Berggren and Sernelius can be used to estimate how the additional correlation effects of a free electron gas at a band edge influences the band gap [89]:

$$\Delta E_{BGR} = \left[\frac{e^2 k_f}{2\pi^2 \varepsilon_\infty \bar{\varepsilon}_0} - \frac{e^2 q_{\mathrm{TF}}}{8\pi \varepsilon_\infty \bar{\varepsilon}_0}\left(1 - \frac{4}{\pi}\arctan\frac{k_f}{q_{\mathrm{TF}}}\right)\right] - \left[\frac{n_c m_c e^4}{4\pi \bar{\varepsilon}_0^2 \varepsilon_\infty^2 \hbar^3 q_{\mathrm{TF}}^3}\right] \tag{2.45}$$

Here, $\bar{\varepsilon}_0$ is the permittivity of free space, m_c is the electron effective mass, n_c is the concentration of free electrons, and k_f is the Fermi wave vector of a free electron gas with concentration n_c and effective mass m_c. The first term in square brackets describes the effect of electron-impurity scattering on the band gap energy while the second describes the influence of enhanced screening by the additional free-electron gas.

A simple yet effective model for the free-carrier contribution of the dielectric tensor diagonal $\varepsilon_{\mathbf{GG}}(\mathbf{q}) = \varepsilon(\mathbf{q}+\mathbf{G}) = \varepsilon(\mathbf{Q})$ can be derived in the Thomas-Fermi model [90]:

$$\varepsilon_{\mathrm{TF}}(\mathbf{Q}) = 1 - \frac{4\pi}{\mathbf{Q}^2}\frac{\rho_{ind}(\mathbf{Q})}{\phi(\mathbf{Q})} = 1 - \frac{4\pi}{\mathbf{Q}^2}\chi(\mathbf{Q}) \tag{2.46}$$

The polarizability χ is given as the ratio between the charge density induced by an external test charge in the system $\rho_{ind}(\mathbf{Q})$ divided by the external potential of the test charge $\phi(\mathbf{Q})$. For a model system of a free electron gas sitting at a band edge of effective mass m^*, we can derive the following expression:

$$\varepsilon_{\mathrm{TF}}(\mathbf{Q}) = 1 - \frac{4\pi\left(\frac{\partial n}{\partial \epsilon_f}\right)}{\mathbf{Q}^2} = 1 - \frac{\mathbf{q}_{\mathrm{TF}}^2}{\mathbf{Q}^2} \tag{2.47}$$

The Thomas-Fermi wave vector $\mathbf{q}_{\mathrm{TF}}$ controls the spatial influence of the dielectric screening by free-carriers. Often, the filling of states at the band extrema remain within and energy range where the effective mass

approximation remains valid. $\mathbf{q}_{\mathrm{TF}}$ can be then expressed as:

$$\mathbf{q}_{\mathrm{TF}} = \sqrt{\frac{3n}{2\epsilon_f}} \tag{2.48}$$

The Thomas-Fermi screening by free-carriers in defective or doped materials is only one contribution to the total dielectric screening. Valence-conduction excitations also contribute to the dielectric screening through the high-frequency dielectric tensor $\varepsilon_{\infty,\mathbf{GG}'}(\mathbf{q},\omega)$. If we consider just the head element in the static approximation, ε_∞, we can combine the influence of both valence-conduction inter-band excitation and free-carrier intra-band excitation in the electron-hole screening by writing the model of the new diagonal of the dielectric tensor as [91, 92]:

$$\varepsilon_{\mathrm{eff}}(\mathbf{Q}) = \varepsilon_\infty \varepsilon_{\mathrm{TF}}(\mathbf{Q}) = \varepsilon_\infty \left(1 - \frac{\mathbf{q}_{\mathrm{TF}}^2}{\varepsilon_\infty \mathbf{Q}^2}\right) \tag{2.49}$$

2.6 Phonons and the Electron-Phonon Vertex

At this point, we will briefly diverge from the topic of optical excitations to a side quest concerning lattice excitations known as phonons. The Born-Oppenheimer approximation works remarkably well to predict many ground state properties of the interacting electron system with an external potential exerted by the ionic background. Yet, this approximation fails to yield reasonable predictions for various measurable material quantities such as free-carrier mobilities, temperature-dependence of the band gap, temperature dependence of thermal resistivity, excited carrier lifetimes, the formation of Cooper pairs in type-I superconductivity, and much more [93]. At the core of all these phenomena is the coupling between the electronic states and phonons: the quantized excitations of the lattice. Later, we will show how phonons contribute to screening of the electron-hole pair produced under optical excitation.

2.6.1 Phonon Frequencies and Eigen-Displacement

Phonons are quantized waves of atomic displacement, with wave vectors $\mathbf{q}$, a band index ν and frequencies $\omega_{\mathbf{q},\nu}$ that form the phonon band structure [90]. The number of bands are designated by the number of ways ions in the system can be displaced relative to the phonon propagation direction and to each other. When the ionic displacement is in the direction of the propagation wave vector $\mathbf{q}$, the modes are longitudinal (designated by the letter L). Alternatively, the ionic displacements can be perpendicular to $\mathbf{q}$ and the modes are labeled as transverse (T). Modes where the relative ionic motions are in phase are labeled as acoustic modes (A) and modes where the relative ionic motion is out of phase are labeled as optical modes (O). Thus, all modes can be labeled as either LA, TA, LO, TO, or a mix between such types of modes.

Determining the phonon frequencies as a function of wave vector $\mathbf{q}$ and band index ν requires the calculation of the inter-atomic force constant $C_{\kappa,\alpha,p,\kappa',\alpha',p'}$, where κ is an ionic index, α is a cartesian direction, and p designates a unit cell where the atom sits. If we have atomic displacements given by $\Delta\tau_{\kappa,\alpha,p}$, then the new energy of the system under a relative pair of displacements in the harmonic approximation is [94]:

$$E = E_0 + \frac{1}{2}\sum_{\kappa,\alpha,p,\kappa',\alpha',p'} \frac{\partial E}{\partial\tau_{\kappa,\alpha,p}\partial\tau_{\kappa',\alpha',p'}}\Delta\tau_{\kappa,\alpha,p}\Delta\tau_{\kappa',\alpha',p'} = E_0 + \frac{1}{2}\sum_{\kappa,\alpha,p,\kappa',\alpha',p'} C_{\kappa,\alpha,p,\kappa',\alpha',p'}\Delta\tau_{\kappa,\alpha,p}\Delta\tau_{\kappa',\alpha',p'} \tag{2.50}$$

The Fourier transform of the force constant matrix renders the dynamical matrix $D_{\kappa,\alpha,\kappa',\alpha'}(\mathbf{q})$:

$$D_{\kappa,\alpha,\kappa',\alpha'}(\mathbf{q}) = \sqrt{\frac{1}{M_\kappa M_{\kappa'}}}\sum_p C_{\kappa,\alpha,p,\kappa',\alpha',0}e^{i\mathbf{q}\cdot\mathbf{R}_p} \tag{2.51}$$

Here, $\mathbf{R}_p$ is an atomic position vector and M_κ is the mass of the κ^{th} atom. Finally, the eigenvalues and eigenvectors of the dynamical matrix determine the squared phonon frequencies and normalized atomic displacement vectors, respectively.

$$\sum_{\kappa',\alpha'} D_{\kappa,\alpha,\kappa',\alpha'}(\mathbf{q})\mathbf{e}_{\kappa',\alpha',\nu}(\mathbf{q}) = \omega^2_{\mathbf{q},\nu}\mathbf{e}_{\kappa,\alpha,\nu}(\mathbf{q}) \tag{2.52}$$

Many methods are available to determine the dynamical matrix and its eigenvalues. One of the most reliable and common is density functional perturbation theory (DFPT). Many good resources are available to better understand DFPT [94].

2.6.2 Polar Phonons and the Low-Frequency Dielectric Tensor

Let us first begin by better defining the vague term *polar crystal*. A polar crystal in the context of this work is one where the displacements of atoms from their equilibrium atomic positions induce macroscopic electric fields over the material. Such displacement are referred to as polar phonons. The fields induced by polar phonons couple to electronic degrees of freedom and can significantly alter their motion. A more mathematical definition of a polar crystal is that the ions have a non-zero Born effective charge. Born effective charge is a tensor with indices $\alpha\beta$ describing the linear relation between the atomic displacement and the polarization per unit cell [95]. The relative displacement of these charges induces the previously

mentioned macroscopic electric fields.

$$Z_{\kappa,\alpha\beta} = \Omega \frac{\partial P_{mac,\beta}}{\partial \tau_{\kappa\alpha}(\mathbf{q}=0)} \tag{2.53}$$

The phonons that induce these macroscopic fields lead to an additional ionic contribution to the materials polarization which can be described by a low-frequency dielectric tensor ε_0 [94]. Previously, we have discussed the high-frequency electronic dielectric tensor which describes screening mediated by electronic polarization in the system. The total inverse dielectric tensor, with both high-frequency electronic contributions and low-frequency ionic contributions are given by [96]:

$$\begin{aligned}\varepsilon^{-1}_{0,\mathbf{G}\mathbf{G}'}(\mathbf{q},\omega) = \varepsilon^{-1}_{\infty,\mathbf{G}\mathbf{G}'}(\mathbf{q},\omega) + (\varepsilon^{-1}_{0,\mathbf{G}\mathbf{G}'}(\mathbf{q},\omega) - \varepsilon^{-1}_{\infty,\mathbf{G}\mathbf{G}'}(\mathbf{q},\omega)) = \\ \varepsilon^{-1}_{\infty,\mathbf{G}\mathbf{G}'}(\mathbf{q},\omega) + \sum_{\mathbf{G}''\mathbf{G}'''} \varepsilon^{-1}_{\infty,\mathbf{G}\mathbf{G}''}(\mathbf{q},\omega)\varepsilon^{-1}_{\infty,\mathbf{G}'''\mathbf{G}'}(\mathbf{q},\omega)\frac{4\pi}{\Omega}\sum_{\nu}\frac{S_{\nu,\mathbf{G}''\mathbf{G}'''}(\mathbf{q})}{-\omega^2_{\nu\mathbf{q}}+\omega^2+i\eta}\end{aligned} \tag{2.54}$$

The mode oscillator strengths S are given by:

$$S_{\nu,\mathbf{G}\mathbf{G}'}(\mathbf{q}) = \sum_{\kappa\kappa'}\frac{1}{\sqrt{M_\kappa M'_\kappa}}\frac{((\mathbf{q}+\mathbf{G})\cdot Z_{\kappa,\alpha\beta}\cdot\mathbf{e}_{\kappa,\alpha,\nu}(\mathbf{q}))\,((\mathbf{q}+\mathbf{G}')\cdot Z_{\kappa',\alpha\beta}\cdot\mathbf{e}^*_{\kappa',\beta,\nu}(\mathbf{q}))}{|\mathbf{q}+\mathbf{G}||\mathbf{q}+\mathbf{G}'|}e^{i(\mathbf{G}'\kappa-\mathbf{G}'\kappa')} \tag{2.55}$$

It can be seen from the previous three equations that when the elements of the Born effective charge tensor are 0 that the ionic contribution to the inverse dielectric tensor is 0, leading to a total dielectric tensor equaling the high-frequency electronic dielectric tensor. We find as well that when the propagation wave vector of the phonon mode is perpendicular to the phonon eigen-displacement that S goes to zero. Thus, the macroscopic fields induced by polar phonon modes are attributed to the LO modes and modes with partial LO character. Inducing such fields requires that the LO modes occur at higher energy compared to the TO modes. This phenomena is know as the LO-TO splitting, and is described by the Lyddanne-Sachs-Teller relation [97]:

$$\frac{\varepsilon_{0,\mathbf{0}\mathbf{0}}(\mathbf{q}=0,\omega=0)}{\varepsilon_{\infty,\mathbf{0}\mathbf{0}}(\mathbf{q}=0,\omega=0)} = \frac{\varepsilon_0}{\varepsilon_\infty} = \frac{\omega^2_{LO}}{\omega^2_{TO}} \tag{2.56}$$

2.6.3 The Electron-Phonon Vertex

The study of phonon band structure and spectra is a rich and extensive topic. However, this thesis is primarily concerned with how change induced in the potential by a phonon mode scatters electronic states. Within the context of density functional perturbation theory, the change in the potential by a phonon mode

with eigen-displacement $\mathbf{e}_{\kappa,\alpha,\nu}(\mathbf{q})$ is given by [93]:

$$\Delta_{\mathbf{q}\nu}V(\mathbf{r}) = l_{\mathbf{q}\nu}\sum_{\kappa\alpha}\sqrt{\frac{M_0}{M_\kappa}}\mathbf{e}_{\kappa,\alpha,\nu}(\mathbf{q})\sum_p e^{-i\mathbf{q}\cdot(\mathbf{r}-\mathbf{R}_p)}\frac{\partial V(\mathbf{r})}{\partial\tau_{\kappa,\alpha,p}}|_{\mathbf{r}-\mathbf{R}} \tag{2.57}$$

Where $l_{\mathbf{q}\nu}$ is called the zero-point displacement amplitude given in atomic units by $(1/(2M_0\omega_{\mathbf{q},\nu}))^{1/2}$. The scattering energy imparted by this change in the potential under a given phonon mode that scatters Bloch state $u_{n\mathbf{k}}$ to $u_{m\mathbf{k}+\mathbf{q}}$, where u are the Bloch components of the total Bloch wave functions, is called the electron-phonon vertex $g_{mn\nu}(\mathbf{k},\mathbf{q})$ and carries units of energy. Alternative and common names for g include the electron-phonon matrix elements and electron-phonon scattering energy. The electron-phonon vertex, measuring the scattering energy of an electron moving from band n and wave vector $\mathbf{k}$ to band m and wave vector $\mathbf{k}+\mathbf{q}$ mediated by a phonon of band index ν and wave vector $\mathbf{q}$, is determined within DFPT as:

$$g_{mn\nu}(\mathbf{k},\mathbf{q}) = \langle u_{m\mathbf{k}+\mathbf{q}}|\Delta_{\mathbf{q}\nu}V(\mathbf{r})|u_{n\mathbf{k}}\rangle_\Omega \tag{2.58}$$

The integral of equation 2.58 is taken over the volume of the unit cell Ω. Modern calculations of sets of g on a grid of $\mathbf{k}$- and $\mathbf{q}$-points is performed by a combinations of equations 2.50, 2.52, 2.57, and 2.58 within DFPT.

The calculation of a set of g currently requires vast computational resources and intricate interpolation methods. Historically, theorists resorted to models of g for individual classes of materials. We will visit two specific models: the simple Bloch model and the simple Fröhlich model. The latter will become important for the work performed herein. The simple Bloch model was proposed by none other than its namesake in 1926 and modified to include electronic screening by Bardeen in 1937, and proposes [71, 98]:

$$g_{mn\nu}(\mathbf{k},\mathbf{q}) = i\sum_\kappa (1/(2M_0\omega_{\mathbf{q},\nu}))^{1/2}\,\mathbf{q}\cdot\mathbf{e}_{\kappa,\nu}(\mathbf{q})\frac{V_\kappa(\mathbf{q})}{\varepsilon_\infty(\mathbf{q})} \tag{2.59}$$

Here, V_κ is the potential of the κ^{th} atom and $\varepsilon_\infty(\mathbf{q})$ is the wave vector dependent high-frequency dielectric constant. While the Bloch model for g is a good attempt to describe the electron-phonon scattering vertex that arises from changes in electronic charge density induced by a phonon mode, fails to describe the scattering process in polar crystals. The reason is the aforementioned macroscopic dipoles induced by phonon modes that separate ions with opposite charge. Fröhlich, Pelzer, and Zienau proposed, in their seminal work to describe polaron formation by self-trapping of electrons by lattice distortion in 1950, that

the electron-phonon vertex take the form [99]:

$$g_{mn\nu}(\mathbf{k},\mathbf{q}) = -i\frac{1}{|\mathbf{q}|}\left(\frac{4\pi\omega_{LO}}{\Omega}\left(\frac{1}{\varepsilon_\infty}-\frac{1}{\varepsilon_0}\right)\right)^{1/2} \tag{2.60}$$

The model assumes that electronic states are described by a parabolic band model and the polarizable background is isotropic with dielectric constant contributions from the lattice and electrons. The potential exerted on the lattice by the electron is given by a $1/|\mathbf{q}|^2$ relationship and is screened by the Fröhlich dielectric constant $(\varepsilon_\infty^{-1}-\varepsilon_0^{-1})^{-1}$. The strength of the vertex of determined by a singular LO phonon frequency.

Recent work has been aimed at determining piecewise contribution to g arising from long-range electric field induced scattering by LO phonons and short-range scattering by perturbation to the local charge density. In this effort, Verdi and Giustino proposed a generalized Fröhlich vertex that does not rely on the parabolic band, single LO phonon mode, and isotropic background assumptions. The authors posit that the electron-phonon vertex can be written as a sum of a long range L and a short range S contribution [100]:

$$g_{mn\nu}(\mathbf{k},\mathbf{q}) = g^L_{mn\nu}(\mathbf{k},\mathbf{q}) + g^S_{mn\nu}(\mathbf{k},\mathbf{q}) \tag{2.61}$$

Where the long range contribution, designated the generalized Fröhloch vertex, is derived to be:

$$g^L_{mn\nu}(\mathbf{k},\mathbf{q}) = i\frac{4\pi}{\Omega}\sum_\kappa\left(\frac{1}{2M_\kappa\omega_{\mathbf{q}\nu}}\right)^{1/2}\sum_{\mathbf{G}}\frac{(\mathbf{q}+\mathbf{G})\cdot Z_\kappa\cdot\mathbf{e}_{\kappa\nu}(\mathbf{q})}{(\mathbf{q}+\mathbf{G})\cdot\varepsilon_{\infty,\mathbf{GG}}(\mathbf{q})\cdot(\mathbf{q}+\mathbf{G})}B^{m\mathbf{k}+\mathbf{q}}_{n\mathbf{k}}(\mathbf{G}) \tag{2.62}$$

Here, Z_κ are the Born effective charges of the ions and B are the Bloch integrals defined previously. Under the assumptions of the original Fröhlich vertex, it can be shown that equation 2.62 reduces to equation 2.60 by the help of LST relation [100]. Though this generalized Fröhlich is originally proposed as a numerical correction to handle Wannier interpolation of the electron-phonon vertices, the authors demonstrate that g^L is the dominant contribution to g at small wave vector. Phonon mediated scattering of electronic states at large distances is therefore well described by the generalized Fröhlich vertex. The changes induced on the system energy by the electron-phonon interaction fundamentally change the quasi-particle self energies. In considering Hedin's equations, these self energy changes propagate as changes to the other four self-consistent equations, including the screened Coulomb interaction. The electron-phonon vertex fundamentally determines the strength of the lattice screened Coulomb interaction, a quantity we seek to describe in this thesis.

2.7 Lattice Screening of the Electron-Hole Coulomb Potential

Equipped with the knowledge of phonons, the low-frequency dielectric tensor arising from polar phonons, and electron-phonon vertices at multiple levels of approximation, we are ready to discuss dynamical lattice screening of the electron-hole Coulomb potential. We will begin with the Fan-Migdal self-energy arising from the interaction of single-particles with the lattice distortions. The Fan-Migdal self-energy is the change in single-particle energies as a function of first-order electron-phonon scattering processes. Next, it will be shown that the screened Coulomb interaction arising from the Fan-Midgal term is a two-frequency term in the electron-hole problem and renders the BSE non-writable as an excitonic Hamiltonian problem. This can be navigated by applying Shindo's approximation to write the dynamical lattice screened Coulomb as a function of a single excitation frequency.

2.7.1 The Lattice Screened Coulomb Interaction from the Fan-Migdal Self Energy

Let us revisit the equation for the electron self energy Σ in the GW approximation. In most calculations of the electronic band energies, the screened Coulomb interaction is only screened by the electronic polarizable background described by the inverse dielectric tensor $\varepsilon^{-1}_{\infty,\mathbf{GG'}}(\mathbf{q},\omega)$. In polar crystals, the polarizable ionic background also contributes to the dielectric tensor leading to the low-frequency dielectric tensor $\varepsilon^{-1}_{0,\mathbf{GG'}}(\mathbf{q},\omega)$. Therefore, it is necessary to reformulate Hedin's equations to include phonon contributions to the screening. The literature concerning this approach is extensive, but the main conclusion pertaining to this work concerns the separation of the screened Coulomb potential into an electronically screened portion W_{el} and a phonon (lattice) screened portion W_{ph}. The two are additive, so the self energy is then also expressed as a sum [38, 93]:

$$\Sigma^{tot}(1,2) = \Sigma^{GW}(1,2) + \Sigma^{FM}(1,2) = \int d(3,4)G(1,3)W_{el}(4,1) + \int d(3,4)G(1,3)W_{ph}(4,1) \tag{2.63}$$

The self energy correction arising from the phonon-screened Coulomb potential is the Fan-Migdal self energy, and can be further expressed by [101, 102]:

$$\Sigma^{FM}(1,2) = i\sum_{\nu\nu'}\int \frac{d\omega}{2\pi}\frac{d\mathbf{q}}{\Omega_{BZ}} d(3,4)e^{-i\omega(t_4-t_1)}G(13)g^{*}_{\mathbf{q}\nu}(\mathbf{r}_4)D_{\mathbf{q}\nu\nu'}(\omega)g_{\mathbf{q}\nu}(\mathbf{r}_1) \tag{2.64}$$

The real-space electron-phonon vertices g are equivalent to the aforementioned changes in the total potential induced by a phonon with wave vector $\mathbf{q}$ and band index ν: $\Delta_{\mathbf{q}\nu}V(\mathbf{r})$. D is the phonon propagator. D can

be taken in the adiabatic limit [93]:

$$D^A_{\mathbf{q}\nu}(\omega) = D_{\mathbf{q}\nu\nu'}(\omega)\delta_{\nu\nu'} = \left(\frac{1}{\omega - \omega_{\mathbf{q}\nu} + i\eta} - \frac{1}{\omega + \omega_{\mathbf{q}\nu} + i\eta}\right) \tag{2.65}$$

Isolating W_{ph}, we find:

$$W_{ph}(1,4;\omega) = \sum_{\nu} g^*_{\mathbf{q}\nu}(\mathbf{r}_4) D^A_{\mathbf{q}\nu}(\omega) g_{\mathbf{q}\nu}(\mathbf{r}_1) \tag{2.66}$$

Equation 2.58 can be used to take matrix elements of W_{ph} between Bloch states, rendering:

$$W^{mm'\mathbf{k}'}_{ph,nn'\mathbf{k}}(\mathbf{q},\omega) = \sum_{\nu} g^*_{mm'\nu}(\mathbf{k}',\mathbf{q}) g_{nn'\nu}(\mathbf{k},\mathbf{q}) D^A_{\mathbf{q}\nu}(\omega) \tag{2.67}$$

For excitations of single-particles, W as a function of a single excitation frequency can be utilized to calculate the self energy. The electron-hole excitation poses a difficulty. Both the electrons and holes under optical excitation may propagate at different frequencies. If the screened Coulomb interaction now carries the frequency dependence, the two-particle correlation function with the kernel Ξ determined in the GW approximation can be expressed as [82]:

$$\begin{aligned} L(1,1',2,2';\omega_j\omega_l) = G(12';\omega_j)G(2,1';\omega_j - \omega_l) + \frac{1}{\beta}\sum_{j'}\int d(3,4,5,6) G(1,3;\omega_j) G(4,1';\omega_j - \omega_l) \\ \times \left[W(3,4;\omega_j - \omega_{j'}) + v_c(5,4)\right] L(5,6,2,2';\omega_j\omega_l) \end{aligned} \tag{2.68}$$

In this case, the the frequencies are Matsubara frequencies index by j and l. The frequencies ω_j and ω'_j are fermionic propagation frequencies whereas ω_l is a bosonic excitation frequency. A BSE of this form poses multiple numerical challenges. The first is the need for the frequency summation over $\omega_{j'}$, for which special consideration is needed to avoid numerical divergences. However, this integration must be performed in the spectral representation along two cuts in the complex plane. This procedure results in two coupled integral equations that would be difficult to solve even with modern computational tools [82]. Therefore, we seek a formulation where this explicit integral over a Fermion frequency is not needed, leading to the construction of the BSE as an eigenvalue problem implicitly dependent on a single excitation frequency. In order to construct one, an approximation must be made. This was done by Shindo in 1970 [103]. In the limit of a weak electron-hole interaction (such as with Wannier-Mott excitons) the two-particle correlation function can be expressed approximately as a function of a single excitation frequency by [103]:

$$L(1,1',2,2';\omega_j\omega_l) \approx \frac{G(1,1;\omega_j) - G(1',1';\omega_j - \omega_l)}{-\frac{1}{\beta}\sum_{j'}\left(G(1,1;\omega_j) - G(1',1';\omega_{j'} - \omega_l)\right)} L(1,1',2,2';\omega_l) \tag{2.69}$$

Now, the two-particle correlation function can be expressed as the exciton wave function expanded in the Bloch basis. The electron-hole problem is restricted to valence to conduction transitions at single $\mathbf{k}$-points and the screening wave vectors are restricted to $\mathbf{q} = \mathbf{k} - \mathbf{k}'$ [103, 82].

$$W^{c'v'\mathbf{k}'}_{ph,cv\mathbf{k}}(\omega_l) = \frac{1}{\beta^2}\sum_{jj'} \frac{G_{c\mathbf{k}}(\omega_j) - G_{v'\mathbf{k}'}(\omega_j - \omega_l)}{f(E^{QP}_{c\mathbf{k}}) - f(E^{QP}_{v'\mathbf{k}'})} W^{c'v'\mathbf{k}'}_{cv\mathbf{k}}(\omega_j - \omega_{j'}) \frac{G_{v\mathbf{k}}(\omega_{j'}) - G_{c'\mathbf{k}'}(\omega_{j'} - \omega_l)}{f(E^{QP}_{v\mathbf{k}}) - f(E^{QP}_{c'\mathbf{k}'})} \tag{2.70}$$

Here, f is the Fermi occupation number at the quasi-particle energies. Now, let's apply this to the lattice screened Coulomb interaction by substituting Eq. 2.67 for W:

$$W^{c'v'\mathbf{k}'}_{ph,cv\mathbf{k}}(\omega_l) = \\ \frac{1}{\beta^2}\sum_{jj'} \frac{G_{c\mathbf{k}}(\omega_j) - G_{v'\mathbf{k}'}(\omega_j - \omega_l)}{f(E^{QP}_{c\mathbf{k}}) - f(E^{QP}_{v'\mathbf{k}'})} \sum_{\nu} g^*_{cc'\nu}(\mathbf{k}', \mathbf{q}) g_{vv'\nu}(\mathbf{k}, \mathbf{q}) D^A_{\mathbf{q}\nu}(\omega_j - \omega_{j'}) \frac{G_{v\mathbf{k}}(\omega_{j'}) - G_{c'\mathbf{k}'}(\omega_{j'} - \omega_l)}{f(E^{QP}_{v\mathbf{k}}) - f(E^{QP}_{c'\mathbf{k}'})} \tag{2.71}$$

We can restrict here the values of $\mathbf{q}$ in W_{ph} to $\mathbf{k} - \mathbf{k}'$ as we are only considering optical excitations. The Matsubara frequency summation only acts on the adiabatic phonon propagator that is dependent on the individual fermion frequencies, as we have approximated the electron-phonon vertices to carry no frequency dependence. After carrying out the sum of Matsubara frequencies and taking the limit of the analytic continuum $\omega_l \to \omega$ we find an expression for the frequency dependent lattice screened Coulomb interaction.

$$W^{c'v'\mathbf{k}'}_{ph,cv\mathbf{k}}(\omega) = \sum_{\nu} g^*_{cc'\nu}(\mathbf{k}', \mathbf{q}) g_{vv'\nu}(\mathbf{k}, \mathbf{q}) \left(\frac{1}{\omega_{\mathbf{q},\nu} + E_{c\mathbf{k}} - E_{v'\mathbf{k}'} - \omega} + \frac{1}{\omega_{\mathbf{q},\nu} + E_{c'\mathbf{k}'} - E_{v\mathbf{k}} - \omega} \right) \tag{2.72}$$

Now, the dynamical BSE can be recast as an implicit eigenvalue problem of the form [103, 104]:

$$(E_{c\mathbf{k}} - E_{v\mathbf{k}}) A_{cv\mathbf{k}} + \sum_{c'v'\mathbf{k}'} \left[\bar{v}^{c'v'\mathbf{k}'}_{cvk} - (W^{c'v'\mathbf{k}'}_{el,cvk} + W^{c'v'\mathbf{k}'}_{ph,cvk}(\omega = E_\Lambda)) \right] A_{c'v'\mathbf{k}'} = E_\Lambda A_{cv\mathbf{k}} \tag{2.73}$$

The excitonic eigenvalue problem is an implicit equation for the excitation frequency ω. The eigenvalues of the excitonic matrix must be determined on a grid of ω to determine the case where $E_\Lambda = \omega$, indicating the dynamical optical excitation energy has been found. At this point, we have determined an equation for the lattice screened Coulomb interaction where the explicit electron-phonon vertices must be utilized. While methods are available to calculate these quantities on dense grids [105], it may not be necessary. In systems hosting Wannier-Mott excitons, the exciton wave function spreads over a small distance in $\mathbf{q}$ space [86]. At small $\mathbf{q}$, the dominant contributor to the electron-phonon vertex is the generalized Fröhlich vertex of equation 2.62 [100]. By replacing the vertex in Eq. 2.72 with the long-range contribution only, as defined in Eq. 2.61, and using the definition of the low-frequency dielectric tensor in Eq. 2.54, W_{ph} can be written

in the long-range approximation:

$$W^{L,c'v'\mathbf{k}'}_{ph,cv\mathbf{k}}(\omega) = -\sum_{\mathbf{G}} \frac{4\pi}{|\mathbf{q}+\mathbf{G}|^2} \times \left[\sum_{\nu} \frac{\omega_{\mathbf{q}\nu}}{2} \left(\varepsilon^{-1}_{\infty,\mathbf{GG}}(\mathbf{q},\omega=\mathbf{0})\right)^2 \frac{4\pi}{\Omega} \frac{S_{\nu,\mathbf{GG}}(\mathbf{q})}{\omega^2_{\mathbf{q},\nu}} \left(\frac{1}{\omega_{\mathbf{q},\nu}+E_{c\mathbf{k}}-E_{v'\mathbf{k}'}-\omega} + \frac{1}{\omega_{\mathbf{q},\nu}+E_{c'\mathbf{k}'}-E_{v\mathbf{k}}-\omega}\right)\right] \times B^{c'\mathbf{k}'}_{c\mathbf{k}}(\mathbf{G}) B^{v'\mathbf{k}'}_{v\mathbf{k}}(\mathbf{G}) \quad (2.74)$$

This proposed model function for the lattice screened Coulomb interaction takes into account the Fröhlich coupling from all possible phonon modes. Naturally, acoustic modes and transverse optical modes exhibit a very low or zero mode oscillator strength, so generally only modes with LO character contribute to the sum. A further approximation can be made considering that the Coulomb term $1/\mathbf{q}^2$ promotes only long wavelength contributions from the screened Coulomb interaction. Additionally, many simple materials only have a single highest frequency LO phonon mode that contributes to lattice polarizability in the small $\mathbf{q}$ limit [90]. Therefore, an approximate model function for the dynamically lattice screened Coulomb interaction can be formulated by replacing g with the simple Fröhlich model [99] of Eq. 2.60 and accounting for one LO phonon mode:

$$W^{L,c'v'\mathbf{k}'}_{ph,cv\mathbf{k}}(\omega) = -\sum_{\mathbf{G}} \frac{4\pi}{|\mathbf{q}+\mathbf{G}|^2} \times \left[\frac{\omega_{LO}}{2} \left(\frac{1}{\varepsilon_\infty} - \frac{1}{\varepsilon_0}\right) \left(\frac{1}{\omega_{LO}+E_{c\mathbf{k}}-E_{v'\mathbf{k}'}-\omega} + \frac{1}{\omega_{LO}+E_{c'\mathbf{k}'}-E_{v\mathbf{k}}-\omega}\right)\right] \times B^{c'\mathbf{k}'}_{c\mathbf{k}}(\mathbf{G}) B^{v'\mathbf{k}'}_{v\mathbf{k}}(\mathbf{G}) \quad (2.75)$$

Equations 2.72, 2.74, and 2.75 represent three descending levels of of sophistication to calculate the lattice screening Coulomb interaction dynamically in Shindo approximation.

2.7.2 Practical Calculations of Optical Response with Dynamical Lattice Screening

In practice, we solve Equation 2.75 to include dynamical lattice screening in the Bethe-Salpeter Equation. The excitonic Hamiltonian with a dynamically screened screened Coulomb interaction must be solved on a grid of ω. When the resulting lowest excitation eigenvalue is equal to the trial frequency, then the true excitation energy (and in turn, the exciton binding energy) is determined. Once the dynamically lattice screened excitation energy $E_{xb,dyn}$ is determined, an effective dielectric constant can be calculated by the

screening term in Eq. 2.75 by replacing the excitation frequency ω with $E_{xb,dyn}$ and adding the electronic screening contribution:

$$\varepsilon_{eff} = \left[\frac{1}{\varepsilon_\infty} - \left(\frac{1}{\varepsilon_\infty} - \frac{1}{\varepsilon_0}\right)\frac{\omega_{LO}}{2}\left(\frac{2}{E_{xb,dyn} + \omega_{LO}}\right)\right]^{-1} \tag{2.76}$$

This equation solves precisely for the effective dielectric screening constant of the lowest optical excitation within the Shindo and simple Fröhlich approximations. This effective dielectric constant can be used to calculate optical spectra by the BSE using model functions that take a single dielectric constant as input [87]. Ideally, each excitation eigenvalue has its own associated effective dielectric constant. However, on the dense **k**-point grids required to determine optical spectra in semiconductors, determining separate dynamically screened excitation energies for each electron-hole pair is computationally intractable. It is worth briefly discussing some limits. When $\omega_{LO} >> E_{xb,dyn}$, we expect the lattice to be able to fully track the motion of the exciton, and thus the effective dielectric constant becomes ε_0. On the other hand, when $\omega_{LO} << E_{xb,dyn}$, the lattice screened term goes to zero and the effective dielectric constant becomes ε_∞. These limits were postulated by Haken and worked out by Shindo in their original works [106, 103].

2.8 Calculating Excitation Energies in Isolated Molecules

2.8.1 Δ-Self Consistent Field Method

The method that would later become known as Δ-Self Consistent Field method (ΔSCF) was first proposed and explored by Gunnarsson and Lundqvist in 1976 [107]. The core concept behind ΔSCF is to enforce the occupation of Kohn-Sham energy states in the self-consistent cycle of DFT. If the set of calculations has a consistent reference energy (for example, the vacuum energy in local basis DFT calculations), then the energy difference between the lowest energy configuration of a given symmetry and the ground state generates a reliable prediction of the excitation energy between the states. For example, the lowest energy triplet state can be prepared in open-shell DFT by taking an electron from the highest occupied Kohn-Sham state and placing, with a spin flip, it in the lowest unoccupied Kohn-Sham state.

2.8.2 Linear Response Time-Dependent Density Functional Theory

Linear response time-dependent density functional theory (LR-TDDFT) provides an alternative to MBPT for calculating electronic and optical excitation spectra. The topic will not be covered extensively here, but many excellent review articles and texts are available for the interested reader[108]. The core concept

behind TDDFT is that one moves from a static external potential to a time-dependent external potential. The Runge-Gross theorem states that, for an initial wave function and analytics time-dependent potential, the time dependent external potential maps one-to-one to a time-dependent charge density [109]. For an applied external potential, one can solve every time step for the time-dependent charge density and wave functions. TDDFT allows for the access of optical excitation by treating the AC electric field as a time-dependent external potential. If the change in charge density is treated as linear with respect to the external potential, one derives linear-response (LR)-TDDFT. For isolated molecular systems, optical excitations between single Kohn-Sham eigen-states are determined by the non-Hermitian eigenvalue problem called the Casida equation within LR-TDDFT [110, 111]:

$$\begin{pmatrix} A & B \\ B^* & A \end{pmatrix} \begin{pmatrix} X \\ Y \end{pmatrix} = E_\Lambda \begin{pmatrix} I & 0 \\ 0 & -I \end{pmatrix} \begin{pmatrix} X \\ Y \end{pmatrix} \tag{2.77}$$

Keeping with the set convention, E_Λ are the optical excitation energies. X and Y, like in the BSE, are eigenvectors of coefficients that weight contributions of pairs of Kohn-Sham eigen-states to the optical excitation E_Λ. The matrix elements are given by:

$$A = \delta_{\sigma\sigma'}\delta_{mm'}\delta_{nn'}(\epsilon_{m\sigma'} - \epsilon_{n\sigma}) + \Xi^{mm'\sigma'}_{nn'\sigma} \tag{2.78}$$

$$B = \Xi^{mn'\sigma'}_{nm'\sigma} \tag{2.79}$$

Here, indices n and m run over occupied and unoccupied KS states, respectively, and the index σ runs over spin. The interaction Kernel is given by:

$$\begin{aligned} \Xi^{mm'\sigma'}_{nn'\sigma} = &\int d\mathbf{r}d\mathbf{r}'\psi_{m',\sigma'}(\mathbf{r}')\psi_{n',\sigma'}(\mathbf{r}')\psi_{m,\sigma}(\mathbf{r})\psi_{n,\sigma}(\mathbf{r}) \\ &+ \int d\mathbf{r}d\mathbf{r}'\psi_{m',\sigma'}(\mathbf{r}')\psi_{n',\sigma'}(\mathbf{r}')\frac{\delta^2 E_{xc}}{\delta\rho_{\sigma'}(\mathbf{r})\delta\rho_\sigma(\mathbf{r})}\psi_{m,\sigma}(\mathbf{r})\psi_{n,\sigma}(\mathbf{r}) \end{aligned} \tag{2.80}$$

The interaction Kernel in LR-TDDFT shares a semblance with that of the excitonic Hamiltonian derived from the BSE. It is a sum of an exchange term and an interaction term, with the interaction operator given by the functional derivative with respect to the spin-polarized charge density of the exchange-correlation energy functional.

It is informative to compare LR-TDDFT with ΔSCF in its advantages and disadvantages. The first

and foremost advantage of LR-TDDFT is that it is not restricted to calculating only the first excitation energy of transitions form the ground state into the lowest alternate symmetry state. Additionally, orbital contributions to optical transitions can be straightforwardly determined by the Casida equation, whereas this information is not available through ΔSCF. Finally, LR-TDDFT can easily determine singlet excitation energies whereas ΔSCF cannot, as the ground state is the lowest energy singlet state and accurate excitation energies of higher energy symmetry states are not guaranteed in ΔSCF. A disadvantage of LR-TDDFT lies in what is known as the triplet instability where, depending on the strength of the exchange-correlation energy, excessively low or even negative triplet excitation energies are predicted [112]. In ΔSCF, the exchange-correlation energy contribution between the ground state and the lowest energy triplet state effectively cancel upon subtraction. Thus, ΔSCF tends to lead to very reliable predictions of the lowest triplet excitation energy [113].

2.9 Summery of Theoretical Approaches

At this point, a summary of the theoretical approach for material optical response calculations from first principles is helpful. Within the DFT+MBPT framework, optical response calculations of materials are a three step process. First, DFT calculations are performed to determine the ground state electron density and Kohn-Sham band structure and linear optical response. Second, the *GW* approximation (or a hybrid functional calculation) is employed to determine an accurate electronic band structure and band gap. Linear optical response, without the electron-hole interaction, can be also calculated at this step. Finally, the Bethe-Salpeter equation reformulated as an excitonic Hamiltonian can be solved to include the electron-hole interaction in linear optical response calculations, thus generating reliable optical absorption spectrum calculations. In considering the screening mechanisms of the electron-hole Coulomb interaction, generally only static electronic screening is accounted for as it is assumed that background electronic excitations can adjust without delay to the motion of the exciton. In real systems, electronic dielectric screening is not the only screening mechanism. Additional background screening by free-carriers can be accounted for by a Thomas-Fermi screening model. Dynamical lattice screening by the Shindo approximation can be applied to determine how the dielectric response of the lattice influences the electron-hole Coulomb potential. In this Chapter, I have detailed my development of the the dynamical lattice screened Coulomb interaction at three levels of theory, given by Eq. 2.72, 2.74, and 2.75. In the coming work, I will apply these methods extensively to determining the optical and excitonic properties of HOP and LHOP materials.

CHAPTER 3

FREE-CARRIER EFFECTS ON THE OPTICAL RESPONSE OF $MAPbI_3$

3.1 Introduction

A factor that critically influences whether a material is a good candidate for a photovoltaic absorbing layer is the electron-hole interaction. If this interaction is strong in a material, strongly bound excitonic states appear near the absorption onset. These are associated with strong optical absorption that is beneficial for harvesting light using as little absorber material as possible. At the same time, strong electron-hole interaction renders separation of electron-hole pairs challenging, which is detrimental in a photovoltaic device [114]. Interestingly, hybrid orgainc-inorganic perovskite $CH_3NH_3PbI_3$ ($MAPbI_3$) balances between low exciton binding energy and large optical absorption across the visible spectrum. This facilitates efficient generation of electron-hole pairs that can be thermally separated and is beneficial for photo-current generation [27]. This interesting balance triggered numerous studies, aimed at a better understanding of excitonic effects in $MAPbI_3$. Experimental results for exciton binding energies range from as high as 62 meV to as low as 2 meV [27], however, a few patterns emerge. First, the line shape of the absorption edge has been reported to be comparable to that of GaAs, with no clear excitonic peak and a binding energy potentially under 10 meV at room temperature [115]. Second, a reduction of the exciton binding energy is observed when going from the low-temperature (LT) orthorhombic phase to the room-temperature (RT) tetragonal phase. Sestu *et al.* measured 34 meV (LT) to 29 meV (RT) [116], Galkowski *et al.* measured between 14 and 25 meV (LT) to 12 meV (RT) [117], and Yang *et al.* measured 16 meV (LT) to between 5 and 12 meV (RT) [118]. However, there are also examples for studies where RT exciton binding energies exceed LT binding energies in others [119, 118, 116, 120, 121, 122, 123, 117, 124].

Further insight into this variability comes from four-wave mixing spectroscopy, to disentangle exciton binding energies of intrinsic and defect-bound excitons [125]. These results indicate that intrinsic excitons have an LT binding energy of 13 meV, whereas values for defect-bound excitons average around 29 meV, linking the variability to different defect concentrations lest uncharacterized. In particular, while exciton binding energies in pure $MAPbI_3$ are consistently lower than 35 meV for LT and RT phases, the addition

of small amounts of chlorine into $MAPbI_3$ thin films tends to increase this value to more than 50 meV [119, 126].

While the variation of experimental results causes ongoing debate of the excitonic character of the absorption edge, first principles theoretical spectroscopy can provide deeper understanding. To this end, Bokdam *et al.* used many-body perturbation theory (MBPT) and solved the Bethe-Salpeter equation (BSE) for the optical polarization function, reporting an exciton binding energy of 45 meV in tetragonal $MAPbI_3$ [127]. Similarly, Zu *et al.* computed 40 meV [51] and Umari *et al.* computed 30 meV using a similar framework [32]. All three studies attribute the dielectric screening of the electron-hole Coulomb interaction exclusively to electronic interband transitions, corresponding to a high-frequency dielectric constant ε_∞ of $MAPbI_3$ between 5 and 7 [127, 32, 51]. In another work Ahmed *et al.* used the BSE framework to predict a binding energy of 153 meV. While these calculations were done on a coarse $4\times4\times4$ **k**-point grid, likely leading to an overestimate of the binding energy [52], the values of 45 meV [127] and 40 meV [51] quoted above still overestimate experimental data.

However, exciton binding energies are critically influenced by the strength of the electron-hole interaction and, thus, dielectric screening in the material, both in experiment and calculations. This is important because the lattice structure of $MAPbI_3$ is very polarizable, leading to a large *static* dielectric constant, possibly contributing to screening. To this end, Frost *et al.* showed that the static dielectric constant of 25.7, accounting for lattice and electronic polarizability, leads to an exciton binding energy of less than 1 meV in a Wannier-Mott model [128]. Evens *et al.* used a value of ε=11 to demonstrate that including lattice contributions to screening improves agreement with measured room-temperature absorption spectra [49]. Menéndez-Proupin *et al.* use a parabolic-band with a Pollman-Büttner type model for polaron screening and find an exciton binding energy of 24 meV [129]. Umari *et al.* also showed that including polar phonon screening reduces the binding energy from 30 meV to 15 meV [32]. Finally, Hakamata *et al.* employed non-adiabatic molecular dynamics to calculate the time-averaged exciton binding energy in a dynamical $MAPbI_3$ lattice, predicting a binding energy of 12 meV and a dielectric constant between 10 and 15, in excellent agreement with RT measured values [130]. Bokdam *et al.* provide arguments against the importance of lattice screening for exciton binding energies of $MAPbI_3$ and instead invoke formation of polarons [127].

In this work, we study the complementary problem of an additional screening contribution due to free electrons, arising from defects or donors in a sample. First principles studies of multiple point defects in $MAPbI_3$ showed that charged defects with low formation energy occupy shallow levels relative to the band extrema [131, 132, 133, 134]. Wang *et al.* showed that synthesis with varying ratios of PbI_2:MAI precursors can change samples from *p*- to *n*-type, with free-electron concentrations as high as 3.5×10^{18} cm^{-3} and even

at a standard precursor ratio of 1:1 moles of PbI_2 and MAI, a free-electron concentration of 1.8×10^{17} cm^{-3} was measured [33]. Other studies confirmed free-carrier concentrations in the range of $10^{17} - 10^{18}$ cm^{-3} [34, 35]. Dielectric screening due to free electrons has been shown to reduce the strength of the electron-hole Coulomb interaction in ZnO [135, 92, 136] and, together with Pauli blocking lead to formation of Mahan excitons [137] at the absorption edge.

We speculate that these effects also affect exciton binding $MAPbI_3$ and to clarify this, we perform accurate first principles simulations of electronic structure and optical properties of $MAPbI_3$[1] The remainder of the chapter is organized as follows. Section 3.2 summarizes the theoretical and computational approach for solving the BSE to calculate optical response. Section 3.3 details results for atomic geometries, electronic structure, and optical properties. We compute exciton-binding energies and optical spectra, explicitly including various concentrations of free electrons that arise in the material for varying defect concentrations. Finally, Sec. 3.4 summarizes and concludes this chapter.

3.2 Computational Methods

We use density functional theory (DFT) [36, 37] to compute fully relaxed atomic geometries of the three experimentally most relevant polymorphs of $MAPbI_3$, i.e. the orthorhombic (O), tetragonal (T), and cubic (C) phase. Their Brillouin zones (BZs) are sampled using Γ-centered $4 \times 4 \times 4$, $4 \times 4 \times 4$, and $6 \times 6 \times 6$ **k**-point meshes, respectively. The projector-augmented wave (PAW) method is used to describe the electron-ion interaction [70] and single-particle wave functions are expanded into a plane-wave basis up to a cutoff energy of 600 eV. These parameters are sufficient to converge the total energy to within 5 meV per atom. The PBEsol exchange-correlation (XC) functional [139] has previously been used to predict accurate relaxed atomic geometries for $MAPbI_3$ [140] and is used here for the same purpose.

In order to obtain equilibrium atomic geometries, we initialize the structures of the O, T, and C phases prior to relaxation using those reported in Ref. [140]. This captures the symmetry of ordered MA cations in the O phase and a pseudo-random ordering of the MA sub-lattice in the T phase. While the C phase exhibits total disordering of the MA cation sub-lattice in experiment [141], we study a pseudo-cubic phase with ordered MA cations. This approach is common in the literature to maintain the uniform alignment of PbI_3 octahedra observed experimentally for the C phase [140, 142, 143]. In experiment the cubic lattice also shows a slight pseudo-cubic behavior, due to rotations of the MA cations [141]. We verify that these atomic coordinates correspond to equilibrium structures by computing total energies for several unit-cell volumina

[1]The results presented in this chapter are published in the article: Joshua Leveillee and André Schleife, Phys. Rev. B 100, 035205 (2019) [138].

within 1 % of the equilibrium value and determine the minimum. All atomic geometries were then relaxed until Hellman-Feynman forces are smaller than 10 meV/Å.

For these relaxed geometries we compute high- and low-frequency dielectric tensors using density functional perturbation theory (DFPT) [144] and the generalized-gradient approximation by Perdew, Burke, and Ernzerhof (PBE) [68] to describe XC. The BZs are sampled using Γ-centered $5 \times 5 \times 5$, $5 \times 5 \times 5$, and $7 \times 7 \times 7$ **k**-point meshes for O, T, and C phases, respectively, for these calculations.

In order to compute electronic structures that can be compared to experiment, we overcome the well-known band gap underestimation of DFT by taking quasiparticle (QP) corrections into account within MBPT [145]. Furthermore, due to the presence of heavy-metal ions in $MAPbI_3$, spin-orbit coupling (SOC) is included within the PAW approach [146]. We performed GW_0+SOC calculations using $1 \times 1 \times 1$, $1 \times 1 \times 1$, and $2 \times 2 \times 2$ Γ-centered **k**-point grids for O, T, and C phases, respectively. The Green's function was iterated four times to converge QP band gaps to within 25 meV. 4000 empty bands were included for the O and T structures, and 2000 for the C phase.

Finally, we study optical response including excitonic effects by solving the Bethe-Salpeter equation (BSE) for the optical polarization function. The BSE in the Bloch basis can be written as an eigenvalue equation [147, 85] for the Hamiltonian as given by Eq. 2.39 and 2.40. The indices c, v, and $\mathbf{k}$, refer to conduction band, valence band, and point in reciprocal space, respectively. The term in parentheses on the right-hand side represents single-QP excitation energies of non-interacting electron-hole pairs, described by the QP band structure. For the QP energies $\epsilon_{c\mathbf{k}}$ and $\epsilon_{v\mathbf{k}}$ we use results computed using PBE+SOC, with the band gap rigidly shifted to the GW_0+SOC gap. Bloch integrals, that enter the exchange interaction $2v^{cv\mathbf{k}}_{c'v'\mathbf{k}'}$ and the screened Coulomb interaction $W^{cv\mathbf{k}}_{c'v'\mathbf{k}'}$ between electrons and holes, are evaluated using spin-polarized DFT-PBE Kohn-Sham eigen-states. Electronic interband screening of the electron-hole Coulomb interaction is computed using the model dielectric function proposed by Bechstedt *et al.* in the absence of free-carriers [148, 149] and approximated as a dielectric constant ε_∞ when free-carriers are taken into account [135, 92]. Optical spectra of C $MAPbI_3$ are computed over a wide energy range using a $11 \times 11 \times 11$ **k**-point grid with a small random shift and for a careful examination of the spectral onset up to an energy of 2.2 eV, a hybrid 5:2:32.5 **k**-point grid is used (see Ref. [150] for nomenclature). Independent-particle spectra for the O and T phases were computed using $7 \times 7 \times 7$ **k** points with a small random shift.

In order to describe the influence of free electrons, we account for (i) Pauli blocking affecting selection rules for optical transitions (Burstein-Moss shift, BMS), (ii) free-electron effects on the single-particle band structure via band-gap renormalization (BGR), and (iii) additional free-electron screening of the electron-hole interaction [135, 151, 152, 136]. This approach has been previously successfully used to describe optical

Table 3.1: Lattice parameters a, b, c (in Å) and unit-cell volume V (in Å^3) computed in this work, compared to other theoretical and experimental data.

	This Work	Ref. PBEsol[140, 159]	Exp.[160, 141]
Orthorhombic			(13 K)
a	8.365	8.350	8.571
b	9.073	9.040	8.855
c	12.665	12.66	12.614
V	961.27	955.63	957.35
Tetragonal			(180 K)
a	8.711	8.700	8.970
b	8.720	8.720	–
c	12.846	12.830	12.768
V	975.810	979.78	986.510
Cubic			300 K – 350 K
a	6.291	6.29	6.26-6.31
b	6.253	6.23	–
c	6.386	6.37	–
V	251.12	246.62	245.31 – 251.24

properties of doped ZnO [135, 92]. BMS arises from Pauli blocking of the lowest conduction-band states that are occupied by the additional free electrons. We account for this by setting the occupation number of these states accordingly when calculating dielectric functions, after the ground-state DFT electronic-structure calculations. BGR is described as a rigid shift of the entire conduction band, computed using the analytic model of Berggren and Sernelius shown in Eq. 2.45 [89]. The model describes two contributions to the electronic self energy: (i) the decreased electron-electron exchange energy attributed to enhanced screening by the Fermi gas of free-carriers in the conduction band and (ii) the self-scattering of free-carriers, referred to as impurity-impurity scattering. Finally, free-carrier screening of the electron-hole Coulomb interaction in the BSE is approximated in this work as a free-electron-like response via an intraband Thomas-Fermi contribution to dielectric screening. This is described in detail in Refs. [135, 136] and in section **??**. We note that in the literature free-carrier screening also has been approximated using Debye screening for non-degenerate free-carrier concentrations [153].

All DFT and *GW* calculations are carried out using the Vienna *Ab-Initio* Simulation Package [144, 154, 155, 156] (VASP). The BSE calculations are performed using the implementation described in Refs. [157, 150]. All input and output is available in the Materials Data Facility [158].

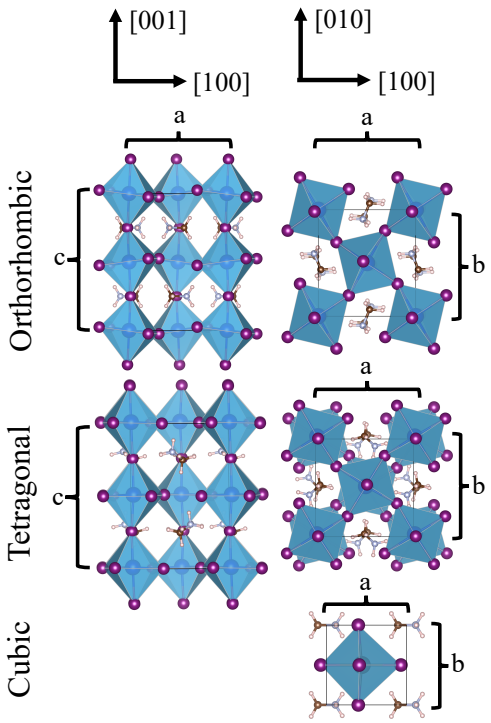

Figure 3.1: Relaxed atomic geometries of orthorhombic, tetragonal, and cubic phases of $MAPbI_3$. Ions are represented as gray (Pb), purple (I), brown (C), pink (H), and blue (N) spheres. Lattice constants a, b, and c align with the [001], [010], and [001] directions, respectively.

3.3 Results and Discussion

3.3.1 Atomic Geometries

First, we study relaxed atomic geometries of the low-temperature equilibrium phase of $MAPbI_3$, the orthorhombic (O) crystal structure with space group Pnma [161, 141]. This phase has minimum entropy by ordering CH_3NH_3 ions periodically [140] and the PbI_3 sub-lattice forms stacked octahedra that are tilted with respect to the [001] axis of the unit cell (see Fig. 3.1). Angles between lattice vectors are all 90° and the lattice parameters are non-equal, with a=8.37, b=9.07, and c=12.67 Å. The c axis agrees well with experimental values between 12.1 – 12.6 Å and the relaxed $a : b$ aspect ratio in this work of 0.921 only slightly underestimates that seen in experiments, 0.97 – 0.98 [160, 141].

Experiment also shows that above T=162 K, $MAPbI_3$ undergoes a phase transformation to a tetragonal (T) phase with space group I4/mcm (see Fig. 3.1) [161, 141]. This first-order phase transition is marked by three phenomena: First, we compute a change in lattice parameters from $a \neq b \neq c$ in the O to a=8.70, b=8.72, and c=12.83 Å in the T phase. The relaxed structure results in good agreement between a and b with a difference of only $\approx$ 0.02 Å. Second, there is disordering of CH_3NH_3 ions in the T phase, that leads to

a disordered cation sub-lattice. To approximate this effect in our unit cell, we disorder the organic cations, based on the structures of Brivio *et al.* [140] This disorder is stabilized by *c*-axis tilting in the T phase. Finally, alternating tilts of the octahedrons in the [001] direction appear, which in turn stabilizes the a=b condition [161, 141].

At even higher temperatures above T=327 K, T $MAPbI_3$ undergoes another transition to a cubic (C) phase with space group $Pm\bar{3}m$ (see Fig. 3.1) [161]. This C phase is stabilized through total disordering of the MA cation sublattice. Since thermal rotation of MA cations is not accounted for in the geometry relaxation [141], we follow the common approach of modelling this phase as a pseudo-cubic distortion of the $Pm\bar{3}m$ cubic perovskite structure with ordered MA cations [161, 141]. This lattice geometry is slightly triclinic; in experiment, it is also pseudo-cubic due to rotations of the MA cations [141]. Relaxed atomic geometries result in slightly tilted axes compared to the experimental $Pm\bar{3}m$ phase, which agrees with earlier computational reports: Ong *et al.* showed that in DFT calculations the distorted C phase (space group $P4mm$) is more stable compared to a constrained $Pm\bar{3}m$ phase [161]. The average of the pseudo-cubic lattice constants $(a + b + c)/3$=6.31 Å agrees well with measurements [141]. Overall, our results for relaxed atomic geometries are in excellent agreement with values from experiment and previous calculations. A more detailed comparison to other work can be found in Table 3.1.

3.3.2 Electronic Structure

Using the GW_0+SOC approach, we compute band gaps of 1.42, 1.39, and 1.38 eV, for the O, T, and C phase, respectively (see Table 3.2). Figure 3.2 shows direct band gaps for each phase that are located at the Γ point of the BZ for O and T phase, and at the R point for the C phase. This change in reciprocal-space location of the direct gap is a consequence of cell symmetry [48]. Our results for $MAPbI_3$ band gaps are consistent with previous GW calculations and only slightly underestimate experimental values of $1.5-1.7$ eV (see Table 3.2). This table also shows that previous calculations produced varying results based on the specific GW approximation and description of SOC [171, 145, 172, 173]. In particular, Filip and Giustino showed that different schemes for including relativistic effects and iterating the GW method resulted in different values for the gap. Using fully relativistic pseudopotentials for Pb and I and the scissor-self consistent GW method [29] to iterate QP wave functions and eigen-energies, they predicted 1.79 eV for the orthorhombic phase [29]. Separately, Umari *et al.* reported 1.62 eV for the T phase [145].

As expected, gaps at the PBE+SOC level of theory severely underestimate experimental results by more than 1 eV for each phase. Using our GW_0+SOC data, we can correct this for the calculation of optical spectra, using a rigid scissor shift; we denote this approach by PBE+Δ_{GW_0}+SOC. Figure 5.2 compares

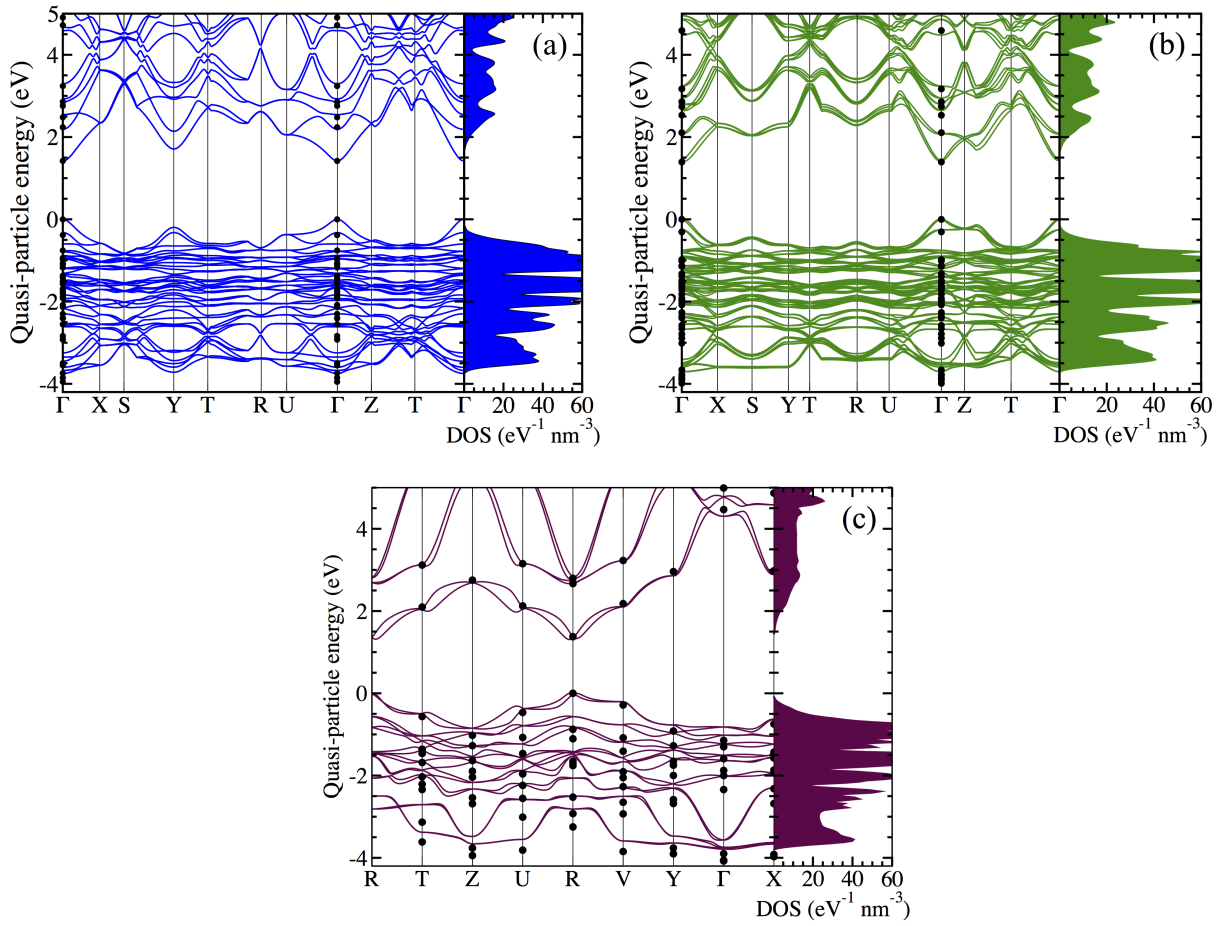

Figure 3.2: Kohn-Sham band structure and density of states from PBE+Δ_{GW_0}+SOC (solid lines) and GW_0+SOC (black circles) calculations for orthorhombic (a), tetragonal (b), and cubic (c) phases of $MAPbI_3$. All conduction states are rigidly shifted to the GW_0+SOC gap. The valence-band maximum is used as energy zero.

Table 3.2: Band gaps E_g (in eV), static (ε_0) and static electronic (ε_∞) dielectric constants, and effective electron (m_c) masses for $MAPbI_3$ from our calculations and the literature. Results from G_0W_0, GW_0 (iteration only of the Green's function), SS-GW (self-consistent scissor GW [29]), and QSGW (quasiparticle self-consistent GW) are shown for E_g. Density-functional perturbation theory (DFPT) and molecular dynamics (MD) are compared for dielectric constants.

	Orthorhombic	Tetragonal	Cubic
E_g (PBE)	1.55	1.40	1.51
E_g (PBE+SOC)	0.66	0.70	0.56
E_g (GW_0+SOC)	1.42	1.39	1.38
E_g (PBE)	1.61[162]	1.45[162], 1.68 [145]	1.44[162]
E_g (G_0W_0+SOC)	1.81 [163], 1.32[29]	1.62 [145], 1.67[163]	1.28 [163], 1.48[52]
E_g (SS-GW+SOC)	1.79[29, 164]	–	–
E_g (QSGW+SOC)	–	–	1.67[165]
E_g (Exp.)	1.65[163]	1.5 – 1.61 [163]	1.69 [163]
ε_∞ (DFPT)	6.22	6.23	6.24
ε_0 (DFPT)	23.17	22.66	22.1
ε_∞ (DFPT)	5.80 [166]	5.50 [145], 6.60[32]	6.83 [127]
ε_∞ (Exp.)	–	5.00[167]	–
ε_0 (DFPT)	25.30[166]	–	–
ε_0 (MD)	–	30.00[127]	–
ε_0 (Exp.)	–	33.50[167], 28.80[168]	–
m_c (PBE+SOC)	0.19	0.16	0.23
m_c (DFT+SOC)	0.19[169], 0.11[164]	0.15[128]	0.23 [170]
m_c (G_0W_0+SOC)	0.16[164]	0.17 [145]	–
m_c (SS-GW+SOC)	0.21[164]	–	–

band structures of O, T, and C $MAPbI_3$ at the PBE+Δ_{GW_0}+SOC and GW_0+SOC levels of theory and illustrates the density of states (PBE+Δ_{GW_0}+SOC). In Fig. 5.2(c) the perfectly direct nature of the gap is broken by Rashba-Dresselhaus spin-orbit splitting for C $MAPbI_3$. However, the effect is small and hard to discern in Fig. 5.2(c). The effect is even smaller for T $MAPbI_3$ and has been studied extensively for T and C phases [172, 174, 175].

By comparing GW_0+SOC energies at high-symmetry $\mathbf{k}$ points to the electronic structure from PBE+Δ_{GW_0}+SOC in Fig. 5.2, we illustrate for C $MAPbI_3$ that the latter is a suitable basis for optical calculations. Here we are interested in optical response in the visible spectral range, hence, we focus on electronic states within 1.6 eV of the band extrema. As can be seen in Fig. 3.2(c) the conduction band dispersions from both approaches are in excellent agreement in this energy range. The Rashba-Dresselhaus split gap appears near R, and the largest deviation for the lowest conduction band amounts to about 0.15 eV at the Γ-point. Overall, the valence bands are also in good agreement between both approaches. PBE+Δ_{GW_0}+SOC results tend to predict valence band energies only slightly higher in energy than those predicted by GW_0+SOC, for instance 0.4 eV at the Γ point [see Fig. 5.2(c)]. The overall width of the uppermost valence block is 0.35 eV larger at the GW_0+SOC level of theory. Hence, overall, our data indicates

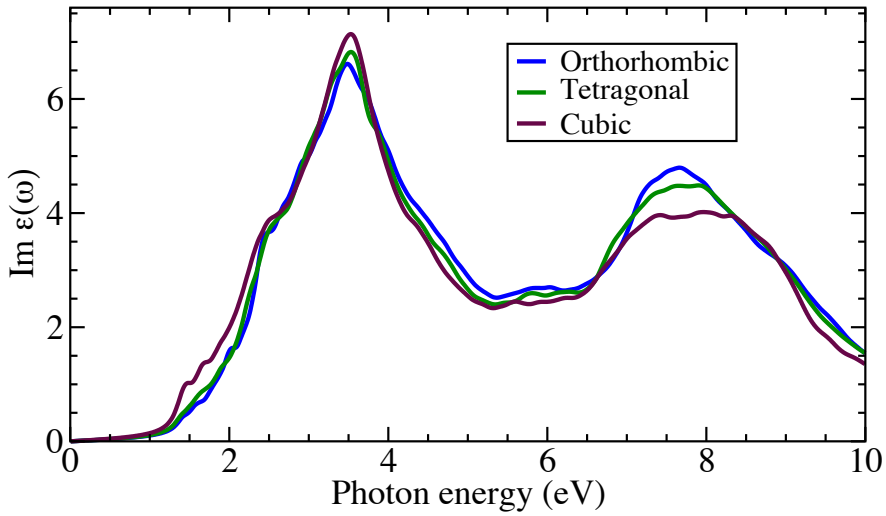

Figure 3.3: Polarization-averaged imaginary part of the frequency-dependent dielectric functions of $MAPbI_3$, calculated within independent-quasiparticle approximation using PBE+Δ_{GW_0}+SOC. Blue, green, and maroon curves correspond to orthorhombic, tetragonal, and cubic phase, respectively.

that excitation energies are underestimated by at most 0.3 – 0.4 eV when computing optical spectra starting from the PBE+Δ_{GW_0}+SOC electronic structure. Finally, effective electron masses are determined by a parabolic fit near the band edge of our PBE+Δ_{GW_0}+SOC data and also reported in Table 3.2.

3.3.3 Optical Response: Independent-Quasiparticle Approximation

The optical absorption spectra of all three $MAPbI_3$ phases share similar spectral features, as shown in Fig. 3.3. In this figure, we illustrate the polarization-averaged imaginary parts of the dielectric functions, computed using the independent-quasiparticle approximation within PBE+Δ_{GW_0}+SOC. Our results agree overall well in the visible region between 1.5 and 3 eV with the absorption coefficient calculated using fully-relativistic G_0W_0+SOC [145] for T $MAPbI_3$, as shown explicitly in Fig. A.4.

Figure 3.3 shows a smooth, gradual onset of absorption at the GW_0 band gap for all three phases. At higher energies near 2.4 eV all spectra show a shoulder feature which we attribute to optical transitions between the uppermost valence band and lowest conduction band at **k** points slightly away from the location of the band extrema (see Fig. A.3). The difference of the lowest conduction and highest valence bands shows that transitions near the Γ, Y, and U point (orthorhombic), near the Γ and S point (tetragonal), and near the T, U, and V point (cubic) dominate between 2.2 and 2.6 eV. From the shoulder, ε_2 further increases into the UV energy region and peaks at 3.48, 3.53, and 3.53 eV for O, T, and C phase, respectively. The major contributions to this peak are optical transitions between the highest valence band and lowest conduction band at **k** points far from the location of the band extrema, e.g. the Z point in C $MAPbI_3$. Fig. A.3

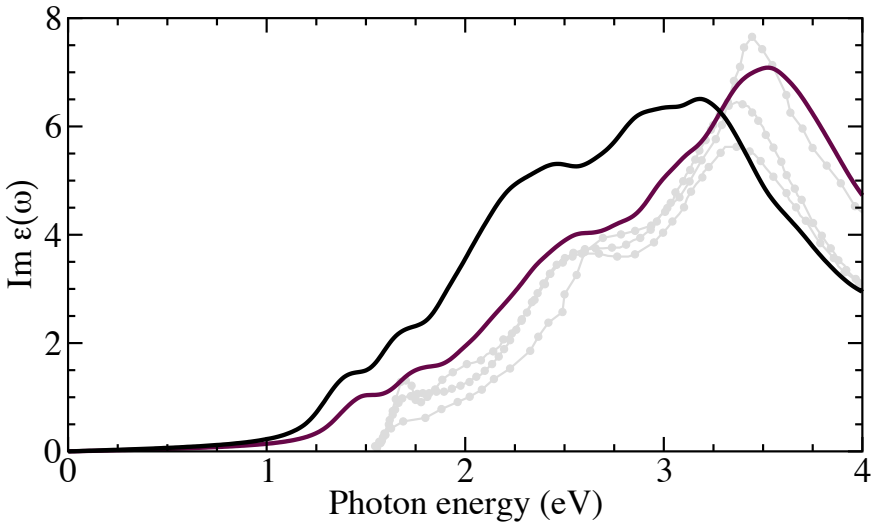

Figure 3.4: Polarization-averaged imaginary part of the frequency-dependent dielectric function of cubic $MAPbI_3$. Results from independent-quasiparticle approximation, here PBE+Δ_{GW_0}+SOC (solid maroon line, identical to that in Fig. 3.3), are compared to the BSE_{el}+Δ_{GW_0}+SOC approach (solid black line) that accounts for electron-hole interaction, and to experimental[177, 178, 179] results (gray diamonds).

also indicates that there are minor contributions from transitions from lower valence bands into the lowest conduction band. Our assignment of these spectral features agrees with that in Ref. [27]. Finally, after this peak optical response, ε_2 decreases until about 5.3 eV and then increases again gradually to a much broader peak, centered around 7.7 eV, which is far outside the visible spectrum.

We also computed the static (ε_0) and static electronic (ε_∞) dielectric constants of $MAPbI_3$ using DFPT and the PBE electronic structure. For ε_∞ we find very similar values around 6.23 for all three phases (see Table 3.2). Our results are in the midst of previously calculated and measured values ranging from 5.5 to 7.0 [166, 145, 127, 176]. We confirmed that the same magnitude but opposite sign of quasi-particle and SOC induced shifts, reported before for band gaps [145], justifies using DFPT based on the PBE electronic structure to compute dielectric constants. Due to the large lattice polarizability of $MAPbI_3$, our DFPT results for ε_0 are much larger than ε_∞, with values of $22.1-23.2$ for the three phases (see Table 3.2). These results are in good agreement with earlier data from DFPT and molecular dynamics simulations, as well as experimental measurements, in the range of $25-35$ [167, 168].

3.3.4 Optical Response: Excitonic Effects

Next, we study the influence of excitonic effects on optical absorption of $MAPbI_3$. To this end, Fig. 3.4 compares the independent-quasiparticle spectrum to the solution of the BSE, accounting for electronic

interband screening as described by a model dielectric function [148, 149] parameterized using a dielectric constant of ε_∞=6.24 (see Table 3.2). Given the similarities of the independent-quasiparticle optical spectra of the three different phases (see Fig. 3.3), we only focus on C $MAPbI_3$ in the following.

For C $MAPbI_3$, Fig. 3.4 shows that excitonic effects cause a significant red shift of the absorption onset and of higher-energy features. While the onset of the independent-quasiparticle spectrum occurs at the GW_0+SOC band gap of 1.38 eV (see Table 3.2), the lowest eigenvalue of the BSE Hamiltonian is about 64.5 meV lower in energy. Note, that this value is not a well-converged result for the exciton binding energy due to **k**-point sampling, as we discuss below [85]. Energy positions of higher-energy spectral features show larger excitonic shifts; for instance, the main peak around 3.5 eV in independent-quasiparticle approximation red-shifts by about 0.5 eV. The shift is accompanied by a redistribution of spectral weight: When including excitonic effects, features at lower energies are amplified, thus increasing the amplitude of optical absorption at lower energies.

Interestingly, in Fig. 3.4 positions of peaks and shoulders in the experimental spectrum seem to agree better with the independent-quasiparticle spectrum. However, we emphasize the notable difference of about 0.2 – 0.3 eV of the absorption onsets that is apparent in the figure and originates from the slightly smaller GW_0+SOC gap, compared to experiment. If this is corrected for, e.g. by rigidly shifting the absorption onset to the experimental value, we find excellent agreement of the BSE_{el}+Δ_{GW_0}+SOC result with experiment across the entire energy range, while the independent-particle spectrum then overestimates the position of the main peak around 3.5 eV by about 0.2 – 0.3 eV. In the following, we analyze how the description of the optical response changes in the presence of free electrons.

3.3.5 Optical Response: Free Electrons

We first study how Burstein-Moss shift (BMS) and band-gap renormalization (BGR), i.e. two effects attributed to free electrons in the conduction band of C $MAPbI_3$, affect the independent-quasiparticle optical spectrum (see top panel of Fig. 3.5). The predicted BMS due to Pauli blocking of optical transitions for a free-electron density of 10^{17} cm^{-3} is less than 2 meV and only reaches a value of about 10 meV for 10^{18} cm^{-3} (see Fig. 3.6). Realistic intrinsic n or p type shallow defect concentrations or free-electron-hole densities under illumination [176] fall within the range of 10^{15} cm^{-3} to 10^{17} cm^{-3} and we conclude that for these BMS is only a minor factor. However, we note that high-intensity illumination has produced free-carrier concentrations around 10^{19} cm^{-3} [176]. In Fig. 3.6 we show that in this regime BMS can be on the order of 0.1 eV and quickly increases thereafter, approximately following a $n_c^{3/2}$ dependence.

At the same time, Fig. 3.6 also illustrates that BGR is on the same order of BMS for C $MAPbI_3$, but

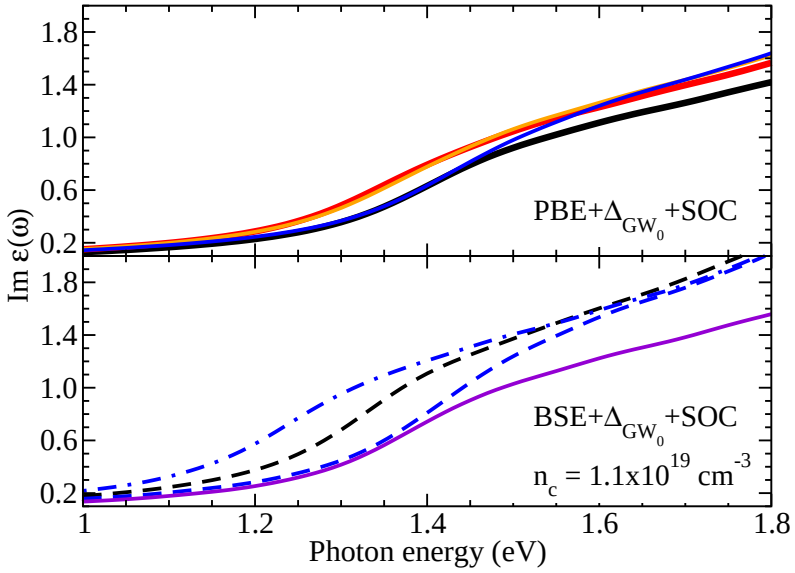

Figure 3.5: Polarization-averaged imaginary part of the frequency-dependent dielectric function of C $MAPbI_3$ without free electrons (black), and with free-electron concentrations of 2.3×10^{18} cm^{-3} (red), 5.0×10^{18} cm^{-3} (orange), and 1.1×10^{19} cm^{-3} (blue). A dense, hybrid 5:2:32.5 **k**-point grid was used. The top panel shows the influence of BMS and BGR on the independent-quasiparticle spectrum (PBE+Δ_{GW_0}+SOC). The bottom panel demonstrates the influence of free electrons, n_c=1.1×10^{19} cm^{-3}, on excitonic effects. The BSE$_{\text{el}}$+Δ_{GW_0}+SOC spectrum without free electrons (black dashed line) is compared to data that includes free-electron screening without (blue dot-dashed line) and with (blue dashed line) Pauli blocking. The violet curve approximately decribes lattice screening via the low-frequency dielectric constant ε_0=22.1 in the model dielectric function [149, 180].

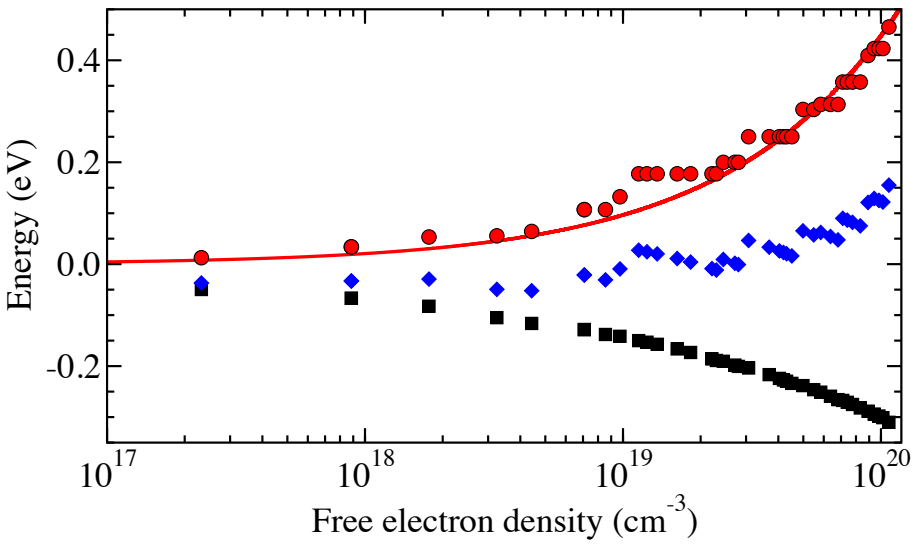

Figure 3.6: Burstein-Moss shift (red circles), band gap renormalization (black squares), and sum of both (blue diamonds) as a function of free-electron concentration in the conduction band of C $MAPbI_3$. A dense, hybrid 5:2:32.5 **k**-point grid was used. The red line is a curve fit to the BMS data of the form E_{BMS}=$An_c^{3/2}$.

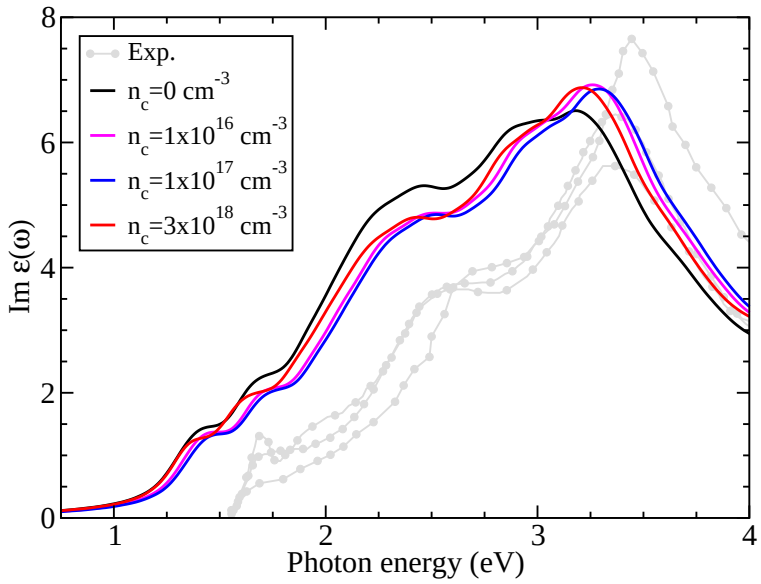

Figure 3.7: Polarization-averaged imaginary part of the frequency-dependent dielectric function, computed using the $\mathrm{BSE_{el+fc}}$+Δ_{GW_0}+SOC approach to account for excitonic effects. Results are shown for three different experimentally relevant free-electron concentrations and compared to data without free electrons and experiment [177, 178, 179]. As BMS and BGR are negligible for small values of n_c, they are only included for n_c=3×10^{18} cm^{-3}.

with an opposite sign. As a result, these two effects compensate each other to very high accuracy across an unusually large free-electron range, up to about 10^{19} cm^{-3}. This explains why experimental observation of BMS+BGR at the absorption edge [176, 181] requires very high free-carrier concentrations: Valverde *et al.* do not explicitly report [182] any effect of BMS or BGR at a free-carrier density of about 3.3×10^{17} cm^{-3}. Manser *et al.* report [176] a rise of the onset by about 0.08 eV for n_c=1.5×10^{19} cm^{-3}, which is between our result for BMS and BMS+BGR.

Next, in order to describe the influence of free electrons on the electron-hole interaction and, thus, excitonic effects, we describe electronic interband screening by a dielectric constant and include free-electron screening, as shown in Eq. 2.49, when solving the BSE. Figure 3.7 compares the resulting imaginary part of the dielectric function of C $\mathrm{MAPbI_3}$ without free electrons to results for three different free-electron concentrations. While we find a blue shift of about 0.2 eV for the main absorption peak around 3 eV, interestingly the absorption onset is almost unaffected by free electrons, both in terms of energy position and line shape. The energy position of the absorption onset barely changes since (i) BMS and BGR largely compensate each other over a large range of free-electron concentrations (see Fig. 3.6), and (ii) at the same time, the exciton binding energy is small already in the system without free-electrons. Hence, its reduction in the presence of free electrons and the formation of a Mahan exciton, does not lead to significant shifts of

the absorption edge. Below we discuss that this Mahan exciton is also the reason why the absorption line shape barely changes in the system with free electrons.

In addition, in Fig. 3.7 we compare to three experimental results [179, 178, 177]. These show good consistency for the major spectral features, i.e. the onset at 1.55 eV, the shoulder at 2.62 – 2.69 eV, and the peak at 3.35 – 3.44 eV. These peaks and shoulders are reproduced well in our simulations. The only major difference is that the computed spectra appear red shifted with respect to experiment, which above we attributed to the difference of the single-QP band gaps (see Table 3.2). The optical absorption band width, captured by the energy difference of absorption onset and main peak, is 0.15 eV larger when free electrons are present and in slightly better agreement with experiment than the spectrum without free electrons. Also, the ratio of the dielectric function at the main peak and the shoulder at about 0.5 eV lower energies of 0.53, 0.58, and 0.66 in experiment [179, 178, 177], improves from 0.82 without free electrons to about 0.7 when accounting for free electrons. Another notable feature is the narrowing of the spectral peak width when free electrons are included, improving agreement with experiment.

Finally, in the bottom panel of Fig. 3.5 we illustrate the Mahan-exciton character of the line shape of the absorption spectrum near the onset, for a high free-electron concentration of 1.1×10^{19} cm^{-3}. To this end, the blue curves show BSE results with (dashed) and without (dot-dashed) the effect of Pauli blocking; both include free-electron screening of the electron-hole interaction as well as BGR. Comparing these two curves, shows that Pauli blocking turns the concave line shape (dot-dashed) into a steeper, more convex line shape (dashed) that resembles the case without free electrons much more closely (black dashed). Hence, this enhancement of the absorption edge can be attributed to the Fermi-edge singularity that only enters when Pauli blocking is included, which is a defining characteristic of the Mahan exciton [137]. In addition, we also compare to the result that accounts for lattice screening via the dielectric constant (violet curve) and find that in this case the line shape is again more concave. Thus, Fig. 3.5 shows that Mahan excitons are the reason that the convex line shape of the case without free electrons is largely preserved up to free-electron concentrations as large as 1.1×10^{19} cm^{-3}. Results that neglect Pauli blocking or approximately capture lattice screening lead to more concave onsets.

3.3.6 Exciton Binding Energy

In order to show that the Mahan exciton indeed corresponds to a bound excitonic state that persists in the material despite the presence of free electrons, we computed converged exciton binding energies as the difference between the lowest eigenvalue of the excitonic Hamiltonian and the lowest single-QP excitation energy. It has been shown before that accurate **k**-point convergence of the lowest-exciton eigenvalue is

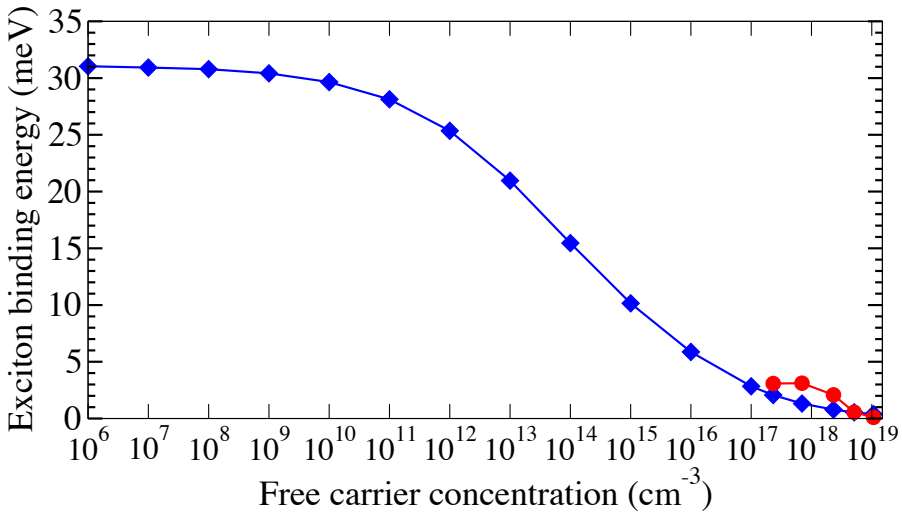

Figure 3.8: Exciton binding energy in C $MAPbI_3$ as a function of free-electron concentration, calculated using the $BSE_{el+fc}+\Delta_{GW_0}$+SOC framework. Electronic and free-electron screening of the electron-hole interaction are included. Data with (red) and without (blue) Pauli blocking is compared.

challenging and requires dense sampling of the band extrema, in particular for Wannier-Mott type excitons [150]. We use hybrid **k**-point meshes to accomplish this and systematically increase the sampling density (see Fig. A.1). The densest grid used here samples the entire Brillouin zone by $5 \times 5 \times 5$ **k** points, but the inner third is replaced by a $14 \times 14 \times 14$ **k**-point mesh. The resulting mesh is shifted to center around the direct gap at the R-point of the BZ of C $MAPbI_3$.

The resulting value for the exciton-binding energy in C $MAPbI_3$ without free-electrons is E_b=31.9 meV. This is in good agreement with the highest values measured experimentally and other first principles calculations: Umari *et al.* [32] predicted 30 meV and Bokdam *et al.* report 45 meV for the tetragonal phase [127]. The degree of Rashba-Dresselhaus shift is also higher in our work due to a large inversion asymmetry of the relaxed pseudo-cubic phase, leaving fewer states closer to the band-edge.

Next, we compute the change of the exciton binding energy of C $MAPbI_3$ for finite free-electron concentrations in the conduction band, using BSE calculations that account for additional free-electron screening via Eq. 2.49. Figure 3.8 shows the resulting decrease of the exciton-binding energy. For free-electron concentrations around 10^{11} cm^{-3}, which is comparable to concentrations of charged and shallow defects in highly pure, single-crystalline samples [183], our results show that the exciton binding energy decreased from 31.9 meV to 28.13 meV. This is still above the thermal dissociation energy at room temperature and, thus, free-electron screening is not a critical factor. The data in Fig. 3.8 also shows a significant drop of the binding energy from 25.35 meV to 10.15 meV for free-electron concentrations of $10^{12} - 10^{15}$ cm^{-3}. We note that this is the range where the q_{TF}^2/q^2 term in Eq. 2.49 becomes significant and, thus, free-electron

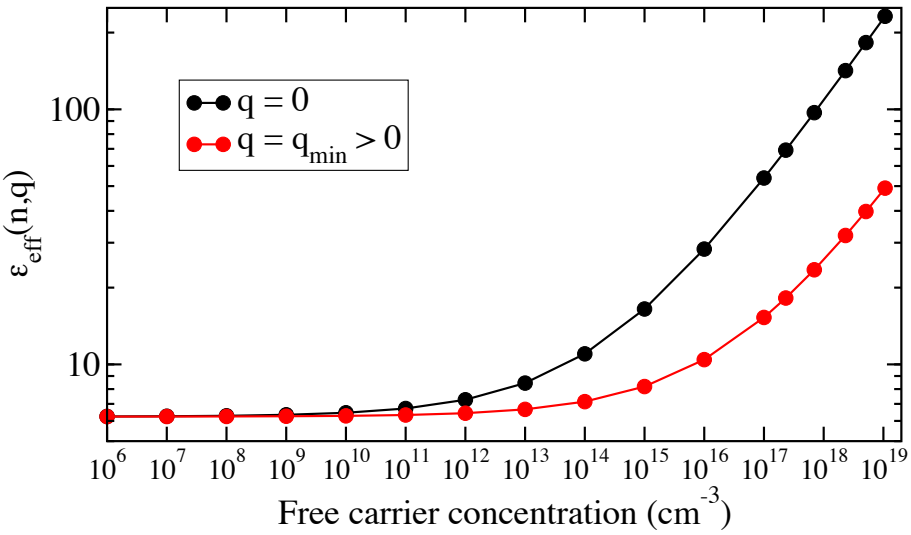

Figure 3.9: The effective dielectric constant as a function of free-electron concentration and for two wave vectors q, resulting from Eqs. (2) and (3) in the main text. This figure demonstrates how the screening strength by free electrons increases as the number of free electrons increases past even a modest density of $n = 1 \times 10^{12}$ cm^{-3}.

screening becomes the dominant mechanism over electronic interband screening. We illustrate this explicitly in Fig. 3.9. This results in the overall decline of the exciton binding energy with increasing free-electron concentration.

At even higher free-electron concentrations between 10^{16} and 10^{17} cm^{-3}, corresponding to those observed in precursor mismatched samples [33], the exciton-binding energy is very small, between 5.87 and 2.84 meV (see Fig. 3.8). Up to free-electron concentrations of $n_c \approx 2.3 \times 10^{17}$ cm^{-3}, finite **k**-point sampling prevents us from explicitly including Pauli blocking in the BSE calculations even for the most dense **k**-point grid. Hence, we explore the effect of Pauli blocking due to filling of the conduction band only for higher free-electron concentrations. For these, Fig. 3.8 shows an increase of the binding-energy by up to 2 meV between n=2.3 $\times$ 10^{17} and 2.3$\times$$10^{18}$ cm^{-3}, compared to calculations that neglect Pauli blocking. This increase has been attributed to the Fermi-edge singularity that arises when Pauli blocking is taken into account and is a characteristic feature of Mahan excitons [137]. While the small increase of the exciton-binding energy itself is not significant enough to recover a bound exciton at room temperature in samples with a large concentration of free electrons, the Mahan exciton still dominates the line shape of the absorption edge in C $MAPbI_3$, as we discussed above for Fig. 3.5.

3.4 Conclusions

In this work we provide a thorough understanding of the absorption line shape and lowest exciton binding energy of $MAPbI_3$. Using cutting-edge first principles theoretical spectroscopy, based on density-functional and many-body perturbation theory, we obtain accurate results for atomic geometries, single-particle electronic structure, and two-particle optical absorption spectra. These results are a solid foundation for our analysis of free-electron induced effects. We show that Burstein-Moss shift and band-gap renormalization cancel each other across a large range of free-electron concentrations. By including these effects as well as free-electron induced dielectric screening when solving the Bethe-Salpeter equation, we explain strongly reduced exciton binding energies, compared to the material without the presence of free electrons. This elucidates how a wide range of intrinsic free-electron concentrations in $MAPbI_3$ results in a range of exciton binding energies between $2-30$ meV, granting insight into a potential source of variance in experimentally measured exciton binding energies.

Furthermore, we show that the excitons in the presence of free electrons arise from the Fermi edge singularity, proving their Mahan-exciton character. They determine the line shape of the absorption onset and as a result, the onset still resembles that of the system without free electrons up to very high free-electron concentrations. Hence, $MAPbI_3$ largely maintains its excellent absorption properties in terms of energy position and line shape. This can explain why the material remains an excellent photovoltaic absorber even though in real samples free electrons will inevitably be present. More generally, our results make clear that additional screening of the electron-hole Coulomb interaction by free-electron effects is important in predicting accurate exciton binding energies in $MAPbI_3$, illustrating that a deeper knowledge of electron-hole Coulomb interaction, beyond electronic interband screening, is required.

CHAPTER 4

POLAR LATTICE SCREENING IN IONIC COMPOUNDS AND $MAPbI_3$

4.1 Introduction

The application of the Bethe-Salpeter equation to determining electron-hole excitation spectra and optical response has seen great success in the past two decades [81, 41]. A major shortcoming of the technique has been the inability to predict reliable exciton binding energies and absorption spectra for materials with differing high-frequency electronic and low-frequency electronic plus lattice dielectric constants (ε_∞ and ε_0, respectively). These materials, denoted polar solids, are typically those where ions have a non-zero Born effective charge. Separation of such ions by lattice vibrations induces macroscopic electric fields that screen the Coulomb interaction. Many popular engineering materials for opto-electronic applications, including MgO, GaN, AlN, and even hybrid perovskite $MAPbI_3$, fall into this category. These discrepancies were discussed by discussed in the context of lattice screening by Bechstedt *et al.* for materials NaCl and AlN [180]. Fuchs *et al.* performed a detailed calculation of the exciton binding energy of MgO with the Bethe-Salpeter equation to find a much higher estimate of the binding energy (400 meV) compared to experiments (145 meV) [86]. Both Bechstedt *et al.* and Fuch *et al.* propose using a dielectric screening constant that is higher than the high-frequency dielectric constant ε_∞ but lower than the low-frequency dielectric constant of ε_0, however a precise theoretical value of the correct constant is not proposed. Finally, Schleife *et al.* make a call for the inclusion of lattice screening for accurate predictions of the optical properties of In_2O_3 [184]. The exclusion of lattice contributions to the screening is purely algorithmic in that only the static electronic screening is accounted for by model functions in the RPA [87]. A theoretically founded and accurate treatment of both electronic and lattice dielectric screening of the electron-hole Coulomb interaction is needed to more fully understand optical response in polar solids.

The screened Coulomb interaction W between electrons and holes is given by a sum of the electronically screened Coulomb interaction W_{el} and the polar lattice (phonon) screened Coulomb interaction W_{ph}. Traditionally, only the electronically screened Coulomb interaction is included in the static approximation for the high-frequency electronic dielectric screening [82]. In polar solids, the lattice contribution to the screened

Coulomb interaction becomes relevant. Polar phonons induce a dielectric response at low frequencies on the order of meV. This polarization is typically induced by the long wavelength longitudinal optical phonon mode. The inclusions of electronic and lattice screening in W has been extensively explored by including the Fan-Migdal self energy (see Equation 2.64) in GW approximation calculations [101, 93, 185]. This has been generally ignored in the screened Coulomb interaction between electrons and holes.

Till now, most attempts at including lattice screening in the electron-hole Coulomb interactions have been made by static models. An early model to treat lattice screening was formulated by Haken [106]. The Haken model treats the electron-hole Coulomb interaction by including lattice and electronic screening when the electron-hole separation is larger than the polaron length and only electronic screening when the separation is smaller than the large polaron length. The Haken model is only valid in the limit that the exciton binding energy, E_{xb}, is much smaller than the LO phonon frequency ω_{LO}, rendering a static screening model. A modified version of the Haken model was proposed by Pollmann and Büttner [186] to account for different electron and hole masses. Yet, the Pollmann-Büttner model is still only formulated in the limit of small exciton binding energy. The exciton binding energy in many polar solids, such as MgO, AlN, and GaN, are about equal to or larger than the LO phonon energy, and thus the application of the Haken model or the Pollmann-Büttner model is not well justified. Nonetheless, researchers have applied these static lattice screening models to predict the excitonic properties and optical spectra of solids, including $MAPbI_3$ [129]. Dynamical effects must be included for a true treatment of the lattice screened electron-hole Coulomb interaction.

A major challenge in treating the combined electronic and lattice screened Coulomb interaction between electrons and holes is treating the dynamical contribution from the lattice screening. In the formalism of the two-particle correlation function, prior to a static screening approximation, the screened Coulomb interaction is a function of two propagation frequencies - one for the electron and one for the hole - and one excitation frequency. This renders the optical polarization function only solvable by a complex coupled integral equation that is not straightforwardly written as an excitonic eigenvalue problem [82]. An approximate solution to this problem was posed by Shindo in 1970 [103] where the dynamically screened Coulomb interaction as a function of two fermion frequencies and an excitation frequency is re-written as a function of a single excitation excitation frequency. In this form, an implicit excitonic Hamiltonian can be written where the screened Coulomb interaction, and thus the matrix itself, is a function of the optical excitation energy eigenvalues. Details of the theory can be found in chapter 2. In the limit of low exciton binding energy relative to the LO-phonon frequency, the screened Coulomb interaction in the Shindo and simple Fr ohlich approximations reduces to the Haken model of electron-hole screening by lattice distortion [106, 103].

In this chapter, we apply dynamical polar lattice screening of the electron-hole Coulomb interaction by Shindo's approximation to predict the exciton binding energies and use an effective dynamical lattice screening constant to predict the optical absorption spectra of four polar compounds: NaCl, MgO, AlN, and GaN. For each system we calculate the ground state atomic structure, phonon frequencies by DFPT, and electronic band structure by the GW_0 method. Additionally, we demonstrate how polar lattice screening strongly influences the exciton binding energy in $MAPbI_3$.

4.2 Computational Methods

Density functional theory calculations of ground state atomic structure and GW_0 calculations of electronic band gaps are performed in the VASP code [187, 155, 188, 154]. Five iterations of the Green's function by the GW_0 method were found to converge the band gaps to under 0.05 eV iteration of the single-particle Green's functions. Calculations of the LO phonon frequencies are determined by the PHonon package of Quantum Espresso [189]. All DFT calculations utilize the projector augmented wave basis and the PBE exchange-correlation energy functional. The BSE calculations are performed using the implementation described in Refs. [157, 150] plus the implementation of the screened Coulomb interaction as defined in Eq. 2.75. Dense hybrid **k**-point grids are used to closely sample the Brillouin zone center for the calculation of exciton binding energies. For NaCl, MgO, AlN, and GaN, the inner half of the BZ is sampled with 33×33×33, 29×29×29, 27×27×15, and 33×33×17 **k**-point grids, respectively for the computation of exciton binding energies. Convergence of these binding energies and the extrapolation of the binding energy to the high **k**-point density limit, as performed in Ref. [86], and are shown in Fig. B.1. Dense, evenly spaced **k**-point grids are used to calculate optical spectra. For $MAPbI_3$ literature values are used for LO phonon frequency, ranging from 14 to 17 meV, and low-frequency dielectric constants, ranging from 22-30 [30, 129]. The same hybrid grids from the prior study are used to calculate exciton binding energies with dynamical lattice screening contributions [138]. Three levels of screening are compared in calculations of exciton binding energy and optical absorption spectra. First, we simply including only the static high-frequency electronic dielectric response as has been done by modern DFT+GW+BSE methodologies. Second, we substitute the high-frequency dielectric constant in the previous method with the low-frequency dielectric constant in an approach we call static lattice screening, as it assumes the lattice statically screens the electron-hole Coulomb interaction. Finally, we include polar lattice screening dynamically by Shindo's approximation and approximate the electron-phonon vertex by the simple Fröhlich model as seen in Eq. 2.75. The high-frequency dielectric constant ε_∞ is determined as the value of the real dielectric function at $\omega = 0$, which is

Table 4.1: Calculated band gaps, dielectric constants, and LO phonon frequencies along with experimental comparisons.

	MgO	GaN	AlN	NaCl
E_g DFT (eV)	4.43	1.71	4.05	5.00
E_g GW_0 (eV)	7.30	3.25	6.20	8.45
E_g Exp. (eV)	7.80[190]	3.28-3.40[191]	6.03-6.28[192, 193]	8.50-8.90[194, 195]
$\varepsilon_\infty^{\mathrm{DFT}}$	3.28	6.08	4.67	2.72
$\varepsilon_\infty^{GW_0}$	2.81	5.11	3.96	2.29
ε_∞ Exp.	2.94-3.18[196]	5.35[191]	4.60-4.84[197, 191]	2.34[198]
$\varepsilon_0^{\mathrm{DFT}}$	10.81	10.97	8.88	6.85
$\varepsilon_0^{GW_0}$	10.34	10.00	8.17	6.42
ε_0 Exp.	9.64 - 10.1[196]	8.9-10.4[199, 191]	8.5-9.14[197, 191]	5.62-5.9[198]
ω_{LO} (meV)	86.72	91.0	88.7	30.27
ω_{LO} Exp. (meV)	82.7-91.0[200]	92.2-92.5[199]	91.4[197]	32.7[201]

in turn calculated by the Kramers-Kronig transformation of the imaginary dielectric functional calculated the the Ehrenreich-Cohen equation [60]. The screening constant $\varepsilon_\infty^{\mathrm{DFT}}$ indicates that ε_∞ is calculated at the DFT level with no band gap modification. $\varepsilon_\infty^{GW_0}$ indicates that ε_∞ is calculated with the minimum energy transition shifted to the GW_0 band gap. The ionic contribution to the dielectric constant was calculated in VASP by DFPT, and $\varepsilon_0^{\mathrm{DFT}/GW_0}$ is simply the addition of $\varepsilon_\infty^{\mathrm{DFT}/GW_0} + \varepsilon_{ion}$.

4.3 Results and Discussion

4.3.1 Phonon Frequencies and Electronic Structure

Calculated LO phonon frequencies and low and high-frequency dielectric constants are in excellent agreement with experimentally determined values. Relevant numbers for this section can be found in Table 4.3.1. NaCl is found to have both the lowest LO phonon frequency (30.3 meV) and the lowest dielectric constants. These results suggest relatively weak and slow lattice polarization response in NaCl. In MgO, the LO phonon frequency is much higher at a value of 86.8 meV. The predicted high-frequency electronic dielectric constant is low at a value of 2.81, compared to a high low-frequency dielectric constant of 10.34. GaN and AlN host high energy LO phonon modes, at 88.7 and 91.0 meV respectively. They each also have relatively high high-frequency electronic dielectric constants.

The GW_0 quasi-particle band energies are well predicted by a rigid shift of the DFT conduction band energies to the GW_0 band gap, in turn generating a reliable electronic structure basis for optical response calculations. In particular, as shown in Fig 4.1, the band edge at the GW_0 level of theory are well predicted at the DFT level of theory. For all four materials, conduction band energies agree excellently within 5 eV of the conduction band minimum. The rigidly shifted DFT conduction bands begin to underestimate the

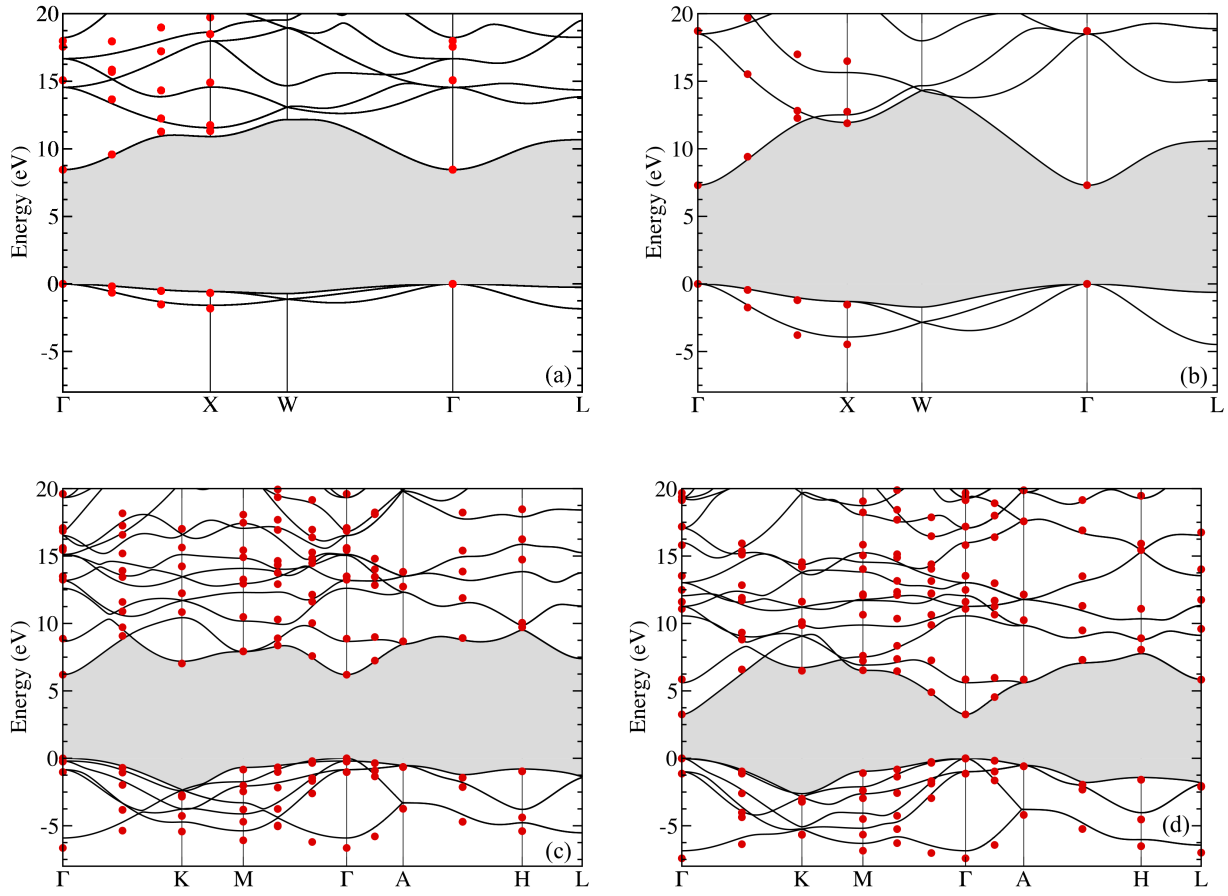

Figure 4.1: Band structures of (a) NaCl, (b) MgO, (c) AlN, and (d) GaN. DFT band structures with the conduction bands rigidly shifted to the GW_0 gap are given by solid black lines, and band energies calculated by GW_0 on a coarse grid are represented by red circles.

Table 4.2: Exciton binding energies (in meV), calculated with static electronic and lattice screening and dynamical lattice screening, and effective screening constants of considered polar compounds.

	MgO	GaN	AlN	NaCl
$E_{xb,\text{ el. stat.}}$	484.4	51.9	198.7, 144.15*	852.3
$E_{xb,\text{ lat. stat.}}$	57.5	18.8	56.4, 51.2*	129.7
$E_{xb,\text{ lat. dyn.}}$	424.7	29.5	159.9, 111.1*	832.4
$E_{xb,exp}$	145[202]	21.0-23.0[203]	55.0[204]	1100[195]
ε_{eff}	3.21	8.10	4.85, 5.91*	2.34
ε_{∞}	2.81	5.11	3.96, 4.67*	2.29

predicted GW_0 conduction band energies at higher energy in NaCl and MgO, but with maximum error of less than 1 eV. In AlN and GaN, rigidly shifted DFT conduction band energies agree well with GW_0 band energies up to high energy in excess of 20 eV above the valence band maximum, with a maximum error of less than 0.5 eV. The DFT valence band widths in NaCl and MgO agree well with the GW_0 band widths with maximum error less than 0.2 eV. For AlN and GaN, DFT underestimates the valence band width by about 0.3 eV. Finally, the GW_0 band gap predictions are all in good agreement with, and in general are slight underestimates of, experimentally determined values.

4.3.2 Optical Response in Test Systems

The results for exciton binding energies and optical absorption spectra for the four test systems are presented here. A summary of numerical results can be found in Table 4.3.2. The electronic structure basis that we solve the BSE upon are the PBE band structure shifted to the GW_0 band gap, a shift indicated by Δ_{GW_0}. Spectra without electron-hole interaction will be by Δ_{GW_0}, and the ones with the electron-hole interaction are denoted BSE+Δ_{GW_0}.

NaCl

We find that polar lattice screening has nearly no influence over the exciton binding energy of NaCl. In calculating the exciton binding energy with only static electronic screening we find E_{xb} to be 852.3 meV. With static lattice screening, the binding energy drastically reduces to 129.7 meV. The exciton binding energy predicted with dynamical lattice screening is 832.4 meV, only a 2.3% reduction compared to the static electronically screened binding energy. This result is generally expected, as the LO phonon frequency is much smaller than both the literature value [195] and the static electronically screened exciton binding energy.

Experimentally, it is difficult to define the exciton binding energy in NaCl due to the extreme isolation of the exciton peaks from the continuum absorption spectrum. Roessler *et al.* suggest a binding energy

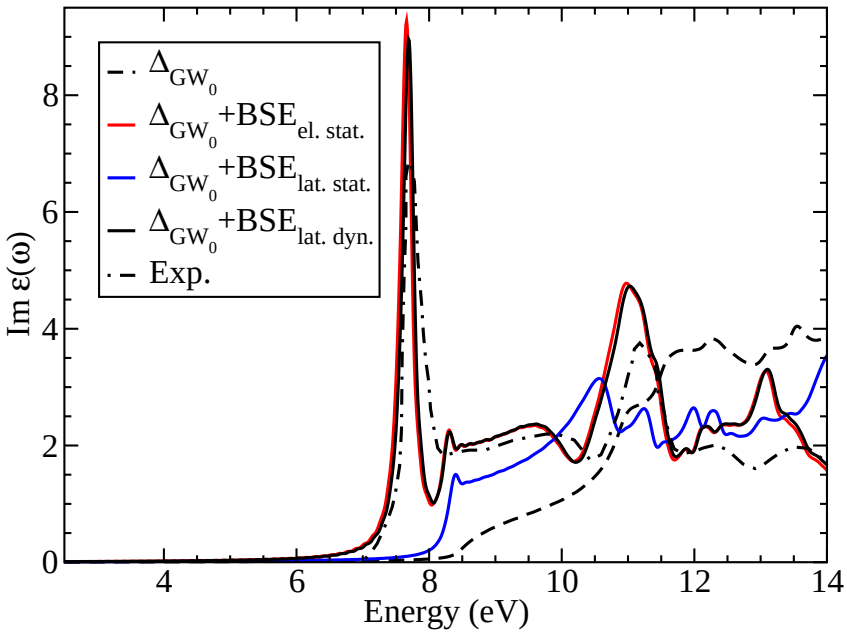

Figure 4.2: Calculated imaginary dielectric function of NaCl at various levels of theory: PBE scissor shifted to the GW_0 gap, denoted Δ_{GW_0} (black dashed line), BSE with static electronic screening (red solid line), BSE with static lattice screening (blue solid line), and BSE with dynamical lattice screening (black solid line). Experimental data is shown as a dot-dashed line[195].

of 1.1 eV, but this interpretation of the spectrum is challenged by Bechstedt *et al.* [180]. Few studies exist that probe the excitonic properties of NaCl. Nonetheless, it is clear that, if a precise exciton binding energy can be pin-pointed, that it is on the order of 1 eV. Our statically screened and dynamically lattice screened predictions of exciton binding energy are nearly equivalent on the order of 1 eV, suggesting good agreement with available experimental data. The exciton binding energy of 129.7 meV by applying static lattice screening far underestimates the experimentally determined value. Coupled with our knowledge that the LO phonon frequency is much smaller than the exciton binding energy, it becomes clear the dynamic lattice screening has little influence on the electron-hole Coulomb interaction.

Optical spectra predicted with both static electronic screening and lattice screening by the effective dynamical dielectric constant of the electron-hole Coulomb interaction are in agreement and in excellent agreement with experimental results [195]. Fig. 4.2 shows the imaginary dielectric function of NaCl computed at different levels of theory along with experimental data from Roessler *et al.*. The most striking feature of the calculations with both static electronic and dynamical lattice screening is the prominent excitonic peak centered around 7.7 eV. There is an additional excitonic peak centered around 8.3 eV, below the single-particle optical spectrum onset (calculated at the GW_0 level of theory) of 8.45 eV, attributed to the

$n = 2$ Wannier-Mott exciton level. The experimental spectrum also exhibits a first exciton peak of high amplitude centered at 7.7 eV. Both the optical spectra predicted with both static electronic screening and dynamical lattice screening exhibit a higher energy peak in the imaginary dielectric function at 11 eV, in good agreement with the experimental peak around 11.2 eV. The optical spectrum predicted with static lattice screening predicts a prominent but much smaller excitonic red shift in the optical spectrum compared the PBE+Δ_{GW_0} spectrum. It does not predict the presence of the large exciton peak that is captured with the two other levels of BSE theory. Given the poor agreement of the static lattice screened calculated spectrum with experiment, it can be stated that static lattice screening is a poor approximation to treat the electron-hole Coulomb interaction in NaCl.

MgO

Dynamical lattice screening has only a small influence over exciton binding energy in MgO by reducing it 12.3% compared to including only static electronic screening. Under the inclusion of electronic static screening, the exciton binding energy in MgO is predicted at 484.4 meV, in good agreement with previous theoretical studies [85]. After dynamical lattice screening is included, the exciton binding energy drops to 424.7 meV, a 12.3% drop. This result is still in poor agreement with the few available experimental studies that measure the exciton binding energy in MgO around 145 meV [202]. In the experimental work itself, the authors assume a screening dielectric constant in the range of 5-10, much lower than the effective dynamical screening constant determined in this work of 3.21, making the comparison more difficult. Due to the lack of more extensive experimental studies on the precise binding energy in MgO, it is hard to determine a quality comparison. The exciton binding energy predicted under static lattice screening is 57.5 meV, much lower than the experimental value.

Despite the overestimate of the binding energy in reference to experiments, the optical spectra determined with dynamical lattice screening is in excellent agreement with experimentally measured spectra. The theoretical curves are shifted up in energy by 0.5 eV to adjust for the disagreement between GW_0 gap and the experimental gap. Fig. 4.3 shows the imaginary dielectric functions of MgO calculated at different levels of theory and an experimental result [205]. To quantify how well our calculations predict experimentally measured spectra, we compare amplitudes and energies of peaks in the imaginary dielectric functions. The optical spectrum calculated with static electronic screening shows a strong excitonic onset centered at 7.4 eV with a value of $\varepsilon_2 = 7.9$. Two higher energy peaks appear centered at 10.4 eV, with $\varepsilon_2 = 3.3$, and 13.0 eV, with $\varepsilon_2 = 5.2$. Under effective dynamical lattice screening the amplitude of the excitonic onset reduces from $\varepsilon_2 = 7.9$ to $\varepsilon_2 = 5.9$ and moves upward in energy to 7.5 eV. At the same time, the second

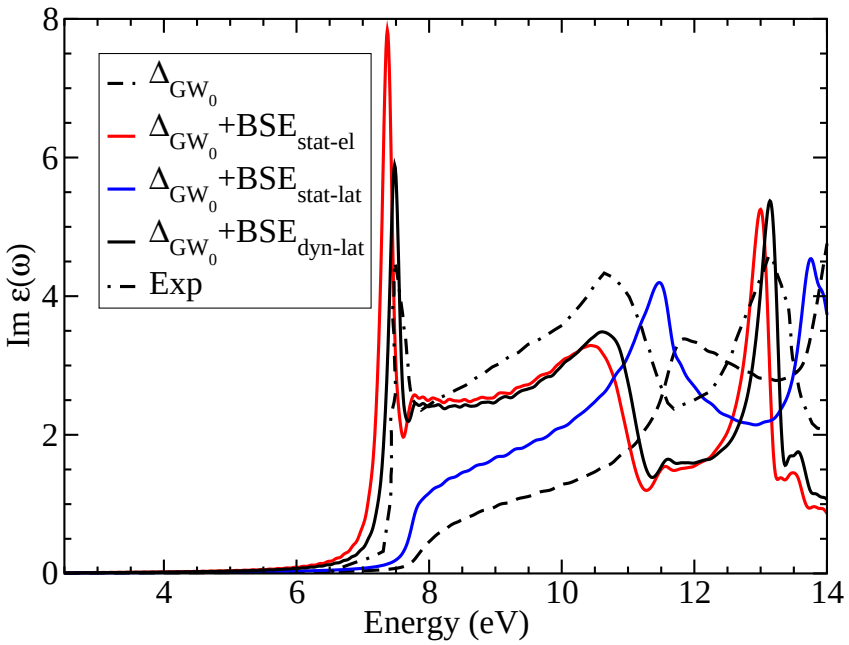

Figure 4.3: Calculated imaginary dielectric function of MgO by: PBE scissor shifted to the GW_0 gap, denoted Δ_{GW_0} (black dashed line), BSE with static electronic screening (red solid line), BSE with static lattice screening (blue solid line), and BSE with dynamical lattice screening (black solid line) compared to experimental data (black dot-dashed line) [205] A constant shift of 0.5 eV has been applied to the theory-predicted curves to match the exciton peak energy of the experimental result.

peak moves up in energy to 10.6 eV and up in amplitude to $\varepsilon_2 = 3.5$. The spectrum calculated under static lattice screening does not exhibit an excitonic onset peak at all. It is important to dwell for a moment on the fact that effective dynamical lattice screening predicts a lowering of the first exciton peak and raising of the 10 eV peak compared to the static electronic screening case. By maintaining the first exciton peak and bring the amplitude of first and second peak closer together, a better agreement with experimental results is achieved. In the experimental spectrum, the first and second peak are about equal amplitude. The spectrum predicted by static lattice screening is in very poor agreement with experiments, and is therefore an inappropriate physical model for predicting optical response in MgO. Overall, it is important to note that while dynamic lattice screening is a rather small effect on exciton binding energy, the influence on the optical spectrum is significant and produces an improved prediction of experimental results.

AlN

Prior to discussing exciton binding energy results in AlN, it is worth discussing the predictions of the dielectric constants at the DFT and GW_0 level. As seen in Table 4.3.1, the dielectric constants predicted at the DFT gap are in far better agreement with experiment compared to those calculated at the GW_0 gap. Therefore, we will calculate exciton binding energies with both sets of dielectric constants and compare the results. The optical spectra will be calculated with the dielectric constants calculated at the DFT gap due to better agreement in both the constants themselves and exciton binding energies with experimental data.

The exciton binding energies are significantly influenced and reduced by the inclusion of dynamical lattice screening. The binding energy is evaluated to be 144.2 meV under static electronic screening by using the DFT dielectric constants (198.7 meV for GW_0 constants), which is significantly higher compared to the the experimentally determined binding energy of about 55 meV [204]. By including dynamical lattice screening, the predictions of exciton binding energies reduce to 111.1 meV by using the DFT dielectric constants (159.9 meV for GW_0 constants), a 22.4% (19.5%) reduction from the static electronic screening results. These still overestimate the exciton binding energies determined by experiment. Similar to the experimental results for MgO, Feneberg *et al.* use an effective dielectric constant of 7.9 in fitting model to their data for AlN. Thus, we expect them to find lower binding energies compared to our effective dynamically lattice screened dielectric constant of 5.91. By applying static lattice screening, a binding energy of 51.2 meV by using the DFT dielectric constants (56.4 meV for GW_0 constants) is found and is in excellent agreement with the experimental value. Though dynamical lattice screening improves the prediction of the exciton binding energy over static lattice screening, it does not fully predict the binding energy of 55 meV.

Effective dynamical lattice screening and static lattice screening of the electron-hole Coulomb interaction

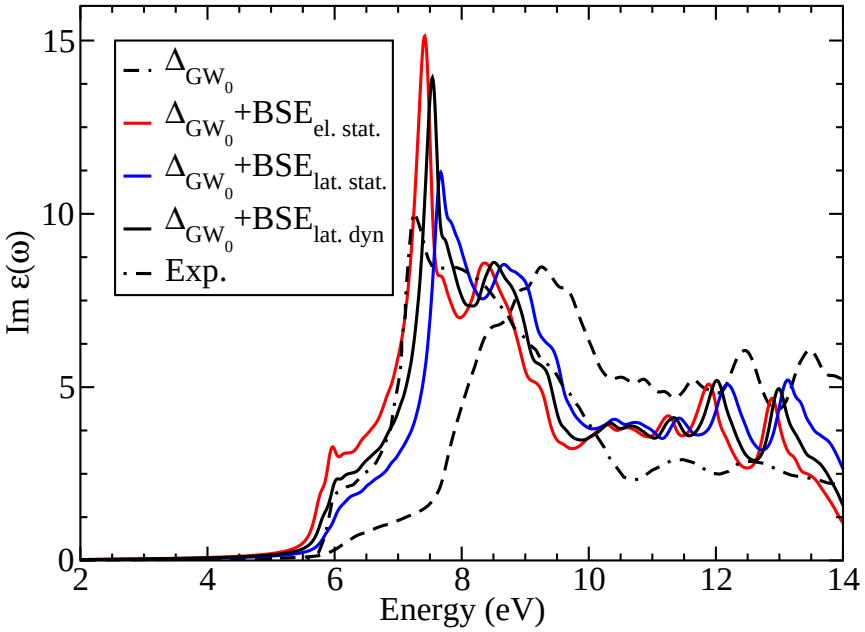

Figure 4.4: Calculated imaginary dielectric function of AlN by: PBE scissor shifted to the GW_0 gap, denoted Δ_{GW_0} (black dashed line), BSE with static electronic screening (red solid line), BSE with static lattice screening (blue solid line), and BSE with dynamical lattice screening (black solid line) compared to experimental data (black dot-dashed line) [206] A constant shift of -0.2 eV has been applied to the theory-predicted curves to match the exciton peak energy of the experimental result.

strongly influences the peak heights and positions of the optical response in AlN and brings the predicted imaginary dielectric function into close agreement with experimental results [206]. The spectrum is shown in Fig 4.4. The theoretical spectra are shifted downwards by -0.2 eV to adjust the band gap to the experimental band gap of 6.0 eV. The spectra calculated by including static electronic screening exhibits a pronounced excitonic onset as a shoulder at 5.8 eV and an excitonic peak at 5.95 eV. The highest peak in the imaginary dielectric function is centered at 7.4 eV at an amplitude of $\varepsilon_2 = 15.1$. The experimental spectrum exhibits a smooth onset without the excitonic peak feature and a maximum peak centered at 7.25 eV with an amplitude of $\varepsilon_2 = 10.0$. By including effective dynamical lattice screening, a smoothing of the onset occurs where no clear exciton peak is visible, bringing the spectrum at the onset into closer agreement with the experimental result. Compared to the static electronic screening result, the high intensity peak increases in energy to 7.54 eV and reduces in amplitude to $\varepsilon_2 = 13.9$. Finally, under static lattice screening, the onset remains smooth and the high intensity peak moves to 7.68 eV and the amplitude reduces to $\varepsilon_2 = 11.1$. Under the inclusion of each screening model, there is a second peak centered around 8.5 eV that is not seen in the experimental measurements. One reason for this is potentially the **k**-point sampling of the Brillouin zone. If this sampling is too coarse, extra peaks may appear in the spectrum calculation. AlN poses an interesting case study, as the best overall prediction seems to be made by the static lattice screening treatment. In this case, it could be that the Shindo and simple Fr ohlich approximation combined for the dynamically lattice screened Coulomb interaction do not fully account for the dynamical effect of the lattice on exciton formation. Nonetheless, dynamical lattice screening improves the prediction of the optical spectrum compared to the traditionally employed static electronic screening.

GaN

The exciton binding energy in GaN calculated with dynamical lattice screening of the electron-hole Coulomb interaction is in excellent agreement with experimentally measured binding energies. When the screening is treated in the static electronic approximation the predicted exciton binding energy is 51.9 meV, a factor of two higher compared to the experimental value of 21.0-23.0 eV [203]. In including dynamical lattice screening, the exciton binding energy drops by 43% to 29.5 meV, in very good agreement with the experimental value. It is thus confirmed that since the exciton binding energy is far lower than the LO phonon frequency the lattice screening will have a heavy influence on the exciton binding energy. The exciton binding energy predicted with static lattice screening of 18.8 meV is also in good agreement with experimental results. This agreement between dynamical lattice and static lattice screening results is in agreement with the expression for the dynamically screened Coulomb interaction approximated by the simple Fröhlich model, as the screening

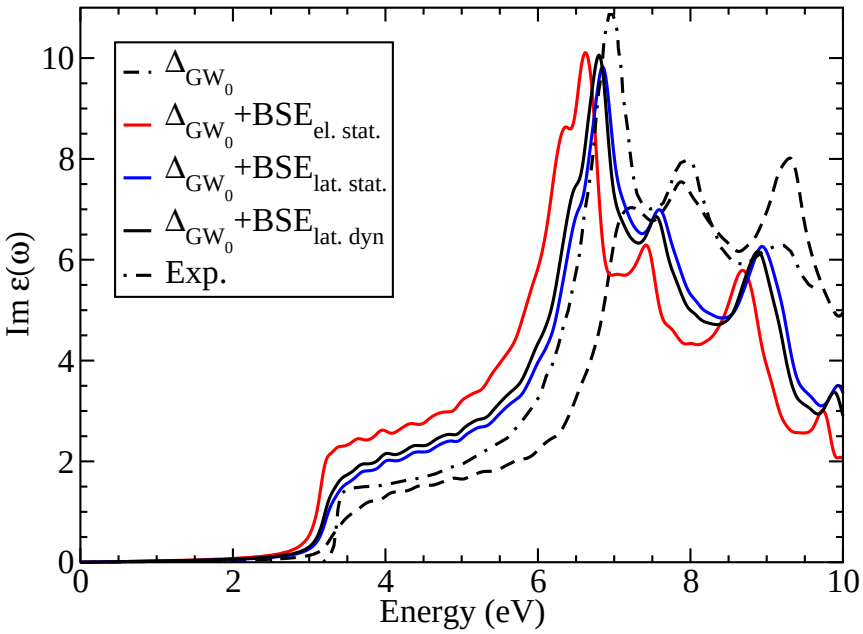

Figure 4.5: Calculated imaginary dielectric function of GaN by: PBE scissor shifted to the GW_0 gap, denoted Δ_{GW_0} (black dashed line), BSE with static electronic screening (red solid line), BSE with static lattice screening (blue solid line), and BSE with dynamical lattice screening (black solid line) compared to experimental data (black dot-dashed line)[207].

constant should reduce to $1/\varepsilon_0$ in the limit of $\omega_{LO} >> E_{xb}$.

The optical spectra of GaN calculated by dynamical and static lattice screening are in good agreement with each other and with experimental measurements. The spectrum is displayed in Fig 4.5. No shift is applied to theory-predicted curves as the band gap is in good agreement with experiments. A prominent plateau like absorption edge occurs at the optical onset when only static electronic screening is accounted for. Interestingly, this same feature is seen in the experimental spectrum but at lower amplitude. A high amplitude absorption peak is predicted around 6.6 eV, about a 0.3 eV underestimate of the experimental peak position. When effective dynamical lattice screening or static lattice screening is accounted for, the optical onset line shape reduces and the curvature of the absorption edge lowers. The amplitude at the absorption edge also falls into better agreement with experiments compared to the static electronic screening case. The high intensity peak also moves up in energy to 6.80 and 6.85 eV for effective dynamical and static lattice screening, respectively. These peak positions more closely predict the experimental measures where the peak is centered around 6.9 eV.

For MgO, AlN, and GaN, the inclusion of dynamical lattice screening in the calculation of the exciton binding energy and effective dynamical lattice screening in the calculation of the optical spectra changes

the predictions of both compared to only accounting for static electronic screening. For all three materials, accounting for only static electronic screening produces binding energies that are higher than those measured predicts higher amplitudes of the absorption onset compared to experimental measurements. Dynamical lattice screening reduce the binding in all three cases, least strongly for MgO and most strongly for GaN. This trend carefully follows the ratio of the LO phonon frequency to the exciton binding energy. When this ω_{LO}/E_{xb} ratio is small, like in MgO, the influence of dynamical screening is relatively small with only the aforementioned 12.3% reduction in binding energy. In GaN, where the ω_{LO}/E_{xb} ratio is larger than 1, the influence of dynamical lattice screening is strong. Our results are found to be consistent with he postulate of Haken and Shindo [106, 103].

4.3.3 $MAPbI_3$

The exciton binding energy in $MAPbI_3$ reduces from 31.9 meV (calculated and detailed in the previous chapter) when only accounting for static electronic screening to between 21 and 25 meV when accounting for dynamical lattice screening. The total reduction is more strongly dependent on the choice of the LO phonon frequency than the low-frequency static dielectric constant. When $\omega_{LO} = 11$ meV, the exciton binding energy reduces from 31.9 meV to 24.6 meV and 24.1 meV for $\varepsilon_0 = 25$ and 30, respectively. The result is only sensitive by half an meV to the choice of the low-frequency dielectric function. When $\omega_{LO} = 11$ is increased to 16 meV, the binding energies decrease further to 22.0 and 21.0 meV for for $\varepsilon_0 = 25$ and 30, respectively. This reduction by up to 34% is in good agreement with recent measurements of the exciton binding energy [119, 118, 116, 120, 121, 122, 123, 117, 208, 27]. Given the evidence, lattice screening clearly has a strong influence over the exciton binding energy in $MAPbI_3$, settling a previous debate in the literature over the influence of polar phonons on the optical response of $MAPbI_3$[50].

4.4 Conclusions

In this chapter, we calculate the exciton binding energies four polar compounds (NaCl, MgO, AlN, and GaN) by including dynamic lattice screening in the Shindo approximation with the screened Coulomb interaction treated by the simple Fröhlich model. Optical spectra are calculated by using an effective dynamical lattice screening dielectric constant determined in the Shindo approximation by Eq. 2.76 and used in the model dielectric function of Cappellini *et al.* [87]. While dynamic lattice screening noticeably reduces the predictions of exciton binding energy in MgO, AlN, and GaN (lattice contributions were found to be negligible in NaCl), its inclusion does not entirely correct the binding energies of MgO and AlN relative to experimental

studies. This comparison to experiments is difficult to make, as the model fitting for the data is performed by assuming dielectric constants that are higher than the effective screening constants determined in this chapter. The inclusion of dynamical lattice screening predicts the exciton binding energy of GaN to good agreement with experimental results [27]. In $MAPbI_3$, the binding energy is reduced from 31.9 meV, when calculated with static electronic screening, to between 21 and 25 meV depending on which ω_{LO} and ε_0. We conclude that dynamical lattice screening of the electron-hole Coulomb interaction is necessary to describe optical properties of polar crystals, with increased influence over the exciton binding energy as the ratio of ω_{LO}/E_{xb} becomes larger. In this limit, dynamical lattice screening captures a valuable physical interplay between the macroscopic electric fields produced by polar phonon modes and the electron-hole Coulomb interaction. Without the inclusion of dynamical lattice screening, the description of the optical excitation process in polar compounds is fundamentally incomplete.

CHAPTER 5

OPTICAL EXCITATIONS AND EXCITONS IN LAYERED HYBRID PEROVSKITES

5.1 Introduction

The previous chapters have focused on a detailed analysis of electron-hole screening and exciton binding in $MAPbI_3$. $MAPbI_3$ is just one of many HOP materials that are being explored for optoelectronic device applications. A much wider array of *layered* HOP materials (LHOPs) with fascinating optical and excitonic properties of their own are currently being explored both experimentally and theoretically. Thus, we will focus now on how we can use state-of-the-art first principles calculations to predict, disentangle, and even design the optical response in LHOP materials. We will find that, unlike in HOPs, the optical response in LHOPs demonstrates an intricate interaction between the optical excitations in the perovskite layer and the optical response within the organic spacer layer, leading to cross-layer optical excitations that could have technological implications for LHOP materials applications.

LHOPs have re-emerged as promising alternatives to their 3D counterparts for opto-electronic materials applications. They have been suggested to be used as highly efficient white LEDs [209] and tunable optical detectors [210]. In these, quantum confinement effects within perovskite layers can be engineered and tailored to specific applications [211, 48, 212, 213]. In particular, they are able to overcome chemical instability seen in 3D HOPs [214, 25, 215], by offering much improved stability and decent photo-conversion performance: Tsai *et al.* reported that non-encapsulated single crystals of n-butylammonium-methylammonium lead-iodine with n=3 and 4 layers resists moisture-driven chemical degradation. They also showed that encapsulation of the crystals resulted in no chemical degradation under highly illuminated conditions, and built solar cells with a PCE of 12.5 with n=3 and n=4 layers % [214]. The broad applications and variability of LHOPs have opened a field of research that is just beginning to produce deeply insightful and practically applicable results.

The LHOPs studied in this chapter fall into the Ruddlesden-Popper crystal class [216] and their characteristic structure consists of 2D layers of n corner-sharing metal-halide octahedra separated by, and ionically bonded to, large charged polyatomic cations (see Fig. 5.1). The inorganic perovskite layer can be tuned to a

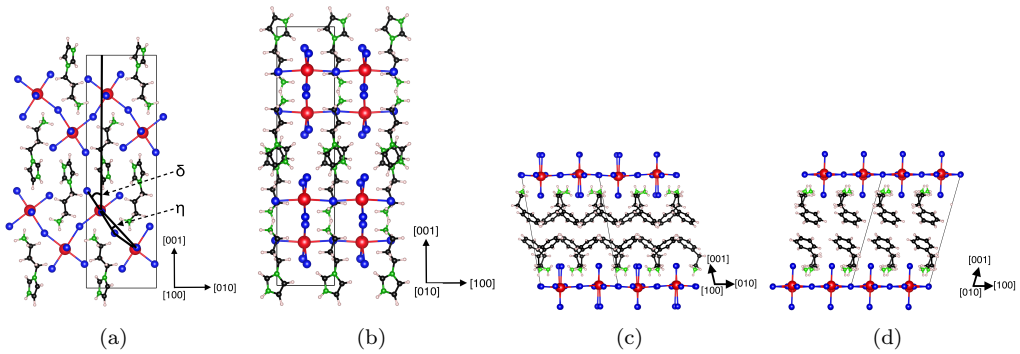

(a) (b) (c) (d)

Figure 5.1: The atomic structure of ammonium-propyl-imidizole (API)-$PbBr_4$ projected along the (a) [100] direction and (b) [010] direction and 2-phenethylammonium (PEA_2)-$PbBr_4$ projected along the (c) [100] and (d) [010] axis. The stacking direction is [001]. Atomic color coding: Pb (red), Br (blue), C (black), N (green), and H (pink). Tilting angle δ and bond angle η are indicated (see text).

specific width of n octahedra or even cleaved along various planes, linking the octahedra in linear or zig-zag corrugated patterns [217, 218, 219]. Opportunities to engineer LHOPs not only originate from changing the inorganic perovskite stoichiometry, but also by choosing one or more of many complex large organic cations to separate the layers [217, 218, 219, 209, 220]. Promising organic cations range from simple carbon chains with ammonium caps to large chromophore complexes [221, 222, 223]. These degrees of freedom allow for the exploration of a wide variety of electronic properties and to tune optical response.

In this context, optically activated charge separation between the organic and inorganic layers of LHOPs has been long sought to reduce the overlap between electron and hole wave functions and, thus, allow utilization of separated electron-hole channels for highly efficient charge transport. The advent of organic solar cells has proven that π-conjugated polymers are fully capable of producing and transporting bound electron-hole pairs (excitons) under illumination [114, 224]. It has further been suggested that inter-chain charge separation of bound electron-hole pairs is possible in these systems [225]. Furthermore, charge transfer between semiconductor CdSe quantum dots and poly-2-methoxy-5-(2-ethyl-hexyloxy-p-phenylenevinylene) bonded functional coatings has been observed [226]. This raises an interesting question whether organic layers in LHOPs with π-conjugated organic cations could similarly carry photo-current under illumination if optical absorption excites electrons and holes that are localized in parallel layers of the LHOP system. If so, extensive chemical degrees of freedom in LHOPs could allow for engineering a layered organic-inorganic compound material that are capable of efficiently separating electrons and holes. These layers may provide separate conduction channels for electrons and holes, potentially reducing detrimental recombination. However, it is unknown how active the π-conjugated organic compounds in LHOPs are under UV-VIS absorption, in particular in the stoichiometric limit of n=1 perovskite layers between each organic layer.

To address this, Li *et al.* conclude from a large Stokes shift in the photoluminescence emission spectrum that charge separation occurs between the organic ammonium-propyl-imidazole (API) layer and inorganic $PbBr_4$ perovskite layer of [110] oriented API lead-bromide (n=1) [227]. They also performed density functional theory (DFT) calculations and report an isolated carbon-π^* state in the fundamental band gap, to which they attribute the carrier separation and resulting massive Stokes shift. However, this material has not been studied by modern first principles approaches that include the effects of spin-orbit coupling (SOC) and electron-hole interaction on the optical-absorption spectrum. In particular, SOC has shown to be very important in determining the correct electronic band structure in Pb-containing hybrid perovskite materials [228, 229, 230, 48]. Furthermore, several reasons for a large Stokes shift are debated and no conclusion has been reached: It has been suggested recently that it originates from strongly bound small-polaron states that form in the perovskite layer, lowering the emission energy of electron-hole pairs [231, 232]. While the extent of octahedral tilting in and out of the perovskite plane has also been correlated with the magnitude of the Stokes shift [24, 233], Du *et al.* found no such correlation from their analysis of the optical absorption and emission character of layered $Pb(I,Br,Cl)_4$ perovskites with acene alkylamine organic cation layers [234]. Hence, the debate to what extent π-conjugated organic layers participate in the optical absorption and emission of LHOPs is still open.

In this chapter[1], we report first principles calculations, for single π-conjugated LHOPs to determine the organic and inorganic layer contributions to electronic structure and optical absorption. We also clarify at what energies this becomes a significant contributor to the total optical response. The materials of interest are the $\langle 110 \rangle$ API-PbX_4 class (X=I, Br, Cl) of layered perovskites, motivated by the work of Li *et al.* [227] and the single π-conjugated organic cation perovskites 2-phenyl-ethylammonium (PEA) PEA_2-PbX_4 (X=I, Br, Cl) due to their readily available experimental atomic geometries and single π-conjugated (benzene) group per organic ion (see Fig. 5.1). We compute the ion-projected electronic structure and single-particle optical response using density functional theory (DFT), including spin-orbit coupling (SOC) and band gap corrections determined by HSE06 hybrid-functional calculations. The PBE+SOC+Δ_{HSE06} calculations reported in this work are an approximation of the full single-particle excitation energy calculations within the GW+SOC many-body perturbation theory formalism [40]. The two-particle optical response, which includes the effect of exciton formation, is calculated from the solution of the Bethe-Salpeter equation (BSE). We seek to clarify energetic alignment of the bands associated with organic and perovskite components in both materials and provide detailed analysis of essential electronic wavefunctions and individual contributions to optical absorption spectra. Subsequently, we seek to determine if optical excitations occur within individual

[1]The results detailed in this chapter are published in the article: Joshua Leveillee *et al.* Phys. Rev. Materials 2, 105406 (2018) [235]

layers of single π-conjugated LHOPs or whether optical excitations partially separate electrons and holes between layers.

5.2 Computational Methods

DFT calculations, using the projector-augmented wave method, are performed with the Vienna *Ab-Initio* Simulation Package (VASP) [187, 155, 188, 154]. The generalized-gradient approximation of Perdew, Burke, and Ernzerhof (PBE) [236] is used to describe exchange and correlation (XC). Kohn-Sham wave functions are expanded into a plane-wave basis with an energy cutoff of 500 eV and the Brillouin zone (BZ) is sampled using a Γ-centered $4 \times 4 \times 2$ **k**-point mesh. With this setup, total energies of the API-PbX_4 structures are converged to within 5 meV per formula unit. Equilibrium positions of all atoms, cell volumes, and unit cell parameters are optimized by minimizing the external pressure and Hellman-Feynman forces to below a threshold of 10^{-2} eV/Å using the PBEsol XC functional [139] and an increased plane-wave cutoff of 900 eV. The use of PBEsol is based on previous studies where lattice parameters of hybrid perovskite materials are predicted to high accuracy [140]. The symmetries of the experimentally determined unit cell are preserved in the first principles atomic position and cell geometry relaxation. Band structures, ion-resolved densities of states (DOS), and ion-resolved optical-absorption spectra are calculated, taking spin-orbit coupling (SOC) into account [28]. The high-frequency dielectric constant ε_∞ is calculated using density functional perturbation theory on a $5 \times 5 \times 2$ Γ-centered **k**-point mesh for API-PbX_4. Band gaps are determined using the Heyd-Scuseria-Ernzerhof (HSE06) hybrid XC functional [237] with a fraction of α=0.25 exact exchange. Due to the high computational cost of including SOC in hybrid functional calculations, these are performed using a $2 \times 2 \times 2$ Γ-centered **k**-point mesh.

Linear optical response, described by the components of the complex frequency-dependent dielectric tensor $\varepsilon_2^{\alpha\beta}(\omega)$, where α and β are Cartesian coordinates, is computed using the Ehrenreich-Cohen formula [60, 144] (see Equation 2.12). We use PBE+SOC Kohn-Sham energies and wave functions and a scissor shift to adjust the energies of the conduction bands to the HSE06+SOC band gap (referred to as PBE+SOC+Δ_{HSE06}). The transition-matrix elements in Eq. (2.12) are computed using the VASP code [144]. We also compute the ion- and angular-momentum resolved optical response by weighting the transition-matrix element for a given transition using the projection $p^N_{lmn\mathbf{k}}$ of the wave function $\phi_{n\mathbf{k}}$ on a spherical harmonic Y_{lm} for a given ion N, with m and l being the magnetic and orbital quantum number, respectively [238]. The sum of $p^N_{lmn\mathbf{k}}$ over all N, l, and m equals to one for each wave function $\phi_{n\mathbf{k}}$. This turns Eq. (2.12)

into:

$$\varepsilon_2^{\alpha\beta}(\omega) = \frac{8\pi^2}{\Omega} \sum_{cv\mathbf{k}} \left(\sum_{N,l,m} p^N_{lmn\mathbf{k}} \right) \frac{\langle \psi_{c\mathbf{k}} | \hat{p}_\alpha | \psi_{v\mathbf{k}} \rangle \langle \psi_{v\mathbf{k}} | \hat{p}_\beta | \psi_{c\mathbf{k}} \rangle^*}{(\epsilon_{c\mathbf{k}} - \epsilon_{v\mathbf{k}})^2} \delta(\epsilon_{c\mathbf{k}} - \epsilon_{v\mathbf{k}} - \hbar\omega) \tag{5.1}$$

Restricting the sum in parentheses to certain ions, angular-momentum components, or bands (e.g. n being v or c when resolving valence or conduction states), allows us to compute ion- and angular-momentum resolved optical response.

In addition, we study excitonic effects on the dielectric functions of API-PbX_4 from the solution of the Bethe-Salpeter equation (BSE) [81, 86, 41] for the optical polarization function. The large computational cost of this approach requires us to restrict these calculations to a $4 \times 4 \times 2$ **k**-point grid. A small random shift of this grid lifts degeneracies and, on DFT level, allows us to reproduce dielectric functions calculated on a well-converged Γ-centered $8 \times 8 \times 2$ **k**-point grid.The absorption edges from shifted and well-converged Γ-centered **k**-point grids disagree by about 100 meV. Converging exciton-binding energies, defined as the difference between the lowest optical and the lowest single-particle excitation energies, to high accuracy requires much denser **k**-point sampling near the band extrema [86], which is beyond the scope of this work. Hence, estimates for exciton-binding energies reported here have error bars of about 100 meV.

The screened electron-hole Coulomb interaction W in the BSE kernel is calculated using the model dielectric function proposed by Cappellini *et al* [87]. The dielectric constant used in the model dielectric function is the average of the diagonal components of the high-frequency dielectric tensor $\varepsilon_\infty^{\alpha\beta}$ calculated by density functional perturbation theory (DFPT) (see table C.3), representing the average dielectric response of the layered material. It has been extensively shown that the organic and perovskite layers of LHOPs have spatially resolved dielectric constants of ≈ 2.5 and 5 respectively [212, 48], and thus this work will use the spatially averaged dielectric constant determined by DFPT as an approximate value [144]. Other methods are available in the literature to handle this spatial variability of the dielectric constant [239, 240, 48]. In this work, the BSE is solved as an eigenvalue problem in the Bloch basis [41, 86] of the excitonic Hamiltonian, and using the Tamm–Dancoff approximation as seen in Eq. 2.39 and Eq. 2.40: Non-interacting electron-hole pairs with energies up to 5 eV (applied to the PBE+SOC bandstructure) are used to compute the excitonic Hamiltonian. These include, in (nv,nc,nk) format: API-PbI4 (112,48,32), API-PbBr4 (110,40,32), and API-PbCl4 (104,32,32). Dielectric functions, including excitonic effects, are calculated from the excitonic Hamiltonian in Eq. (**??**) using a time-propagation technique [88, 241]. The rigid band gap shift is added to the diagonal of the excitonic Hamiltonian, increasing the energy window of the excitonic Hamiltonian from 5 eV to $5+\Delta_{HSE06}$ eV. For the above-mentioned energy window of 5 eV, 5594 time steps of 0.0022 per eV are required. The lowest excitation energies are found by applying a

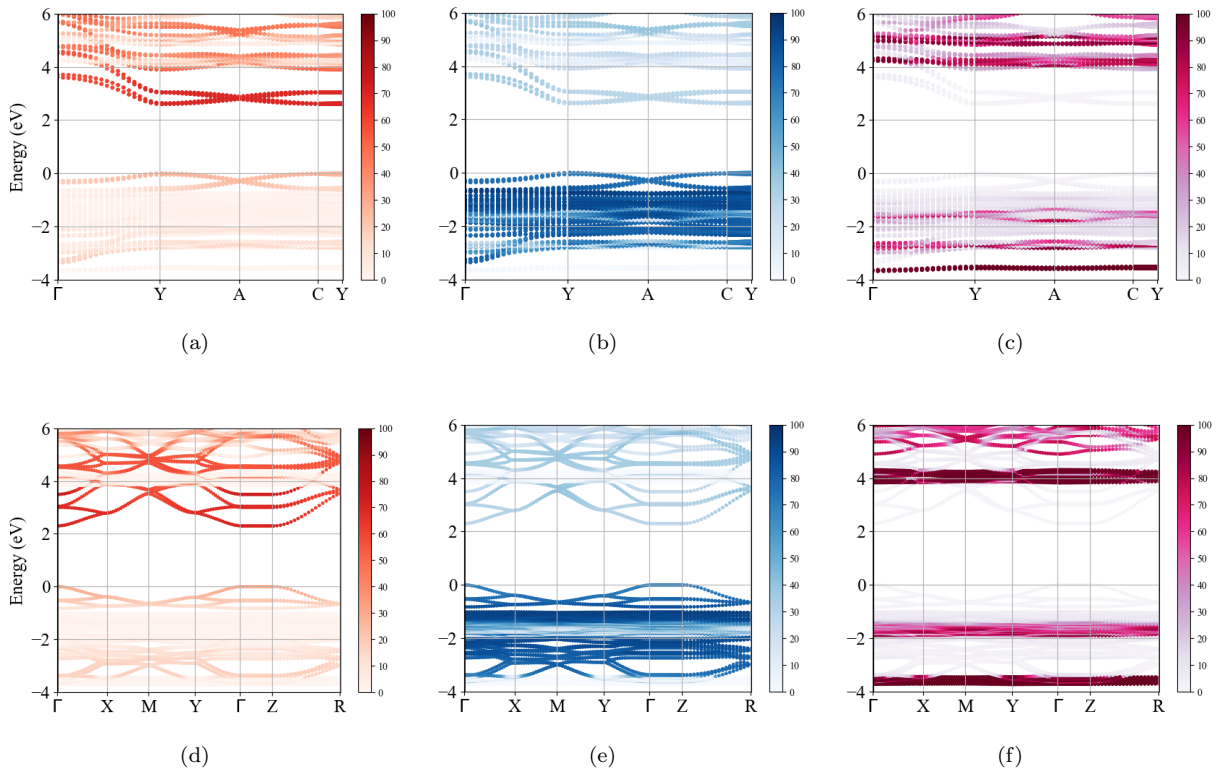

Figure 5.2: The ion-projected band structures, computed using PBE+SOC+Δ_{HSE06}, of API-$PbBr_4$ (a-c) and PEA_2-$PbBr_4$ (d-f). The color bar indicates the contribution of Pb (red), Br (blue), and API/PEA (magenta) to each state as a percentage.

conjugate-gradient scheme to iteratively compute the lowest eigenvalues. All these calculations are carried out using the BSE implementation discussed in Refs. [157, 86].

5.3 Results and Discussion

5.3.1 Atomic Structure

The structure of single-layer ⟨110⟩ API-PbX_4 compounds resembles that of the ⟨100⟩ class of layered perovskites: The major difference is the corrugation of the perovskite layer with a zig-zag type octahedral linking in the ⟨110⟩ compounds and a linear-type linking in the ⟨100⟩ compounds. Figure 5.1 shows the [100] and [010] projections of both API-$PbBr_4$ and PEA_2-$PbBr_4$. PEA_2-PbX_4 experimental structures are used in our study [242, 243, 244]. Since experimental data is available only for API-$PbBr_4$ [227], we fully relax all API-PbX_4 atomic geometries in the $P2_1/c$ symmetry space group. The resulting lattice parameters and vector angles, unit-cell volumes, octahedron tilting angles, and Pb–X–Pb bond length ranges are reported

Table 5.1: Energy gaps (in eV) computed using different levels of theory. PBE+SOC+Δ_{HSE06} refers to the PBE+SOC electronic structure with the band gap rigidly shifted to the HSE06+SOC band gap value (see text).

Level of theory	API-PbI_4	API-$PbBr_4$	API-$PbCl_4$
PBE+SOC	1.44	1.94	2.41
HSE06+SOC	2.10	2.74	3.32
$\pi-\pi^*$ gap (PBE+SOC+Δ_{HSE06})	5.87	5.88	5.7
BSE Optical gap	1.74	2.23	2.68
Exp. Optical gap [227]	–	3.18	–
	PEA_2-PbI_4	PEA_2-$PbBr_4$	PEA_2-$PbCl_4$
PBE+SOC	1.33	1.75	2.12
HSE06+SOC	1.95	2.45	2.95
$\pi-\pi^*$ gap (PBE+SOC+Δ_{HSE06})	5.39	5.82	5.53
Exp. optical gap [234]	2.45	3.0	3.6

in Table C.1 for all systems. The relaxed API-$PbBr_4$ atomic structure is in excellent agreement with the experimental structure determined by Li *et al.* [227], with errors of under 1 % for lattice parameters, 0.2 % for unit-cell volume, 1 % for lattice vector angles, 2.5 % for out-of-plane tilting, and 15 % for in-plane tilting angles. The out-of-plane tilting angles δ_1 and δ_2 in the corrugated $\langle 110 \rangle$ API-PbX_4 systems should be 45°, if no tilting is present. For the relaxed API-PbX_4 structures we find two distinct δ_1 and δ_2 in the range between 33.7° and 33.8° and 51.4° and 53.9°, respectively.

In the linearly-linked PEA_2-PbX_4 systems, δ=0° under no tilting and indeed in the experimental structures, the out-of-plane tilting angles remain small, in the range of 1° to 3°. The in-plane-tilting angles, ranging between η=12.2° and η=14.5°, are larger compared to those found in the API-PbX_4 systems, ranging from η=8.5° to η=10.5°. This in-plane tilting is very similar to the octahedron tilting in orthorhombic $MAPbX_3$ 3D HOPs [140].

5.3.2 Electronic Structure

The band structures of API-PbX_4 and PEA-$_2PbX_4$ reveal dispersive band frontiers attributed to states localized on the perovskite as well as flat, non-dispersive bands, situated more than 1 eV away from the band frontiers, that are attributed to the organic π and π^* states (see Fig. 5.2). Throughout the remainder of this chapter, the label PBE+SOC+Δ_{HSE06} refers to the PBE+SOC band structure with conduction bands rigidly shifted to higher energy to match the HSE06+SOC band gap, and HSE06+SOC refers to fully non-collinear HSE06 hybrid-functional calculations that take SOC into account. Table 5.1 reports relevant calculated and experimentally determined energy gaps of these materials.

Ion-projected PBE+SOC+Δ_{HSE06} band structures are plotted for API-$PbBr_4$ in Fig. 5.2(a)-(c). Similar data for the other API and PEA LHOPs considered in this work can be found in SI Figs. S2 and S3.

Due to the $P2_1/c$ symmetry, the API-PbX_4 materials exhibit direct gaps of 2.10 eV, 2.74 eV, and 3.32 eV for API-Pb(I, Br, and Cl), respectively, at the Y point of the Brillouin zone (BZ). The Y point folds back to the Γ point when a 2×2 conventional cell is considered as demonstrated by Pedesseau *et al.* [48] The band gap we computed for API-PbBr4 using the HSE06 exchange-correlation functional with spin-orbit coupling underestimates the gap of 3.18 eV measured from the optical onset by Li *et al.* [227]. This can be attributed to the fact that HSE06, albeit it improves over the DFT-PBE description, does not fully capture quasiparticle effects for the systems studied here. More sophisticated, but computationally more expensive methods, such as many-body perturbation theory, could mitigate these shortcomings [245]. Additionally, in this comparison the electron-hole interaction was neglected and, thus, the calculated electronic gap differs from the measured optical gap by the exciton binding energy. This will be discussed in the results for optical response. Differences between our relaxed structure and the experimental structure of API-$PbBr_4$ are expected to result in only small changes of the band gap, within 0.2 eV, based on the effects of in- and out-of-plane angles on gap values explored by Pedesseau *et al.* [48]. Figure 5.2 clearly shows that the band dispersion of API-$PbBr_4$ along the $Y-\Gamma$ direction is free-electron like, with a parabolic curvature near the Y point. Along the $Y-A$ direction, the dispersion has a lower curvature, indicating a higher electron effective mass. Finally, along the $Y-C$ direction the bands are effectively flat due to the layered and reduced periodicity of the LHOP crystals along the [001] direction. We observe the same trend for API-PbI_4 and API-$PbCl_4$.

In contrast, band structures of the PEA_2-PbX_4 LHOPs, with space groups $P2_1/c$, $P\bar{1}$, and $P\bar{1}$ for I, Br, and Cl, respectively, exhibit direct gaps of 1.95 eV, 2.45 eV, and 2.95 eV at the Γ-point. The difference between the space groups of PEA_2-PbI_4 and PEA_2-$Pb(Br,Cl)_4$ is due to the bis-phenylethylammonium conformation of the chosen PEA_2-PbI_4 structure [234]. The general PEA_2 conformation explored by Du *et al.* assumed the same $P\bar{1}$ space group as the PEA_2-$PbBr_4$ and PEA_2-$PbCl_4$ systems. The band structure of PEA_2-$PbBr_4$, illustrated in Fig. 5.2(d)-(f), exhibits highly dispersive, free-electron like band frontiers along the $\Gamma-X$ and $\Gamma-Y$ directions, as well as flat, non-dispersive band frontiers in the $\Gamma-Z$ direction. Unlike the API-PbX_4 corrugated perovskites, the PEA_2-PbX_4 perovskites explored in this work are not corrugated in either in-plane direction. Thus, they have a higher periodicity in both in-plane lattice directions which manifests itself in highly dispersive band frontiers along two reciprocal-lattice directions. As a consequence, corrugated API-PbX_4 shows low effective-mass band frontiers only along $\Gamma-Y$, whereas PEA_2-PbX_4 shows low effective masses along both $\Gamma-X$ and $\Gamma-Y$.

In traditional 3D HOPs such as $MAPbX_3$, valence and conduction band frontiers are comprised of X:p+Pb:$6s$ and Pb:$6p$ states, respectively [246]. While in principle, in the layered systems with conjugated

organic cations explored in this work, API and PEA π and π^* states could contribute in the near-gap region, we find from the ion-projected band structure that the valence and conduction band frontiers are comprised of X:p+Pb:6s and Pb:6p states, respectively. This is very similar to the 3D $MAPbX_3$ HOPs. However, unlike 3D $MAPbX_3$ HOPs that have organic states far below (about 6 eV) and above the band frontiers [246], API-PbX_4 and PEA_2-PbX_4 have flat, non-dispersive bands attributed to API and PEA_2 π and π^* orbitals within 1.0 to 2.0 eV of the band frontiers, as shown in Fig. 5.2.

Furthermore, due to the strong contributions of Pb-derived states to the band frontiers in API-PbX_4 and PEA_2-PbX_4, the spin-orbit interaction lowers the energy of conduction-band minimum states (see Fig. S5). This energy reduction of Pb:p conduction-band states is well known in Pb- and Sn-containing HOP and LHOP systems [228, 229, 230, 48] and attributed to the large mass of Pb atoms. Hence, SOC-related energy contributions are critical for correctly predicting the energetic ordering of states near the band-extrema and, in particular, to *qualitatively* explain the relative energy position of organic π and π^* states. In Fig. 5.2 (as well as Figs. S4 (a) and (b) and S5 (a) in the SI) we clearly show that once SOC is taken into account, the ion-resolved band ordering at the Γ-point conduction band minimum changes: The Pb:p states are lowered in energy relative to the API π^* states which remain unaffected by the spin-orbit interaction. As a result, we observe Pb:p character for all $\mathbf{k}$ points throughout the BZ. In contrast, without the inclusion of SOC, a band inversion occurs at the Γ-point and the conduction band minimum would be attributed to mostly API π^* states. Hence, if SOC is neglected, electronic-structure calculations could, depending on transition matrix element amplitude, incorrectly predict that excitations from the Γ-point band frontiers result in charge separation between perovskite and API layers. This behavior is different from what has been observed for 3D $MAPbX_3$ HOPs, for which ion projection of the band frontiers remain the same, with X+Pb and Pb attributed to the valence and conduction band frontiers, respectively [246], whether or not SOC is included. Finally, we note that the difference between HSE06+SOC and the PBE+SOC+Δ_{HSE06} approach is minimal, and PBE+SOC+Δ_{HSE06} calculations are a good basis for optical response calculations. To this end we show in detail in the SI that for optical excitations energies below 5 eV, only small errors of under 0.5 eV are expected for spectral features.

The ion-resolved density of states (DOS) in Fig. 5.3 illustrates that in all six perovskite systems, the valence- and conduction-band frontiers are attributed to halide and Pb states, respectively. For this analysis, we aligned the Pb:5d states at -15.3 eV across the different materials. Importantly, Fig. 5.3 shows a reduction of the valence-band maximum in energy with decreasing halide mass: The valence band maxima of API-PbX_4 shift from 0.0, to -0.24, and -0.48 eV for X = I, Br, and Cl, respectively. The same trend of the valence band maximum located at 0.0, -0.17, and -0.47 eV occurs for the PEA_2-PbX_4 systems for

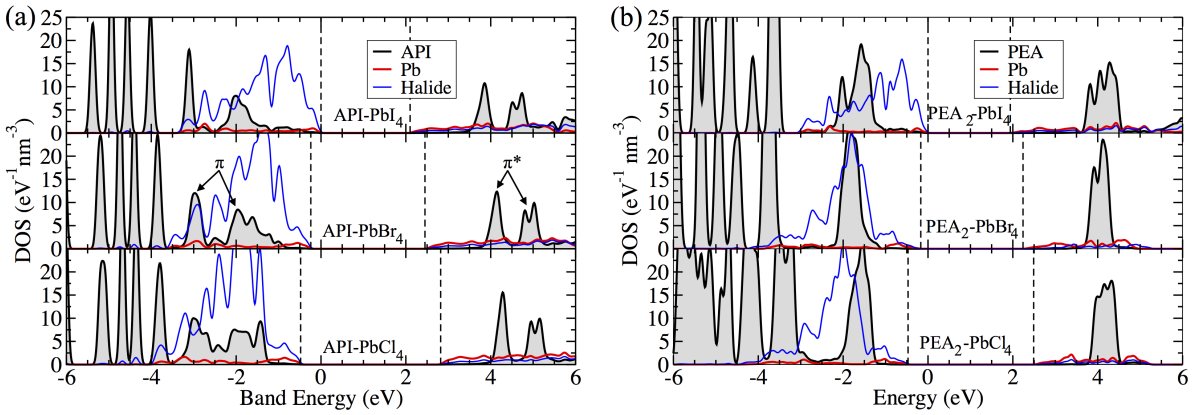

Figure 5.3: The PBE+SOC+Δ_{HSE06} ion-projected DOS of (a) API-PbI_4, API-$PbBr_4$, API-$PbCl_4$ and (b) PEA_2-PbI_4, PEA_2-$PbBr_4$, and PEA_2-$PbCl_4$. The energies of the Pb $5d$ states at -15.3 eV are used for alignment, and the valence band maxima of API-PbI_4 and PEA_2-PbI_4 are used as energy zero. Dashed lines mark the band extrema. Color coding: Pb (red), halide (blue), organic layer (shaded brown).

X = I, Br, and Cl, respectively. This decrease can be understood by examining standard atomic ionization energies of halide atoms, with I, Br, and Cl having ionization energies of 10.45, 11.81, and 12.96 eV (from the NIST Atomic Spectra Database Ionization Energies Form) [247]. Since the valence-band maximum of each perovskite material in this work is attributed to halide p-states, our findings are commensurate with trends of these atomic ionization energies.

At the same time, this figure shows that organic π and π^* states are not affected by the changing halide mass and remain approximately aligned in both systems. The API π states appear as broad peaks at -2.00, -1.78, and -1.40 eV for I, Br, and Cl, respectively. This broadening is due to static molecular disorder and coupling between organic molecular states. The lowest energy π^* states appears as sharp peaks centered around 3.87, 4.10, and 4.30 eV for I, Br, and Cl, respectively. The resulting $\pi-\pi^*$ gaps, defined as the energy differences of these peaks, are 5.87, 5.88, and 5.70 eV and show a width of about 0.5 eV from the broadening of the π^* state. The PEA_2-PbX_4 systems display a highest occupied π state peak spanning the range between -1.3 and -2.1 eV. A single lowest unoccupied π^* peak is located between 3.84 and 4.10 eV for all PEA_2-PbX_4 materials. This leads to $\pi-\pi^*$ gaps of 5.39, 5.82, and 5.53 eV for I, Br, and Cl, respectively, with a width of about 1.0 eV. The variations in the $\pi-\pi^*$ gaps in the PEA_2-PbX_4 systems are attributed to differences in the experimental X-ray atomic structures of the organic layers used in the unit cells of this study. As we chose to relax the API-PbX_4 structures (due to the similarities of the relaxed and experimental API-$PbBr_4$ structures and the lack of available experimental data for API-$Pb(I,Cl)_4$) the $\pi-\pi^*$ gaps are uniform across the choice of halide. We note that quasiparticle corrections computed within

HSE06+SOC also produce an energy-dependent band dilation, not reproduced by the scissor approach. This increases the $\pi-\pi^*$ gaps of the API and PEA systems to about $6.1-6.3$ eV, suggesting that $\pi-\pi^*$ optical transitions will occur well in the UV photon energy range. The PBE+SOC+Δ_{HSE06} approximation captures the UV response of the intra-organic transitions, albeit at slightly lower energies compared to HSE06+SOC, and therefore provides a reasonable approximation for optical response calculations. It should be mentioned that, in reality, the absorption onset of such molecules is at lower energies due to large exchange energy contributions. For example, benzene in an alcohol solution has an absorption onset of about 4.8 eV [248]. However, this is still in the UV energy range.

Figure 5.3 also shows that, due to a lower cation charge of +1 on PEA compared to +2 in API, the ratio of organic to inorganic density of states is higher in the PEA_2-PbX_4 structures. This implies that, if organic-perovskite optical transitions are allowed, the PEA_2-PbX_4 systems have more possible charge-separation pathways under optical excitation. In examining the ion-resolved density of states of API-PbX_4, it can be seen that the optical response below the 5.7 eV $\pi-\pi^*$ gap contains mostly transitions between perovskite-derived states. Only small contributions due to transitions from perovskite- to API-derived states are expected between the optical onset and 5.7 eV. This changes in the PEA_2-PbX_4 systems, where the PEA density of states amplitude in the valence and is about equal to or greater than the perovskite density of states at the PEA π-state energy. Consequently, the optical response could have a large contribution from perovskite to PEA transitions at lower energies than the $\pi-\pi^*$ gap. This implies that if transitions between perovskite and PEA are optically allowed, the PEA_2-PbX_4 systems have more possible charge separation states available.

Finally, in the context of achieving charge separation between organic and perovskite layers upon optical excitation, we find that PEA_2-$PbCl_4$ is a particularly promising candidate. The ion-resolved DOS in Fig. 5.3 shows a pronounced peak associated with the organic molecule that is centered near 1.5 eV below the valence-band maximum. Not only is this peak higher in energy than another peak at -2 eV that is attributed to Cl ions, but it also is of the same magnitude, as discussed above. This energetic positioning of states suggests the strong potential for partial charge separation, generating holes in the PEA_2 π state and electrons in the conduction-band Pb:6p state. The actual probability of charge separation between layers, however, depends again on the dipole matrix elements for the corresponding optical transitions between these organic and perovskite states. This will be discussed next.

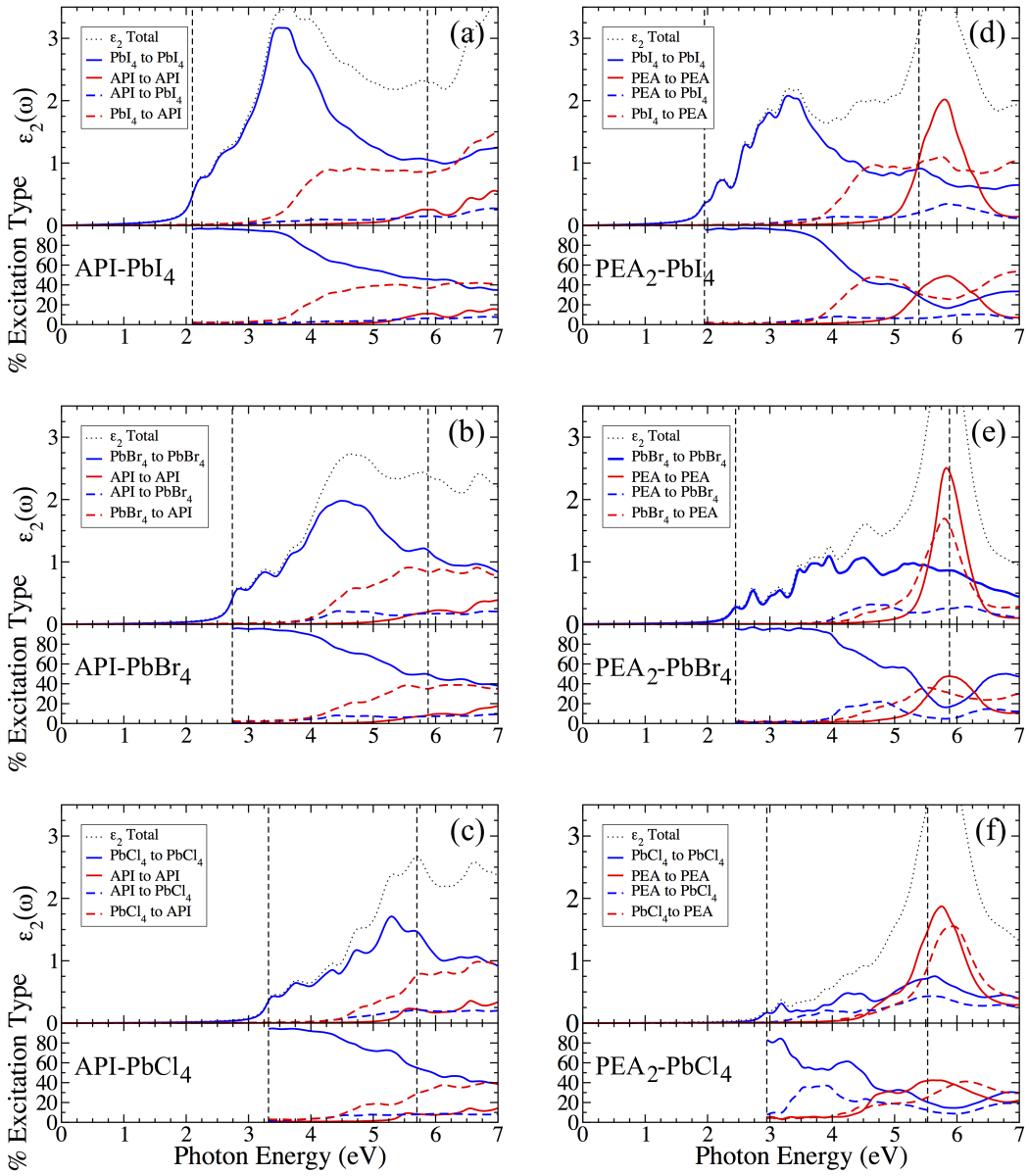

Figure 5.4: The ion-resolved imaginary dielectric functions of (a) API-PbI_4, (b) API-$PbBr_4$, (c) API-$PbCl_4$, (d) PEA_2-PbI_4, (e) PEA_2-$PbBr_4$, and (f) PEA_2-$PbCl_4$. The color coding indicates the resolution of ε_2 along specific ion-to-ion transitions, which are (in valence ions → conduction ions notation) perovskite→perovskite (blue, solid), organic→organic (red, solid), organic→perovskite (blue, dashed), perovskite→organic (red, dashed), and all (black, dotted). The bottom panels show the percent that each type of transitions contributes to the total ε_2 as a function of photon energy.

5.3.3 Optical Response

The ion-projected dielectric function $\varepsilon_2(\omega)$ is illustrated in Fig. 5.4 for all considered materials. Here we distinguish between transitions among perovskite ions ('inorganic') and organic cations ('organic') by bundling them into the inorganic-inorganic, organic-organic, organic-inorganic and inorganic-organic subcategories. The first two correspond to intra-layer transitions and the latter two to inter-layer transitions. If the two sub-layers were to act as separate optically active materials, the amplitude of inter-layer $\varepsilon_2(\omega)$ is vanishing. In the case of intra-layer optical excitation, these projections are finite.

By ion-resolving the imaginary dielectric function of API-PbX_4, we show that optical excitations below 4 eV are entirely dominated by intra-perovskite transitions, whereas inter-layer transitions contribute significantly to the optical response above 4 eV. As discussed above, this is because states in the vicinity of the gap are attributed entirely to perovskite states (Fig. 5.3). Absorption between API-derived states, with an onset around the $\pi-\pi^*$ gap, contributes weakly to the overall optical response even in the UV energy range due to a low relative API-π density of states compared the halide density of states in the valence band. Figure 5.4 also shows that transitions from PbX_4 to API states are responsible for a significant portion of the optical response in the UV energy range, and thus partial electron and hole separation occurs between the API and PbX_4 layers. However, this partial separation has little utility for optoelectronic applications requiring charge separation for visible light energy excitations.

The PEA_2-PbX_4 systems demonstrate a much stronger intra-organic optical response within the PEA layers, along with significant inter-layer absorption in the UV energy range. As with API-PbX_4, the near-gap and visible energy range of the spectra is governed by intra-perovskite optical response. Around the $\pi-\pi^*$ gap, a large peak appears in the imaginary dielectric function which is attributed to the intra-PEA optical transitions and transitions from PbX_4 to PEA states. Transitions from PbX_4 to PEA states appear at higher energies at lower halide masses, corresponding to the increased VBM-π^* gap by the decrease in the valence band energy. In PEA_2-PbI_4, strong transitions are observed from PbI_4 to PEA states at lower energies than those between PEA states, leading to the same partial charge separating activity seen in API-PbX_4 above 4 eV. In PEA_4-$PbBr_4$, the contributions due to transitions from $PbBr_4$ to PEA and PEA to $PbBr_4$ are roughly equal in the 4 to 5 eV photon range, leading to a cancellation in partial charge separation character due to hybridization. PEA_2-$PbCl_4$ shows a change in behavior: The optical response between 3.5 and 4 eV largely arises from intra-perovskite transitions and contributions from PEA to $PbCl_4$ states, partially separating holes to the PEA layer and electrons to the $PbCl_4$ layer. This behavior is due to the proximity of the PEA π states to the $PbCl_4$ attributed valence band maximum, leading to inter-layer transitions closer to the absorption onset. However, overall, in PEA_2-PbX_4, where the organic optical activity is more significant

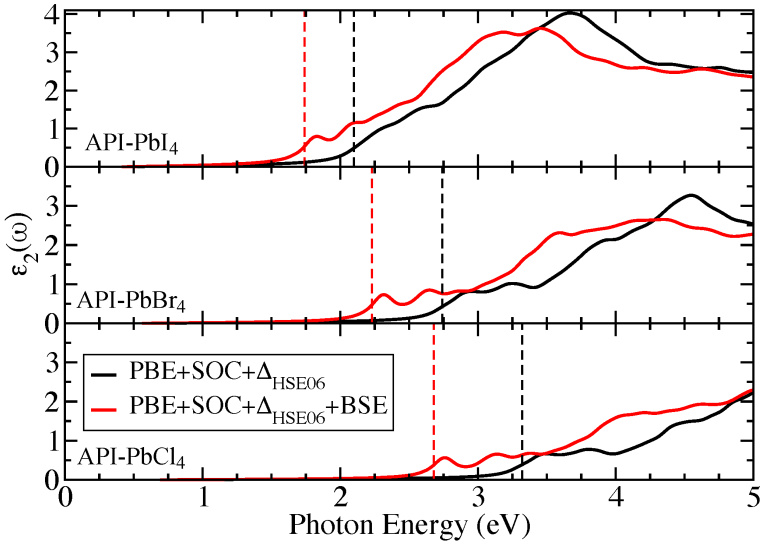

Figure 5.5: Imaginary part of the dielectric function of API-PbI_4 (top), API-$PbBr_4$ (middle), and API-$PbCl_4$ (bottom) with (red lines) and without (black lines) excitonic effects. The PBE+SOC Kohn-Sham energies and states are used as input to the BSE and the single-particle band gap is shifted to the HSE06+SOC value. That band gap and the lowest excitation from the BSE are marked by vertical black and red dashed lines, respectively.

compared to API-PbX_4, partial charge separation only occurs in the UV energy range.

In all three LHOP API-PbX_4 compounds, excitonic effects are expected to be stronger compared to their 3D HOP $MAPbX_3$ counterparts owing to quantum and dielectric confinement effects [212]. This increased binding energy was first explained by the works of Rytova and Keldysh, who separately established the theory of quantum confinement of charge carriers and the Coulomb interaction in low dimensional systems [15, 16]. This was further explored in layered semiconductors by Hanamura and layered perovskites by Ishihara and Koutselas [249, 250, 251, 252]. In 3D HOPs such as $MAPbI_3$, $MAPbBr_3$, and $MAPbCl_3$, the high-frequency dielectric constants ε_∞ are about $4-7$ [166, 167, 229, 50]. $MAPbX_4$ also has highly dispersive band frontiers, leading to a low reduced electron-hole mass of about $0.1m_0$ [253]. Using a simple Wannier-Mott model, the exciton binding energy is in the range of 25 to 85 meV. As determined in experiments and predicted by theory, the low-frequency dielectric constants are also large ($\varepsilon_s > 20$), which enhances the screening of the electron-hole Coulomb potential [49, 122, 253, 1, 48]. Given the API-$PbBr_4$ electronic structure determined in this work, the high-frequency dielectric constant is determined to be 3.94 by density-functional perturbation theory (DFPT) and the reduced electron-hole mass at the band frontiers is approximately $0.610m_0$, based on an averaged parabolic fit to the dispersive, in-plane, $Y \rightarrow G$ and $Y \rightarrow A$ directions. This leads to

a Wannier-Mott binding energy of 525 meV, which is an order of magnitude higher compared to the 3D counterparts. The lower high-frequency dielectric constants predicted by DFPT range from 3.47 to 4.76 for the LHOP systems (see Tab. S2) and originate from the alternating low and high values of ε_∞ between layers averaged over the unit cell volume [144]. This leads to an average dielectric constant that is lower than those typically measured and calculated for 3D HOPs [212, 48].

The excitation energies of lone API molecules in air are calculated in the Gaussian suite [254] to determine if the organic optical response will comprise a significant portion of the optical response near the perovskite absorption edge. The HSE, B3LYP, and CAM-B3LYP functionals are used to calculate the homo-lumo gaps of 5.60, 5.84, and 8.05 eV respectively in the singlet-relaxed geometry. The HSE and B3LYP agree very well with the π-$\pi*$ gap found in API-PbX_4 at the PBE+SOC+Δ_{HSE06} level of theory. Excitation energies are calculated using time-dependent DFT and are found to be 5.42, 5.23, and 5.75 eV within the HSE, B3LYP, and CAM-B3LYP functionals, respectively. These results suggest that the excitonic absorption onset of the API spacer will not occur near the perovskite excitonic absorption edge.

Strong excitonic effects and, hence, large exciton binding energies are predicted for the API-PbX_4 materials from first principles, with values comparable to available experimental data for LHOP systems. For API-PbX_4, we show in Fig. 5.5 that excitonic effects significantly influence the optical-absorption spectra. The gradual absorption onset observed in the single-particle dielectric function becomes a pronounced excitonic peak, red-shifted to lower energy, that is associated with the lowest-energy electron-hole bound state. In addition, there is also a significant red shift of broad high-energy peak structures between 3.5 eV and 4.5 eV, resulting in strongly increased absorption at lower energies. In our calculations, the energy difference of the onsets of single-particle and BSE spectrum correspond to the binding energy of the lowest electron-hole pair. The high computational cost of the BSE calculations in this work, due to large unit cells and inclusion of spin-orbit coupling, does not allow a dense enough multiple **k**-point sampling [86] to provide fully converged results for this quantity. Given the choice of k-point mesh, we estimate that our numbers are within 100 meV of the converged result (see SI figure S6). From our data we extract ≈357 meV (see Fig. 5.5) for the exciton-binding energy of API-PbI_4, which is the smallest value for the three API-PbX_4 compounds studied in this work. API-$PbBr_4$ shows a stronger exciton binding energy due to the lower dielectric constant compared to API-PbI_4, and consequently a stronger red shift of the onset by ≈505 meV. Finally, the strongest excitonic red shift in the optical spectrum of ≈638 meV is predicted for API-$PbCl_4$, with the lowest high-frequency dielectric constant. High-frequency dielectric constants are slightly overestimated as they are calculated at the PBE+SOC level of theory. However, from test calculations we estimate that increasing the band gap to the experimental value would decrease the dielectric constant by less than

15%. Since we do not have accurate band gap data to compare with for the API-PbX_4 materials, we use the PBE+SOC high-frequency dielectric constant as a good approximation.

The predicted exciton binding energies and relative positions of spectral peaks are in good agreement with available experimental data of layered perovskite systems [227]. Wang *et al.* measured exciton binding energies of 218 meV in hexadecammonium-lead bromide $(HA)_2PbBr_4$ [255], Blancon *et al.* measured binding energies of 380, 270, and 220 meV in $n = 1$, $n = 2$, and $n > 2$-layered $(BA)_2(MA)_{n-1}Pb_nI_{3n+1}$ [220], and Ishihara *et al.* calculated a binding energy of 320 meV in n=1 layered PbI_4 octahedra with no organic spacer [250]. As a model function relying on a single, material-averaged, dielectric constant is used to compute the screened Coulomb interaction between electrons and holes, we do not account for the local field effects arising from the high spatial variability of the dielectric constant in LHOPs [212, 48]. More precise techniques such as including the full inverse dielectric tensor $\varepsilon_{G,G'}(q)^{-1}$ or semi-classical and semi-empirical methods that describe dielectric constant fluctuations can be used for a higher degree of accuracy [239, 240, 48, 256]. These high binding energies are also potentially detrimental to solar cell applications. which rely on splitting of electron-hole pairs. Investigations by Smith *et al.* have shown that the introduction of halogens by I_2 intercalation into the organic layer strongly reduces binding energy and the dielectric confinement of the layered perovskite systems [26], potentially lowering the exciton binding energy of LHOPs which is preferable for photovoltaic application.

5.4 Conclusions

The calculations performed in this chapter predict that the optical response of single-layered lead-halide perovskites with single-π-conjugated organic layers API and PEA_2 is dominated by intra-perovskite optical excitations in the visible energy range. A partial charge separation between the organic perovskite states can only be achieved at UV energies. Given these results, we conclude that single-layered PbX_4 LHOP systems with π-organic cation spacing layers composed of moieties with single aromatic rings act as one optically active perovskite material. Transitions involving both layers only occur at UV photon energies. Importantly, the lack of π and π^* states near the band extrema causes transitions in the visible energy range to be contained within the perovskite layer, meaning all electron-hole generation for optoelectronic applications in this energy range will be localized to the PbX_4 octahedral layers. At UV energies, significant electronic delocalization and charge separation is allowed, however the corresponding excitation energies are close to or above the ionization energy of perovskite systems.

The natural follow-up question is: How can charge separation be further achieved in layered hybrid

perovskite systems? The first item that must be addressed is the $\pi - \pi*$ gap of the conjugated groups. As discussed above, the absorption onset of single aromatic ring moieties occurs well below the homo-lumo gap due to large exciton binding energies on the order of electron volts[257]. Benzene, with an optical onset of 4.8 eV experimentally and between 4.7 and 6.9 eV theoretically by PBE0+BSE and GW+BSE calculations [248, 258], has a predicted homo-lumo gap in solution of between 4.5 and 6 eV [259]. Likewise, imidazole has a range of predicted excitation energies between 5.61 and 6.96 eV [258]. Thus, the interplay between the homo-lumo gap and the optical gap should be carefully considered in further engineering of layered perovskites for inter-layer charge separation application. Ideally, the homo-lumo gap can be lowered by adding more conjugated groups such as aromatic rings to the system. For example, layered perovskites with naphthalene groups have been investigated experimentally and have shown signs of exciton energy transfer between perovskite and organic layers [222, 223]. Secondly, the orbital overlap between the layers must be improved to increase the amplitude of the inter-layer transition dipole matrix elements. Larger overlap could be achieved by including heavier elements, such as chlorine, in the organic layer which has been recently explored experimentally [260, 217, 219]. Our future studies of such compounds will include organic-PbX_4 ion-projected band structures and densities of states to map the effects of decreased homo-lumo organic gap and organic halogenation.

Currently, $n = 1$ LHOPs with single conjugated rings face challenges as effective solar cell materials but show promise in a wide range of optoelectronic application. Quantum confinement of the perovskite layer increases the gap relative to the 3D HOPs and thus reduces the absorption range of the material in the visible optical spectrum. LHOPs with $n > 1$ help to decrease the gap [214], but at the cost of reducing the density of states of, and degree of optical coupling to, the organic lattice. Secondly, minimal π-stacking is observed in these systems, leading to highly localized electron and hole states in the organic layer. This in turn results in a high effective mass, low mobility in the form of incoherent hopping, and large binding energies of electron-hole pairs. Improving π-stacking of the organic conjugated layer in LHOPs is a promising future research direction, to achieve improvements [261]. Recent investigations have also shown that interfacing 2D LHOPs with 3D HOPs can lead to increased photovoltaic efficiency in Sn-based systems, opening the intriguing question of whether this can be done with Pb-based systems as well[262]. Besides applications as solar cells, $n = 1$ layered perovskites have shown promise as light-emitters [263]. Resonant coupling between the organic and perovskite layered of $n = 1$ systems opens the possibility of engineering the emission wavelength and intensity as a function of LHOP stoichiometry [264, 223].

It is important to note that everything studied in this manuscript is related purely to absorption in the singlet spin state. Thus, nothing is said about relaxation in the excited state or emission in the explored

LHOP systems. Both triplet and singlet energy levels and their post-optical absorption dynamics are fundamental to understanding how organic compounds behave in the excited state. The interplay between perovskite band energies and the organic singlet and triplet states must be understood to determine excited state charge transport, ion dynamics, and recombination in LHOPs with conjugated organic layers. The combination of methods in this work for determining optical absorption properties and methods such as time-dependent density functional theory and molecular dynamics can be used to predict and disentangle the full optical excitation and relaxation process of conjugated LHOP materials.

CHAPTER 6

TRIPLET LIGHT EMISSION IN LHOPs BY ORGANIC SPACER SUBSTITUTION

6.1 Introduction

The electronic structures of 2D layered hybrid organic-inorganic perovskites (LHOPs) are broadly tunable by the versatile alignment between the electronic levels of the perovskite and the organic spacer components. Depending on the degree of conjugation and polarity of the spacer moiety, one can precisely align desired electronic states including the perovskite levels and the singlet and triplet manifolds of the organic spacer layer. Knowledge of this provides materials scientists with a rich tool to control energy and charge dynamics via independent tunability of energy levels in the perovskite and organic components. Different applications require distinct electronic dynamics and transport, from separating p and n charge carrier channels between the perovskite and spacer layers, to storing excitons in the triplet states of the organic spacer layer and then re-using them as in thermally activated delayed florescence (TADF) emitters [265], to attaining white-like broad-band dual emission characteristics [266]. Of particular technological interest for many applications is engineering of the directed energy transfer between the perovskite layer and the organic spacer layer. Typically in these LHOP systems, the perovskite layer is the dominant component of band edge absorption [48, 267, 234, 235, 268]. Therefore, a way to demonstrate energy transfer would be to observe triplet emission from the organic spacer layer, which itself could be harnessed for several applications.

Markedly, over the past two decades, select LHOPs have demonstrated the ability to induce energy transfer from perovskite layer exciton states to low energy spin-triplet exciton states in the organic layer [269, 221, 223]. The fundamental differences of the singlet-triplet exciton energy split between the perovskite and organic layers is critical to inducing such energy transfer processes. Within the perovskite layer, strong spin-orbit coupling and a high dielectric constant cause the differences between the singlet and triplet exchange integrals to be small and thus cause a little difference between singlet and triplet states. Consequently, these weakly bound and delocalized S_1 and T_1 Wannier-Mott excitons are hardly distinguishable in optical emission spectra [270, 235, 271]. In contrast, the collinear spin nature and small dielectric screening in the organic layer leads to a large difference in singlet and triplet exchange integrals, resulting in a drastic

lowering of the T_1 excitation energy compared to the S_1 excitation energy [272]. The excitons in the organic layer are strongly bound Frenkel excitons. When the energy of the weakly bound exciton in the perovskite layer aligns with the energy T_1 of the strongly bound exciton in the organic layer, charge transfer from the perovskite to the organic layer may occur [269, 221, 223]. After transfer, the T_1 excitation energy in the organic relaxes to a lower T_1^* energy due to enhanced short-range atomic deformation, thus reaching optimal triplet molecular geometry. Phosphorescent photo-emission is subsequently measured at the T_1^* excitation energy [273]. The choice and alignment of the exciton energy in the perovskite and T_1 in the organic, and the photo-emission energy T_1^* from the organic, are key design parameters leading to different options for LHOP photo-emission materials. Subsequent light emission due to recombination from this triplet exciton is referred to as triplet emission. Electronic structure methods provide a tool to better understand how to choose the various components within LHOPs to achieve desired material properties and optical response.

In this chapter, we detail our first principles survey of organic spacer triplet emission candidates for LHOPs. Each candidate consists of a conjugated chromophore attached to an ethyl-ammonia tail (C_2H_4–NH_2). The lowest spin-triplet excitation levels are calculated on the ground state (S_0) geometries to obtain the triplet energy T_1 and the excited triplet geometry to obtain the triplet energy T_1^* in the ΔSCF framework. The ΔSCF approach has been shown to be a robust framework for predicting the lowest energy triplet state [274, 275, 276, 277]. We also calculate the singlet and triplet excitation energies of several organic spacer candidates in clustered geometries and in the perovskite environment, and predict similar excitation energies compared to the vacuum-relaxed molecular geometries. By means of molecular dynamics simulations for a few LHOP systems, we verify that our initial conclusions hold also under dynamic conditions. We are able to successfully identify promising triplet emission candidates for pairing with known layered perovskite exciton levels to obtain possible triplet emission devices. We consider pairings with perovskite layers of varying layer thickness and halide stoichiometry, and the results herein provide the fundamental concepts for crafting materials with the desired response to various stimuli (light, field, charge injection).

Four classes of organic cation spacer molecules have been explored in this work (see molecular structures in Fig. 6.1). The choices are motivated by organic spacers successfully used in LHOPs experimentally [234, 269, 221, 223, 278] and span diverse forms of conjugation (polycarbocyclic, heterocyclic, and electron rich/poor functionalization): First, five polycarbocyclic compounds with ethylammonium (EA) tails are studied. Amongst them are the basic phenylethylammonium (PEA), used extensively in LHOP synthesis, and the two-ring naphthylethylammonium (NEA), a different isomer of which was investigated by Ema *et al.* and has shown promising application as a triplet emitter [223]. Three-ring anthrylethylammonium (AEA) were explored more seldom, but have promising low singlet and triplet energy states [269]. Four-ring

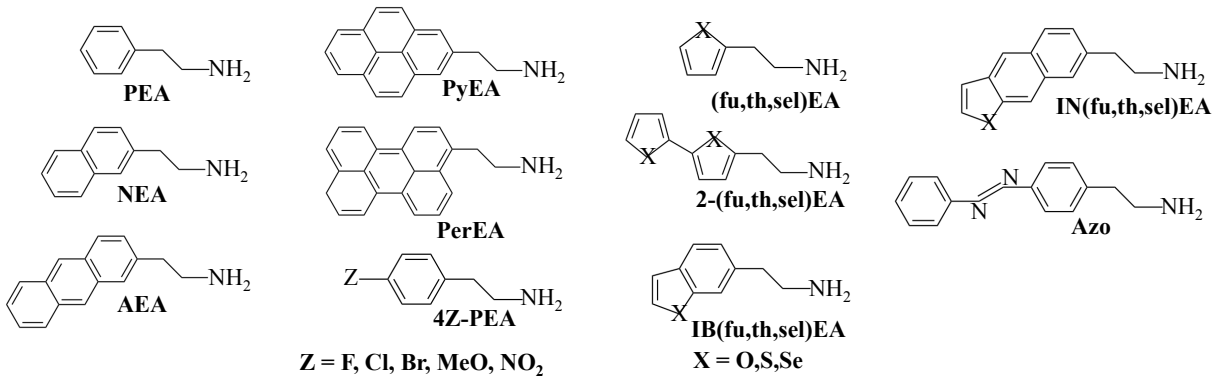

Figure 6.1: Organic spacer candidates considered in this work. Abbreviations include furan (fu), thiophene (th), selenophene (sel), isobenzol (IB), isonaphthyl (IN), 2-2'-bis (2), and Azobenzene ethylammonia (Azo).

pyrene-ethylammonium (PyEA) has only briefly been studied for its triplet emission properties [221], whereas five-ring perylene-ethylammonium (PerEA) was not explored for its photo-emission properties as spacers in LHOP systems [278]. The second class is functionalized PEA with the goal of adding electron-rich or -poor groups and additional linearly conjugated compounds. For electron-rich additions, halides F, Cl, and Br and NO_2 are added to the para position, opposite from the EA bonding site, on the phenyl group. Electron-poor methoxy (MeO) is attached to the same site. The third class are the heterocyclic compounds with carbon and chalcogen based rings. These include the pentacyclic furan-, thiophene-, and selenophene-ethylammonium (XEA, X=fu,th,sel) and their 2,2' linked pentacyclic counterparts (2-XEA, X=fu,th,sel). Further, there are the fused ring compounds isobenzyl(furan,thiophene,selenophene)-ethylammonium (IBXEA, X=fu,th,sel) and isonaphthyl(furan,thiophene,selenophene)-ethylammonium (INXEA, X=fu,th,sel). As a fourth class, we included azobenzene-ethylammonium to examine the effects of extended conjugation featuring the N–N double bond. In this work we refer to the atomic positions of the organic cation layers without the inorganic perovskite lattice, taken from a single unit cell of the experimental LHOP structures, as organic cluster geometries. PEA and NEA [234], and PyOPA [278] clusters are investigated and initialized from atomic structures determined experimentally.

6.2 Computational Methods

First principles simulations for the singlet excitation, triplet excitation, and the energy gap between the highest occupied and lowest unoccupied molecular orbitals (HOMO-LUMO gap) based on ΔSCF and time-dependent density functional theory (TDDFT) are undertaken. Ground state closed- and open-shell DFT calculations of spin singlet and triplet excitations are conducted using the Gaussian code [254]. These use

occupation number and spin orientation constraints to enforce the total spin S to 0 or 1, respectively. As such, the pure spin states are eigen-states of the Kohn-Sham Hamiltonian. Charge densities and single-particle wave functions are calculated in a Gaussian 6-31G* basis set on pruned ultra-fine real space grids with 99,590 real space integration points around the atoms. For heavy Br ions, a LANL2DZ Gaussian basis set is tested and found to be comparable in accuracy to 6-31G* (see Table D.9). For neutral molecules in vacuum, structural relaxations are performed in the singlet configuration with the B3LYP exchange-correlation functional [279].

Triplet excitations are calculated using the ΔSCF approach, due to its predictive power for the S_0 geometry triplet and T_1^* geometry triplet energies. In addition, ΔSCF avoids triplet instability errors that occur in TDDFT [277, 112, 280, 276]: In TDDFT, the difference between singlet and triplet can become larger than the HOMO-LUMO gap [277], forcing the triplet excitation energies to become excessively small or even negative in some cases. Sears *et al.* point to the difference of the exchange contribution between singlet and triplet within a given exchange-correlation functional as the source of this triplet instability. The ΔSCF approach avoids this issue, since it relies on the difference between total Kohn-Sham energies of singlet and triplet states. Lowest-energy singlet excitations are calculated within the TDDFT framework in the frequency domain, from the solution of the Casida equation [281]. TDDFT has been shown to provide reliable singlet excitation energies in organic molecules for charge transfer and optical excitations [282]. While T_1 excitation energies are also calculated by TDDFT (see Tables D.3 through D.12), they underestimate the excitation energies due to the aforementioned triplet instability [112] and are thus not discussed in the main text. Excitation energies are separately calculated using HSE[283], B3LYP [279], and CAM-B3LYP [284] exchange-correlation functionals within ΔSCF and TDDFT. It is found that the introduction of solvent effects of water using the polarization continuum model [285] does not change the predicted S_1 and T_1 energies significantly (see Table D.13). CAM-B3LYP is used to compare the excitation energies of charged (NH_3^+-terminated) and uncharged (NH_2-terminated) species, due to it's improved handling of long-range exchange under charged conditions. The results are comparable within tens of meV (see Tables S8 through S12 in the SI). As tail charge is inconsequential to the chromophore excitation energies and since B3LYP better handles the triplet instability compared to CAM-B3LYP and HSE in extensively conjugated systems, B3LYP results are presented in this letter. However, for natural bonding orbital analysis and to predict changes in natural atomic charges when going from tails with NH_2 to NH_3^+, we use CAM-B3LYP due to its ability to better handle excitations in the charged state. All these simulations are done on geometries relaxed in the vacuum and detailed results are tabulated in Tables D.3 through D.12.

To understand how finite temperature in the perovskite environment effects molecular geometry and

singlet and triplet excitation energies, we run ab-initio molecular dynamics simulations. These are performed using the VASP code [187, 155, 188, 154], the PAW method, and the PBE exchange-correlation functional [68] with Grimme-D2 Van der Waals corrections [286] in the NVT ensemble with a Nose-Hoover thermostat at 300 K. The simulations are initialized with experimental geometries [234] and after thermal equilibrium is reached, molecular geometries at each time step are used for simulating the singlet and triplet excitation energies using the Gaussian code.

6.3 Results and Discussion

The predicted T_1 and T_1^* energies of organic spacer candidates calculated by the ΔSCF approach (see section Methods) span the visible and near-UV energy range (see Table D.1). Our calculations are in agreement with available experimental data. For the most simple conjugated spacer, PEA, we compute T_1 of 4.43 eV and T_1^* of 3.77 eV using B3LYP. Since benzene is identical to the phenyl group in PEA we use it for comparison here, in the absence of PEA experimental data. This is further justified by the good agreement of ΔSCF results for benzene, T_1^*=3.88 eV, and PEA as well as the good agreement between ΔSCF and phosphorescence emission data of 3.40 – 3.60 eV [287]. The lowest phosphorescence emission energy T_1^* is predicted for NEA and PyEA, within 0.2 eV of the experimental NEA-$PbBr_4$ [223] isomer and PyEA-PbI_4 [221]. Furthermore, the ΔSCF model also predicts the T_1 excitation energies of fuEA and thEA to within 100 meV of experimental results [288]. Given such good agreement, the ΔSCF model can be used to make predictions on a number of other organic spacer candidates. We note that while this agreement is encouraging, these data were computed for vacuum-optimized isolated molecules. It is, thus, important to check what influence geometric and thermal effects have on these results, which will be discussed later.

Spin densities of triplet state (defined as the difference between up and down spin densities), and natural bonding orbitals (calculated by the Gaussian code as the eigenfunctions of the density matrix), are visualized for selected organic spacer candidates in Fig. 6.2 to analyze spatial localization of triplet excitations. It is found for all candidate spacers that the spin density is dispersed around the π-conjugated bonds of organic rings or on the non-tail functional group. None of the cases studied here exhibits significant spin density localized on the EA tail. The natural orbitals for the two spins of the triplet configuration are generally localized in the same fashion. This indicates that orbitals delocalized over the conjugated rings or localized on the non-tail functional group are the main participants in triplet excitations, while the non-conjugated tails provide little contributions.

Unlike other conjugated ring spacer candidates considered, the triplet excitation on 4NO_2–PEA is lo-

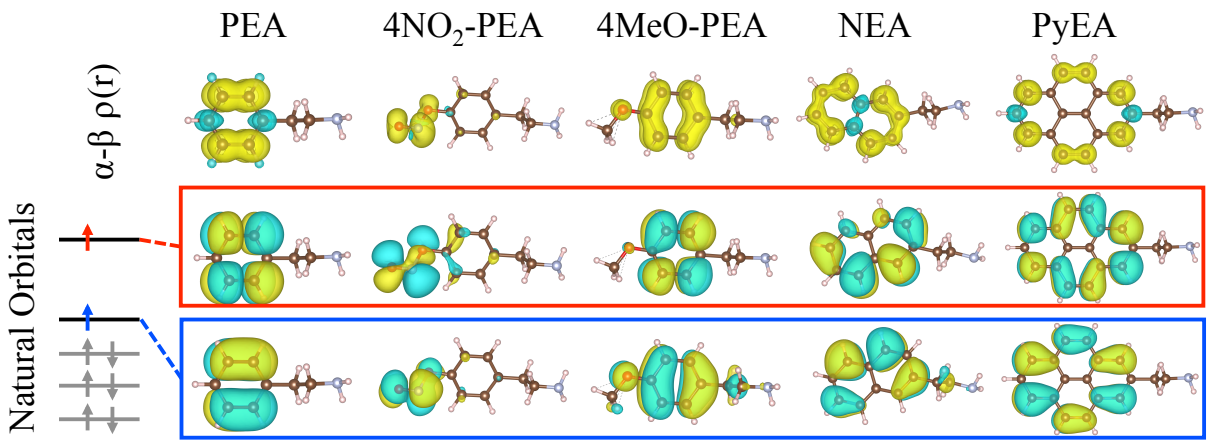

Figure 6.2: Spin density of the triplet state (top row) and natural orbitals of the open shell states in selected organic spacer candidates.

calized near the bonds of the NO_2 as opposed to the conjugated ring. This removal of the excitation from the PEA ring causes $4NO_2$–PEA to exhibit a much lower T_1 energy of 2.29 eV compared to the other functionalized PEA candidates (4.05 – 4.59 eV). This predicted T_1 energy of $4NO_2$–PEA is good agreement with the experimental T_1 energy of NO_2 of 2.35 eV [289]. The origin of the lowered excitation energy is the conjugated bond series of O – N=O. The localization of the spin density, predicted at the density functional level of theory, is validated for this case and confirmed by performing second order Møller-Plesset perturbation theory (MP2) calculations [59, 290]. $4NO_2$–PEA highlights the possibility of conjugated compounds as alternative to ring structures for lowered triplet energy level.

After calculating the excitation energies of organic organic spacer candidates in the gas phase, we move on to predict the excitation energies of clusters of organic spacers without the perovskite layer, in the geometries determined by X-ray diffraction experiments [234, 278]. The geometries and orientation of individual organic molecules in LHOP crystals differ from that of isolated molecules due to interactions with each other and the perovskite layers. Du *et al.* examined PEA, PMA, NEA, and NMA organic spacers in $Pb(I,Br,Cl)_4$ systems and found varying behavior of tail geometries and penetration depth of the ammonium group into the perovskite octahedra layer [234]. One uniform characteristic of the conjugated ring organic spacers in the ⟨100⟩ oriented class of LHOPs is the curling of the tail relative to the geometries of isolated molecules in vacuum. For example, the primary carbon of the naphthyl ring (C_1) in NEA of the EA in the vacuum relaxed geometry is 3.8 Å away from the nitrogen of the EA tail. In the perovskite environment, the tail curls back resulting in the nitrogen moving closer to the carbon rings with a C_1 – N distance of 3.02 Å in NEA–PbI_4 [234]. Smaller conjugated groups like PEA tend to arrange parallel to the perovskite layer while larger chromophores begin to tilt to a perpendicular position. Direct face-to-face π-stacking is not present

in the organic layers considered in this study. Instead, the conjugated rings tend to arrange edge-to-face, a formation that is favorable to template the perovskite network [278]. Given these fundamental differences between perovskite and isolated geometries, it is important to understand how excitation spectra of organic spacer candidates change in the perovskite environment.

To this end, we examine how excitation energies of clusters of organic candidates PEA, NEA, and PyOPA in their experimental geometries differ compared to their isolated counterparts calculated in the gas-phase. These organic compounds are chosen by available experimental atomic structures of layered perovskites in which they are the spacer. While PEA is unlikely to be a triplet emission candidate, NEA and PyEA (or PyOPA) show great potential due to their low T_1 energies. PEA and NEA layer geometries of four and eight molecules, respectively, are taken from Ref. [234] and pyrene-based organic-layer geometries with OPA tails are taken from Ref. [278]. First, no relaxations are performed on C, N, and O atoms, but since H atoms are not present in the XRD data, their positions are relaxed around the experimentally known atomic positions. Below we also test the effects of tail geometry by relaxing O, N, and C atoms, while keeping the tails fixed. We also note that one H atom is omitted from each NH_3^+ group to simulate neutral layers. This does not introduce detrimental effects on the geometries, since the tails are kept fixed.

The T_1 energies calculated via the ΔSCF method using the B3LYP XC functional for the organic-spacer layer geometry without the perovskite layer, taken from experimental data of PEA ($T_1 = 4.0$ eV) and PyOPA ($T_1 = 2.35$ eV), are predicted within 0.5 eV of the vacuum relaxed molecules of PEA ($T_1 = 4.43$ eV) and PyEA ($T_1 = 2.43$ eV). In contrast, the NEA experimental organic-layer geometry ($T_1 = 2.26$ eV) is predicted to have a ≈ 0.96 eV decrease in excitation energies compared to the isolated NEA molecule relaxed in vacuum ($T_1 = 3.14$ eV). The source of this discrepancy lies with the molecular geometry differences where the experimental C – C bond lengths on the conjugated ring vary between 1.29 and 1.51 Å, whereas the isolated molecule has a smaller variation of 1.36 – 1.42 Å. It is worth noting that X-ray diffraction measurements do not pinpoint well the positions of light atoms such as carbon [291], and therefore some variation in experimentally measured C – C bond lengths and atomic positions is to be expected. Finite temperature can induce additional variation in the molecular structure of spacers and, consequently, spacer excitation energies. Other crystallographic measurements of NEA and NMA (naphthal-methylammonium) structures have observed a C – C bond length range in the naphthal ring between 1.34 – 1.43 Å in NEA-$CuCl_4$ [292] and NMA-SnI_4 [293]. This is very similar to the range found here for the isolated structures. Nonetheless it needs to be clarified (i) how the curled tail geometry influences the conjugated rings and (ii) how the periodic potential of the perovskite and other conjugated rings affects the variance of the chromophore geometry.

To further test the effects of tail geometry on the predicted T_1 energies of organic candidates, a second

set of calculations are performed where tail geometries are kept fixed at experimental geometries [234, 278] while the conjugated rings are optimized. This test serves to determine if the bent tail significantly changes the orbital nature on the conjugated ring, thus changing the excitation spectrum. The resulting ring-relaxed B3LYP ΔSCF T_1 energies for the PEA cluster (T_1 = 4.42 eV), NEA cluster (T_1 = 3.07 eV), and PyOPA cluster (T_1 = 2.35 eV) are predicted within 0.15 eV compared to the respective energies computed for isolated geometries. We find that tail curling alone does not strongly affect the excitation spectrum of these molecules and does not change the spin density of the molecule, which remains localized on the ring (see Fig. 6.2). Therefore, differences in the excitation energies calculated for isolated geometries and experimental structures, must originate from distinct conjugated ring geometries. This might be explained by the difficulties of pinpointing the precise position of light atoms, such as carbon, in XRD when heavy atoms, such as lead, are present in the system.

Using ab-initio molecular dynamics (AIMD) simulations we further explore how the excitation energies of the organic spacer embedded in the perovskite layers, at finite temperature, differ from those relaxed in a vacuum. To this end, atomic geometries for PEA-PbI_4 and NEA-PbI_4 are initialized from atomic positions determined by XRD measurements by Du *et al.* [234] Prior to performing AIMD, we calculate the S_1 and T_1 energies of each unique crystalline organic PEA and NEA in these experimental geometries using TDDFT for S_1 and ΔSCF for T_1 excitation energies. We find that the calculated T_1 energy of PEA remains in a narrow range between 4.43 eV and 4.46 eV for the individual spacer molecule geometries in the unit cell taken from the experimental XRD data. In contrast, the calculated T_1 energies of the NEA molecules vary between 2.23 – 3.26 eV, warranting further investigation by AIMD as discussed next.

AIMD results demonstrate that the excitation energies of PEA and NEA in the PbI_4 LHOP environment experience a broadening as a consequence of thermal fluctuations in the molecular geometries. Table D.2 lists the explicit results and Fig. 6.3 shows the distributions of S_1 and T_1 excitation energies calculated across post-equilibrium molecular conformations from AIMD. The average excitation energies for the different post-equilibration MD geometries are noticeably lower, compared to their isolated vacuum-relaxed counterparts. This results from a combination of longer average bond lengths in MD compared to XRD as well as complex torsion and bending in the NEA and PEA. The standard deviation in excitation energies lay between 0.11 and 0.20 eV, with the highest attributed to the T_1 excitation in PEA. The C–C bond lengths show high variability in PEA and NEA. For PEA, the simulated C–C variation exceeds the C–C bond length variations observed in XRD (1.39 – 1.41 Å). Alternatively, the variation in NEA bond length in the AIMD simulations remains lower compared to the XRD results. This explains why the T_1 energies calculated in XRD PEA conformation fall within a narrow range whereas geometries sampled from AIMD show a higher variation.

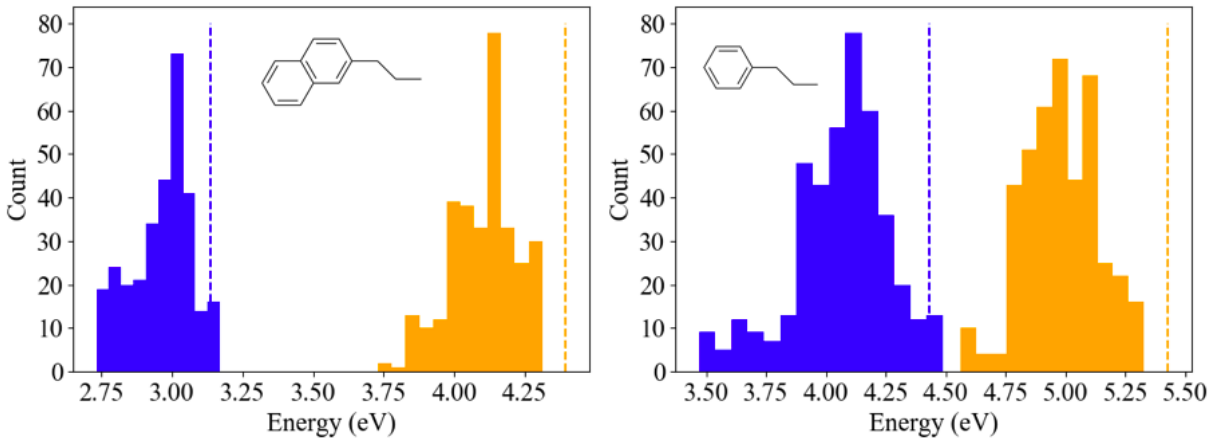

Figure 6.3: Histograms of ΔSCF T_1 (blue) and TDDFT S_1 (orange) energies calculated on MD molecular conformations of NEA in NEA-PbI_4 (left) and PEA in PEA-PbI_4 (right). The vertical dashed line indicates the vacuum-relaxed result for S_1 (orange) and T_1 (blue).

Overall, the findings herein demonstrate the importance of finite temperature dynamics on the broadening of S_1 and T_1 excitation energies of organic spacer candidates in LHOPs. As good agreement is observed between $\bar{T}_1$ obtained from AIMD and T_1 calculated from vacuum-relaxed simulations, the latter results can be used for first principles materials design of LHOPs for applications requiring specific alignments of electronic features.

Thus, from our analysis of the calculated excitation energies we identify multiple organic spacer candidates with low-lying triplet states in Pb-based LHOPs with a variety of halides and number of perovskite layers (see Table 6.1 and Fig. 6.4). The first major design consideration is the relative T_1 excitation energy of the organic spacer to the $n = 1$ exciton energy of the perovskite (E_x). When T_1 is less than but close to E_x, strongly-bound exciton energy transfer can be initiated from the perovskite to the organic. Once this transfer occurs, the organic spacer relaxes in the excited state, leading to a new T_1^* emission energy which is the lowest energy phosphorescence peak. In the following, energy pairings will be given in E_x:T_1:T_1^* notation. Starting with single-layer $PbCl_4$, the two optimal pairings are thEA-$PbCl_4$ and selEA-$PbCl_4$ with energy alignments of 3.7:3.69:3.02 and 3.7:3.57:2.93 eV, respectively. These LHOPs could produce a violet or indigo phosphorescence spectrum with a lowest emission wave length of ≈400 nm. As the functionalized PEA T_1 tends to be higher than 3.7 eV, thEA and selEA seem to be the only viable options for pairing with $n = 1$ $PbCl_4$ found in our work.

For $n = 1$ $PbBr_4$ perovskite layers, we also identify two promising organic spacer pairings: The optimal pairing is NEA-$PbBr_4$, with an energy alignment of 3.20:3.14:2.67 eV. This first principles prediction is supported by experimental evidence of highly efficient energy transfer from $PbBr_4$ to the triplet state of a NEA

Table 6.1: Suggested pairings of organic spacers with perovskite layers of varying halide and layer compositions. The energy alignment shows the perovskite exciton level E_x, the organic triplet level in the ground state geometry T_1 (charge transfer energy), and the organic triplet level in the excited state geometry T_1^* (triplet emission energy), i.e. E_x:T_1:T_1^* (in eV).

Perovskite	Org. Spacer	Energy Alignment (eV)
PbI_4 (n=1)	PyEA	2.5:2.43:2.10
	AEA	2.5:2.17:1.75
	IBselEA	2.5:2.17:1.77
	$4NO_2$-PEA	2.5:2.29:0.68
Pb_2I_7 (n=2)	PerEA	2.15:1.80:1.50
	Azo	2.15:1.95:1.25
$PbBr_4$ (n=1)	NEA	3.20:3.14:2.67
	2fuEA	3.20:3.14:2.40
$PbCl_4$ (n=1)	thEA	3.70:3.69:3.02
	selEA	3.70:3.57:2.93

isomer by Ema *et al.* [223] They observe this process in a variety of naphthyl-based PbI_4 systems, encouraging further studies of these. Another possible pairing is 2-fuEA-$PbBr_4$, which has an energy alignment of 3.20:2.91:2.40 eV and could exhibit triplet emission at 516 nm, corresponding to a green light.

The highest number of promising pairings of organic spacers for triplet emission occurs with $n = 1$ PbI_4 and $n = 2$ Pb_2I_7. The most obvious pairing for $n = 1$ PbI_4 is PyEA-PbI_4 with an energy alignment of 2.5:2.43:2.10 eV. This material would show triplet emission of yellow/orange light, which has been experimentally verified by Braun *et al.* [221] Another possibility is AEA-PbI_4 for an alignment of 2.5:2.17:1.75 eV, leading to red light triplet emission. Interestingly, AEA spacers in layered perovskites have rarely been explored for their light-emitting properties, despite promising exciton energy level alignment. A similar energy alignment of 2.5:2.17:1.77 eV and potential red light triplet emission can be achieved by the pairing IBselEA-PbI_4. Finally, $4NO_2$-PEA is predicted to have an alignment with $n = 1$ PbI_4 of 2.5:2.29:0.68 eV, indicating potential infrared triplet emission in $4NO_2$-PEA-PbI_4. As previously discussed, a low T_1^* in $4NO_2$-PEA is attributed to the localization of the triplet excitation on the NO_2 functional group (Fig. 6.2).

Two-layer $n = 2$ Pb_2I_7 is also predicted to have spacer candidates for deep red triplet emission: The first two are PerEA and AzEA, with alignments of 2.15:1.80:1.50 eV and 2.15:2.08:1.75 eV, respectively. The pairing with PerEA should be given careful attention, given the recent inclusion of PerEA in layered perovskite by Passarelli *et al.* [278] Finally, Azo can be paired with $n = 2$ Pb_2I_7 for an alignment of 2:15:1.95:1.25 eV, giving yet another spacer for possible infrared triplet emission.

In addition to these, multiple of the considered compounds have non-ideal alignment with the known perovskite layer absorption edges, but should not be entirely discounted. Compounds with T_1 energies between 2.5 and 2.8 eV are mismatched with $n = 1$ PbI_4 and are unlikely to induce energy transfer from $n = 1$ $PbBr_4$, including 2-(th,sel)EA and IN(fu,th,sel)EA. However, little is currently known about the

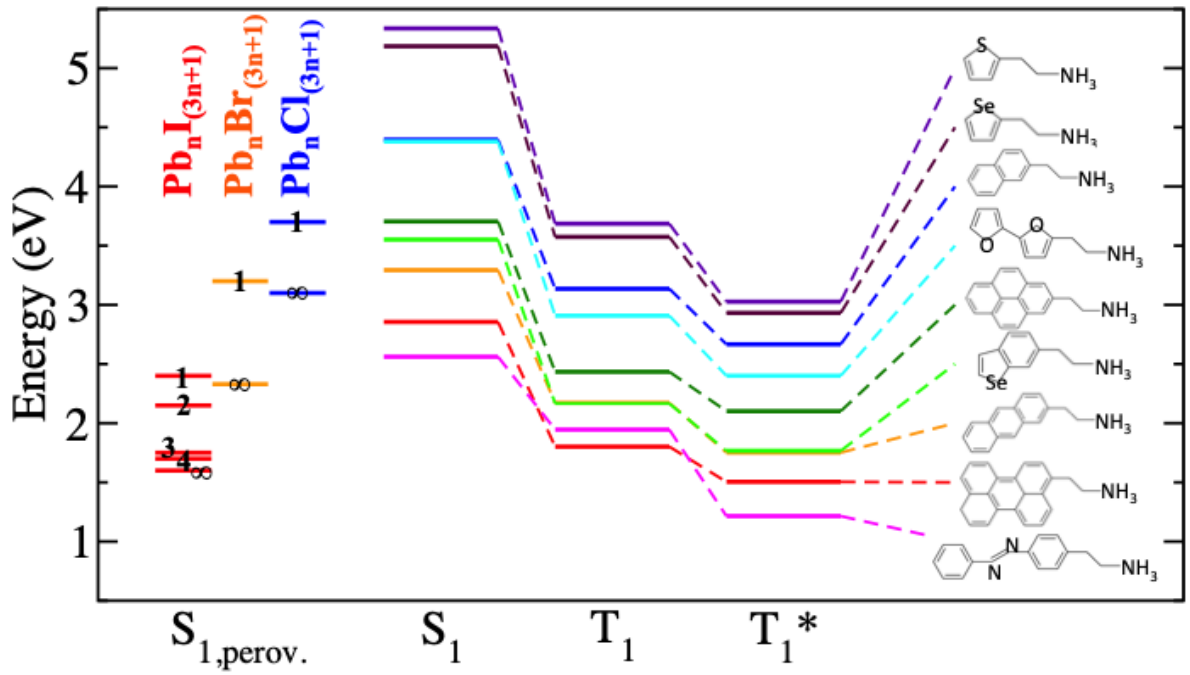

Figure 6.4: Alignment between perovskite S_1 exciton levels, organic triplet T_1 excitation energies, and organic T_1^* excited state geometry emission energies for a select subset of examined organic spacers.

perovskite exciton levels of $n = 2$ Pb_2Br_7 and it is possible that alignment is better in this case. Given experimental evidence from $n = 2$ Pb_2I_7 [11], it is likely that $n = 2$ Pb_2Br_7 would demonstrate a E_x level between 3.2 eV for $n = 1$ $PbBr_4$ and 2.4 eV for $n = \infty$ $PbBr_3$. Thus, some of the aforementioned non-ideal compounds for pairing with PbI_4 or $PbBr_4$ could provide an ideal pairing with $n = 2$ Pb_2Br_7. Experimental observation of E_x from $n = 2$ Pb_2Br_7 would be required to make a definite claim. In contrast, the single ring compounds and {Br, Cl, F, MeO}-functionalized PEA all have high T_1 compared to E_x of $n = 1$ $PbCl_4$, and, therefore, are highly unlikely to induce excitation transfer.

6.4 Conclusions

In conclusion, we use electronic-structure calculations to predict multiple viable pairings of organic spacer candidates with single perovskite layers, to facilitate design of LHOPs with desired energy level alignments. These pairings may achieve potential triplet emission across the visible spectral range, offering potential solutions for tuned light emission applications. We carefully verified that our predictions remain consistent even when tail geometries are altered and organic candidates are placed into their clustered LHOP geometries. Finally, finite temperature dynamics of organic spacers in the perovskite crystal, as simulated by ab-initio molecular dynamics, result in a broadening of excitation energies slightly below the results obtained for iso-

lated geometries. Altogether our computational predictions demonstrate that electronic structure of LHOPs paired with conjugated organic spacers is extremely tunable, which suggests broad variability and control over dynamics of energy and charge carriers. In particular, light-emitting applications involving LHOPs is a promising field of research and should be further investigated to discover potential next generation, wave length tuned, highly efficient light sources.

CHAPTER 7

CONCLUSION AND FUTURE OUTLOOK

In this doctoral thesis, I present my work on modeling the optical response of hybrid organic-inorganic perovskites and their layered variant from first principles. I have employed and developed state-of-the-art computational techniques based on density functional theory and many-body perturbation theory to predict and understand the nature of the electron-hole interaction in hybrid organic-inorganic perovskites. Furthermore, I have used these prediction to propose novel material stoichiometry in layered hybrid perovskite to design wavelength-tuned triplet optical emission materials.

The first half of my thesis is focused on the simulation of the electron-hole interaction in $MAPbI_3$ while accounting for electron-hole Coulomb screening effects beyond the standard static electronic screening. The conclusions of chapter 3 found that moderate to high concentrations of free-carriers from shallow intrinsic or extrinsic defects lower the exciton binding energies while maintains high absorption response at the band edge. We used the DFT+GW+BSE class of computational approaches to determine the optical excitation energies and imaginary dielectric functions of cubic $MAPbI_3$. We found that, even though free-carrier screening reduces the strength of the electron-hole Coulomb interaction, the balance between Pauli-blocking and band gap re-normalization maintains a high amplitude absorption onset around the intrinsic band gap. Binding energy in $MAPbI_3$ is reduced from 32 meV intrinsic to less than 2 meV at high concentrations over 10^{19} cm^{-3}. We additionally predict the formation of a Mahan exciton at free-carrier concentrations over 10^{17} cm^{-3}. The presence of a Mahan exciton can help maintain a high absorption edge amplitude even at high free-carrier concentrations. This study succeeds in two aspects of materials prediction and design. The first is that we predict that under experimentally verified ranges of free-carrier concentrations, the exciton binding energy ranges between 5 meV and 32 meV, matching well with the variable measurements of exciton binding energy in MAPbI3 made by experimental researchers. The second is that light doping can be used to reduce exciton binding energy, thus increasing photo-conversion efficiency, and to increase optical absorption at the band edge.

In chapter 4, polar lattice screening was found to have a strong influence over the optical response and exciton binding energies of polar semiconductors AlN, GaN, and $MAPbI_3$ while not heavily influencing polar

compounds like MgO and AlN. The Fan-Migdal contribution is added to the screened Coulomb interaction to include dynamical lattice screening of the electron-hole Coulomb interaction by the LO phonon modes. Shindo's approximation allows us to write an excitonic Hamiltonian where one can solve implicitly for the dynamical excitation energies on a frequency grid. For polar compounds with a high exciton binding energy to LO phonon frequency ratio (NaCl and MgO), lattice screening is found to have little influence on the exciton binding energy and optical absorption spectrum. In polar compounds with a moderate to low exciton binding energy to LO phonon frequency ratio (GaN, AlN), the influence of polar lattice screening significantly reduces the exciton binding energies and heavily reduces the the amplitudes of the optical absorption spectrum edges. Thus, we confirm the postulates made by Haken and Shindo that dynamical lattice screening has a prominent effect on exciton binding energy when the longitudinal optical phonon frequency is comparable to or greater than the exciton binding energy. In particular, we show how including dynamical lattice screening improves the previous prediction for the exciton binding energy in GaN of 56 meV to 29 meV, in excellent agreement with experimental measurements of 23 meV. In $MAPbI_3$, the binding energy is reduced from 31.9 meV to between 20 and 24 meV, based on the LO phonon frequency ranging from between 14 and 16 meV and the low-frequency dielectric constant ranging from 25-30. This significant drop in binding energy under dynamical lattice screening, coupled with possible reduced screening from free-carriers, explains the low and varied binding energies observed in experimental studies.

The second half of this thesis moves on to predicting the optical response of layered hybrid organic-inorganic perovskite systems which display a higher structural, electronic, and optical response diversity compared to their non-layered hybrid organic-inorganic perovskite counterparts. In chapter 5, we resolve the optical response of six LHOP materials - API-PbX_4 and PEA_2-PbX_4 with X=(I,Br,Cl) - into contributions from electron-hole excitation between and within orgnic and inorganic layers to predict if single conjugated ring organic spacers can achieve layer-separated electrons and holes under optical excitation. For the single conjugated ring compounds used as organic spacers (API and PEA), the band edge excitation remains confined to the perovskite layer whereas organic-organic excitation occurs above 5 eV. We confirm that cross-layer excitation occurs where the electron and hole can be separated along different ion channels at excitation energies above the band gap. In PEA_2-$PbCl_4$, these excitations occur above but very close to the band edge, suggesting that $PbCl_4$ perovskite layers with a more highly conjugated organic spacer could produce band-edge separation of the electron-hole pair. We use the DFT+HSE+BSE formalism to determine exciton binding energies in API-PbX_4. The exciton binding energies start at 218 for X=I, in excellent agreement with previous experiments, and reach 638 meV for X=Cl. Our findings herein confirm that cross-layer excitation is possible in LHOPs with conjugated organic layers, potentially moving the field

towards realizing layer-separated electron-hole generation in perovskite solar cells.

Finally, we examine how organic spacers can be selected to achieve possible triplet light emission by exciton transfer from the perovskite to the organic spacer. We perform first principles calculations based on the ΔSCF and linear-response time-dependent density functional theory (LR-TDDFT) to predict the first singlet and triplet excitation energies and relaxed triplet emission energies of 25 organic spacer candidates. By comparing the energy level alignments with known absorption edge energies of perovskite layers, we recommend perovskite-organic pairings to achieve triplet light emission at various wavelengths across the visible spectrum. We additionally perform ab-initio molecular dynamics simulations of two perovskite compounds - PEA_2PbI_4 and NEA_2PbI_4 - to determine how the geometries of the organic spacers change with temperature. By simulating the excitation energies of each molecular configuration, we determine a significant thermally induced optical broadening of the first singlet and triplet energies at room temperature of about 0.5 eV.

The field of computational materials science from first principles is ever evolving to adapt more advanced methods and algorithms on larger computational resources. Moving forward, higher levels of theory will be able to be applied to the problems investigated in this thesis. One clear place for improvement is moving away from model functions to describe the dielectric screening in the screened Coulomb interaction and more towards explicit dielectric tensors. The model screening function by Cappellini *et al.* does not account for (i) local field effects and (ii) dielectric layering. The explicit dielectric tensor with all matrix elements calculated at at the *GW* level of theory would include these effects seamlessly into the Bethe-Salpeter equation. While this remains intractable on dense **k**-point grids with current computing capabilities, it is already being applied to coarse **k**-point grids on low-dimensional systems with subsequent interpolation of the excitonic Hamiltonian elements [294]. It will soon be possible to perform explicit calculations of the electron(hole)-phonon vertices in Eq. 2.74 by Wannier-interpolation for dynamical lattice screening of the electron-hole interaction. Such interpolation efforts are currently well underway [105]. Including the explicit vertices would allow one to move away from using models such as the general or simple Fröhlich vertex and provide a more detailed and precise treating of lattice polarization influence on exciton binding energy.

The program of computational materials science is to provide predictions and answers for novel materials design. I aspire to help bring sustainable energy solutions closer to realization in applying these methods to understanding fundamentally how solar cell and light-emitting materials function at the atomic and electronic scale. The overarching goal of all materials science and engineering is to provide technological solutions for a healthier and happier world for all. I hope I have contributed some small part in this effort by continuing to research and understand how materials can be harnessed for efficient and clean energy.

APPENDIX A

FREE-CARRIER EFFECTS ON OPTICAL RESPONSE OF $MAPbI_3$

The use of a highly converged **k**-point sampling is critical to achieving accurate exciton binding energy results. A plot of k-point convergence of exciton binding energies can be seen in Fig. A.1. Convergence is achieved at a hybrid **k**-point grid of 5:2:32.5, see Ref. [85] for details of the nomenclature. To gain a deeper understanding of the electronic structure of $MAPbI_3$, we resolved the band structure according to atomic-orbital projections for each type of ion (Pb, I, or MA). Figure A.2 demonstrates this for the cubic phase. It is found that the valence and conduction band frontiers are attributed mostly to I_{5p}+I_{6s} and Pb_{6p}, respectively. The states attributed to the organic MA cations only occur lower than 5 eV below the valence band maximum and 2.5 eV above the conduction band minimum. Figure A.3 shows the single-particle optical response of cubic $MAPbI_3$ resolved by transitions between individual electronic states. An important conclusion found herein is that a vast majority of the optical response between the absorption onset and 3 eV is attributed to transitions between the valence band maximum and conduction band minimum. Figure A.4 compares the single-particle optical spectrum of tetragonal $MAPbI_3$ calculated at the PBE+Δ_{GW_0}+SOC level of theory in this study to the G_0W_0+SOC results from Ref. [145]. The agreement between the spectra further verifies that the electronic structure found in this study serves as a good basis for optical response calculations. The values of the BMS at increasing free-electron concentrations n_c are plotted for each phase in Fig. A.5. Though the curves are similar, the difference in effective masses of the conduction band causes the BMS in the orthorhombic phase (lowest effective mass) to rise more quickly as a function of n_c compared to tetragonal and cubic (lowest effective mass) phases.

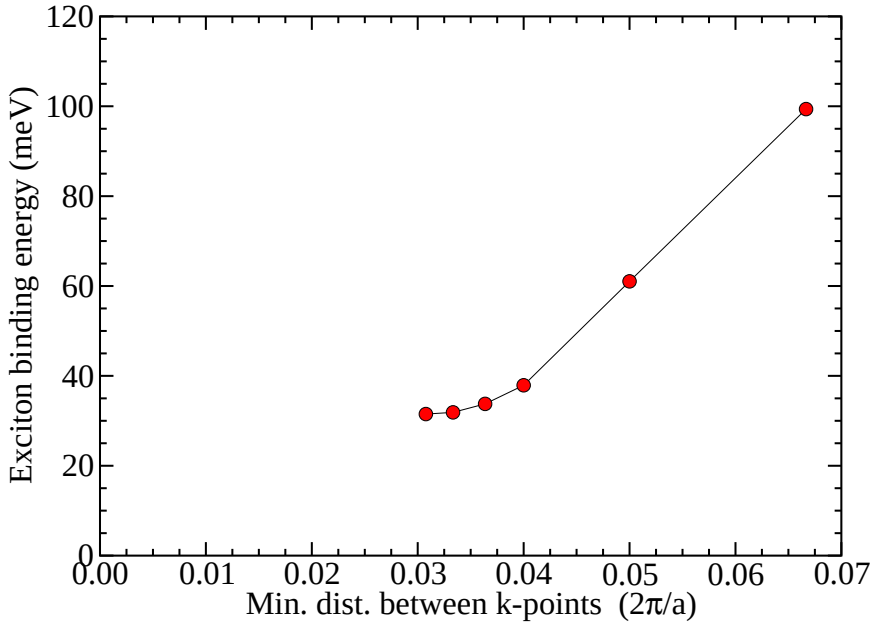

Figure A.1: Convergence of exciton binding energy with respect to **k**-point grid density. 5:2:15, 5:2:20, 5:20:25, 5:2:27, 5:5:2:30, and 5:2:32.5 type hybrid meshes are used to sample Brillouin zone, ascending in order of **k**-point sampling density.

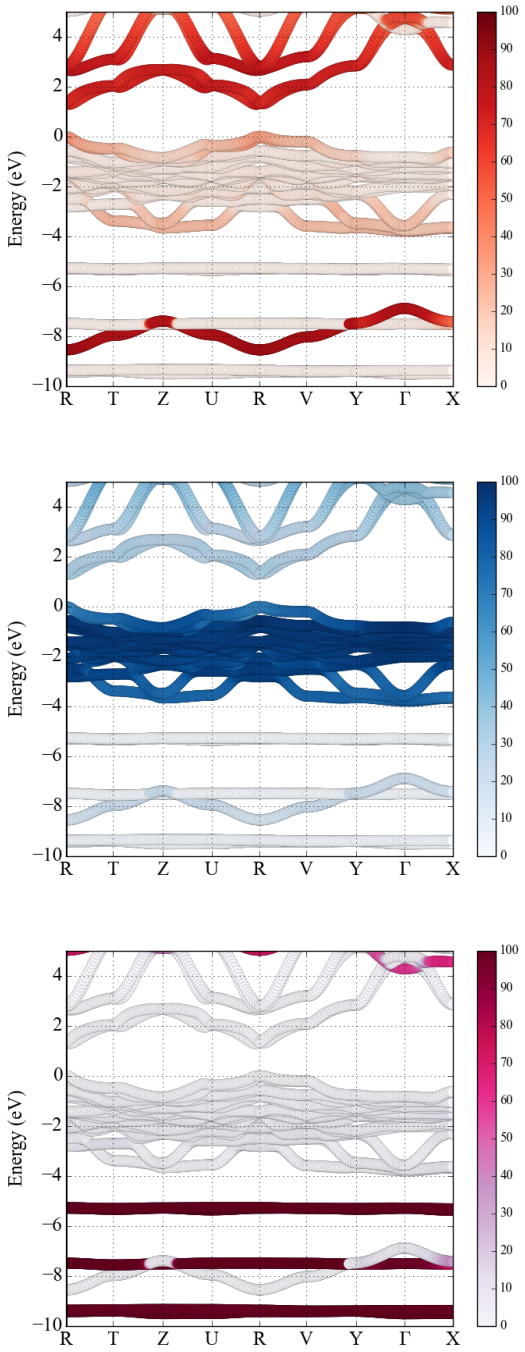

Figure A.2: Band structure of C $MAPbI_3$, resolved along atomic orbital contributions of Pb (orange), I (blue), and CH_3NH_3 (magenta). The color intensity indicates the percent atomic contribution in accordance with the provided color bars.

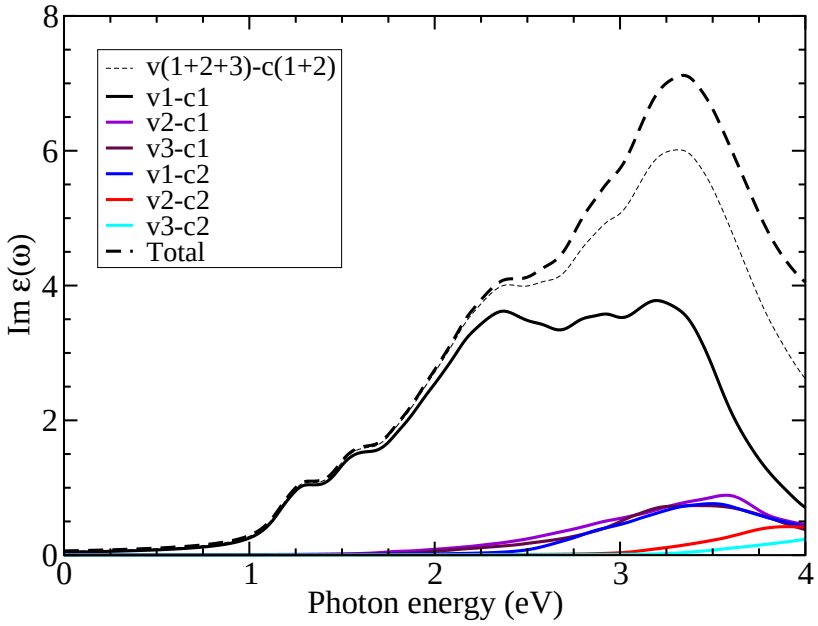

Figure A.3: The imaginary dielectric function of cubic $MAPbI_3$ resolved by band-pair excitation. v indicates valence bands and c indicates conduction bands. Indexing for valence bands starts at the VBM and indices increase as energy decreases. Indexing for conduction bands starts at the CBM and increases in energy. A single index covers a spin-split band pair.

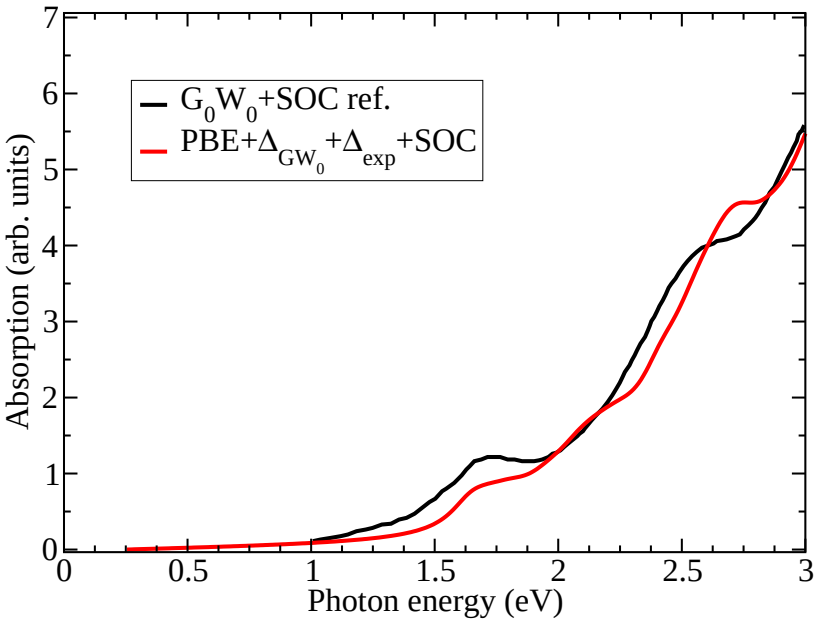

Figure A.4: Comparison between the optical absorption spectrum of tetragonal $MAPbI_3$ calculated using PBE+Δ_{GW_0}+SOC, shifted further to the experimental gap of 1.6 eV, and $7 \times 7 \times 7$ **k** points with a small random shift (red curve) and the G_0W_0+SOC results from Ref. [145] (black curve), on a $4 \times 4 \times 4$ **k**-point grid.

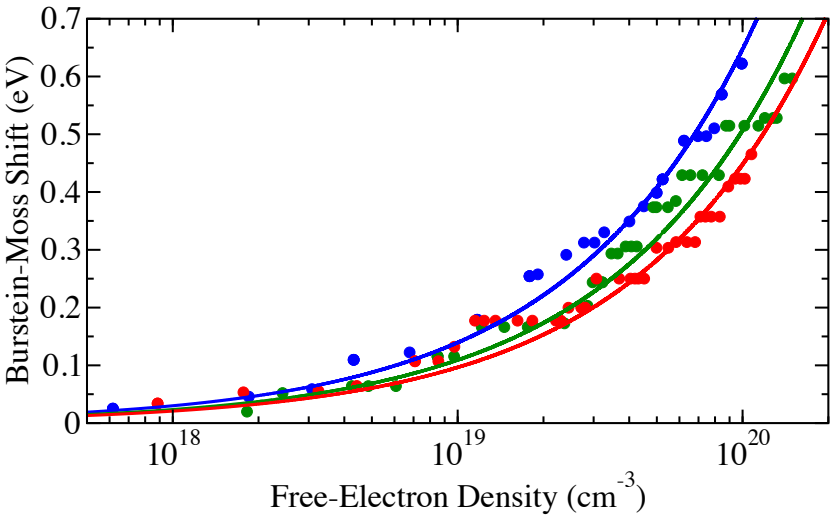

Figure A.5: The calculated Burstein-Moss shifts (circles) of O (blue), T (green) and C (red) as a function of free electron density. The associated solid lines are functional fits of the form $E_{\mathrm{BMS}}=An_c^{3/2}$. Dense, hybrid 5:2:15, 5:2:15, and 5:2:32.5 **k**-point grids were used for O, T, and C phase, respectively (see Ref. [150] for nomenclature).

APPENDIX B

LATTICE SCREENING IN POLAR SOLIDS

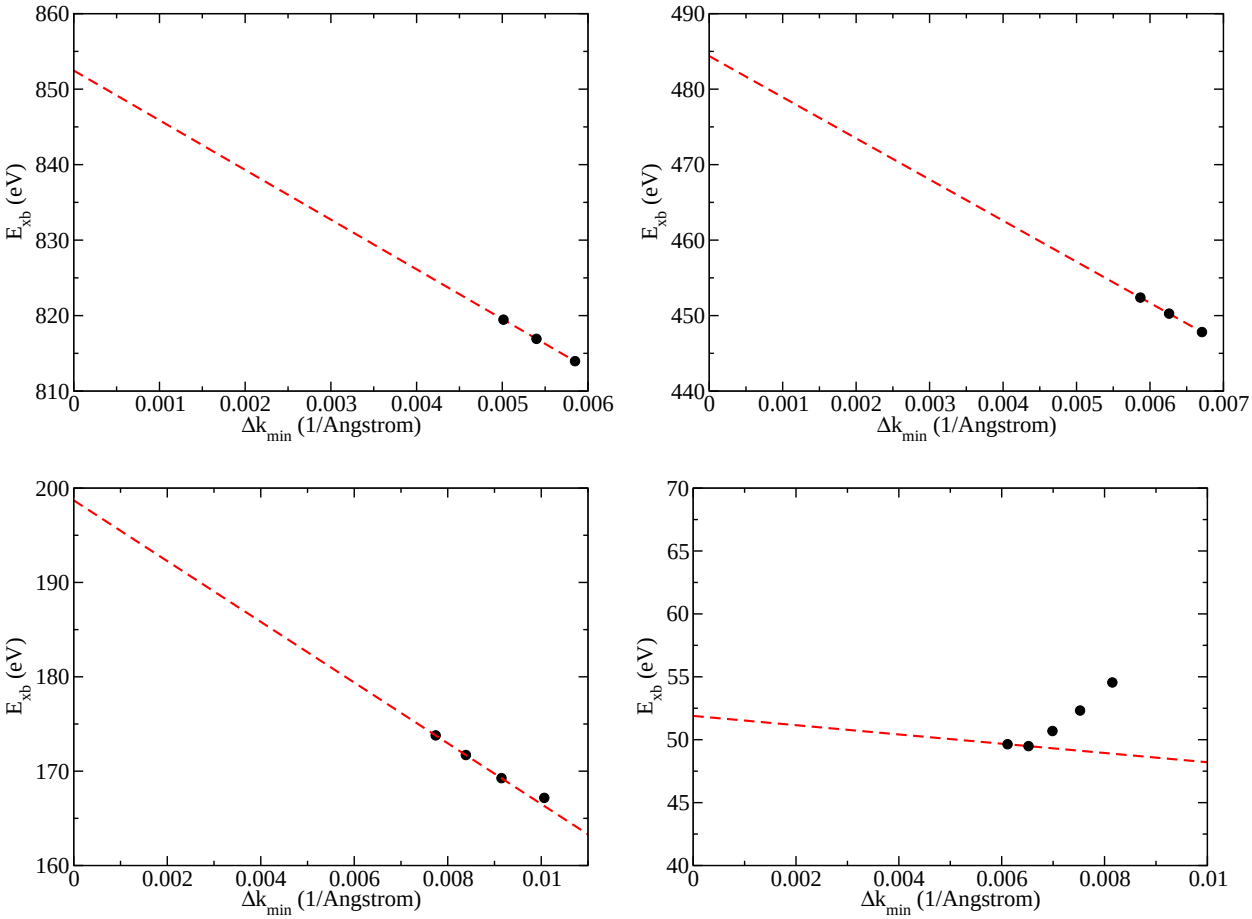

Figure B.1: Convergence of exciton binding energies by zero-point extrapolation of (top left) NaCl, (top right) MgO, (bottom left) AlN, and (bottom right) GaN. Black circles indicate explicitly calculated exciton binding energies at a given **k**-point density and the red-dashed lines are the extrapolation of the binding energies by linear fit to determine the exciton binding energy in the high **k**-point density limit. Calculations of the extrapolation functions are performed with static electronic screening of the electron-hole Coulomb interaction.

APPENDIX C

ELECTRON-HOLE EXCITATIONS IN LAYERED PEROVSKITES

Table C.1 and C.2 displays the detailed structural data of the relaxed API-PbX_4 and literature values for PEA_2-PbX_4.

Table C.1: Lattice geometries of $\langle 110 \rangle$ API-PbX_4 and $\langle 100 \rangle$ PEA_2-PbX_4 compounds. Lattice constants a, b, c, and Pb – X bond lengths are in Å, cell volumes V in Å^3. Experimental reference values are shown for API-$PbBr_4$.

	a (Å)	b (Å)	c (Å)	V (Å^3)	α	β	γ	bond len.
API-PbI_4	6.55	28.47	8.91	1654.79	90.0	94.9	90.0	3.01 – 3.38
API-$PbBr_4$	6.19	27.67	8.38	1429.37	90.0	95.1	90.0	2.81 – 3.22
API-$PbBr_4$ (Exp.) [227]	6.16	27.63	8.45	1432.85	90.0	95.7	90.0	2.79 – 3.26
API-$PbCl_4$	5.95	27.13	8.04	1291.59	90.0	95.3	90.0	2.65 – 3.14
PEA_2-PbI_4 (Exp.) [242]	8.79	9.39	14.64	1190.52	90.0	100.1	90.0	3.18 – 3.32
PEA_2-$PbBr_4$ (Exp.) [243]	11.62	11.63	17.58	2250.52	99.6	105.7	90.0	2.99 – 3.01
PEA_2-$PbCl_4$ (Exp.) [244]	11.15	11.22	17.70	2112.1	99.1	104.6	90.0	2.76 – 2.91

Table C.2: Lattice geometries of $\langle 110 \rangle$ API-PbX_4 and $\langle 100 \rangle$ PEA_2-PbX_4 compounds continued. Bond angles η are in degrees. Experimental reference values are shown for API-$PbBr_4$.

API-PbI_4	33.8, 53.9	10.2, 10.5
API-$PbBr_4$	33.7, 52.3	9.7, 10.12
API-$PbBr_4$ (Exp.) [227]	32.9, 53.6	8.5, 8.9
API-$PbCl_4$	33.7, 51.4	9.8, 9.9
PEA_2-PbI_4 (Exp.) [242]	2.55	12.2, 12.4
PEA_2-$PbBr_4$ (Exp.) [243]	1.8, 1.9	14.0,14.5
PEA_2-$PbCl_4$ (Exp.) [244]	2.2, 2.7	13.6, 14.3

Table C.3 displays the calculated diagonal and averaged components of the high-frequency dielectric tensor as calculated by density functional perturbation theory.

Table C.3: The static high-frequency dielectric constants for each material, calculated using the PBE XC functional without the inclusion of spin-orbit coupling from density functional perturbation theory. Reference values are included for 3D HOPs.

	API-PbI_4	API-$PbBr_4$	API-$PbCl_4$
$\varepsilon^{\infty}_{xx}$	4.51	3.90	3.51
$\varepsilon^{\infty}_{yy}$	4.76	4.14	3.77
$\varepsilon^{\infty}_{zz}$	4.45	3.79	3.47
$\varepsilon^{\infty}_{\text{ave}}$	4.57	3.94	3.57
	$MAPbI_3$	$MAPbBr_3$	$MAPbCl_3$
$\epsilon^{\infty}_{\text{ave}}$ (theory)[50]	6.83	5.15	4.12

APPENDIX D

TRIPLET EMISSION IN LHOPs BY ORGANIC SPACER SUBSTITUTION

D.1 Notes on comparison to experiments

In Table D.1, the experimental comparisons for triplet energies for PEA and PerEA (T_1^*) and fuEA and thEA (T_1) are made to studies that examine just the optical emission from the aromatic groups without the EA tails. This is primarily due to the lack of emission data for the exact compounds available for comparison. Nonetheless, the comparisons for T_1 and T_1^* are in very good agreement. Our spin charge density and natural bonding orbital analysis shows that the excitations are localized to the aromatic rings, further justifying these comparisons.

D.2 Tabulated calculated data

Table D.1: Triplet excittion (T_1) and emission (T_1^*) energies calculated with the ΔSCF method and the B3LYP XC functional. Comparison to experiment is given in the right two columns. The † symbol indicates comparisons to experiments that study only the aromatic group without the EA tail.

Spacer	T_1	T_1^*	exp. T_1	exp. T_1^*
PEA	4.43	3.77		3.40 – 3.60† [287]
NEA	3.14	2.68		2.30 – 2.50 [223],2.50 – 2.60 [269]
AEA	2.17	1.75		1.50-1.85† [269]1.80 [295]
PyEA	2.43	2.10		1.80 – 2.00 [221]
PerEA	1.80	1.50		1.56† [296]
AzEA	2.077	1.75		
4Br-PEA	4.58	3.20		
4Cl-PEA	4.59	3.36		
4F-PEA	4.49	3.57		
4MeO-PEA	4.05	4.06		
$4NO_2$PEA	2.29	0.683		
fuEA	4.097	3.30	3.99† [288]	
thEA	3.69	3.02	3.75† [288]	
selEA	3.57	2.93		
2-fuEA	2.91	2.40		
2-thEA	2.68	2.10		
2-selEA	2.525	1.970		
IBfuEA	2.36	1.95		
IBthEA	2.28	1.87		
IBselEA	2.17	1.77		
INfuEA	2.68	2.32		
INthEA	2.59	2.25		
INselEA	2.60	2.26		
Azo	1.946	1.215		

Table D.2: Average singlet and triplet excitation energies ($\bar{S}_1$ and $\bar{T}_1$, in eV), standard deviations (σ, in eV) and bond length ranges (in Å) on post-equilibration molecular conformations from molecular dynamics simulations of A=PEA and A=NEA in A_2PbI_4.

	$\bar{S}_1$	σ_{S_1}	$S_{1,vac}$	$\bar{T}_1$	σ_{T_1}	$T_{1,vac}$	C–C (Å)
PEA	4.98	0.15	5.43	4.06	0.20	4.43	1.36 – 1.45
NEA	4.10	0.12	4.40	2.96	0.11	3.14	1.36 – 1.48

Table D.3: Singlet and triplet first excitation energies and homo-lumo gaps for polycarbocyclic compounds calculated by time-dependent DFT (TD) and ΔSCF methods in the singlet and triplet spin multiplicity geometries (MG) for various exchange-correlation (xc) functional. Molecular geometries herein are relaxed using the **B3LYP** xc-functional vacuum. 6-31G* is used for the Gaussian basis set unless otherwise stated. All values are in eV.

	MG	xc-functional	TD S_1	TD T_1	ΔSCF T_1	Homo-Lumo	Exp. T_1*
PEA	singlet	HSE	5.498	3.54	4.338	6.054	
		B3LYP	5.429	3.755	4.433	6.418	
		CAM-B3LYP	5.543	3.508	4.406	9.292	
	triplet	HSE		2.677	3.714	3.575	3.4-3.6
		B3LYP		2.88	3.771	3.629	
		CAM-B3LYP		2.599	3.763	3.887	
NEA	singlet	HSE	4.457	2.563	3.106	4.391	
		B3LYP	4.396	2.728	3.136	4.788	
		CAM-B3LYP	4.630	2.524	3.277	7.315	
	triplet	HSE		1.679	2.654	3.09	2.3-2.5
		B3LYP		1.871	2.677	3.027	
		CAM-B3LYP		1.524	2.761	3.346	
AEA	singlet	HSE	3.333	1.685	2.136	3.202	
		B3LYP	3.293	1.841	2.172	3.619	
		CAM-B3LYP	3.65	1.603	2.282	5.953	
	triplet	HSE		0.857	1.724	2.185	1.8
		B3LYP		1.093	1.752	2.142	
		CAM-B3LYP		0.43	1.824	2.422	
PyEA	singlet	HSE	3.757	1.977	2.402	3.435	
		B3LYP	3.705	2.121	2.434	3.84	
		CAM-B3LYP	3.964	1.866	2.552	6.089	
	triplet	HSE		1.302	2.076	2.560	1.8-2.0
		B3LYP		1.474	2.101	2.509	
		CAM-B3LYP		0.951	2.161	2.898	
PerEA	singlet	HSE	2.892	1.393	1.770	2.611	
		B3LYP	2.855	1.526	1.802	3.028	
		CAM-B3LYP	3.177	1.306	1.955	5.194	
	triplet	HSE		0.722	1.47	1.808	
		B3LYP		0.913	1.504	1.78	
		CAM-B3LYP		-0.185	1.598	2.108	

Table D.4: Singlet and triplet first excitation energies and homo-lumo gaps for functionalized 4Z-PEA compounds calculated by time-dependent DFT (TD) and ΔSCF methods in the singlet and triplet spin multiplicity geometries (MG) for various exchange-correlation (xc) functional. Molecular geometries herein are relaxed using the **B3LYP** xc-functional vacuum. 6-31G* is used for the Gaussian basis set unless otherwise stated. All values are in eV.

Compound	MG	xc-functional	TD S_1	TD T_1	ΔSCF T_1	Homo-Lumo
4Br-PEA	singlet	HSE	5.156	3.448	4.570	5.482
		B3LYP	5.083	3.64	4.578	5.853
		CAM-B3LYP	5.363	3.4249	4.7489	8.643
	triplet	HSE		-0.436	3.262	
		B3LYP		0.391	3.202	
		CAM-B3LYP		-0.554	3.386	
4Cl-PEA	singlet	HSE	5.197	3.455	4.58	5.517
		B3LYP	5.123	3.648	4.59	5.886
		CAM-B3LYP	5.381	3.423	4.745	8.727
	triplet	HSE		0.462	3.353	
		B3LYP		0.833	3.359	
		CAM-B3LYP		-0.26	3.44	
4F-PEA	singlet	HSE	5.253	3.556	4.4749	5.514
		B3LYP	5.18	3.753	4.493	5.884
		CAM-B3LYP	5.423	3.515	4.605	8.717
	triplet	HSE		-0.570	3.535	
		B3LYP		0.471	3.573	
		CAM-B3LYP		-0.851	3.577	
4MeO-PEA	singlet	HSE	5.149	3.519	3.987	5.429
		B3LYP	5.08	3.697	4.05	5.810
		CAM-B3LYP	5.248	3.476	4.368	8.523
	triplet	HSE		3.245	4.051	
		B3LYP		3.44	4.054	
		CAM-B3LYP		3.173	4.163	
4NO2-PEA	singlet	HSE	3.031	2.0684	2.254	3.398
		B3LYP	2.9653	2.136	2.287	3.695
		CAM-B3LYP	3.192	2.091	2.254	6.709
	triplet	HSE		-0.576	0.788	
		B3LYP		-0.523	0.683	
		CAM-B3LYP		-0.807	0.683	

Table D.5: Singlet and triplet first excitation energies and homo-lumo gaps for single and linked heterocyclic ring compounds calculated by time-dependent DFT (TD) and ΔSCF methods in the singlet and triplet spin multiplicity geometries (MG) for various exchange-correlation (xc) functional. Molecular geometries herein are relaxed using the **B3LYP** xc-functional vacuum. 6-31G* is used for the Gaussian basis set unless otherwise stated. All values are in eV.

Compound	MG	xc-functional	TD S_1	TD T_1	ΔSCF T_1	Homo-Lumo
fuEA	singlet	HSE	6.255	3.616	4.034	6.052
		B3LYP	6.177	3.749	4.097	6.403
		CAM-B3LYP	6.326	3.617	4.107	9.305
	triplet	HSE		1.279	3.265	
		B3LYP		1.531	3.305	
		CAM-B3LYP		1.068	3.318	
2-fuEA	singlet	HSE	4.433	2.497	2.882	4.147
		B3LYP	4.380	2.597	2.908	4.534
		CAM-B3LYP	4.6254	2.498	3.038	7.138
	triplet	HSE		1.463	2.405	
		B3LYP		1.2497	2.401	
		CAM-B3LYP			2.495	
thEA	singlet	HSE	5.424	3.236	3.634	5.370
		B3LYP	5.336	3.353	3.686	5.734
		CAM-B3LYP	5.708	3.210	3.690	8.547
	triplet	HSE		1.204	3.005	
		B3LYP		1.4232	3.0266	
		CAM-B3LYP		0.938	3.0326	
2-thEA	singlet	HSE	3.996	2.269	2.667	3.814
		B3LYP	3.9417	2.361	2.683	4.204
		CAM-B3LYP	4.211	2.242	2.817	6.721
	triplet	HSE		1.150	2.111	
		B3LYP		1.290	2.096	
		CAM-B3LYP		0.809	2.180	
selEA	singlet	HSE	5.269	3.114	3.520	5.243
		B3LYP	5.185	3.236	3.574	5.613
		CAM-B3LYP	5.507	3.086	3.578	8.402
	triplet	HSE		1.037	2.906	
		B3LYP		1.285	2.932	
		CAM-B3LYP		0.713	2.934	
2-selEA	singlet	HSE	3.805	2.106	2.504	3.635
		B3LYP	3.7563	2.2039	2.525	4.029
		CAM-B3LYP	4.010	2.061	2.641	6.510
	triplet	HSE		1.000	1.982	
		B3LYP		1.154	1.970	
		CAM-B3LYP		0.530	2.043	

Table D.6: Singlet and triplet first excitation energies and homo-lumo gaps for fused heterocyclic ring compounds calculated by time-dependent DFT (TD) and ΔSCF methods in the singlet and triplet spin multiplicity geometries (MG) for various exchange-correlation (xc) functional. Molecular geometries herein are relaxed using the **B3LYP** xc-functional vacuum. 6-31G* is used for the Gaussian basis set unless otherwise stated. All values are in eV.

Compound	MG	xc-functional	TD S_1	TD T_1	ΔSCF T_1	Homo-Lumo
IBfuEA	singlet	HSE	3.847	1.878	2.302	3.702
		B3LYP	3.802	2.034	2.360	4.113
		CAM-B3LYP	4.078	1.813	2.412	6.656
	triplet	HSE		0.903	1.912	
		B3LYP		1.156	1.949	
		CAM-B3LYP		0.514	1.982	
INfuEA	singlet	HSE	3.936	2.227	2.650	3.795
		B3LYP	3.881	2.361	2.680	4.197
		CAM-B3LYP	4.243	2.183	2.810	6.621
	triplet	HSE		1.507	2.301	
		B3LYP		1.672	2.330	
		CAM-B3LYP		1.330	2.416	
IBthEA	singlet	HSE	3.750	1.816	2.234	3.571
		B3LYP	3.696	1.951	2.276	3.977
		CAM-B3LYP	3.958	1.714	2.304	6.450
	triplet	HSE		0.818	1.856	
		B3LYP		1.053	1.869	
		CAM-B3LYP		0.206	1.885	
INthEA	singlet	HSE	3.712	2.131	2.554	3.623
		B3LYP	3.667	2.268	2.587	4.033
		CAM-B3LYP	4.065	2.095	2.736	6.434
	triplet	HSE		1.421	2.206	
		B3LYP		1.591	2.246	
		CAM-B3LYP		1.246	2.344	
IBselEA	singlet	HSE	3.604	1.700	2.122	3.442
		B3LYP	3.552	1.835	2.166	3.849
		CAM-B3LYP	3.803	1.583	2.182	3.301
	triplet	HSE		0.670	1.753	
		B3LYP		0.932	1.767	
		CAM-B3LYP		-0.438	1.776	
INselEA	singlet	HSE	3.627	2.140	2.562	3.578
		B3LYP	3.587	2.275	2.595	3.992
		CAM-B3LYP	4.018	2.115	2.759	6.392
	triplet	HSE		1.442	2.216	
		B3LYP		1.609	2.257	
		CAM-B3LYP		1.282	2.368	

Table D.7: Singlet and triplet first excitation energies and homo-lumo gaps for azobenzene-EA (Azo) calculated by time-dependent DFT (TD) and ΔSCF methods in the singlet and triplet spin multiplicity geometries (MG) for various exchange-correlation (xc) functional. Molecular geometries herein are relaxed using the **B3LYP** xc-functional vacuum. 6-31G* is used for the Gaussian basis set unless otherwise stated. All values are in eV.

Compound	MG	xc-functional	TD S_1	TD T_1	ΔSCF T_1	Homo-Lumo
Azo	singlet	HSE	2.579	1.733	1.900	3.523
		B3LYP	2.562	1.793	1.946	3.907
		CAM-B3LYP		2.726	1.971	6.399
	triplet	HSE		-0.2743	1.174	
		B3LYP		-0.317	1.215	
		CAM-B3LYP		-0.3048	1.233	

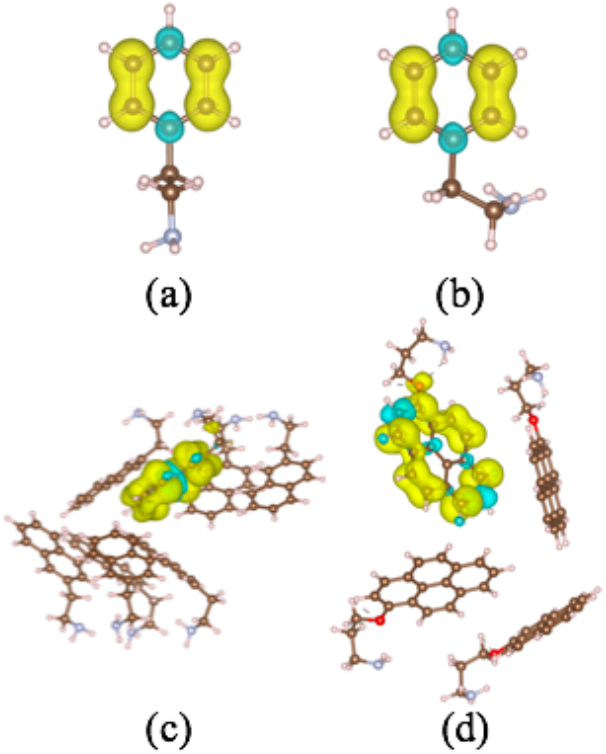

Figure D.1: The magnetization density of (a) fully vacuum relaxed PEA with CAM-B3LYP, (b) relaxed phenyl ring by CAM-B3LYP with fixed EA tail in the perovskite geometry, (c) relaxed naphthalene rings on fixed EA tails in the perovskite geometry, and (d) relaxed pyrene rings on OPA tailed with fixed perovskite geometries.

Table D.8: Singlet and triplet first excitation energies and homo-lumo gaps for polycarbocyclic compounds calculated by time-dependent DFT (TD) and ΔSCF methods in the singlet and triplet spin multiplicity geometries (MG) for various exchange-correlation (xc) functional. Molecular geometries herein are relaxed using the **CAM-B3LYP** xc-functional. Values outside of parentheses indicate the neutral compound with an ethyl ammonia NH_2 tail whereas values in the parentheses indicate the charged species with NH_3^+. 6-31G* is used for the Gaussian basis set unless otherwise stated. All values are in eV. The † symbol indicates instances where the xc-functional cannot appropriately handle range-separation for charged species (HSE and B3LYP).

	MG	xc-functional	TD S_1	TD T_1	ΔSCF T_1	Homo-Lumo
PEA	singlet	HSE	5.547 (5.088†)	3.604 (3.595)	4.389 (4.485)	6.060 (5.239)
		B3LYP	5.478 (4.745†)	3.815 (3.571)	4.840 (4.374)	6.422 (5.323)
		CAM-B3LYP	5.594 (5.581)	3.576 (3.571)	4.480 (5.199)	9.340 (8.090)
	triplet	HSE		0.788 (2.686)	1.549 (3.095)	
		B3LYP		1.158 (2.882)	1.669 (3.196)	
		CAM-B3LYP		0.548 (2.613)	1.551 (2.083)	
NEA	singlet	HSE	4.518 (3.902†)	2.642 (2.623)	3.181 (3.138)	4.462 (3.970)
		B3LYP	4.457 (3.607†)	2.804 (2.779)	3.209 (3.165)	4.859 (4.067)
		CAM-B3LYP	4.696 (4.645)	2.615 (2.601)	3.362 (3.318)	7.399 (6.705)
	triplet	HSE		1.648 (1.661)	2.148 (2.144)	
		B3LYP		1.839 (1.846)	2.204 (2.198)	
		CAM-B3LYP		1.487 (1.508)	2.196 (2.195)	
AEA	singlet	HSE	3.401 (3.085†)	1.772 (1.709)	2.214 (2.126)	3.280 (3.108)
		B3LYP	3.360 (2.841†)	1.923 (1.853)	2.248 (2.160)	3.694 (3.236)
		CAM-B3LYP	3.728 (3.563)	1.712 (1.654)	2.372 (2.286)	6.045 (5.734)
	triplet	HSE		0.804 (0.826)	1.376 (1.358)	
		B3LYP		1.048 (1.056)	1.428 (1.416)	
		CAM-B3LYP		0.289 (0.383)	1.394 (1.386)	
PyEA	singlet	HSE	3.829 (3.246†)	2.073 (2.074)	2.494 (2.478)	3.533 (3.292)
		B3LYP	3.776 (2.976†)	2.212 (2.209)	2.523 (2.507)	3.926 (3.385)
		CAM-B3LYP	4.040 (3.982)	1.986 (1.989)	2.661 (2.641)	6.195 (5.878)
	triplet	HSE		1.259 (1.307)	1.682 (1.708)	
		B3LYP		1.431 (1.472)	1.734 (1.760)	
		CAM-B3LYP		0.878 (0.967)	1.672 (1.700)	
PerEA	singlet	HSE	2.967 (2.855)	1.497 (1.4838)	1.867 (1.822)	2.702 (2.616)
		B3LYP	2.932 (2.619)	1.624 (1.599)	1.896 (1.848)	3.118 (3.009)
		CAM-B3LYP	3.266 (3.177)	1.444 (1.429)	2.073 (2.017)	5.309 (5.197)
	triplet	HSE		0.667 (0.765)	1.121 (1.156)	
		B3LYP		0.863 (0.931)	1.170 (1.201)	
		CAM-B3LYP		-0.361* (0.218)	1.140 (1.179)	

Table D.9: Singlet and triplet first excitation energies and homo-lumo gaps for functionalized 4Z-PEA compounds calculated by time-dependent DFT (TD) and ΔSCF methods in the singlet and triplet spin multiplicity geometries (MG) for various exchange-correlation (xc) functional. Molecular geometries herein are relaxed using the **CAM-B3LYP** xc-functional. Values outside of parentheses indicate the neutral compound with an ethyl ammonia NH_2 tail whereas values in the parentheses indicate the charged species with NH_3^+. 6-31G* is used for the Gaussian basis set unless otherwise stated. All values are in eV.

	MG	xc-functional	TD S_1	TD T_1	ΔSCF T_1	Homo-Lumo
MeO-PEA	singlet	HSE	5.189 (4.110†)	3.582 (3.556)	4.038 (3.951)	5.466 (4.222)
		B3LYP	5.120 (3.800†)	3.757 (3.694)	4.100 (3.993)	5.847 (4.319)
		CAM-B3LYP	5.288 (5.230)	3.545 (3.531)	4.404 (4.394)	8.563 (7.037)
	triplet	HSE		3.498 (3.306)	3.832 (3.651)	
		B3LYP		3.241 (3.467)	3.855 (3.671)	
		CAM-B3LYP		3.306 (3.246)	3.924 (3.796)	
NO2-PEA	singlet	HSE	3.250 (3.365)	2.132 (2.197)	2.315 (2.375)	3.664 (4.348)
		B3LYP	3.205 (3.346)	2.216 (2.274)	2.354 (2.414)	3.953 (4.637)
		CAM-B3LYP	3.314 (3.358)	2.147 (2.196)	2.315 (2.364)	7.011 (7.587)
	triplet	HSE		1.619 (1.623)	1.828 (1.835)	
		B3LYP		1.7245 (1.726)	1.879 (1.884)	
		CAM-B3LYP		1.628 (1.640)	1.819 (1.832)	
Br-PEA	singlet	HSE	5.185 (4.521)	3.507 (3.461)	4.601 (4.388)	5.499 (4.607)
		B3LYP	5.111 (4.222)	3.694 (3.631)	4.609 (4.081)	5.870 (4.693)
		CAM-B3LYP	5.401 (5.353)	3.488 (3.451)	4.781 (4.837)	8.678 (7.442)
	singlet	HSE	4.837	3.489	4.575	
	lanl2dz	B3LYP	4.740	3.643	4.546	
		CAM-B3LYP	5.306	3.421	4.770	
	triplet	HSE		2.633 (3.159)	3.043 (3.765)	
		B3LYP		2.817 (3.355)	3.130 (4.103)	
		CAM-B3LYP		2.570 (3.111)	3.088 (4.286)	
	triplet	HSE		3.091	3.949	
	lanl2dz	B3LYP		3.266	3.919	
		CAM-B3LYP		2.989	4.165	
Cl-PEA	singlet	HSE	5.282 (4.728)	3.620 (3.486)	4.403 (4.723)	5.532 (4.837)
		B3LYP	5.208 (4.413)	3.815 (3.664)	4.525 (4.131)	5.901 (4.926)
		CAM-B3LYP	5.466 (5.404)	3.584 (3.461)	4.540 (4.865)	8.745 (7.677)
	triplet	HSE		0.380 (0.520)	1.245 (1.316)	
		B3LYP		0.805 (0.897)	1.339 (1.410)	
		CAM-B3LYP		-0.429 (-0.310)	1.262 (1.315)	
F-PEA	singlet	HSE	5.282 (4.855)	3.620 (3.624)	4.403 (4.679)	5.532 (4.994)
		B3LYP	5.208 (4.520)	3.815 (3.810)	4.525 (4.689)	5.901 (5.082)
		CAM-B3LYP	5.466 (5.404)	3.584 (3.461)	4.640 (4.865)	8.745 (7.677)
	triplet	HSE		-2.091 (-2.212)	0.654 (0.947)	
		B3LYP		-1.924 (-2.037)	0.378 (0.618)	
		CAM-B3LYP		-2.262 (-2.392)	0.813 (1.121)	

Table D.10: Singlet and triplet first excitation energies and homo-lumo gaps for single and linked heterocyclic ring compounds calculated by time-dependent DFT (TD) and ΔSCF methods in the singlet and triplet spin multiplicity geometries (MG) for various exchange-correlation (xc) functional. Molecular geometries herein are relaxed using the **CAM-B3LYP** xc-functional. Values outside of parentheses indicate the neutral compound with an ethyl ammonia NH_2 tail whereas values in the parentheses indicate the charged species with NH_3^+. 6-31G* is used for the Gaussian basis set unless otherwise stated. All values are in eV.

	MG	xc-functional	TD S_1	TD T_1	ΔSCF T_1	Homo-Lumo
selEA	singlet	HSE	5.339 (4.637)	3.222 (3.231)	3.620 (3.621)	5.328 (4.785)
		B3LYP	5.254 (4.291)	3.340 (3.348)	3.673 (3.675)	5.696 (4.872)
		CAM-B3LYP	5.601 (5.483)	3.201 (3.201)	3.682 (3.674)	8.499 (7.656)
	triplet	HSE		0.995 (0.773)	1.630 (1.454)	
		B3LYP		1.248 (1.070)	1.726 (1.561)	
		CAM-B3LYP		0.658 (0.237)	1.585 (1.408)	
2-selEA	singlet	HSE	3.933 (3.376)	2.280 (2.258)	2.675 (2.633)	3.800 (3.447)
		B3LYP	3.8805 (3.101)	2.372 (2.340)	2.692 (2.646)	4.191 (3.536)
		CAM-B3LYP	4.1564 (4.046)	2.260 (2.238)	2.833 (2.785)	5.294 (6.184)
	triplet	HSE		0.997 (1.061)	1.446 (1.469)	
		B3LYP		1.148 (1.198)	1.491 (1.512)	
		CAM-B3LYP		0.517 (0.638)	1.385 (1.407)	
thEA	singlet	HSE	5.480 (4.658)	3.336 (3.345)	3.728 (3.725)	5.447 (4.817)
		B3LYP	5.389 (4.3117)	3.450 (3.316)	3.778 (3.778)	5.810 (4.904)
		CAM-B3LYP	5.791 (5.732)	3.318 (3.316)	3.787 (3.776)	8.635 (7.709)
	triplet	HSE		1.162 (1.175)	1.735 (1.726)	
		B3LYP		1.385 (1.401)	1.827 (1.826)	
		CAM-B3LYP		0.891 (0.924)	1.689 (1.691)	
2-thEA	singlet	HSE	4.130 (3.417)	2.449 (2.422)	2.846 (2.803)	3.987 (3.487)
		B3LYP	4.073 (3.140)	2.535 (2.450)	2.859 (2.811)	4.374 (3.578)
		CAM-B3LYP	4.368 (4.253)	2.443 (2.419)	3.017 (2.970)	6.920 (6.238)
	triplet	HSE		1.139 (1.196)	1.563 (1.586)	
		B3LYP		1.277 (1.323)	1.605 (1.626)	
		CAM-B3LYP		0.786 (0.867)	1.521 (1.542)	
fuEA	singlet	HSE	6.328 (4.476)	3.709 (3.629)	4.121 (4.022)	6.140 (4.638)
		B3LYP	6.244 (4.142)	3.839 (3.636)	4.184 (4.081)	6.489 (4.745)
		CAM-B3LYP	6.408 (5.584)	3.714 (3.634)	4.197 (4.106)	9.398 (7.565)
	triplet	HSE		1.325 (1.569)	1.908 (2.084)	
		B3LYP		1.570 (1.796)	2.023 (2.200)	
		CAM-B3LYP		1.123 (1.394)	1.898 (2.078)	
2-fuEA	singlet	HSE	4.529 (3.210)	2.621 (2.566)	3.003 (2.938)	4.625 (3.290)
		B3LYP	4.475 (2.929)	2.717 (2.656)	3.026 (2.957)	4.650 (3.401)
		CAM-B3LYP	4.732 (4.484)	2.636 (2.583)	3.169 (3.107)	7.273 (6.063)
	triplet	HSE		1.455 (1.447)	1.853 (1.832)	
		B3LYP		1.595 (1.584)	1.904 (1.882)	
		CAM-B3LYP		1.231 (1.217)	1.843 (1.822)	

Table D.11: Singlet and triplet first excitation energies and homo-lumo gaps for fused heterocyclic ring compounds calculated by time-dependent DFT (TD) and ΔSCF methods in the singlet and triplet spin multiplicity geometries (MG) for various exchange-correlation (xc) functional. Molecular geometries herein are relaxed using the **CAM-B3LYP** xc-functional. Values outside of parentheses indicate the neutral compound with an ethyl ammonia NH_2 tail whereas values in the parentheses indicate the charged species with NH_3^+. 6-31G* is used for the Gaussian basis set unless otherwise stated. All values are in eV.

	MG	xc-functional	TD S_1	TD T_1	ΔSCF T_1	Homo-Lumo
IBSelEA	singlet	HSE	3.693 (3.461)	1.824 (1.823)	2.233 (2.235)	3.543 (3.500)
		B3LYP	3.640 (3.170)	1.952 (1.979)	2.273 (2.276)	3.949 (3.637)
		CAM-B3LYP	3.904 (3.822)	1.733 (1.776)	2.305 (2.306)	6.417 (6.262)
	triplet	HSE		0.690 (0.832)	1.319 (1.371)	
		B3LYP		0.943 (1.043)	1.387 (1.438)	
		CAM-B3LYP		-0.412 (0.287)	1.273 (1.333)	
INSelEA	singlet	HSE	3.674 (3.080)	2.210 (2.151)	2.623 (2.513)	3.634 (3.116)
		B3LYP	3.633 (2.849)	2.341 (2.263)	2.655 (2.541)	4.048 (3.221)
		CAM-B3LYP	4.072 (3.788)	2.202 (2.165)	2.827 (2.726)	6.460 (5.782)
	triplet	HSE		1.400 (1.418)	1.831 (1.804)	
		B3LYP		1.570 (1.568)	1.885 (1.853)	
		CAM-B3LYP		1.230 (1.275)	1.910 (1.896)	
IBThEA	singlet	HSE	3.833 (3.520)	1.932 (1.958)	2.338 (2.327)	3.668 (3.576)
		B3LYP	3.772 (3.229)	2.059 (2.075)	2.378 (2.367)	4.071 (3.695)
		CAM-B3LYP	4.052 (3.943)	1.851 (1.883)	2.420 (2.410)	6.560 (6.324)
	triplet	HSE		0.826 (0.936)	1.409 (1.447)	
		B3LYP		1.0567 (1.138)	1.477 (1.514)	
		CAM-B3LYP		0.223 (0.534)	1.376 (1.423)	
INThEA	singlet	HSE	3.764 (3.197)	2.203 (2.159)	2.618 (2.528)	3.683 (3.238)
		B3LYP	3.718 (2.952)	2.336 (2.276)	2.650 (2.556)	4.093 (3.340)
		CAM-B3LYP	4.124 (3.879)	2.1831 (2.155)	2.807 (2.724)	6.507 (5.907)
	triplet	HSE		1.380 (1.407)	1.831 (1.801)	
		B3LYP		1.553 (1.562)	1.872 (1.852)	
		CAM-B3LYP		1.195 (1.2457)	1.884 (1.879)	
IBFuEA	singlet	HSE	3.925 (3.411)	1.988 (1.949)	2.402 (2.318)	3.795 (3.477)
		B3LYP	3.877 (3.138)	2.137 (2.087)	2.457 (2.376)	4.203 (3.600)
		CAM-B3LYP	4.167 (3.948)	1.943 (1.911)	2.524 (2.437)	6.762 (6.239)
	triplet	HSE		0.903 (0.951)	1.472 (1.458)	
		B3LYP		1.1542 (1.181)	1.555 (1.541)	
		CAM-B3LYP		0.506 (0.627)	1.477 (1.471)	
INFuEA	singlet	HSE	3.994 (3.393)	2.301 (2.291)	2.716 (2.668)	3.861 (3.445)
		B3LYP	3.938 (3.128)	2.431 (2.408)	2.745 (2.695)	4.263 (3.543)
		CAM-B3LYP	4.307 (4.139)	2.271 (2.269)	2.884 (2.843)	6.699 (6.132)
	triplet	HSE		1.475 (1.529)	1.905 (1.919)	
		B3LYP		1.641 (1.679)	1.957 (1.968)	
		CAM-B3LYP		1.288 (1.362)	1.957 (1.981)	

Table D.12: Singlet and triplet first excitation energies and homo-lumo gaps for azobenzene-EA (Azo) calculated by time-dependent DFT (TD) and ΔSCF methods in the singlet and triplet spin multiplicity geometries (MG) for various exchange-correlation (xc) functional. Molecular geometries herein are relaxed using the **CAM-B3LYP** xc-functional. Values outside of parentheses indicate the neutral compound with an ethyl ammonia NH_2 tail whereas values in the parentheses indicate the charged species with NH_3^+. 6-31G* is used for the Gaussian basis set unless otherwise stated. All values are in eV.

	MG	xc-functional	TD S_1	TD T_1	ΔSCF T_1	Homo-Lumo
azoEA	singlet	HSE	2.614 (2.516)	1.765 (1.698)	1.932 (1.869)	3.641 (3.491)
		B3LYP	2.598 (2.495)	1.825 (1.756)	1.977 (1.915)	3.990 (3.817)
		CAM-B3LYP	2.764 (2.692)	1.887 (1.835)	2.009 (1.956)	6.547 (6.426)
	triplet	HSE		-0.253 (-0.288)	0.577 (0.410)	
		B3LYP		-0.107 (-0.324)	0.494 (0.331)	
		CAM-B3LYP		-0.338 (-0.339)	0.680 (0.494)	

Table D.13: Comparison of T_1 and S_1 calculated energy on the B3LYP-relaxed geometries in vacuum and water solvent effects treated by the polarization continuum model[285].

		Vacuum			Water		
	xc-functional	S_1^{TD}	T_1^{TD}	$T_1^{\Delta SCF}$	S_1^{TD}	T_1^{TD}	$T_1^{\Delta SCF}$
PEA	HSE	5.498	3.54	4.338	5.506	3.777	4.353
	B3LYP	5.429	3.755	4.433	5.436	3.534	4.447
	CAM-B3LYP	5.543	3.508	4.400	5.552	3.568	4.421
AEA	HSE	4.457	2.563	3.106	4.437	2.582	3.114
	B3LYP	4.396	2.728	3.136	4.377	2.743	3.143
	CAM-B3LYP	4.630	2.524	3.277	4.633	2.545	3.285
AEA	HSE	3.333	1.685	2.136	3.304	1.697	2.139
	B3LYP	3.293	1.841	2.172	3.265	1.850	2.174
	CAM-B3LYP	3.65	1.603	2.282	3.013	1.619	2.287
PyEA	HSE	3.757	1.977	2.402	3.707	1.991	2.409
	B3LYP	3.705	2.121	2.434	3.656	2.152	2.440
	CAM-B3LYP	3.964	1.866	2.552	3.959	1.883	2.558
4MeO-PEA	HSE	5.149	3.519	3.987	5.129	3.539	3.99
	B3LYP	5.08	3.697	4.05	5.061	3.713	4.050
	CAM-B3LYP	5.248	3.476	4.368	5.234	3.496	4.335
$4NO_2$-PEA	HSE	3.031	2.0684	2.254	2.967	2.082	2.242
	B3LYP	2.9653	2.136	2.287	2.878	2.136	2.265
	CAM-B3LYP	3.192	2.091	2.254	3.196	2.114	2.256
4Br-PEA	HSE	5.156	3.448	4.570	5.184	3.477	4.568
	B3LYP	5.083	3.640	4.578	5.114	3.666	4.576
	CAM-B3LYP	5.363	3.4249	4.7489	5.391	3.452	4.755

References

[1] T. Ishihara, "Optical properties of pbi-based perovskite structures," *J. Lumin.*, vol. 60-61, pp. 269 – 274, 1994.

[2] M. Saliba, T. Matsui, K. Domanski, J.-Y. Seo, A. Ummadisingu, S. M. Zakeeruddin, J.-P. Correa-Baena, W. R. Tress, A. Abate, A. Hagfeldt, and M. Grätzel, "Incorporation of rubidium cations into perovskite solar cells improves photovoltaic performance," *Science*, vol. 354, no. 6309, pp. 206–209, 2016.

[3] M. Green, K. Emery, Y. Hishikawa, W. Warta, and E. Dunlop, "Solar cell efficiency tables (version 45)," *Prog. Photovolt. Res. Appl.*, vol. 23, no. 1, 2015.

[4] Y. Zhou and K. Zhu, "Perovskite solar cells shine in the "valley of the sun"," *ACS Energy Lett.*, vol. 1, no. 1, pp. 64–67, 2016.

[5] L. Zhang, X. Yang, Q. Jiang, P. Wang, Z. Yin, X. Zhang, H. Tan, Y. M. Yang, M. Wei, B. R. Sutherland, E. H. Sargent, and J. You, "Ultra-bright and highly efficient inorganic based perovskite light-emitting diodes," *Nat. Comm.*, vol. 8, p. 15640, 2017.

[6] A. R. Bin, M. Yusoff, and J. Jang, "Highly efficient photoelectrochemical water splitting by a hybrid tandem perovskite solar cell," *Chem. Commun.*, vol. 52, pp. 5824–5827, 2016.

[7] S. Yakunin, M. Sytnyk, D. Kriegner, S. Shrestha, M. Richter, G. J. Matt, H. Azimi, C. J. Brabec, J. Stangl, M. V. Kovalenko, and W. Heiss, "Detection of x-ray photons by solution-processed lead halide perovskites," *Nat Photonics*, vol. 9, p. 444, 2015.

[8] K. T. Cho, G. Grancini, Y. Lee, E. Oveisi, J. Ryu, O. Almora, M. Tschumi, P. A. Schouwink, G. Seo, S. Heo, J. Park, J. Jang, S. Paek, G. Garcia-Belmonte, and M. K. Nazeeruddin, "Selective growth of layered perovskites for stable and efficient photovoltaics," *Energy Environ. Sci.*, vol. 11, pp. 952–959, 2018.

[9] E. R. Dohner, A. Jaffe, L. R. Bradshaw, and H. I. Karunadasa, "Intrinsic white-light emission from layered hybrid perovskites," *J Am Chem Soc*, vol. 136, no. 38, pp. 13154–13157, 2014.

[10] M. D. Smith and H. I. Karunadasa, "White-light emission from layered halide perovskites," *Acc Chem Res*, vol. 51, no. 3, pp. 619–627, 2018.

[11] L. Mao, W. Ke, L. Pedesseau, Y. Wu, C. Katan, J. Even, M. R. Wasielewski, C. C. Stoumpos, and M. G. Kanatzidis, "Hybrid dion–jacobson 2d lead iodide perovskites," *Journal of the American Chemical Society*, vol. 140, no. 10, pp. 3775–3783, 2018. PMID: 29465246.

[12] H. Tsai, W. Nie, J.-C. Blancon, C. C. Stoumpos, C. M. M. Soe, J. Yoo, J. Crochet, S. Tretiak, J. Even, A. Sadhanala, G. Azzellino, R. Brenes, P. M. Ajayan, V. Bulović, S. D. Stranks, R. H. Friend, M. G. Kanatzidis, and A. D. Mohite, "Stable light-emitting diodes using phase-pure ruddlesden–popper layered perovskites," *Advanced Materials*, vol. 30, no. 6, p. 1704217, 2018.

[13] J. Wang, C. Zhang, H. Liu, R. McLaughlin, Y. Zhai, S. R. Vardeny, X. Liu, S. McGill, D. Semenov, H. Guo, R. Tsuchikawa, V. V. Deshpande, D. Sun, and Z. V. Vardeny, "Spin-optoelectronic devices based on hybrid organic-inorganic trihalide perovskites," *Nature Communications*, vol. 10, no. 1, p. 129, 2019.

[14] F. Dogan, H. Lin, M. Guilloux-Viry, and O. Peña, "Focus on properties and applications of perovskites," *Science and Technology of Advanced Materials*, vol. 16, p. 020301, apr 2015.

[15] N. S. Rytova, "Screened potential of a point charge in a thin film," *Moscow University Physics Bulletin*, vol. 30, pp. 1–5, 1967.

[16] L. V. Keldysh, "Coulomb interaction in thin semiconductor and semimetal films," *JEPT Letters*, vol. 29, p. 658, 1979.

[17] A. Kojima, K. Teshima, Y. Shirai, and T. Miyasaka, "Organometal halide perovskites as visible-light sensitizers for photovoltaic cells," *J Am Chem Soc*, vol. 131, pp. 6050–6051, 2009.

[18] H.-S. Kim, C.-R. Lee, J.-H. Im, K.-B. Lee, T. Moehl, A. Marchioro, S.-J. Moon, R. Humphry-Baker, J.-H. Yum, J. E. Moser, M. Grätzel, and N.-G. Park, "Lead iodide perovskite sensitized all-solid-state submicron thin film mesoscopic solar cell with efficiency exceeding 9%," *Scientific Reports*, vol. 2, p. 591, 2012.

[19] M. M. Lee, J. Teuscher, T. Miyasaka, T. N. Murakami, and H. J. Snaith, "Efficient hybrid solar cells based on meso-superstructured organometal halide perovskites," *Science*, vol. 338, no. 6107, pp. 643–647, 2012.

[20] J. M. Ball, M. M. Lee, A. Hey, and H. J. Snaith, "Low-temperature processed meso-superstructured to thin-film perovskite solar cells," *Energy Environ. Sci.*, vol. 6, pp. 1739–1743, 2013.

[21] Q. Chen, H. Zhou, Z. Hong, S. Luo, H.-S. Duan, H.-H. Wang, Y. Liu, G. Li, and Y. Yang, "Planar heterojunction perovskite solar cells via vapor-assisted solution process," *Journal of the American Chemical Society*, no. 2, pp. 622–625, 2014. PMID: 24359486.

[22] M. Liu, M. B. Johnston, and H. J. Snaith, "Efficient planar heterojunction perovskite solar cells by vapour deposition," *Nature*, vol. 501, p. 395, 2013.

[23] W. Yang, J. Noh, N. Jeon, Y. Kim, S. Ryu, J. Seo, and S. Seok, "High-performance photovoltaic perovskite layers fabricated through intramolecular exchange," *Science*, vol. 348, pp. 1234–1237, 6 2015.

[24] M. D. Smith, A. Jaffe, E. R. Dohner, A. M. Lindenberg, and H. I. Karunadasa, "Structural origins of broadband emission from layered pb-br hybrid perovskites," *Chem. Sci.*, vol. 8, pp. 4497–4504, 2017.

[25] M. D. Smith and H. I. Karunadasa, "White-light emission from layered halide perovskites," *Accounts of Chemical Research*, vol. 51, no. 3, pp. 619–627, 2018.

[26] M. D. Smith, L. Pedesseau, M. Kepenekian, I. C. Smith, C. Katan, J. Even, and H. I. Karunadasa, "Decreasing the electronic confinement in layered perovskites through intercalation," *Chem. Sci.*, vol. 8, pp. 1960–1968, 2017.

[27] L. M. Herz, "Charge-carrier dynamics in organic-inorganic metal halide perovskites," *Annu. Rev. Phys. Chem.*, vol. 67, no. 1, pp. 65–89, 2016.

[28] J. Even, L. Pedesseau, M.-A. Dupertuis, J.-M. Jancu, and C. Katan, "Electronic model for self-assembled hybrid organic/perovskite semiconductors: Reverse band edge electronic states ordering and spin-orbit coupling," *Phys. Rev. B*, vol. 86, p. 205301, 2012.

[29] M. R. Filip and F. Giustino, "Gw quasiparticle band gap of the hybrid organic-inorganic perovskite ch3nh3pbi3: Effect of spin-orbit interaction, semicore electrons, and self-consistency," *Phys. Rev. B*, vol. 90, p. 245145, Dec 2014.

[30] A. D. Wright, C. Verdi, R. L. Milot, G. E. Eperon, M. A. Pérez-Osorio, H. J. Snaith, F. Giustino, M. B. Johnston, and L. M. Herz, "Electron–phonon coupling in hybrid lead halide perovskites," *Nat. Comm.*, vol. 7, p. 11755, 2016.

[31] A. J. Neukirch, W. Nie, J.-C. Blancon, K. Appavoo, H. Tsai, M. Y. Sfeir, C. Katan, L. Pedesseau, J. Even, J. J. Crochet, G. Gupta, A. D. Mohite, and S. Tretiak, "Polaron stabilization by cooperative lattice distortion and cation rotations in hybrid perovskite materials," *Nano Lett.*, vol. 16, no. 6, pp. 3809–3816, 2016. PMID: 27224519.

[32] P. Umari, E. Mosconi, and F. De Angelis, "Infrared dielectric screening determines the low exciton binding energy of metal-halide perovskites," *J. Phys. Chem. Lett.*, vol. 9, no. 3, pp. 620–627, 2018.

[33] Q. Wang, Y. Shao, H. Xie, L. Lyu, X. Liu, Y. Gao, and J. Huang, "Qualifying composition dependent p and n self-doping in ch3nh3pbi3," *Appl. Phys. Lett.*, vol. 105, no. 16, p. 163508, 2014.

[34] A. Dymshits, A. Henning, G. Segev, Y. Rosenwaks, and L. Etgar, "The electronic structure of metal oxide/organo metal halide perovskite junctions in perovskite based solar cells," *Sci. Rep.*, vol. 5, p. 8704, 2015.

[35] A. Guerrero, E. J. Juarez-Perez, J. Bisquert, I. Mora-Sero, and G. Garcia-Belmonte, "Electrical field profile and doping in planar lead halide perovskite solar cells," *Appl. Phys. Lett.*, vol. 105, no. 13, p. 133902, 2014.

[36] W. Kohn and L. J. Sham, "Self-consistent equations including exchange and correlation effects," *Phys. Rev.*, vol. 140, pp. A1133–A1138, 1965.

[37] P. Hohenberg and W. Kohn, "Inhomogeneous electron gas," *Phys. Rev.*, vol. 136, pp. B864–B871, Nov 1964.

[38] G. Baym, "Field-theoretic approach to the properties of the solid state," *Annals of Physics*, vol. 14, pp. 1 – 42, 1961.

[39] L. Hedin, "New method for calculating the one-particle green's function with application to the electron-gas problem," *Phys. Rev.*, vol. 139, pp. A796–A823, 1965.

[40] M. S. Hybertsen and S. G. Louie, "Electron correlation in semiconductors and insulators: Band gaps and quasiparticle energies," *Phys. Rev. B*, vol. 34, pp. 5390–5413, 1986.

[41] M. Rohlfing and S. G. Louie, "Electron-hole excitations and optical spectra from first principles," *Phys. Rev. B*, vol. 62, pp. 4927–4944, 2000.

[42] I. Borriello, G. Cantele, and D. Ninno, "Ab initio investigation of hybrid organic-inorganic perovskites based on tin halides," *Phys. Rev. B*, vol. 77, p. 235214, 2008.

[43] F. Brivio, A. B. Walker, and A. Walsh, "Structural and electronic properties of hybrid perovskites for high-efficiency thin-film photovoltaics from first-principles," *APL Materials*, vol. 1, no. 4, p. 042111, 2013.

[44] E. Mosconi, A. Amat, M. K. Nazeeruddin, M. Grätzel, and F. De Angelis, "First-principles modeling of mixed halide organometal perovskites for photovoltaic applications," *The Journal of Physical Chemistry C*, vol. 117, no. 27, pp. 13902–13913, 2013.

[45] Y. Wang, T. Gould, J. F. Dobson, H. Zhang, H. Yang, X. Yao, and H. Zhao, "Density functional theory analysis of structural and electronic properties of orthorhombic perovskite ch3nh3pbi3," *Phys. Chem. Chem. Phys.*, vol. 16, pp. 1424–1429, 2014.

[46] W.-J. Yin, J.-H. Yang, J. Kang, Y. Yan, and S.-H. Wei, "Halide perovskite materials for solar cells: a theoretical review," *J. Mater. Chem. A*, vol. 3, pp. 8926–8942, 2015.

[47] J. S. Manser, J. A. Christians, and P. V. Kamat, "Intriguing optoelectronic properties of metal halide perovskites," *Chemical Reviews*, vol. 116, no. 21, pp. 12956–13008, 2016.

[48] L. Pedesseau, D. Sapori, B. Traore, R. Robles, H.-H. Fang, M. A. Loi, H. Tsai, W. Nie, J.-C. Blancon, A. Neukirch, S. Tretiak, A. D. Mohite, C. Katan, J. Even, and M. Kepenekian, "Advances and promises of layered halide hybrid perovskite semiconductors," *ACS Nano*, vol. 10, no. 11, pp. 9776–9786, 2016.

[49] J. Even, L. Pedesseau, and C. Katan, "Analysis of multivalley and multibandgap absorption and enhancement of free carriers related to exciton screening in hybrid perovskites," *J. Phys. Chem. C*, vol. 118, no. 22, pp. 11566–11572, 2014.

[50] M. Bokdam, T. Sander, A. Stroppa, S. Picozzi, D. D. Sarma, C. Franchini, and G. Kresse, "Role of polar phonons in the photo excited state of metal halide perovskites," *Sci Rep - UK*, vol. 6, pp. 28618 EP –, 2016.

[51] X. Zhu, H. Su, R. A. Marcus, and M. E. Michel-Beyerle, "Computed and Experimental Absorption Spectra of the Perovskite CH3nh3pbi3," *J. Phys. Chem. Lett.*, vol. 5, pp. 3061–3065, 2014.

[52] T. Ahmed, C. La-o-vorakiat, T. Salim, Y. M. Lam, E. E. M. Chia, and J.-X. Zhu, "Optical properties of organometallic perovskite: An ab initio study using relativistic GW correction and bethe-salpeter equation," *Europhys. Lett.*, vol. 108, no. 6, p. 67015, 2014.

[53] X. Leng, F. Jin, M. Wei, and Y. Ma, "Gw method and bethe–salpeter equation for calculating electronic excitations," *Wiley Interdisciplinary Reviews: Computational Molecular Science*, vol. 6, no. 5, pp. 532–550, 2016.

[54] M. Born and R. Oppenheimer, "Zur quantentheorie der molekeln," *Annalen der Physik*, vol. 389, no. 20, pp. 457–484, 1927.

[55] D. R. Hartree, "The wave mechanics of an atom with a non-coulomb central field. part i. theory and methods," *Mathematical Proceedings of the Cambridge Philosophical Society*, vol. 24, no. 1, p. 89–110, 1928.

[56] J. C. Slater, "The self consistent field and the structure of atoms," *Phys. Rev.*, vol. 32, pp. 339–348, 1928.

[57] V. Fock, "Näherungsmethode zur lösung des quantenmechanischen mehrkörperproblems," *Zeitschrift für Physik*, vol. 61, pp. 126–148, Jan 1930.

[58] T. Koopmans, "Über die zuordnung von wellenfunktionen und eigenwerten zu den einzelnen elektronen eines atoms," *Physica*, vol. 1, no. 1, pp. 104 – 113, 1934.

[59] C. Møller and M. S. Plesset, "Note on an approximation treatment for many-electron systems," *Phys. Rev.*, vol. 46, pp. 618–622, 1934.

[60] H. Ehrenreich and M. H. Cohen, "Self-consistent field approach to the many-electron problem," *Phys. Rev.*, vol. 115, pp. 786–790, 1959.

[61] R. de L. Kronig, "On the theory of dispersion of x-rays," *J. Opt. Soc. Am.*, vol. 12, pp. 547–557, Jun 1926.

[62] R. M. Martin, *Electronic Structure: Basic Theory and Practical Methods*. Cambridge University Press, 2004.

[63] D. S. Sholl and J. A. Steckel, *Density Functional Theory*. John Wiley Sons, Ltd, 2009.

[64] P. A. M. Dirac, "Note on exchange phenomena in the thomas atom," *Mathematical Proceedings of the Cambridge Philosophical Society*, vol. 26, no. 3, p. 376–385, 1930.

[65] M. Gell-Mann and K. A. Brueckner, "Correlation energy of an electron gas at high density," *Phys. Rev.*, vol. 106, pp. 364–368, 1957.

[66] D. M. Ceperley and B. J. Alder, "Ground state of the electron gas by a stochastic method," *Phys. Rev. Lett.*, vol. 45, pp. 566–569, 1980.

[67] J. P. Perdew, J. A. Chevary, S. H. Vosko, K. A. Jackson, M. R. Pederson, D. J. Singh, and C. Fiolhais, "Atoms, molecules, solids, and surfaces: Applications of the generalized gradient approximation for exchange and correlation," *Phys. Rev. B*, vol. 46, pp. 6671–6687, 1992.

[68] J. P. Perdew, K. Burke, and M. Ernzerhof, "Generalized gradient approximation made simple," *Phys. Rev. Lett.*, vol. 77, pp. 3865–3868, 1996.

[69] H. Hellmann, "A new approximation method in the problem of many electrons," *J. Chem. Phys.*, vol. 3, 1935.

[70] P. E. Blöchl, "Projector augmented-wave method," *Phys. Rev. B*, vol. 50, pp. 17953–17979, 1994.

[71] F. Bloch, "Über die quantenmechanik der elektronen in kristallgittern," *Zeitschrift für Physik*, vol. 52, no. 7, pp. 555–600, 1929.

[72] S. F. Boys and M. V. Wilkes, "The integral formulae for the variational solution of the molecular many-electron wave equation in terms of gaussian functions with direct electronic correlation," *Proceedings of the Royal Society of London. Series A. Mathematical and Physical Sciences*, vol. 258, no. 1294, pp. 402–411, 1960.

[73] W. J. Hehre, R. F. Stewart, and J. A. Pople, "Self-consistent molecular-orbital methods. i. use of gaussian expansions of slater-type atomic orbitals," *The Journal of Chemical Physics*, vol. 51, no. 6, pp. 2657–2664, 1969.

[74] R. Ditchfield, W. J. Hehre, and J. A. Pople, "Self-consistent molecular-orbital methods. ix. an extended gaussian-type basis for molecular-orbital studies of organic molecules," *The Journal of Chemical Physics*, vol. 54, no. 2, pp. 724–728, 1971.

[75] H. Yang, A. Liang, C. Chen, C. Zhang, N. B. M. Schroeter, and Y. Chen, "Visualizing electronic structures of quantum materials by angle-resolved photoemission spectroscopy," *Nature Reviews Materials*, vol. 3, no. 9, pp. 341–353, 2018.

[76] G. D. Mahan, *Many-Particle Physics*. Springer, 2000.

[77] R. M. Martin, L. Reining, and D. Ceperly, *Interacting Electrons*. Cambridge University Press, 2016.

[78] S. L. Adler, "Quantum theory of the dielectric constant in real solids," *Phys. Rev.*, vol. 126, pp. 413–420, 1962.

[79] N. Wiser, "Dielectric constant with local field effects included," *Phys. Rev.*, vol. 129, pp. 62–69, 1963.

[80] T. Kotani, M. van Schilfgaarde, and S. V. Faleev, "Quasiparticle self-consistent *gw* method: A basis for the independent-particle approximation," *Phys. Rev. B*, vol. 76, p. 165106, 2007.

[81] E. E. Salpeter and H. A. Bethe, "A relativistic equation for bound-state problems," *Phys. Rev.*, vol. 84, pp. 1232–1242, 1951.

[82] F. Bechstedt, *Many-Body Approach to Electronic Excitations*, vol. 181. Springer, 1 ed., 2015.

[83] S. M. Dancoff, "Non-adiabatic meson theory of nuclear forces," *Phys. Rev.*, vol. 78, pp. 382–385, 1950.

[84] T. Sander, E. Maggio, and G. Kresse, "Beyond the tamm-dancoff approximation for extended systems using exact diagonalization," *Phys. Rev. B*, vol. 92, p. 045209, 2015.

[85] F. Fuchs, C. Rödl, A. Schleife, and F. Bechstedt, "Efficient $\mathcal{O}(N^2)$ approach to solve the bethe-salpeter equation for excitonic bound states," *Phys. Rev. B*, vol. 78, p. 085103, Aug 2008.

[86] F. Fuchs, C. Rödl, A. Schleife, and F. Bechstedt, "Efficient $\mathcal{O}(N^2)$ approach to solve the bethe-salpeter equation for excitonic bound states," *Phys. Rev. B*, vol. 78, p. 085103, Aug 2008.

[87] G. Cappellini, R. Del Sole, L. Reining, and F. Bechstedt, "Model dielectric function for semiconductors," *Phys. Rev. B*, vol. 47, pp. 9892–9895, 1993.

[88] P. H. Hahn, W. G. Schmidt, and F. Bechstedt, "Bulk excitonic effects in surface optical spectra," *Phys. Rev. Lett.*, vol. 88, p. 016402, 2001.

[89] K. F. Berggren and B. E. Sernelius, "Band-gap narrowing in heavily doped many-valley semiconductors," *Phys. Rev. B*, vol. 24, pp. 1971–1986, 1981.

[90] N. W. Ashcroft and N. D. Mermin, *Solid State Physics*. Holt, Rinehart and Winston, 1976.

[91] A. Schleife, C. Rödl, F. Fuchs, K. Hannewald, and F. Bechstedt, "Optical absorption in degenerately doped semiconductors: Mott transition or mahan excitons?," *Phys. Rev. Lett.*, vol. 107, p. 236405, Nov 2011.

[92] A. Kronenberger, A. Polity, D. M. Hofmann, B. K. Meyer, A. Schleife, and F. Bechstedt, "Structural, electrical, and optical properties of hydrogen-doped zno films," *Phys. Rev. B*, vol. 86, p. 115334, 2012.

[93] F. Giustino, "Electron-phonon interactions from first principles," *Rev. Mod. Phys.*, vol. 89, p. 015003, Feb 2017.

[94] X. Gonze and C. Lee, "Dynamical matrices, born effective charges, dielectric permittivity tensors, and interatomic force constants from density-functional perturbation theory," *Phys. Rev. B*, vol. 55, pp. 10355–10368, 1997.

[95] M. Born and K. Huang, "Dynamical theory of crystal lattices," *Acta Crystallographica Section A*, vol. 26, p. 702, Nov 1970.

[96] O. Dolgov and M. E.G., "The dielectric function of crystalline systems," *Modern problems in condensed matter physics*, vol. 24, pp. 221 – 298, 1989.

[97] R. H. Lyddane, R. G. Sachs, and E. Teller, "On the polar vibrations of alkali halides," *Phys. Rev.*, vol. 59, pp. 673–676, 1941.

[98] J. Bardeen, "Conductivity of monovalent metals," *Phys. Rev.*, vol. 52, pp. 688–697, 1937.

[99] H. Fröhlich, H. Pelzer, and S. Zienau, "Properties of slow electrons in polar materials," *The London, Edinburgh, and Dublin Philosophical Magazine and Journal of Science*, vol. 41, no. 314, pp. 221–242, 1950.

[100] C. Verdi and F. Giustino, "Fröhlich electron-phonon vertex from first principles," *Phys. Rev. Lett.*, vol. 115, p. 176401, Oct 2015.

[101] H. Y. Fan, "Temperature dependence of the energy gap in semiconductors," *Phys. Rev.*, vol. 82, pp. 900–905, 1951.

[102] A. B. Migdal, "Interaction between electrons and lattice vibrations in a normal metal," *JETP*, vol. 6, p. 996, 1958.

[103] K. Shindo, "Effective electron-hole interaction in shallow excitons," *Journal of the Physical Society of Japan*, vol. 29, no. 2, pp. 287–296, 1970.

[104] R. Zimmermann, "Dynamical screening of the wannier exciton," *physica status solidi (b)*, vol. 48, no. 2, pp. 603–618, 1971.

[105] S. Poncé, E. Margine, C. Verdi, and F. Giustino, "Epw: Electron–phonon coupling, transport and superconducting properties using maximally localized wannier functions," *Computer Physics Communications*, vol. 209, pp. 116 – 133, 2016.

[106] H. Haken, "Zur quantentheorie des mehrelektronensystems im schwingenden gitter. i," *Zeitschrift für Physik*, vol. 146, pp. 527–554, Oct 1956.

[107] O. Gunnarsson and B. I. Lundqvist, "Exchange and correlation in atoms, molecules, and solids by the spin-density-functional formalism," *Phys. Rev. B*, vol. 13, pp. 4274–4298, May 1976.

[108] M. Marques and E. Gross, "Time-dependent density functional theory," *Ann Rev Phys Chem*, vol. 55, no. 1, pp. 427–455, 2004.

[109] E. Runge and E. K. U. Gross, "Density-functional theory for time-dependent systems," *Phys. Rev. Lett.*, vol. 52, pp. 997–1000, 1984.

[110] M. E. Casida, *Time-Dependent Density Functional Response Theory for Molecules*, pp. 155–192. World Scientific, 1995.

[111] K. Lopata, B. E. Van Kuiken, M. Khalil, and N. Govind, "Linear-response and real-time time-dependent density functional theory studies of core-level near-edge x-ray absorption," *Journal of Chemical Theory and Computation*, vol. 8, no. 9, pp. 3284–3292, 2012.

[112] M. J. G. Peach, M. J. Williamson, and D. J. Tozer, "Influence of triplet instabilities in tddft," *Journal of Chemical Theory and Computation*, vol. 7, no. 11, pp. 3578–3585, 2011.

[113] F. Alary, M. Boggio-Pasqua, J.-L. Heully, C. J. Marsden, and P. Vicendo, "Theoretical characterization of the lowest triplet excited states of the tris-(1,4,5,8-tetraazaphenanthrene) ruthenium dication complex," *Inorganic Chemistry*, vol. 47, no. 12, pp. 5259–5266, 2008. PMID: 18491894.

[114] B. A. Gregg, "Excitonic solar cells," *J. Phys. Chem. B*, vol. 107, no. 20, pp. 4688–4698, 2003.

[115] X. Chen, H. Lu, Y. Yang, and M. C. Beard, "Excitonic effects in methylammonium lead halide perovskites," *J. Phys. Chem. Lett.*, vol. 9, no. 10, pp. 2595–2603, 2018.

[116] N. Sestu, M. Cadelano, V. Sarritzu, F. Chen, D. Marongiu, R. Piras, M. Mainas, F. Quochi, M. Saba, A. Mura, and G. Bongiovanni, "Absorption F-Sum Rule for the Exciton Binding Energy in Methylammonium Lead Halide Perovskites," *J. Phys. Chem. Lett.*, vol. 6, pp. 4566–4572, 2015.

[117] K. Galkowski, A. Mitioglu, A. Miyata, P. Plochocka, O. Portugall, G. E. Eperon, J. T.-W. Wang, T. Stergiopoulos, S. D. Stranks, H. J. Snaith, and R. J. Nicholas, "Determination of the exciton binding energy and effective masses for methylammonium and formamidinium lead tri-halide perovskite semiconductors," *Energy Environ. Sci.*, vol. 9, pp. 962–970, 2016.

[118] Y. Yang, D. P. Ostrowski, R. M. France, K. Zhu, J. van de Lagemaat, J. M. Luther, and M. C. Beard, "Observation of a hot-phonon bottleneck in lead-iodide perovskites," *Nat. Photonics*, vol. 10, p. 53, 2015.

[119] V. D'Innocenzo, G. Grancini, M. J. P. Alcocer, A. R. S. Kandada, S. D. Stranks, M. M. Lee, G. Lanzani, H. J. Snaith, and A. Petrozza, "Excitons versus free charges in organo-lead tri-halide perovskites," *Nat. Comm.*, vol. 5, p. 3586, 2014.

[120] T. J. Savenije, C. S. Ponseca, L. Kunneman, M. Abdellah, K. Zheng, Y. Tian, Q. Zhu, S. E. Canton, I. G. Scheblykin, T. Pullerits, A. Yartsev, and V. Sundström, "Thermally activated exciton dissociation and recombination control the carrier dynamics in organometal halide perovskite," *J. Phys. Chem. Lett.*, vol. 5, no. 13, pp. 2189–2194, 2014.

[121] Q. Lin, A. Armin, R. C. R. Nagiri, P. L. Burn, and P. Meredith, "Electro-optics of perovskite solar cells," *Nat. Photonics*, vol. 9, p. 106, 2014.

[122] A. Miyata, A. Mitioglu, P. Plochocka, O. Portugall, J. T.-W. Wang, S. D. Stranks, H. J. Snaith, and R. J. Nicholas, "Direct measurement of the exciton binding energy and effective masses for charge carriers in organic–inorganic tri-halide perovskites," *Nat. Phys.*, vol. 11, p. 582, 2015.

[123] S. Sun, T. Salim, N. Mathews, M. Duchamp, C. Boothroyd, G. Xing, T. C. Sum, and Y. M. Lam, "The origin of high efficiency in low-temperature solution-processable bilayer organometal halide hybrid solar cells," *Energy Environ. Sci.*, vol. 7, pp. 399–407, 2014.

[124] W. S. Yang, B.-W. Park, E. H. Jung, N. J. Jeon, Y. C. Kim, D. U. Lee, S. S. Shin, J. Seo, E. K. Kim, J. H. Noh, and S. I. Seok, "Iodide management in formamidinium-lead-halide–based perovskite layers for efficient solar cells," *Science*, vol. 356, no. 6345, pp. 1376–1379, 2017.

[125] S. A. March, C. Clegg, D. B. Riley, D. Webber, I. G. Hill, and K. C. Hall, "Simultaneous observation of free and defect-bound excitons in ch3nh3pbi3 using four-wave mixing spectroscopy," *Sci. Rep.*, vol. 6, p. 39139, 2016.

[126] K. Wu, A. Bera, C. Ma, Y. Du, Y. Yang, L. Li, and T. Wu, "Temperature-dependent excitonic photoluminescence of hybrid organometal halide perovskite films," *Phys. Chem. Chem. Phys.*, vol. 16, pp. 22476–22481, 2014.

[127] M. Bokdam, T. Sander, A. Stroppa, S. Picozzi, D. D. Sarma, C. Franchini, and G. Kresse, "Role of polar phonons in the photo excited state of metal halide perovskites," *Sci. Rep.*, vol. 6, p. 28618, 2016.

[128] J. M. Frost, K. T. Butler, F. Brivio, C. H. Hendon, M. van Schilfgaarde, and A. Walsh, "Atomistic origins of high-performance in hybrid halide perovskite solar cells," *Nano Lett.*, vol. 14, no. 5, pp. 2584–2590, 2014.

[129] E. Menéndez-Proupin, C. L. Beltrán Ríos, and P. Wahnón, "Nonhydrogenic exciton spectrum in perovskite ch3nh3pbi3," *Phys. Status Solidi R.*, vol. 9, no. 10, pp. 559–563, 2015.

[130] T. Hakamata, K. Shimamura, F. Shimojo, R. K. Kalia, A. Nakano, and P. Vashishta, "The nature of free-carrier transport in organometal halide perovskites," *Sci. Rep.*, vol. 6, p. 19599, 2016.

[131] W.-J. Yin, T. Shi, and Y. Yan, "Unusual defect physics in ch3nh3pbi3 perovskite solar cell absorber," *Appl. Phys. Lett.*, vol. 104, no. 6, p. 063903, 2014.

[132] J. Kim, S.-H. Lee, J. H. Lee, and K.-H. Hong, "The role of intrinsic defects in methylammonium lead iodide perovskite," *J. Phys. Chem. Lett.*, vol. 5, no. 8, pp. 1312–1317, 2014.

[133] N. Liu and C. Yam, "First-principles study of intrinsic defects in formamidinium lead triiodide perovskite solar cell absorbers," *Phys. Chem. Chem. Phys.*, vol. 20, pp. 6800–6804, 2018.

[134] J.-H. Yang, W.-J. Yin, J.-S. Park, and S.-H. Wei, "Self-regulation of charged defect compensation and formation energy pinning in semiconductors," *Sci. Rep.*, vol. 5, p. 16977, 2015.

[135] A. Schleife, C. Rödl, F. Fuchs, K. Hannewald, and F. Bechstedt, "Optical absorption in degenerately doped semiconductors: Mott transition or Mahan excitons?," *Phys. Rev. Lett.*, vol. 107, p. 236405, 2011.

[136] K. Kang, A. Kononov, C.-W. Lee, J. A. Leveillee, E. P. Shapera, X. Zhang, and A. Schleife, "Pushing the frontiers of modeling excited electronic states and dynamics to accelerate materials engineering and design," *Comp. Mater. Sci.*, vol. 160, pp. 207 – 216, 2019.

[137] G. D. Mahan, "Excitons in degenerate semiconductors," *Phys. Rev.*, vol. 153, pp. 882–889, Jan 1967.

[138] J. Leveillee and A. Schleife, "Free-electron effects on the optical absorption of the hybrid perovskite $ch_3nh_3pbi_3$ from first principles," *Phys. Rev. B*, vol. 100, p. 035205, 2019.

[139] J. P. Perdew, A. Ruzsinszky, G. I. Csonka, O. A. Vydrov, G. E. Scuseria, L. A. Constantin, X. Zhou, and K. Burke, "Restoring the density-gradient expansion for exchange in solids and surfaces," *Phys. Rev. Lett.*, vol. 100, p. 136406, 2008.

[140] F. Brivio, J. M. Frost, J. M. Skelton, A. J. Jackson, O. J. Weber, M. T. Weller, A. R. Goñi, A. M. A. Leguy, P. R. F. Barnes, and A. Walsh, "Lattice dynamics and vibrational spectra of the orthorhombic, tetragonal, and cubic phases of methylammonium lead iodide," *Phys. Rev. B*, vol. 92, p. 144308, 2015.

[141] P. S. Whitfield, N. Herron, W. E. Guise, K. Page, Y. Q. Cheng, I. Milas, and M. K. Crawford, "Structures, phase transitions and tricritical behavior of the hybrid perovskite methyl ammonium lead iodide," *Sci. Rep.*, vol. 6, p. 35685, 10 2016.

[142] K. T. Butler, J. M. Frost, and A. Walsh, "Band alignment of the hybrid halide perovskites ch3nh3pbcl3, ch3nh3pbbr3 and ch3nh3pbi3," *Mater. Horiz.*, vol. 2, pp. 228–231, 2015.

[143] F. F. Targhi, Y. S. Jalili, and F. Kanjouri, "Mapbi3 and fapbi3 perovskites as solar cells: Case study on structural, electrical and optical properties," *Results Phys.*, vol. 10, pp. 616 – 627, 2018.

[144] M. Gajdoš, K. Hummer, G. Kresse, J. Furthmüller, and F. Bechstedt, "Linear optical properties in the projector-augmented wave methodology," *Phys. Rev. B*, vol. 73, p. 045112, 2006.

[145] P. Umari, E. Mosconi, and F. Angelis, "Relativistic GW calculations on $ch_3nh_3pbi_3$ and $ch_3nh_3sni_3$ Perovskites for Solar Cell Applications," *Sci. Rep.*, vol. 4, no. 4, p. 4467, 2014.

[146] S. Steiner, S. Khmelevskyi, M. Marsmann, and G. Kresse, "Calculation of the magnetic anisotropy with projected-augmented-wave methodology and the case study of disordered $fe_{1-x}co_x$ alloys," *Phys. Rev. B*, vol. 93, p. 224425, 2016.

[147] M. Rohlfing and S. G. Louie, "Electron-hole excitations and optical spectra from first principles," *Phys. Rev. B*, vol. 62, pp. 4927–4944, Aug 2000.

[148] F. Bechstedt, R. D. Sole, G. Cappellini, and L. Reining, "An efficient method for calculating quasiparticle energies in semiconductors," *Solid State Commun.*, vol. 84, pp. 765–770, 1992.

[149] G. Cappellini, R. Del Sole, L. Reining, and F. Bechstedt, "Model dielectric function for semiconductors," *Phys. Rev. B*, vol. 47, pp. 9892–9895, Apr 1993.

[150] F. Fuchs, C. Rödl, A. Schleife, and F. Bechstedt, "Efficient $\mathcal{O}(N^2)$ approach to solve the Bethe-Salpeter equation for excitonic bound states," *Phys. Rev. B*, vol. 78, p. 085103, 2008.

[151] A. Schleife, *Electronic and optical properties of MgO, ZnO, and CdO*. Südwestdeutscher Verlag für Hochschulschriften, 2011.

[152] A. Schleife, *Exciting Imperfection: Real-structure effects in magnesium-, cadmium-, and zinc-oxide*. Phd thesis, Friedrich-Schiller-Universität, Jena, 2010.

[153] H. Peelaers, E. Kioupakis, and C. G. Van de Walle, "Free-carrier absorption in transparent conducting oxides: Phonon and impurity scattering in sno_2," *Phys. Rev. B*, vol. 92, p. 235201, 2015.

[154] G. Kresse and D. Joubert, "From ultrasoft pseudopotentials to the projector augmented-wave method," *Phys. Rev. B*, vol. 59, pp. 1758–1775, 1999.

[155] G. Kresse and J. Furthmüller, "Efficiency of ab-initio total energy calculations for metals and semiconductors using a plane-wave basis set," *Comp. Mater. Sci.*, vol. 6, pp. 15–50, 1996.

[156] M. Shishkin and G. Kresse, "Implementation and performance of the frequency-dependent *GW* method within the PAW framework," *Phys. Rev. B*, vol. 74, p. 035101, 2006.

[157] C. Rödl, F. Fuchs, J. Furthmüller, and F. Bechstedt, "Ab initio theory of excitons and optical properties for spin-polarized systems: Application to antiferromagnetic MnO," *Phys. Rev. B*, vol. 77, p. 184408, 2008.

[158] J. Leveillee and A. Schleife, "Data set for free-electron effects on optical absorption of hybrid perovskite $ch_3nh_3pbi_3$ from first principles," 2019.

[159] X. Qian, X. Gu, and R. Yang, "Lattice thermal conductivity of organic-inorganic hybrid perovskite ch3nh3pbi3," *Appl. Phys. Lett.*, vol. 108, no. 6, p. 063902, 2016.

[160] W. Kong, Z. Ye, Z. Qi, B. Zhang, M. Wang, A. Rahimi-Iman, and H. Wu, "Characterization of an abnormal photoluminescence behavior upon crystal-phase transition of perovskite ch3nh3pbi3," *Phys. Chem. Chem. Phys.*, vol. 17, pp. 16405–16411, 2015.

[161] K. P. Ong, T. W. Goh, Q. Xu, and A. Huan, "Structural evolution in methylammonium lead iodide ch3nh3pbi3," *J. Phys. Chem. A*, vol. 119, no. 44, pp. 11033–11038, 2015.

[162] A. S. Thind, X. Huang, J. Sun, and R. Mishra, "First-principles prediction of a stable hexagonal phase of ch3nh3pbi3," *Chem. Mater.*, vol. 29, no. 14, pp. 6003–6011, 2017.

[163] C. Quarti, E. Mosconi, J. M. Ball, V. D'Innocenzo, C. Tao, S. Pathak, H. J. Snaith, A. Petrozza, and F. De Angelis, "Structural and optical properties of methylammonium lead iodide across the tetragonal to cubic phase transition: implications for perovskite solar cells," *Energy Environ. Sci.*, vol. 9, pp. 155–163, 2016.

[164] M. R. Filip, C. Verdi, and F. Giustino, "Gw band structures and carrier effective masses of ch3nh3pbi3 and hypothetical perovskites of the type apbi3: A = nh4, ph4, ash4, and sbh4," *J. Phys. Chem. C*, vol. 119, no. 45, pp. 25209–25219, 2015.

[165] F. Brivio, K. T. Butler, A. Walsh, and M. van Schilfgaarde, "Relativistic quasiparticle self-consistent electronic structure of hybrid halide perovskite photovoltaic absorbers," *Phys. Rev. B*, vol. 89, p. 155204, 2014.

[166] M. A. Pérez-Osorio, R. L. Milot, M. R. Filip, J. B. Patel, L. M. Herz, M. B. Johnston, and F. Giustino, "Vibrational properties of the organic–inorganic halide perovskite ch3nh3pbi3 from theory and experiment: Factor group analysis, first-principles calculations, and low-temperature infrared spectra," *J. Phys. Chem. C*, vol. 119, no. 46, pp. 25703–25718, 2015.

[167] M. Sendner, P. K. Nayak, D. A. Egger, S. Beck, C. Muller, B. Epding, W. Kowalsky, L. Kronik, H. J. Snaith, A. Pucci, and R. Lovrincic, "Optical phonons in methylammonium lead halide perovskites and implications for charge transport," *Mater. Horiz.*, vol. 3, pp. 613–620, 2016.

[168] A. Poglitsch and D. Weber, "Dynamic disorder in methylammoniumtrihalogenoplumbates (ii) observed by millimeter-wave spectroscopy," *J. Chem. Phys.*, vol. 87, no. 11, pp. 6373–6378, 1987.

[169] J. Feng and B. Xiao, "Crystal structures, optical properties, and effective mass tensors of ch3nh3pbx3 (x = i and br) phases predicted from hse06," *J. Phys. Chem. Lett.*, vol. 5, no. 7, pp. 1278–1282, 2014.

[170] G. Giorgi, J.-I. Fujisawa, H. Seqawa, and K. Yamashita, "Small photocarrier effective masses featuring ambipolar transport in methylammonium lead iodide perovskite: A density functional analysis," *J. Phys. Chem. Lett.*, vol. 4, pp. 4213–4216, 2013.

[171] J. Even, L. Pedesseau, J.-M. Jancu, and C. K. Katan, "Importance of Spin–Orbit Coupling in Hybrid Organic/Inorganic Perovskites for Photovoltaic Applications," *J. Phys. Chem. Lett.*, vol. 4, pp. 2999–3005, 2013.

[172] E. Mosconi, P. Umari, and F. De Angelis, "Electronic and optical properties of mapbx3 perovskites (x = i, br, cl): a unified dft and gw theoretical analysis," *Phys. Chem. Chem. Phys.*, vol. 18, pp. 27158–27164, 2016.

[173] N.-G. Park, "Perovskite solar cells: an emerging photovoltaic technology," *Mater. Today*, vol. 18, no. 2, pp. 65 – 72, 2015.

[174] T. Etienne, E. Mosconi, and F. De Angelis, "Dynamical origin of the rashba effect in organohalide lead perovskites: A key to suppressed carrier recombination in perovskite solar cells?," *J. Phys. Chem. Lett.*, vol. 7, no. 9, pp. 1638–1645, 2016.

[175] E. Mosconi, T. Etienne, and F. De Angelis, "Rashba band splitting in organohalide lead perovskites: Bulk and surface effects," *J. Phys. Chem. Lett.*, vol. 8, no. 10, pp. 2247–2252, 2017.

[176] J. S. Manser and P. V. Kamat, "Band filling with free charge carriers in organometal halide perovskites," *Nat. Photonics*, vol. 8, p. 737, 2014.

[177] M. Shirayama, H. Kadowaki, T. Miyadera, T. Sugita, M. Tamakoshi, M. Kato, T. Fujiseki, D. Murata, S. Hara, T. N. Murakami, S. Fujimoto, M. Chikamatsu, and H. Fujiwara, "Optical transitions in hybrid perovskite solar cells: Ellipsometry, density functional theory, and quantum efficiency analyses for $ch_3nh_3pbi_3$," *Phys. Rev. Applied*, vol. 5, p. 014012, 2016.

[178] C.-W. Chen, S.-Y. Hsiao, C.-Y. Chen, H.-W. Kang, Z.-Y. Huang, and H.-W. Lin, "Optical properties of organometal halide perovskite thin films and general device structure design rules for perovskite single and tandem solar cells," *J. Mater. Chem. A*, vol. 3, pp. 9152–9159, 2015.

[179] P. Löper, M. Stuckelberger, B. Niesen, J. Werner, M. Filipič, S.-J. Moon, J.-H. Yum, M. Topič, S. D. Wolf, and C. Ballif, "Complex refractive index spectra of ch3nh3pbi3 perovskite thin films determined by spectroscopic ellipsometry and spectrophotometry," *J. Phys. Chem. Lett.*, vol. 6, no. 1, pp. 66–71, 2015.

[180] F. Bechstedt, K. Seino, P. H. Hahn, and W. G. Schmidt, "Quasiparticle bands and optical spectra of highly ionic crystals: Aln and nacl," *Phys. Rev. B*, vol. 72, p. 245114, 2005.

[181] J. Fu, Q. Xu, G. Han, B. Wu, C. H. A. Huan, M. L. Leek, and T. C. Sum, "Hot carrier cooling mechanisms in halide perovskites," *Nat. Comm.*, vol. 8, no. 1, p. 1300, 2017.

[182] D. A. Valverde-Chávez, C. S. Ponseca, C. C. Stoumpos, A. Yartsev, M. G. Kanatzidis, V. Sundström, and D. G. Cooke, "Intrinsic femtosecond charge generation dynamics in single crystal $ch_3nh_3pbi_3$," *Energy Environ. Sci.*, vol. 8, pp. 3700–3707, 2015.

[183] D. Shi, V. Adinolfi, R. Comin, M. Yuan, E. Alarousu, A. Buin, Y. Chen, S. Hoogland, A. Rothenberger, K. Katsiev, Y. Losovyj, X. Zhang, P. A. Dowben, O. F. Mohammed, E. H. Sargent, and O. M. Bakr, "Low trap-state density and long carrier diffusion in organolead trihalide perovskite single crystals," *Science*, vol. 347, no. 6221, pp. 519–522, 2015.

[184] A. Schleife, M. D. Neumann, N. Esser, Z. Galazka, A. Gottwald, J. Nixdorf, R. Goldhahn, and M. Feneberg, "Optical properties of in2o3 from experiment and first-principles theory: influence of lattice screening," *New Journal of Physics*, vol. 20, no. 5, p. 053016, 2018.

[185] J. P. Nery and P. B. Allen, "Influence of fröhlich polaron coupling on renormalized electron bands in polar semiconductors: Results for zinc-blende gan," *Phys. Rev. B*, vol. 94, p. 115135, Sep 2016.

[186] J. Pollmann and H. Büttner, "Effective hamiltonians and bindings energies of wannier excitons in polar semiconductors," *Phys. Rev. B*, vol. 16, pp. 4480–4490, Nov 1977.

[187] G. Kresse and J. Hafner, "Ab initio molecular dynamics for liquid metals," *Phys. Rev. B*, vol. 47, pp. 558–561, 1993.

[188] G. Kresse and J. Furthmüller, "Efficient iterative schemes for ab initio total-energy calculations using a plane-wave basis set," *Phys. Rev. B*, vol. 54, pp. 11169–11186, 1996.

[189] P. Giannozzi, S. Baroni, N. Bonini, M. Calandra, R. Car, C. Cavazzoni, D. Ceresoli, G. L. Chiarotti, M. Cococcioni, I. Dabo, A. D. Corso, S. de Gironcoli, S. Fabris, G. Fratesi, R. Gebauer, U. Gerstmann, C. Gougoussis, A. Kokalj, M. Lazzeri, L. Martin-Samos, N. Marzari, F. Mauri, R. Mazzarello, S. Paolini, A. Pasquarello, L. Paulatto, C. Sbraccia, S. Scandolo, G. Sclauzero, A. P. Seitsonen,

A. Smogunov, P. Umari, and R. M. Wentzcovitch, "QUANTUM ESPRESSO: a modular and open-source software project for quantum simulations of materials," *Journal of Physics: Condensed Matter*, vol. 21, no. 39, p. 395502, 2009.

[190] S. Heo, E. Cho, H.-I. Lee, G. S. Park, H. J. Kang, T. Nagatomi, P. Choi, and B.-D. Choi, "Band gap and defect states of mgo thin films investigated using reflection electron energy loss spectroscopy," *AIP Advances*, vol. 5, no. 7, p. 077167, 2015.

[191] L. M. R. S. Bougrov, V. and A. Zubrilov. Wiley, 2001.

[192] Q. Guo and A. Yoshida, "Temperature dependence of band gap change in InN and AlN," *Japanese Journal of Applied Physics*, vol. 33, pp. 2453–2456, may 1994.

[193] O. Madelung, U. Rössler, and M. Schulz, eds., *Aluminum nitride (AlN), energy gap*, pp. 1–4. 2002.

[194] R. T. Poole, J. Liesegang, R. C. G. Leckey, and J. G. Jenkin, "Electronic band structure of the alkali halides. ii. critical survey of theoretical calculations," *Phys. Rev. B*, vol. 11, pp. 5190–5196, 1975.

[195] D. M. Roessler and W. C. Walker, "Electronic spectra of crystalline nacl and kcl," *Phys. Rev.*, vol. 166, pp. 599–606, Feb 1968.

[196] O. Madelung, U. Rössler, and M. Schulz, eds., *Magnesium oxide (MgO) dielectric constants, optical and photoelectric properties*, pp. 1–12. Springer Berlin Heidelberg, 1999.

[197] A. T. Collins, E. C. Lightowlers, and P. J. Dean, "Lattice vibration spectra of aluminum nitride," *Phys. Rev.*, vol. 158, pp. 833–838, Jun 1967.

[198] M. C. Robinson and A. C. H. Hallett, "The static dielectric constant of nacl, kcl, and kbr at temperatures between 4.2 °k and 300 °k," *Canadian Journal of Physics*, vol. 44, no. 10, pp. 2211–2230, 1966.

[199] A. S. Barker and M. Ilegems, "Infrared lattice vibrations and free-electron dispersion in gan," *Phys. Rev. B*, vol. 7, pp. 743–750, Jan 1973.

[200] J. Watson, F. Wiffen, J. Bishop, and B. Breeden, "Radiation effects and tritium technology for fusion reactors. volume iii. proceedings of the international conference held at gatlinburg, tennessee, october 1–3, 1975," 3 1976.

[201] G. Raunio, L. Almqvist, and R. Stedman, "Phonon dispersion relations in nacl," *Phys. Rev.*, vol. 178, pp. 1496–1501, 1969.

[202] R. Whited, C. J. Flaten, and W. Walker, "Exciton thermoreflectance of mgo and cao," *Solid State Communications*, vol. 13, no. 11, pp. 1903 – 1905, 1973.

[203] W. Shan, B. D. Little, A. J. Fischer, J. J. Song, B. Goldenberg, W. G. Perry, M. D. Bremser, and R. F. Davis, "Binding energy for the intrinsic excitons in wurtzite gan," *Phys. Rev. B*, vol. 54, pp. 16369–16372, 1996.

[204] M. Feneberg, R. A. R. Leute, B. Neuschl, K. Thonke, and M. Bickermann, "High-excitation and high-resolution photoluminescence spectra of bulk aln," *Phys. Rev. B*, vol. 82, p. 075208, 2010.

[205] J. Wang, Y. Tu, L. Yang, and H. Tolner, "Theoretical investigation of the electronic structure and optical properties of zinc-doped magnesium oxide," *J. Comp. Elec.*, vol. 15, no. 4, pp. 1521–1530, 2016.

[206] M. Röppischer, R. Goldhahn, G. Rossbach, P. Schley, C. Cobet, N. Esser, T. Schupp, K. Lischka, and D. J. As, "Dielectric function of zinc-blende aln from 1 to 20 ev: Band gap and van hove singularities," *Journal of Applied Physics*, vol. 106, no. 7, p. 076104, 2009.

[207] A. B. Djurišić and E. H. Li, "Dielectric function models for describing the optical properties of hexagonal gan," *Journal of Applied Physics*, vol. 89, no. 1, pp. 273–282, 2001.

[208] Z. Yang, A. Surrente, K. Galkowski, N. Bruyant, D. K. Maude, A. A. Haghighirad, H. J. Snaith, P. Plochocka, and R. J. Nicholas, "Unraveling the exciton binding energy and the dielectric constant in single-crystal methylammonium lead triiodide perovskite," *J. Phys. Chem. Lett.*, vol. 8, no. 8, pp. 1851–1855, 2017.

[209] E. L. Lucas and E. R. Jarvo, "Keeping track of the electrons," *Accounts Chem Res*, vol. 51, no. 2, pp. 567–572, 2018.

[210] J. Zhou, Y. Chu, and J. Huang, "Photodetectors based on two-dimensional layer-structured hybrid lead iodide perovskite semiconductors," *ACS Applied Materials & Interfaces*, vol. 8, no. 39, pp. 25660–25666, 2016.

[211] J. Even, L. Pedesseau, and C. Katan, "Understanding quantum confinement of charge carriers in layered 2d hybrid perovskites," *Chem Phys Chem*, vol. 15, no. 17, pp. 3733–3741, 2014.

[212] B. Traore, L. Pedesseau, L. Assam, X. Che, J.-C. Blancon, H. Tsai, W. Nie, C. C. Stoumpos, M. G. Kanatzidis, S. Tretiak, A. D. Mohite, J. Even, M. Kepenekian, and C. Katan, "Composite nature of layered hybrid perovskites: Assessment on quantum and dielectric confinements and band alignment," *ACS Nano*, vol. 12, no. 4, pp. 3321–3332, 2018.

[213] J. Even, L. Pedesseau, J. Jancu, and C. Katan, "Dft and k · p modelling of the phase transitions of lead and tin halide perovskites for photovoltaic cells," *Phys Status Solidi - R*, vol. 8, no. 1, pp. 31–35, 2014.

[214] H. Tsai, W. Nie, J.-C. Blancon, C. C. Stoumpos, R. Asadpour, B. Harutyunyan, A. J. Neukirch, R. Verduzco, J. J. Crochet, S. Tretiak, L. Pedesseau, J. Even, M. A. Alam, G. Gupta, J. Lou, P. M. Ajayan, M. J. Bedzyk, M. G. Kanatzidis, and A. D. Mohite, "High-efficiency two-dimensional ruddlesden–popper perovskite solar cells," *Nature*, vol. 536, pp. 312–316, 2016.

[215] N. Kawano, M. Koshimizu, Y. Sun, N. Yahaba, Y. Fujimoto, T. Yanagida, and K. Asai, "Effects of organic moieties on luminescence properties of organic–inorganic layered perovskite-type compounds," *J Phys Chem C*, vol. 118, no. 17, pp. 9101–9106, 2014.

[216] S. N. Ruddlesden and P. Popper, "The Compound $Sr_3Ti_2O_7$ and its Structure," *Acta. Crystallogr.*, vol. 11, no. 1, pp. 54–55, 1958.

[217] G. Papavassiliou, "Three- and low-dimensional inorganic semiconductors," *Prog Solid State Ch*, vol. 25, no. 3, pp. 125 – 270, 1997.

[218] D. B. Mitzi, K. Chondroudis, and C. R. Kagan, "Design, structure, and optical properties of organic-inorganic perovskites containing an oligothiophene chromophore," *Inorganic Chemistry*, vol. 38, no. 26, pp. 6246–6256, 1999. PMID: 11671340.

[219] N. Mercier, N. Louvain, and W. Bi, "Structural diversity and retro-crystal engineering analysis of iodometalate hybrids," *Cryst Eng Comm*, vol. 11, pp. 720–734, 2009.

[220] J.-C. Blancon, H. Tsai, W. Nie, C. C. Stoumpos, L. Pedesseau, C. Katan, M. Kepenekian, C. M. M. Soe, K. Appavoo, M. Y. Sfeir, S. Tretiak, P. M. Ajayan, M. G. Kanatzidis, J. Even, J. J. Crochet, and A. D. Mohite, "Extremely efficient internal exciton dissociation through edge states in layered 2d perovskites," *Science*, vol. 355, no. 6331, pp. 1288–1292, 2017.

[221] M. Braun, W. Tuffentsammer, H. Wachtel, and H. Wolf, "Pyrene as emitting chromophore in organic–inorganic lead halide-based layered perovskites with different halides," *Chemical Physics Letters*, vol. 307, no. 5, pp. 373 – 378, 1999.

[222] M. Era, K. Maeda, and T. Tsutsui, "Enhanced phosphorescence from naphthalene-chromophore incorporated into lead bromide-based layered perovskite having organic–inorganic superlattice structure," *Chem. Phys. Lett.*, vol. 296, no. 3, pp. 417 – 420, 1998.

[223] K. Ema, M. Inomata, Y. Kato, H. Kunugita, and M. Era, "Nearly perfect triplet-triplet energy transfer from wannier excitons to naphthalene in organic-inorganic hybrid quantum-well materials," *Phys. Rev. Lett.*, vol. 100, pp. 257401–257404, 2008.

[224] R. H. Friend, R. W. Gymer, A. B. Holmes, J. H. Burroughes, R. N. Marks, C. Taliani, D. D. C. Bradley, D. A. D. Santos, J. L. Brédas, M. Lögdlund, and W. R. Salaneck, "Electroluminescence in conjugated polymers," *Nature*, vol. 397, pp. 121 EP –, 1999.

[225] L. Rothberg, M. Yan, F. Papadimitrakopoulos, M. Galvin, E. Kwock, and T. Miller, "Photophysics of phenylenevinylene polymers," *Synthetic Met*, vol. 80, no. 1, pp. 41 – 58, 1996.

[226] N. C. Greenham, X. Peng, and A. P. Alivisatos, "Charge separation and transport in conjugated-polymer/semiconductor-nanocrystal composites studied by photoluminescence quenching and photoconductivity," *Phys. Rev. B*, vol. 54, pp. 17628–17637, Dec 1996.

[227] Y. Y. Li, C. K. Lin, G. L. Zheng, Z. Y. Cheng, H. You, W. D. Wang, and J. Lin, "Novel 110-oriented organicinorganic perovskite compound stabilized by n-(3-aminopropyl) imidazole with improved optical properties," *Chem. Mater.*, vol. 18, no. 15, pp. 3463–3469, 2006.

[228] J. Even, L. Pedesseau, J.-M. Jancu, and C. Katan, "Importance of spin–orbit coupling in hybrid organic/inorganic perovskites for photovoltaic applications," *J. Phys. Chem. Lett.*, vol. 4, no. 17, pp. 2999–3005, 2013.

[229] P. Umari, E. Mosconi, and F. De Angelis, "Relativistic gw calculations on ch3nh3pbi3 and ch3nh3sni3 perovskites for solar cell applications," *Scientific Reports*, vol. 4, p. 4467, 2014.

[230] M. Kepenekian and J. Even, "Rashba and dresselhaus couplings in halide perovskites: Accomplishments and opportunities for spintronics and spin–orbitronics," *J. Phys. Chem. Lett.*, vol. 8, no. 14, pp. 3362–3370, 2017.

[231] J. Yin, H. Li, D. Cortecchia, C. Soci, and J.-L. Brédas, "Excitonic and polaronic properties of 2d hybrid organic–inorganic perovskites," *ACS Energy Letters*, vol. 2, no. 2, pp. 417–423, 2017.

[232] D. Cortecchia, J. Yin, A. Bruno, S.-Z. A. Lo, G. G. Gurzadyan, S. Mhaisalkar, J.-L. Bredas, and C. Soci, "Polaron self-localization in white-light emitting hybrid perovskites," *J. Mater. Chem. C*, vol. 5, pp. 2771–2780, 2017.

[233] L. Mao, Y. Wu, C. C. Stoumpos, B. Traore, C. Katan, J. Even, M. R. Wasielewski, and M. G. Kanatzidis, "Tunable white-light emission in single-cation-templated three-layered 2d perovskites (ch3ch2nh3)4pb3br10–xclx," *J Am Chem Soc*, vol. 139, no. 34, pp. 11956–11963, 2017.

[234] K.-z. Du, Q. Tu, X. Zhang, Q. Han, J. Liu, S. Zauscher, and D. B. Mitzi, "Two-dimensional lead(ii) halide-based hybrid perovskites templated by acene alkylamines: Crystal structures, optical properties, and piezoelectricity," *Inorg Chem*, vol. 56, no. 15, pp. 9291–9302, 2017.

[235] J. Leveillee, C. Katan, L. Zhou, A. D. Mohite, J. Even, S. Tretiak, A. Schleife, and A. J. Neukirch, "Influence of π-conjugated cations and halogen substitution on the optoelectronic and excitonic properties of layered hybrid perovskites," *Phys. Rev. Materials*, vol. 2, p. 105406, 2018.

[236] J. P. Perdew and Y. Wang, "Accurate and simple analytic representation of the electron-gas correlation energy," *Phys. Rev. B*, vol. 45, pp. 13244–13249, 1992.

[237] A. V. Krukau, O. A. Vydrov, A. F. Izmaylov, and G. E. Scuseria, "Influence of the exchange screening parameter on the performance of screened hybrid functionals," *J. Chem. Phys.*, vol. 125, no. 22, p. 224106, 2006.

[238] G. Kresse, M. Marsman, and Furthmüller, "Vasp: The guide," 2016. VASP Manual, available at http://cms.mpi.univie.ac.at/vasp/vasp/vasp.html.

[239] E. A. Muljarov, S. G. Tikhodeev, N. A. Gippius, and T. Ishihara, "Excitons in self-organized semiconductor/insulator superlattices: Pbi-based perovskite compounds," *Phys. Rev. B*, vol. 51, pp. 14370–14378, 1995.

[240] S.-L. Chuang, S. Schmitt-Rink, D. A. B. Miller, and D. S. Chemla, "Exciton green's-function approach to optical absorption in a quantum well with an applied electric field," *Phys. Rev. B*, vol. 43, pp. 1500–1509, 1991.

[241] W. G. Schmidt, S. Glutsch, P. H. Hahn, and F. Bechstedt, "Efficient $\mathcal{O}(N^2)$ method to solve the Bethe-Salpeter equation," *Phys. Rev. B*, vol. 67, p. 085307, 2003.

[242] D. G. Billing, "Bis(1-PhenylEthylAmmonium) TetraIodoPlumbate(II)," *Acta Crystallogr E*, vol. 58, pp. m669–m671, 2002.

[243] K. Shibuya, M. Koshimizu, F. Nishikido, H. Saito, and S. Kishimoto, "Poly[bis(PhenethylAmmonium) [diBromidoPlumbate(II)]-di-μ-Bromido]]," *Acta Crystallogr E*, vol. 65, no. 11, pp. m1323–m1324, 2009.

[244] "A layered solution crystal growth technique and the crystal structure of (c6h5c2h4nh3)2pbcl4," *Journal of Solid State Chemistry*, vol. 145, no. 2, pp. 694 – 704, 1999.

[245] A. Fraccarollo, V. Cantatore, G. Boschetto, L. Marchese, and M. Cossi, "Ab initio modeling of 2d layered organohalide lead perovskites," *J Chem Phys*, no. 16, p. 164701, 2016.

[246] B. Joseph, B. Tonio, E. D. A., H. Gary, K. Leeor, L. Yueh-Lin, L. Igor, M. S. R., M. Yitzhak, M. J. S., M. D. B., P. Yaron, R. A. M., R. Ilan, R. Boris, S. Oscar, S. Vladan, T. M. F., Z. David, K. Antoine, G. David, and C. David, "Hybrid organic–inorganic perovskites (hoips): Opportunities and challenges," *Adv Mater*, vol. 27, no. 35, pp. 5102–5112, 2015.

[247] W. Martin, A. Musgrove, J. Kotochigova, and J. Sansonetti, "Ground levels and ionization energies for the neutral atoms," *National Institute of Standards and Technology*, 2013.

[248] T. Inagaki, "Absorption spectra of pure liquid benzene in the ultraviolet region," *J Chem Phys*, vol. 57, no. 6, pp. 2526–2530, 1972.

[249] E. Hanamura, "Rapid radiative decay and enhanced optical nonlinearity of excitons in a quantum well," *Phys. Rev. B*, vol. 38, pp. 1228–1234, 1988.

[250] T. Ishihara, J. Takahashi, and T. Goto, "Optical properties due to electronic transitions in two-dimensional semiconductors $(c_nh_{2n+1}nh_3)_2pbi_4$," *Phys. Rev. B*, vol. 42, pp. 11099–11107, 1990.

[251] T. Ishihara, J. Takahashi, and T. Goto, "Exciton state in two-dimensional perovskite semiconductor (c10h21nh3)2pbi4," *Solid State Communications*, vol. 69, no. 9, pp. 933 – 936, 1989.

[252] I. B. Koutselas, L. Ducasse, and G. C. Papavassiliou, "Electronic properties of three- and low-dimensional semiconducting materials with pb halide and sn halide units," *Journal of Physics: Condensed Matter*, vol. 8, no. 9, p. 1217, 1996.

[253] K. Galkowski, A. Mitioglu, A. Miyata, P. Plochocka, O. Portugall, G. E. Eperon, J. T.-W. Wang, T. Stergiopoulos, S. D. Stranks, H. J. Snaith, and R. J. Nicholas, "Determination of the exciton binding energy and effective masses for methylammonium and formamidinium lead tri-halide perovskite semiconductors," *Energy Environ. Sci.*, vol. 9, pp. 962–970, 2016.

[254] M. J. Frisch, G. W. Trucks, H. B. Schlegel, G. E. Scuseria, M. A. Robb, J. R. Cheeseman, G. Scalmani, V. Barone, G. A. Petersson, H. Nakatsuji, X. Li, M. Caricato, A. V. Marenich, J. Bloino, B. G. Janesko, R. Gomperts, B. Mennucci, H. P. Hratchian, J. V. Ortiz, A. F. Izmaylov, J. L. Sonnenberg, D. Williams-Young, F. Ding, F. Lipparini, F. Egidi, J. Goings, B. Peng, A. Petrone, T. Henderson, D. Ranasinghe, V. G. Zakrzewski, J. Gao, N. Rega, G. Zheng, W. Liang, M. Hada, M. Ehara, K. Toyota, R. Fukuda, J. Hasegawa, M. Ishida, T. Nakajima, Y. Honda, O. Kitao, H. Nakai, T. Vreven, K. Throssell, J. A. Montgomery, Jr., J. E. Peralta, F. Ogliaro, M. J. Bearpark, J. J. Heyd, E. N. Brothers, K. N. Kudin,

V. N. Staroverov, T. A. Keith, R. Kobayashi, J. Normand, K. Raghavachari, A. P. Rendell, J. C. Burant, S. S. Iyengar, J. Tomasi, M. Cossi, J. M. Millam, M. Klene, C. Adamo, R. Cammi, J. W. Ochterski, R. L. Martin, K. Morokuma, O. Farkas, J. B. Foresman, and D. J. Fox, "Gaussian˜16 Revision B.01," 2016. Gaussian Inc. Wallingford CT.

[255] Q. Wang, X.-D. Liu, Y.-H. Qiu, K. Chen, L. Zhou, and Q.-Q. Wang, "Quantum confinement effect and exciton binding energy of layered perovskite nanoplatelets," *AIP Advances*, vol. 8, no. 2, p. 025108, 2018.

[256] J. C. Blancon, A. V. Stier, H. Tsai, W. Nie, C. C. Stoumpos, B. Traoré, L. Pedesseau, M. Kepenekian, F. Katsutani, G. T. Noe, J. Kono, S. Tretiak, S. A. Crooker, C. Katan, M. G. Kanatzidis, J. J. Crochet, J. Even, and A. D. Mohite, "Scaling law for excitons in 2d perovskite quantum wells," *Nature Communications*, vol. 9, no. 1, p. 2254, 2018.

[257] M. L. Tiago, J. E. Northrup, and S. G. Louie, "Ab initio calculation of the electronic and optical properties of solid pentacene," *Phys. Rev. B*, vol. 67, p. 115212, 2003.

[258] D. Jacquemin, I. Duchemin, and X. Blase, "Benchmarking the bethe–salpeter formalism on a standard organic molecular set," *J Chem Theory Comp*, vol. 11, no. 7, pp. 3290–3304, 2015. PMID: 26207104.

[259] "Computational chemistry comparison and benchmark data base," *The Journal of Chemical Physics*, 2013. Computational Chemistry Comparison and Benchmark Data Base from National Institute of Standards and Technology available at https://cccbdb.nist.gov/gap1.asp.

[260] O. J. Weber, K. L. Marshall, L. M. Dyson, and M. T. Weller, "Structural Diversity in Hybrid Organic–Inorganic Lead Iodide Materials," *Acta. Crystallogr. B*, vol. 71, pp. 668–678, 2015.

[261] T. S. van der Poll, A. Zhugayevych, E. Chertkov, R. C. Bakus, J. E. Coughlin, S. J. Teat, G. C. Bazan, and S. Tretiak, "Polymorphism of crystalline molecular donors for solution-processed organic photovoltaics," *J Phys Chem Lette*, vol. 5, no. 15, pp. 2700–2704, 2014. PMID: 26277966.

[262] S. Shao, J. Liu, G. Portale, H.-H. Fang, G. R. Blake, G. H. ten Brink, L. J. A. Koster, and M. A. Loi, "Highly reproducible sn-based hybrid perovskite solar cells with 9% efficiency," *Advanced Energy Materials*, vol. 8, no. 4, p. 1702019, 2017.

[263] X. Yang, X. Zhang, J. Deng, Z. Chu, Q. Jiang, J. Meng, P. Wang, L. Zhang, Z. Yin, and J. You, "Efficient green light-emitting diodes based on quasi-two-dimensional composition and phase engineered perovskite with surface passivation," *Nat Comm*, vol. 9, no. 1, p. 570, 2018.

[264] K. Jemli, P. Audebert, L. Galmiche, G. Trippé-Allard, D. Garrot, J.-S. Lauret, and E. Deleporte, "Two-dimensional perovskite activation with an organic luminophore," *ACS Appl. Mater. Interfaces*, vol. 7, no. 39, pp. 21763–21769, 2015. PMID: 26340054.

[265] H. Uoyama, K. Goushi, K. Shizu, H. Nomura, and C. Adachi, "Highly efficient organic light-emitting diodes from delayed fluorescence," *Nature*, vol. 492, pp. 234–238, 2012.

[266] C. X. Sheng, S. Singh, A. Gambetta, T. Drori, M. Tong, S. Tretiak, and Z. V. Vardeny, "Ultrafast intersystem-crossing in platinum containing -conjugated polymers with tunable spin-orbit coupling," *Sci. Rep.*, vol. 3, p. 2653, 2013.

[267] J. Gebhardt, Y. Kim, and A. M. Rappe, "Influence of the dimensionality and organic cation on crystal and electronic structure of organometallic halide perovskites," *The Journal of Physical Chemistry C*, vol. 121, no. 12, pp. 6569–6574, 2017.

[268] C. Katan, N. Mercier, and J. Even, "Quantum and dielectric confinement effects in lower-dimensional hybrid perovskite semiconductors," *Chem. Rev.*, vol. 119, no. 5, pp. 3140–3192, 2019.

[269] M. Braun, W. Tuffentsammer, H. Wachtel, and H. Wolf, "Tailoring of energy levels in lead chloride based layered perovskites and energy transfer between the organic and inorganic planes," *Chemical Physics Letters*, vol. 303, no. 1, pp. 157 – 164, 1999.

[270] P. Tamarat, M. I. Bodnarchuk, J.-B. Trebbia, R. Erni, M. V. Kovalenko, J. Even, and B. Lounis, "The ground exciton state of formamidinium lead bromide perovskite nanocrystals is a singlet dark state," *Nature Materials*, 2019.

[271] F. Thouin, D. A. Valverde-Chávez, C. Quarti, D. Cortecchia, I. Bargigia, D. Beljonne, A. Petrozza, C. Silva, and A. R. Srimath Kandada, "Phonon coherences reveal the polaronic character of excitons in two-dimensional lead halide perovskites," *Nature Materials*, vol. 18, no. 4, pp. 349–356, 2019.

[272] K. Tanaka, T. Takahashi, T. Kondo, K. Umeda, K. Ema, T. Umebayashi, K. Asai, K. Uchida, and N. Miura, "Electronic and excitonic structures of inorganic–organic perovskite-type quantum-well crystal (c4h9nh3)2pbbr4," *Japanese Journal of Applied Physics*, vol. 44, pp. 5923–5932, aug 2005.

[273] T. Jüstel, S. Möller, H. Winkler, and W. Adam, *Luminescent Materials*. 2012.

[274] I. Frank, J. Hutter, D. Marx, and M. Parrinello, "Molecular dynamics in low-spin excited states," *The Journal of Chemical Physics*, no. 10, pp. 4060–4069, 1998.

[275] S. Grimm, C. Nonnenberg, and I. Frank, "Restricted open-shell kohn–sham theory for –* transitions. i. polyenes, cyanines, and protonated imines," *The Journal of Chemical Physics*, vol. 119, no. 22, pp. 11574–11584, 2003.

[276] J. Gavnholt, T. Olsen, M. Engelund, and J. Schiøtz, "Δ self-consistent field method to obtain potential energy surfaces of excited molecules on surfaces," *Phys. Rev. B*, vol. 78, p. 075441, Aug 2008.

[277] J. S. Sears, T. Koerzdoerfer, C.-R. Zhang, and J.-L. Brédas, "Communication: Orbital instabilities and triplet states from time-dependent density functional theory and long-range corrected functionals," *The Journal of Chemical Physics*, vol. 135, no. 15, p. 151103, 2011.

[278] J. V. Passarelli, D. J. Fairfield, N. A. Sather, M. P. Hendricks, H. Sai, C. L. Stern, and S. I. Stupp, "Enhanced out-of-plane conductivity and photovoltaic performance in n = 1 layered perovskites through organic cation design," *Journal of the American Chemical Society*, vol. 140, no. 23, pp. 7313–7323, 2018.

[279] A. D. Becke, "Density-functional thermochemistry. iii. the role of exact exchange," *The Journal of Chemical Physics*, vol. 98, no. 7, pp. 5648–5652, 1993.

[280] D. J. Tozer and N. C. Handy, "On the determination of excitation energies using density functional theory," *Phys. Chem. Chem. Phys.*, vol. 2, pp. 2117–2121, 2000.

[281] M. Casida, A. Ipatov, and F. Cordova, *Linear-Response Time-Dependent Density Functional Theory for Open-Shell Molecules*, pp. 243–257. Berlin, Heidelberg: Springer Berlin Heidelberg, 2006.

[282] C. A. Guido, S. Knecht, J. Kongsted, and B. Mennucci, "Benchmarking time-dependent density functional theory for excited state geometries of organic molecules in gas-phase and in solution," *Journal of Chemical Theory and Computation*, vol. 9, no. 5, pp. 2209–2220, 2013.

[283] J. Heyd, G. E. Scuseria, and M. Ernzerhof, "Hybrid functionals based on a screened coulomb potential," *The Journal of Chemical Physics*, vol. 118, no. 18, pp. 8207–8215, 2003.

[284] T. Yanai, D. P. Tew, and N. C. Handy, "A new hybrid exchange–correlation functional using the coulomb-attenuating method (cam-b3lyp)," *Chemical Physics Letters*, vol. 393, no. 1, pp. 51 – 57, 2004.

[285] J. Tomasi, B. Mennucci, and R. Cammi, "Quantum mechanical continuum solvation models," *Chemical Reviews*, vol. 105, no. 8, pp. 2999–3094, 2005.

[286] S. Grimme, "Semiempirical gga-type density functional constructed with a long-range dispersion correction," *Journal of Computational Chemistry*, vol. 27, no. 15, pp. 1787–1799, 2006.

[287] H. Ishikawa and W. A. Noyes, "The triplet state of benzene," *Journal of the American Chemical Society*, vol. 84, no. 8, pp. 1502–1503, 1962.

[288] W. M. Flicker, O. A. Mosher, and A. Kuppermann, "Triplet states of furan, thiophene, and pyrrole," *Chemical Physics Letters*, vol. 38, no. 3, pp. 489 – 492, 1976.

[289] R. M. Hochstrasser and A. P. Marchetti, "Electronic, vibrational, and zeeman spectra of triplet no2," *J. Chem Phys.*, vol. 50, no. 4, pp. 1727–1736, 1969.

[290] M. Head-Gordon, J. A. Pople, and M. J. Frisch, "Mp2 energy evaluation by direct methods," *Chemical Physics Letters*, vol. 153, no. 6, pp. 503 – 506, 1988.

[291] B. Cullity and S. Stock, *Elements of X-ray Diffraction, Third Edition*. Prentice-Hall, 2001.

[292] H. M. Mande, P. S. Ghalsasi, and A. Navamoney, "Synthesis, structural and spectroscopic characterization of the thermochromic compounds a2cucl4: [(naphthyl ethylammonium)2cucl4]," *Polyhedron*, vol. 91, pp. 141 – 149, 2015.

[293] A. Lemmerer, *Phase transitions and structural motifs of inorganic-organic lead halide hybrids*. PhD thesis, University of the Witwatersrand, Johannesburg, 2008.

[294] D. Y. Qiu, F. H. da Jornada, and S. G. Louie, "Optical spectrum of mos_2: Many-body effects and diversity of exciton states," *Phys. Rev. Lett.*, vol. 111, p. 216805, 2013.

[295] P. Avakian and R. E. Merrifield, "Triplet excitons in anthracene crystals – a review," *Molecular Crystals*, vol. 5, no. 1, pp. 37–77, 1968.

[296] C. Joblin, F. Salama, and L. Allamandola, "Absorption and emission spectroscopy of perylene (c20h12) isolated in ne, ar, and n2 matrices," *The Journal of Chemical Physics*, vol. 110, no. 15, pp. 7287–7297, 1999.